
Droplets and Supersolids in Dipolar Bose-Einstein Condensates

विद्या वाचस्पति की
उपाधि की अपेक्षाओं की आंशिक पूर्ति में प्रस्तुत शोध प्रबंध

*A thesis submitted in partial fulfillment of the requirements
for the degree of Doctor of Philosophy*

द्वारा / By

रथीजित घोष / Ratheejit Ghosh

पंजीकरण सं. / Registration No.: 20182014

शोध प्रबंध पर्यवेक्षक / Thesis Supervisor:

डॉ. रेजिश नाथ / Dr. Rejish Nath



भारतीय विज्ञान शिक्षा एवं अनुसंधान संस्थान पुणे

INDIAN INSTITUTE OF SCIENCE EDUCATION AND RESEARCH
PUNE

2025

Certificate

Certified that the work incorporated in the thesis entitled "Droplets and Supersolids in Dipolar Bose-Einstein Condensates" submitted by **Ratheejit Ghosh** was carried out by the candidate, under my supervision. The work presented here or any part of it has not been included in any other thesis submitted previously for the award of any degree or diploma from any other university or institution.

Date: July 29, 2025



(Dr. Rejish Nath)
Supervisor

Declaration of Authorship

Name of Student : Ratheejit GHOSH
Reg. No. : 20182014
Thesis Supervisor : Dr. Rejish NATH
Department : Physics
Date of joining program : August 01, 2018
Date of Pre-Synopsis Seminar : February 20, 2025

Title of Thesis: Droplets and Supersolids in Dipolar Bose-Einstein Condensates

I declare that this written submission represents my idea in my own words and where others' ideas have been included; I have adequately cited and referenced the original sources. I declare that I have acknowledged collaborative work and discussions wherever such work has been included. I also declare that I have adhered to all principles of academic honesty and integrity and have not misrepresented or fabricated or falsified any idea/data/fact/source in my submission. I understand that violation of the above will be cause for disciplinary action by the Institute and can also evoke penal action from the sources which have thus not been properly cited or from whom proper permission has not been taken when needed.

The work reported in this thesis is the original work done by me under the guidance of Dr. Rejish Nath.

Date: 31.07.2025

Signature: Ratheejit Ghosh

Dedicated to my dear Thakur, grandmother and parents.

Acknowledgements

I would like to express my sincere gratitude to the individuals and institutions who have supported me throughout my doctoral studies.

First and foremost, I am profoundly grateful to my supervisor, Dr. Rejish Nath, for his unwavering support, insightful guidance, and encouragement. His guidance fostered a strong foundation for critical thinking and nurtured my growth as an independent and collaborative researcher. I deeply appreciate his immense patience and the stimulating and supportive environment.

My sincere thanks also go to Dr. Chinmayee Mishra for her valuable suggestions, insightful feedback, and engaging discussions during the initial phase of my Ph.D.

I extend my gratitude to Prof. Luis Santos for the opportunity to collaborate and for his constructive comments on one of the projects included in this thesis.

I am also thankful to Dr. Fabio Cinti and Dr. Matteo Ciardi for their fruitful collaboration on another research project. Their expertise, insightful input, and sustained encouragement were pivotal to the successful completion of our work. It was a pleasure to learn from their experience and collaborate with them.

I would also like to thank the members of my research advisory committee, Prof. M.S. Santhanam and Dr. Bijay Kumar Agarwalla, for their valuable feedback, guidance, and continuous support throughout my progress evaluations.

I gratefully acknowledge the financial support provided by IISER Pune and I-HUB Quantum Technology Foundation during my doctoral studies. I appreciate the assistance of the Physics office staff and the administrative department, whose support ensured that all official work proceeded smoothly. I also thank the Infosys Travel Grant and the Anusandhan National Research Foundation International Travel Support scheme for supporting my participation in national and international conferences, which provided me the opportunity to present my work and engage with the broader research community.

I thank National Supercomputing Mission (NSM) for providing computing resources of “PARAM Brahma” at IISER Pune, which is implemented by C-DAC and supported by the Ministry of Electronics and Information Technology (MeitY) and Department of Science and Technology (DST), Government of India. PARAM Brahma has been instrumental in the heavy computational simulations throughout my Ph.D.

I am grateful to all past and present members of our research group for fostering a stimulating and supportive environment. I extend a special thanks to my seniors, Chinmayee, Yashwant, and Ankita, for their guidance and for creating a welcoming atmosphere. I would also like to thank Sandra, Dhiya, Siddharth, Inderpreet, Gopal, Pranay, Vighnesh, Varna, Ashwath, and Nargis for the engaging discussions on physics and the enjoyable moments and fun. I appreciate the opportunity to learn and discuss with Kumar, Salman, Ashutosh, Shreyas, Gautam, Keshav, Vaishakh, Anupam, Shobhana, Paramjeet, and Manish during our group meetings. I thank Vishal, Soumik, and Hrushikesh for their discussions and for providing motivation.

I would also like to express my gratitude for the invaluable time spent outside of my research. I will always cherish the time in the hostel, particularly the shared cooking times and bike trips with Arnab and Tamaghna. I was fortunate to have a supportive community of seniors and juniors, including Arunabha, Aslam, Ajit, Dipta, Abhijit, Sagnik, Sanjit, Amit da, Sadhu da, Pradyut, Sumit, Panda, Sayan, Pratim, Sudipto, Maity, Rahul, Uttaran, Souradeep, Kaustabh, Deepak, and Unmesh, with whom I shared many enjoyable moments. I am also thankful for the companionship of my batchmates Saurabh, Dhruv, Anant, Loveleen, Subhayan, Ritwik, Sajid, Narayanan, and Karthik, as well as other friends, Basava and Abhishek. A special note of thanks goes to Sandra, who was a constant source of motivation and support throughout my Ph.D. journey. The hours spent playing at the IISER Pune cricket ground were a constant source of inspiration and balance for me. I am grateful to the many friends I made there, including Projjwal da, Sakil, Prasun, Krishnendu, Pulak, Dipnajan, Ajad, Deep, Kartik da, Alok Mishra, Avinash, Arhum, Sukanya, Joyeeta, Manjeet, Onkar, Manzoor, Soumendu da, and Partha da, from whom I gained valuable life experiences.

Most importantly, I owe my deepest gratitude to my parents and grandparents, whose unconditional love, sacrifices, and encouragement have been the foundation of my academic pursuits. I am also thankful to my Guru and Acharya Dev for consistently guiding me on the right path in life. I would like to express my gratitude to Sanjib sir for his mentorship and encouragement to pursue research in Physics. Finally, I extend my heartfelt thanks to my close friends, including Akash, Anurag, Sayan Ghosh, Neelabha, Souvik, and Soumya, for their invaluable support and friendship throughout this journey.

List of Publications

Included in the thesis:

- *Droplet arrays in doubly dipolar Bose-Einstein condensates.*
Ratheejit Ghosh, Chinmayee Mishra, Luis Santos, and Rejish Nath
Phys. Rev. A, 2022
<https://link.aps.org/doi/10.1103/PhysRevA.106.063318>
- *Path integral Monte Carlo study of a doubly dipolar Bose gas.*
Ratheejit Ghosh, Matteo Ciardi, Rejish Nath, and Fabio Cinti
Phys. Rev. B, 2024
<https://link.aps.org/doi/10.1103/PhysRevB.110.014513>
- *Dilute supersolids in rotating dipolar Bose-Einstein Condensates.*
Ratheejit Ghosh and Rejish Nath
**Manuscript under preparation, 2025*

Not included in the thesis:

- *Density engineering via intercondensate dipole-dipole interactions.*
Pranay Nayak*, **Ratheejit Ghosh*** and Rejish Nath
Phys. Rev. A, 2024
<https://doi.org/10.1103/PhysRevA.110.053319>
(*Equal contribution)
- *Stripe and checkerboard patterns in a stack of driven quasi-one-dimensional dipolar condensates.*
Shreyas Nadiger, Sandra M. Jose, **Ratheejit Ghosh**, Inderpreet Kaur and Rejish Nath
Phys. Rev. A, 2024
<https://link.aps.org/doi/10.1103/PhysRevA.109.033309>

- *Soliton dimer-soliton scattering in coupled quasi-one-dimensional dipolar Bose-Einstein condensates.*

Gautam Hegde, Pranay Nayak, **Ratheejit Ghosh**, and Rejish Nath

Journal of Physics B: Atomic, Molecular and Optical Physics, 2021

<https://doi.org/10.1088/1361-6455/ac3370>

Contents

Acknowledgements	ix
List of Publications	xiii
Abstract	xxiii
1 Introduction and Background	1
1.1 Introduction	1
1.2 Long-range Interactions	3
Definition of long-range	4
1.3 Dipole-Dipole Interaction	4
Long-range nature	5
Anisotropic nature	6
Electric dipoles	6
Magnetic dipoles	7
1.4 Dipolar Quantum Gases	9
Dipolar Bose quantum gases	9
Dipolar Fermi quantum gases	10
Diverse platforms for dipolar quantum gases	12
1.5 Dipolar Bose-Einstein Condensates	12
1.5.1 Bose-Einstein condensates	13
Ideal Bose gas	13
Weakly interacting BEC	14
Gross-Pitaevskii equation	15
1.5.2 Nonlocal Gross-Pitaevskii equation	17
1.5.3 Roton minima	19
1.5.4 Beyond mean-field: LHY corrections	21
Generalized Gross-Pitaevskii equation	21
1.5.5 Quantum droplets	22
1.6 Supersolids	24
1.7 Quantized Vortices	29
1.7.1 Hydrodynamic theory of vortices	30

1.7.2	Quantized vortices in superfluids	31
1.7.3	Vortices in Bose-Einstein condensates	33
1.7.4	Experimental generation of vortices in BEC	33
1.7.5	Quantized vortices in dipolar condensates	34
1.7.6	Quantized vortices in supersolids	35
1.8	Outline of the Thesis	36
2	Doubly Dipolar Bose-Einstein Condensate: Setup and Methodologies	39
2.1	Introduction	39
2.2	Dysprosium Atoms under Magnetic & Electric Fields	40
2.2.1	The Dysprosium atom	40
2.2.2	Doubly dipolar interactions in Dy atoms	41
2.2.3	Experimental realization of doubly dipolar Dy atoms	43
2.3	Doubly Dipolar Potential	44
2.4	Doubly Dipolar BEC	47
2.4.1	Bogoliubov excitations and sound velocity in a homogeneous doubly DBEC	47
2.4.2	Lee-Huang-Yang correction	49
2.4.3	Generalized Gross-Pitaevskii equation	50
2.5	Path Integral Monte Carlo Simulation	51
2.5.1	Classical action and Lagrangian	51
2.5.2	Quantum path integral	52
2.5.3	Thermal density matrix	53
2.5.4	Worm algorithm	57
2.5.5	Measurement of observables	58
2.5.6	Model for the doubly dipolar Bose gas	59
	Energy	60
	Superfluid fraction: area estimator	61
3	Quantum Droplet in Doubly Dipolar Bose-Einstein Condensates	65
3.1	Introduction	65
3.2	Self-Bound Quantum Droplet	67
3.2.1	Variational analysis	67
3.2.2	Anisotropic properties of a self-bound droplet	70
3.3	Doubly Dipolar Bose Gas at Finite Temperatures	72
3.3.1	Ground state transition	73
	Convergence with time slices	74
	PIMC vs gGPE comparison	76
3.3.2	Superfluid fraction across BEC-droplet transition	77

3.3.3	Doubly dipolar gas with varying temperatures	79
	Thermal gas to DDBEC transition	79
	Thermal gas to pancake droplet transition	81
3.3.4	Structural transition with varying electric dipole moment . .	82
3.4	Conclusion	84
4	Droplet Arrays and Supersolids in Doubly Dipolar Bose-Einstein Con-	
	densates	87
4.1	Introduction	87
4.2	Droplet Arrays and Supersolids	88
4.3	Weaker Confinement on the Dipole Plane	88
4.3.1	Physics of magnetic dipolar condensates	89
4.3.2	Finding the phase boundaries	90
4.3.3	Supersolid-supersolid transition	94
4.3.4	Single droplet and density-modulated droplets	95
4.3.5	Quasi one-dimensional DDBEC	97
	Effective Q1D excitation spectrum	97
4.4	Weak Confinement Perpendicular to the Dipole Plane	99
4.4.1	Pancake supersolids	100
4.5	Conclusion	102
5	Rotation-induced Supersolidity in Dipolar Bose Gases	103
5.1	Introduction	103
5.2	Dipolar Bose Gas in a Rotating Frame	105
5.2.1	GPE in the rotating frame	106
5.3	Ground-state Phases in the Rotating Frame	107
5.3.1	Ground-state phases	108
	Searching for the ground state:	108
	The different phases	108
	The angular momentum across ground-state transition . . .	111
	Signature of crystallization	113
5.4	Excitation Spectrum of a Q1D Homogeneous DBEC	113
5.4.1	Bogoliubov-de Gennes excitations	113
5.4.2	Effective Q1D Excitation Spectrum	114
5.5	Stability of the Rotating Dipolar Bose Gas	116
5.6	Effect of Trap Geometry	118
5.7	Conclusion	120

6 Conclusion	121
6.1 Summary	121
6.2 Outlook	123
A Beyond mean-field LHY corrections	125
B Path Integral Monte Carlo Algorithms	127
B.1 Discrete Path Integrals	127
B.2 Markov Chain and Metropolis Algorithm	129
B.3 PIMC Algorithm	131
B.4 Monte Carlo and worm algorithm moves	132
C Hamiltonian in the rotating frame	141
C.1 Unitary Operator for Rotation	141
C.2 Harmonic trap in the rotating frame	142
Bibliography	145

List of Figures

1.1	Dipole-dipole interaction between two particles	5
1.2	Bose-Einstein Condensate of Dysprosium	8
1.3	Quantum degenerate dipolar Fermi gas	10
1.4	BEC of dipolar NaCs molecules	17
1.5	Roton Minima of a dipolar BEC	19
1.6	Observation of dipolar quantum droplets	23
1.7	Scematic of droplets and supersolids	26
1.8	Dipolar supersolids	28
1.9	Observation of vortices in a dipolar BEC	34
1.10	Magnetostirring of a dipolar supersolid	35
2.1	Relevant atomic structures of Dy atom	40
2.2	Doubly dipolar Dysprosium	42
2.3	Doubly dipolar particles	44
2.4	Anisotropy of the doubly dipolar potential	45
2.5	Polarization angle	46
2.6	Attractive doubly dipolar potential and sound velocity	48
2.7	LHY correction and stability criteria	50
2.8	Worm Algorithm	57
3.1	Self-bound quantum droplets	69
3.2	Equilibrium widths of the droplets	71
3.3	Doubly dipolar gas	72
3.4	Convergence of energy with time slices	74
3.5	PIMC vs gGPE ground state results	75
3.6	Anisotropic superfluidity	78
3.7	Thermal gas to DDBEC transition	79
3.8	3D isodensity plots from PIMC simulations	80
3.9	Thermal gas to a pancake droplet transition	81
3.10	Structural transition of quantum droplet	83
4.1	Droplet arrays and supersolids	89

4.2	Ground state properties	91
4.3	Supersolid-supersolid transitions	93
4.4	Shape change of a single droplet	94
4.5	Modulated droplet	95
4.6	Various kinds of modulated droplets	96
4.7	Roton minima in DDBEC	98
4.8	Ground-state phase diagram as a function of scattering length and relative angle between the two dipole moments	99
4.9	Exotic supersolids in DDBEC	100
4.10	Novel pancake supersolids	101
5.1	Schematic diagram showing the rotation of a cigar-shaped dipolar Bose gas	105
5.2	Ground state phase diagram	107
5.3	Density and Phase plots	109
5.4	Supersolid-supersolid transition	110
5.5	Ground-state properties	112
5.6	Signature of crystallization	114
5.7	Dynamics of the kinetic energy and widths	117
5.8	Effect of trap geometry	119
5.9	Supersolids in different trap geometries	120
6.1	Thesis Summary	121
6.2	Vortex lines through supersolids	124
B.1	Open-Close move	134
B.2	Advance-recede move	136
B.3	Swap move	138

List of Abbreviations

BEC	B ose E instein C ondensate
DBEC	D ipolar B ose E instein C ondensate
DQG	D ipolar Q uantum G ases
DDI	D oubly D ipolar I nteraction
DDBEC	D oubly D ipolar B ose E instein C ondensate
EDM	E lectric D ipole M oment
MDM	M agnetic D ipole M oment
GPE	G ross P itaevskii E quation
GGPE	G eneralized G ross P itaevskii E quation
PIMC	P ath I ntegral M onte C arlo
WA	W orm A lgorithm
LHY	L ee H uang Y ang
Q1D	Q uasi O ne D imensional
SF	S uperfluid
SS	S upersolid
SFV	S uperfluid V ortex
SSV	S upersolid V ortex

Abstract

Ultracold quantum gases have emerged as a powerful platform for exploring complex quantum many-body physics due to their tunability and precise control. Engineering interatomic potentials via external fields leads to a wealth of exciting phenomena in ultracold gases. In particular, dipole-dipole interaction, characterized by its long-range and anisotropic nature, introduces intriguing physics. Notably, it leads to the formation of quantum droplets: self-bound liquid-like states stabilized by quantum fluctuations, and the fascinating supersolid phase, which simultaneously exhibits superfluidity and crystalline order.

We have investigated a unique scenario in cold atom physics, where a single atom possesses both the electric and magnetic dipole moments, leading to the prediction of doubly dipolar Bose-Einstein condensates (DDBEC). The additional control parameters of relative strength and orientation between the two dipole moments pave the pathway to realize a novel pancake quantum droplet, contrary to the typical cigar droplets in dipolar condensates.

Thermal fluctuations critically affect the properties of quantum gases. In this thesis, we explore the characteristics of a doubly dipolar Bose gas at finite temperatures, using quantum Monte Carlo techniques. Our investigation demonstrates the highly anisotropic superfluid behavior of a pancake droplet and the shift in critical temperature for condensation due to the doubly dipolar interactions.

The interplay between doubly dipolar interactions, quantum stabilization, and external confinement results in a rich ground-state physics of supersolids and incoherent droplet arrays in doubly dipolar condensates. Our research under a beyond-mean-field framework reveals the supersolid-supersolid transitions and the realization of a novel pancake array of supersolids. We also observe the formation of a single density-modulated droplet.

Finally, we have investigated the exciting possibility of creating a supersolid in dipolar Bose gases, without relying on the quantum stabilization. Rotating a dipolar condensate perpendicular to its dipole polarization direction, we observe the formation of mean-field dilute supersolids stabilized by the emergence of quantized vortex lines.

Chapter 1

Introduction and Background

1.1 Introduction

"Physics is the belief that a simple and consistent description of nature is possible."

—Niels Bohr

Since the early 20th century, quantum physics has revolutionised our understanding of the fundamental principles of physics. The advent of quantum mechanics has given rise to the exciting field of quantum many-body physics, which explores complex emergent phenomena arising from the collective behavior of numerous interacting quantum particles. Quantum many-body systems span various different branches of physics, and aim to understand phenomena ranging from superconductivity and magnetism to superfluidity and quantum phase transitions. They are also key to the development of new age quantum technologies. There are several experimental platforms to study quantum many-body physics, which include ultracold gases [1], trapped ions [2], superconducting qubits [3], and photonic crystals [4].

Among them, ultracold quantum gases have emerged as a powerful platform, due to their precise experimental control [1, 5, 6]. Since the experimental realization of Bose-Einstein Condensates (BEC) [7–9], and quantum degenerate Fermi gases [10–12], these systems have drawn significant interest within the physics community. The broad implications have been cited in several Nobel Prizes for this field in the last three decades. Recent research interests include the study of dipolar [13] & spinor [14] gases, Rydberg atoms [15], quantum gases in optical lattices [16], low-dimensional quantum gases [17], quantum gases under rotation, and polar molecules [18]. The advent of powerful experimental techniques such as Feshbach resonances [19], and quantum gas microscopy [20, 21] gives the ability to precisely control their interactions or even detect and manipulate a single atom in the experiments. It has led to several applications, including quantum simulation [5], atom interferometry [22], precision measurement [23], and modelling astrophysical phenomena [24].

Interparticle interactions play a fundamental role in determining the properties

of a quantum gas. Typically, quantum gases are dilute, and the low-energy scattering is basically given by the s-wave contribution, and hence the interaction potential can be replaced simply by a two-body (isotropic) contact pseudo-potential [25, 26]. The contact interparticle interactions can be tuned by varying the scattering length via Feshbach resonances [19, 27]. Electromagnetic fields [1, 28], optical dipole potentials [29, 30], and artificial gauge fields [31–33] enable external field control of ultracold gases. It is also possible to engineer long-range and anisotropic interatomic potentials via external fields [34]. In particular, dipole-dipole interactions are at the forefront, giving rise to the field of dipolar quantum gases (DQG). Since the experimental realization of BEC with magnetic Chromium (Cr) atoms in 2004, the study of quantum gases with dominant dipolar interactions has gained great interest in the last two decades. Dipole-dipole interactions lead to a wide variety of novel quantum phenomena, such as roton-like excitations, anisotropic superfluidity, quantum droplets, and the formation of fascinating supersolids [35–41]. Dipolar quantum gases include magnetic atoms [13, 42], polar molecules [43], and Rydberg atoms [15]. Unlike the magnetic atoms, the latter two systems possess electric dipole moments. In this thesis, we discuss a unique scenario in cold atom physics, where a single atom simultaneously possesses substantial electric and magnetic dipole moments [44]. Engineering this novel doubly dipolar potential in quantum gases has led to the prediction of the doubly dipolar Bose-Einstein condensate (DDBEC) [45, 46], and quantum spin models [47].

Temperature plays a key role and serves as a control knob to explore the properties of quantum gases. The advancement in combined laser and evaporative-cooling techniques [48] has made it possible to realize cold atoms in the nanokelvin (nk) regime. While at high temperatures, the kinetic energy of the particles is very high and the system is well-described by Maxwell-Boltzmann statistics, in the ultracold regime, the de Broglie wavelength becomes larger than the typical interparticle distance, and thus, quantum statistics governs the many-body dynamics of these systems. In a Bose gas, a thermodynamic phase transition from a thermal gas to a condensate occurs, driven by the particle statistics, even without the presence of any interaction. However, in any real system, the presence of interactions modifies the characteristics. Notably, the critical temperature for condensation is shifted in both short-range interacting [49] and dipolar interacting Bose gases [50]. An increase in temperature enhances the condensation depletion of an interacting Bose gas, which correspondingly reduces the condensate fraction [51]. Temperature also influences key properties like the superfluid response and collective oscillations of a quantum gas [52, 53]. The ability to precisely tune temperature leads to novel phenomena like, Berezinskii–Kosterlitz–Thouless (BKT) transition in Bose gases [54, 55] and

the Bardeen-Cooper-Schrieffer (BCS) pairing [56] and BEC of molecules [57] in Fermi gases. Intriguingly, thermal effects can also induce a supersolid phase by heating a dipolar superfluid [58]. In this thesis, we investigate the characteristics of the doubly dipolar Bose gases with varying temperatures.

Even at absolute zero temperature, quantum gases exhibit distinct quantum phases of matter due to the presence of inherent quantum fluctuations. These phases emerge from the microscopic interactions between the many elementary constituents. Advanced preparation and detection techniques of quantum states [59], interaction tuning via Feshbach resonances, and the implementation of optical lattices have enabled the realization of various quantum phases. The quantum phase transition between superfluid and Mott insulator [60–63], and between metallic and insulating phases [64] have been explored in bosonic and fermionic systems. Experiments with cold atomic platforms have demonstrated more exotic and nontrivial quantum phases, including symmetry-breaking spatially ordered states [65], antiferromagnetic phase [66], quantum spin liquids [67], Moiré crystals [68], and topologically nontrivial phases [69]. The long-range and anisotropic nature of dipolar interactions has led to the formation of novel phases of droplet crystals [70], supersolids [41, 71, 72], and dipolar quantum solids [73]. Rotating a quantum gas can also lead to the emergence of various quantum phases, such as quantized vortices and quantum Hall states [74]. These phases arise from the interplay of rotation and the complex behavior of interacting particles in a rotating frame. In this thesis, we predict the emergence of a supersolid phase in rotating dipolar Bose gases.

This thesis presents a theoretical investigation into exotic quantum phases that emerge in doubly dipolar condensates and rotating dipolar Bose gases. In this chapter, we first introduce the details of the long-range interactions and the characteristics of dipole-dipole interactions. Following that, we discuss the theoretical background and experimental progress in the field of dipolar quantum gases. Subsequently, we discuss the emergence of quantum droplets and supersolids in dipolar gases. Finally, we introduce the quantized vortices and their properties in rotating dipolar gases.

1.2 Long-range Interactions

Long-range interactions play a fundamental role across diverse physical, chemical, and biological systems, giving rise to emergent phenomena distinct from those observed in systems with only short-range interactions. Long-range interactions lead to galaxy clustering in cosmology [75], plasma formation in condensed matter systems [76], exotic quantum phases of droplets and supersolids in many-body quantum

systems [13], and also play a crucial role in the structural organization of protein fragments during protein folding [77], and charge transport in organic materials [78].

Definition of long-range

Long-range interaction can be defined by a two-body interaction potential that decays slowly with distance r , typically following a power law form,

$$V(r) \propto \frac{1}{r^\alpha}, \quad (1.1)$$

where α is the power exponent.

A key distinction between long-range and short-range interactions arises when α is smaller than the spatial dimension (D) of the system. In systems with short-range interactions, the total energy remains thermodynamically extensive, a condition that holds if the integral $\int_0^\infty V(r)d^D r$ converges, which occurs only if $\alpha > D$. Conversely, for $\alpha \leq D$, the interaction energy of homogeneous systems becomes infinite due to the divergent long-distance contribution, characterizing $V(r)$ as a long-range interaction [13, 34, 79]. The non-extensive nature of the internal energy in systems with long-range interactions leads to a breakdown of traditional thermodynamics. This gives rise to distinctive characteristics, including the non-equivalence of thermodynamic ensembles, the possibility for negative specific heat, and the spontaneous formation of structures. These effects arise due to the breakdown of the additivity assumption in the thermodynamic limit, i.e., the total energy of two subsystems, $E(A \cup B)$, is not simply the sum of their individual energies, $E(A) + E(B)$, when interactions between subsystems remain significant.

There are various systems in physics with long-range interactions, such as gravitational systems ($V(r) \propto -1/r$), Coulomb systems, and plasmas ($V(r) \propto 1/r$), magnetic dipoles and dipolar gases ($V(r) \propto 1/r^3$), multi-mode cavity QED systems and many more. In this thesis, we explore the effect of dipole-dipole interactions in ultracold quantum gases.

1.3 Dipole-Dipole Interaction

The interaction between two dipoles that are separated by a distance r (see Fig. 1.1 (a)) is described by:

$$V_{\text{dd}}(\mathbf{r}) = \frac{C_{\text{dd}}}{4\pi} \frac{\hat{\mathbf{d}}_1 \cdot \hat{\mathbf{d}}_2 - 3(\hat{\mathbf{d}}_1 \cdot \hat{\mathbf{r}})(\hat{\mathbf{d}}_2 \cdot \hat{\mathbf{r}})}{r^3}, \quad (1.2)$$

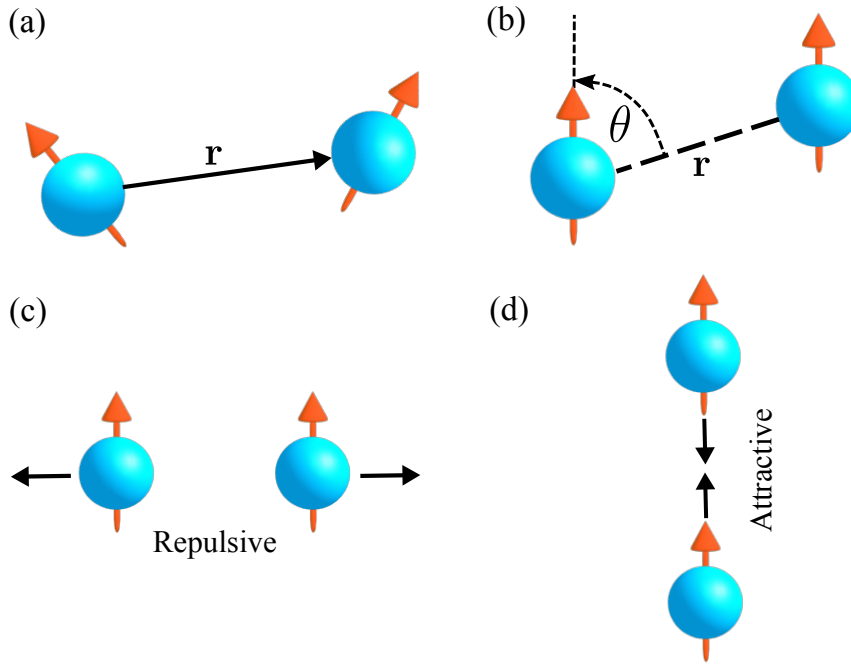


FIGURE 1.1: **Dipole-dipole interaction between two particles.** (a) Two unpolarized dipoles \mathbf{d}_1 and \mathbf{d}_2 . (b) Two polarized dipoles where θ is the angle between the polarization direction and the radial vector \mathbf{r} . The dipole-dipole interaction is repulsive for (c) side-by-side alignment ($\theta = \pi/2$) and (d) attractive for head-to-tail alignment ($\theta = 0$).

where $\hat{\mathbf{d}}_i = \mathbf{d}_i/|\mathbf{d}_i|$ and $\hat{\mathbf{r}} = \mathbf{r}/|\mathbf{r}|$. The coupling constant C_{dd} is $\mu_0 d_1 d_2$ for particles having magnetic dipole moments and $d_1 d_2 / \epsilon_0$ for particles having electric dipole moments with μ_0 and ϵ_0 being the permeability and permittivity of vacuum, respectively. For two particles polarized in the same direction (Fig. 1.1 (b)) the expression (1.2) simplifies to

$$V_{\text{dd}}(\mathbf{r}) = \frac{C_{\text{dd}}}{4\pi} \frac{1 - 3 \cos^2 \theta}{r^3}, \quad (1.3)$$

where θ is the angle between the dipole polarization direction and the radial vector joining the two dipoles.

Long-range nature

The dipole-dipole interaction follows a power law dependence of the form $r^{-\alpha}$ with $\alpha = 3$. As discussed in the previous section from a thermodynamic perspective, an interaction is considered long-range when $\alpha < D$ (the spatial dimension). Consequently, the dipole-dipole interaction exhibits a long-range character in three dimensions, whereas it remains short-range in one and two dimensions.

In the regime of ultra-cold temperatures, the long-range nature of the dipole-dipole interaction can also be understood from a quantum scattering point of view

[13, 36, 80]. For a general two-body interaction potential, $V(r) \propto 1/r^\alpha$, the low-momentum behavior of the scattering phase shift $\delta_l(k)$ for the l -th partial wave in the limit $k \rightarrow 0$ is given by,

$$\delta_l(k) \propto \begin{cases} k^{2l+1}, & \text{for } l < \frac{\alpha-3}{2} \\ k^{\alpha-2}, & \text{for } l \geq \frac{\alpha-3}{2}. \end{cases} \quad (1.4)$$

For interactions characterized by $\alpha \geq 4$, scattering at low energy is dominated by the s-wave ($l = 0$), indicating a short-range nature. In contrast, for $\alpha = 3$, $\delta_l(k) \propto k$ for all l . Therefore, all partial waves contribute to the scattering process even at low collision energy and the dipole-dipole interaction is long-range in nature. Moreover, due to its anisotropic character as discussed below, there is coupling between different partial waves.

Anisotropic nature

A key characteristic of the dipole-dipole interactions is their intrinsic anisotropy. The interaction can be attractive or repulsive depending on the relative position and orientation of the dipoles. For a simple understanding, consider two dipoles polarized in the same direction, as θ varies from 0 to $\pi/2$ the term $(1 - 3 \cos^2 \theta)$ varies between -2 and 1. Consequently, the dipole-dipole interaction is repulsive for particles sitting side by side, while it is attractive for dipoles in a ‘head-to-tail’ configuration (see 1.1(c,d)). The dipole-dipole interaction exhibits an attractive nature along one particular direction, while it is repulsive along the other two directions. The interaction’s form is characterized by a d -wave pattern, mathematically represented by the j components of the spherical harmonics, Y_2^j , in particular, $j = 0$ for a fully polarized situation. Due to this d -wave nature of the dipole-dipole interactions, it is not invariant under individual rotations of the spin or the orbital angular momentum. As a result, neither the total spin nor the total orbital angular momentum of the system is individually conserved. However, the total angular momentum remains conserved, as the interaction is symmetric under simultaneous rotations of both spin and orbital angular momentum.

Electric dipoles

In classical systems, an electric dipole moment (EDM) arises due to the spatial separation of opposite charges. In quantum mechanics, the EDM of a particle or a system is defined as the charge separation along its angular momentum axis. However, a stable elementary or composite particle cannot possess a permanent EDM unless both time-reversal and parity symmetries are violated [81–83].

Atoms and molecules in their non-degenerate rotational ground state don't possess EDM due to their rotational symmetry. When an electric field mixes states of opposite parity, a linear Stark shift occurs, the rotational symmetry is broken, and an electric dipole moment is induced [84, 85]. The strength of the induced EDM is maximized when the opposite-parity states are nearly degenerate. Some systems possess degenerate states of opposite parity, which allows the induced electric moment to arise at a vanishingly small electric field [86].

Examples of systems with permanent EDMs include polar molecules, where an electric field mixes two rotational states within the electronic molecular ground state. Ultracold polar molecules such as KRb, RbCs, NaRb, and NaCs, etc. possess large electric dipole moments. Similarly, Rydberg states in a hydrogen atom possesses electronically excited states of opposite parity that can be arbitrarily close. Associating a Rydberg atom with a ground-state atom allows the formation of a Rydberg molecule with a permanent electric dipole moment [87]. Another notable example is atomic Dysprosium (Dy), which has a pair of nearly degenerate energy levels of opposite parity with electronic angular momentum $J = 9$ and $J = 10$. An applied electric field can mix these levels, thereby inducing an electric dipole moment in the laboratory frame [44].

Magnetic dipoles

The magnetic dipole moment (MDM) manifests either as classical current loops or as a consequence of quantum mechanical spin and orbital angular momentum. In a rotating system of charged particles, the MDM is directly proportional to the system's angular momentum. For a current-carrying loop, the MDM is the product of the current (I) and the area (A) of the loop: $\mathbf{d}_m = IA\hat{n}$, \hat{n} is the normal vector to the plane of the loop. In quantum mechanics, the magnetic dipole moment is associated with the angular momentum of particles, given by:

$$\mathbf{d}_m = g \frac{q}{2m} \mathbf{J}, \quad (1.5)$$

where q and m are the charge and mass of the particle, \mathbf{J} is the total angular momentum, and g is called the Lande g -factor. For an orbiting electron, the constant $g = 1$, whereas the dipole moment associated with spin angular momentum has $g \sim 2$. The magnetic dipole moment in atoms is primarily attributed to the spin (\hat{S}) and orbital (\hat{L}) angular momentum of the electrons. An atomic dipole moment is calculated by summing all of the electron dipole moments for a given atomic species. Additionally, nuclei also possess magnetic dipole moments, though they are typically three orders

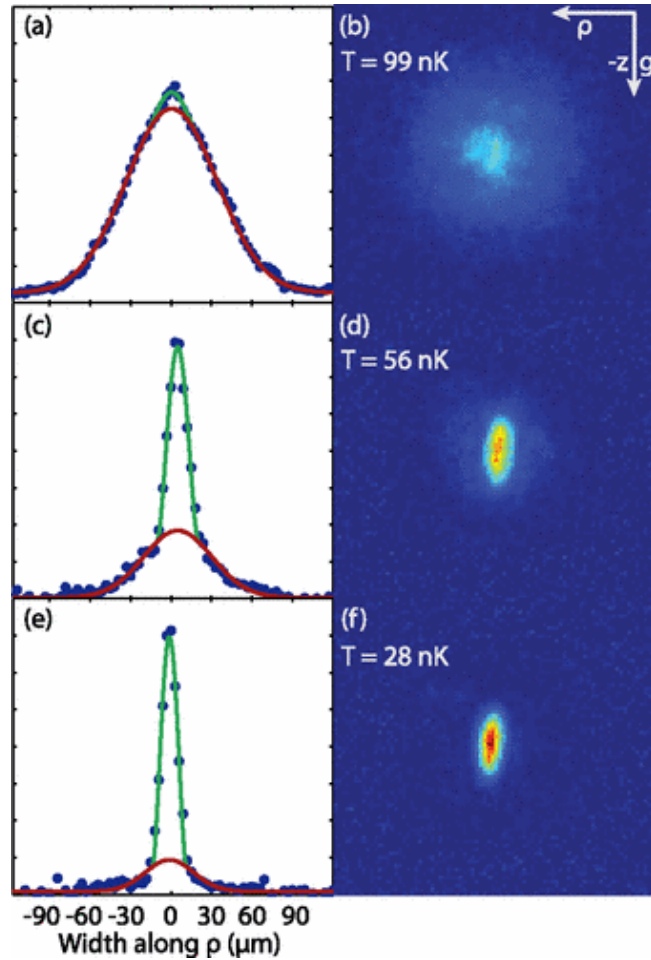


FIGURE 1.2: **Bose-Einstein Condensate of Dysprosium.** Time of flight profiles of Dysprosium gas for different evaporation rates. The left column shows the data, with a fit to a parabolic profile at centers, and a fit to a Gaussian profile at the wings. The right column shows the absorption images of the emerging BEC with the transition temperature at 99(5) nK. Reprinted with permission from [91] ©2011, American Physical Society.

of magnitude smaller than the electron's. The interaction of magnetic dipole moments with external magnetic fields leads to the Zeeman effect, where energy levels split in response to the applied field.

While alkali atoms provide a platform for studying dipolar physics, their magnetic dipole moment is relatively small, reaching a maximum of one Bohr magneton (μ_B). Significant progress has been achieved with highly magnetic atoms, particularly transition metals and lanthanides. Chromium (Cr) atoms exhibit a magnetic dipole moment of $6 \mu_B$ [88], while lanthanide (Ln) atoms like Erbium (Er; $6\mu_B$) [89, 90] and Dysprosium (Dy, $10\mu_B$) [91, 92] have been studied extensively due to their strong dipolar interactions. Other highly magnetic atoms include, holmium (Ho; $9\mu_B$) [93], thulium (Tm; $4\mu_B$) [94] or europium (Eu; $9\mu_B$) [95].

1.4 Dipolar Quantum Gases

Dipolar quantum gases have been thoroughly studied and experimentally realized in various systems; here we briefly discuss some of them.

Dipolar Bose quantum gases

Dipole-dipole interaction has heavily influenced the properties of weakly interacting Bose gases. To describe a system of dipolar bosons, the Hamiltonian is conveniently expressed using the formalism of second quantization. In this framework, we introduce the bosonic creation and annihilation field operators $\hat{\Psi}^\dagger(\mathbf{r})$ and $\hat{\Psi}(\mathbf{r})$ satisfying the standard commutation relation,

$$\begin{aligned} [\hat{\Psi}(\mathbf{r}), \hat{\Psi}^\dagger(\mathbf{r}')] &= \hat{\Psi}(\mathbf{r})\hat{\Psi}^\dagger(\mathbf{r}') - \hat{\Psi}^\dagger(\mathbf{r}')\hat{\Psi}(\mathbf{r}) = \delta(\mathbf{r} - \mathbf{r}'), \\ [\hat{\Psi}^\dagger(\mathbf{r}), \hat{\Psi}^\dagger(\mathbf{r}')] &= [\hat{\Psi}(\mathbf{r}), \hat{\Psi}(\mathbf{r}')] = 0. \end{aligned}$$

The corresponding second-quantized Hamiltonian of the system is given by,

$$\begin{aligned} \hat{H} &= \int d\mathbf{r} \hat{\Psi}^\dagger(\mathbf{r}) \left[-\frac{\hbar^2}{2m} + V_T(\mathbf{r}) - \mu \right] \hat{\Psi}(\mathbf{r}) \\ &+ \frac{1}{2} \int d^3\mathbf{r} d^3\mathbf{r}' \hat{\Psi}^\dagger(\mathbf{r}') \hat{\Psi}^\dagger(\mathbf{r}) V(\mathbf{r} - \mathbf{r}') \hat{\Psi}(\mathbf{r}') \hat{\Psi}(\mathbf{r}), \end{aligned} \quad (1.6)$$

where m is the mass of the bosons, $V_T(\mathbf{r})$ is the external trapping potential, μ is the chemical potential, and $V(\mathbf{r} - \mathbf{r}')$ is the interparticle interaction that contains both the short-range isotropic and long-range anisotropic interactions. It can be replaced by a pseudo-potential, $V(\mathbf{r}) = g\delta(\mathbf{r}) + V_{dd}(\mathbf{r})$. Here, $g = 4\pi\hbar^2 a_s/m$ is characterized by the s-wave scattering length. The a_s can have a dependence on the dipole moment d , near the scattering shape resonances [96–98]. The pseudo-potential has been shown to be valid away from these resonances [97, 98]. The dipole-dipole interaction $V_{dd}(\mathbf{r})$ between two particles is expressed as introduced in Eq. (1.3). For a homogeneous dipolar Bose gas to be stable against local collapses, the scattering length has to be positive, $a_s > 0$. The relative strength between the repulsive short-range and the dipole-dipole interactions plays a crucial role in determining the properties of the system. It is defined with the parameter,

$$\epsilon_{dd} = C_{dd}/3g = a_{dd}/a_s, \quad (1.7)$$

where $C_{dd} = \mu_0 d^2$ for magnetic dipoles and d^2/ϵ_0 for electric dipoles and $a_{dd} = C_{dd}m/3\hbar^2 a$ is called the *dipolar length*. For $\epsilon_{dd} < 1$, the dipolar interaction is weak

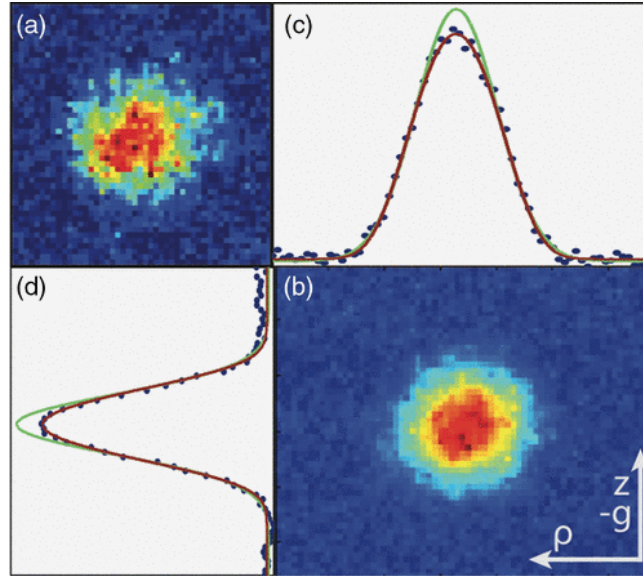


FIGURE 1.3: **Quantum degenerate dipolar Fermi gas.** (a) Single-shot time-of-flight absorption image at $t = 6$ ms. (b) Average of six images. Integrated density versus $\hat{\rho}$ (c) and \hat{z} (d). The Fermi velocity and temperature are 5.6(2) mm/s and 306(20) nK, respectively, and the gas temperature is 64(16) nK. Reprinted with permission from [92] ©2012, American Physical Society.

and the isotropic short-range interactions dominate the system; conversely, the dipolar interactions become dominant for $\epsilon_{dd} > 1$.

In the weakly dipole-dominated regime, a stable dipolar BEC is formed. Fig. 1.2 shows the formation of a condensate with magnetic Dy atoms, which was performed by M Lu et al. in 2011 [91]. In the regime of dominant dipole-dipole interactions, the partially attractive nature of the interaction leads to system instabilities and the emergence of dipolar droplets and supersolid phases. We will discuss these topics extensively in the subsequent sections.

Dipolar Fermi quantum gases

Dipolar interactions induce distinctive phenomena in Fermi gases. The key differences in the behavior of many-body fermionic systems as compared to bosonic ones are due to the Pauli exclusion principle, which prohibits identical fermions from occupying the same quantum state. Consequently, the many-body wave function of a Fermi gas should be antisymmetric under particle exchange. In second quantization field operators $\hat{\Psi}^\dagger(\mathbf{r})$ and $\hat{\Psi}(\mathbf{r})$ satisfy the canonical anticommutation relations,

$$\begin{aligned} \{\hat{\Psi}(\mathbf{r}), \hat{\Psi}^\dagger(\mathbf{r}')\} &= \hat{\Psi}(\mathbf{r})\hat{\Psi}^\dagger(\mathbf{r}') + \hat{\Psi}^\dagger(\mathbf{r}')\hat{\Psi}(\mathbf{r}) = \delta(\mathbf{r} - \mathbf{r}'), \\ \{\hat{\Psi}^\dagger(\mathbf{r}), \hat{\Psi}^\dagger(\mathbf{r}')\} &= \{\hat{\Psi}(\mathbf{r}), \hat{\Psi}(\mathbf{r}')\} = 0. \end{aligned}$$

The low-energy scattering of two identical fermions is insensitive to the short-range part of their interaction and is solely determined by the long-range dipolar part, V_{dd} . As a consequence, for polarized Fermi gases, we can remove the contact term from the equation. (1.6) and the corresponding second-quantized Hamiltonian is given as follows,

$$\hat{H} = \int d\mathbf{r} \hat{\Psi}^\dagger(\mathbf{r}) \left[-\frac{\hbar^2}{2m} + V_T(\mathbf{r}) - \mu \right] \hat{\Psi}(\mathbf{r}) + \frac{1}{2} \int d^3\mathbf{r} d^3\mathbf{r}' \hat{\Psi}^\dagger(\mathbf{r}') \hat{\Psi}^\dagger(\mathbf{r}) V_{dd}(\mathbf{r} - \mathbf{r}') \hat{\Psi}(\mathbf{r}') \hat{\Psi}(\mathbf{r}), \quad (1.8)$$

where $V_{dd}(\mathbf{r})$ is given by eq (1.3).

Many-body systems of ideal fermions follow the Fermi-Dirac distribution at a low temperature T , and the average number of fermions in a quantum state is given by,

$$n(\epsilon_i) = \frac{1}{\exp[(\epsilon_i - \mu)/k_B T] + 1}, \quad (1.9)$$

where ϵ_i is the energy of the quantum state i , μ is the chemical potential that depends on T and fixes the total number of particles, $N = \sum_i n(\epsilon_i)$, and k_B is the Boltzmann constant. The ground state corresponds to all quantum states with $\epsilon_i \leq \mu(T = 0) \equiv \epsilon_F$ being completely occupied, $n(\epsilon_i) = 1$, and the states with $\epsilon_i > \epsilon_F$ are empty. The energy ϵ_F is called the Fermi energy. The ground state of an ideal homogeneous Fermi gas corresponds to a *Fermi sphere*.

While non-dipolar fermions are typically non-interacting, dipolar fermions exhibit significant interparticle interactions, offering a unique platform to investigate novel physical phenomena arising from the interplay of the Fermi statistics and dipolar interactions. The first quantum degenerate dipolar Fermi gas was realized with magnetic ^{161}Dy atoms by Lu et al. [92]. Fig. 1.3 shows the time-of-flight absorption images of a degenerate dipolar Fermi gas from this experiment. One of the significant effects of dipolar interactions in a degenerate Fermi gas is the deformation of the Fermi surface. In contrast to the spherical Fermi surface observed in non-dipolar Fermi gases, anisotropic dipolar interactions induce a deformation in the Fermi surface. Due to the maximum attraction of the dipole-dipole interactions in the dipole alignment direction, the Fermi surface is elongated and takes an ellipsoidal shape. This has been observed by Aikawa et al. in an experiment with magnetic Er atoms [99]. Another interesting feature of dipolar Fermi gases is that Bardeen–Cooper–Schrieffer (BCS) pairing becomes possible at sufficiently low temperatures due to the partially attractive character of the dipolar interaction and leads to anisotropic superfluidity [100, 101]. Dipolar Fermi gases provide a versatile platform for investigating a range of emergent phenomena, including novel Fermi liquids

[92, 102], interlayer superfluid [103, 104], and topological phases [105].

Diverse platforms for dipolar quantum gases

Dipolar quantum gases offer a versatile experimental platform for investigating a wide array of novel many-body phenomena. Confining dipolar atoms in optical lattices enables the exploration of exotic quantum phases. The significant intersite interactions arising from the long-range dipolar character, which are typically exponentially suppressed in non-dipolar gases, become prominent here. Experiments with dipolar Erbium atoms have realized an Extended Bose-Hubbard model, allowing for the study of how dipolar interactions influence the conventional superfluid-Mott insulator transition [106]. More recently, dipolar quantum solids exhibiting stripe and checkerboard density patterns have been observed with dipolar atoms in optical lattices [73].

When dipolar atoms possess spin degrees of freedom, such as spin-3 Chromium (Cr) atoms in lattices, they become powerful tools for exploring quantum magnetism [107–110]. These systems have also been utilized to study the dynamics of large spin models [111] and to measure bipartite spin correlations [112].

BECs formed with Chromium and Europium atoms have been instrumental in exploring spinor physics [113], and have also successfully realized the Einstein-de Haas Effect [114] in dipolar condensates.

Low-dimensional dipolar quantum gases provide unique insights into strongly correlated systems [115]. For instance, one-dimensional dipolar gases have been used to implement Newton’s cradle and investigate quantum thermalization [116]. Furthermore, a one-dimensional super-Tonks-Girardeau gas of Dysprosium atoms facilitated topological pumping, leading to the creation of increasingly excited prethermal states [117]. Beyond these, the signature of supersolidity has been observed in an experiment with driven dipolar gas [118]. Overall, these diverse investigations underscore that dipolar quantum gases are at the forefront of realizing a wide spectrum of weakly and strongly correlated phenomena in quantum many-body physics.

Among these various platforms of dipolar quantum gases, in this thesis, we have focused on the physics of dipolar Bose-Einstein condensates.

1.5 Dipolar Bose-Einstein Condensates

In this section, we will review Bose-Einstein condensates and subsequently discuss how dipole-dipole interactions influence BEC.

1.5.1 Bose-Einstein condensates

The origin of the theory of BEC goes back 100 years to the work of S.N. Bose, where he introduced a statistical method for deriving Planck's black-body radiation formula [119]. The concept was to treat the electromagnetic waves of the black-body as a gas of identical particles, and the mysterious light quanta introduced by Planck in 1900 could be thought of as particles of light, now known as 'photons'. Einstein generalized this idea to an ideal gas of massive particles [120], and predicted that a macroscopic number of bosons would occupy a single quantum state, giving rise to a new state of matter known as the Bose-Einstein condensate.

Ideal Bose gas

Unlike the classical gas or Fermi gas, an ideal Bose gas can undergo a thermodynamic phase transition, driven by the particle statistics and not their interactions. Many-body systems of ideal bosons follow the Bose-Einstein statistics; the average number of bosons in a quantum state at temperature T is given by [25, 121],

$$n(\epsilon) = \frac{1}{\exp[(\epsilon - \mu)/k_B T] - 1}. \quad (1.10)$$

We consider an ideal gas of N bosons occupying a volume V in a grand canonical ensemble, i.e., the system can exchange particles with a reservoir maintaining a fixed chemical potential μ . From eq.(1.10), μ should be negative and it can reach a maximum value of 0. The total number of particles is given by $N = \sum_{\epsilon} n(\epsilon)$. In the thermodynamic limit, $N \rightarrow \infty, V \rightarrow \infty$, the energy levels become continuum, the density $n = N/V$ is constant and can be written as,

$$n = \frac{N}{V} = \int \frac{1}{\exp[(\epsilon - \mu)/k_B T] - 1} g(\epsilon) d\epsilon, \quad (1.11)$$

where $g(\epsilon)$ is the density of state for a three-dimensional homogeneous system,

$$g(\epsilon) = V \frac{m^{3/2}}{\sqrt{2\pi^2 \hbar^3}} \sqrt{\epsilon}. \quad (1.12)$$

While maintaining the density constant, if the temperature is reduced, μ increases and eventually becomes zero at a critical temperature T_c . Putting $\mu = 0$ and $\epsilon = \hbar^2 k^2 / 2m$ in (1.11), we obtain,

$$n = \frac{N}{V} = \frac{(mk_B T_c)^{3/2}}{\sqrt{2\pi^2 \hbar^3}} \int_0^{\infty} \frac{\sqrt{x}}{e^x - 1} dx = \zeta\left(\frac{3}{2}\right) \left(\frac{mk_B T_c}{2\pi \hbar^2}\right)^{3/2} = 2.612 \left(\frac{mk_B T_c}{2\pi \hbar^2}\right)^{3/2}, \quad (1.13)$$

where $x = \epsilon/k_B T$, $\zeta(x)$ is the Riemann zeta function. The critical temperature for BEC is given by,

$$T_c = \frac{2\pi\hbar^2}{k_B m} \left(\frac{n}{2.612} \right)^{2/3}. \quad (1.14)$$

Below the critical temperature, the chemical potential μ becomes zero, and the number of particles in the lowest energy quantum state can be infinite. A non-zero fraction of the bosons condenses into the lowest energy state with $\epsilon = 0$. For $T < T_c$ the transition from the discrete sum to the continuous integral is only applicable for particles having positive energy, i.e., $\epsilon > 0$, since the particles with $\epsilon = 0$ cannot contribute to the integral in eq. (1.13). We have to consider other excited states in addition to the lowest energy state, $n = n_0 + n_{ex}$. So for $T < T_c$, the density of the particles can be written as follows,

$$n = n_0 + 2.612 \left(\frac{mk_B T}{2\pi\hbar^2} \right)^{3/2}. \quad (1.15)$$

The particle density can be divided into condensate (n_0) and non-condensate (n_{ex}) parts. The condensate fraction is defined as,

$$\frac{n_0}{n} = 1 - \left(\frac{T}{T_c} \right)^{3/2}. \quad (1.16)$$

BEC occurs as the de Broglie waves of bosons begin to overlap, i.e., when the quantum degeneracy sets in. The thermal de Broglie length ($\lambda_{th} = h/\sqrt{2\pi M k_B T}$) characterizes the spatial extension of a wave packet of an individual boson. Substituting this in eq. (1.13) we obtain,

$$n\lambda_{th}^3 = \zeta(3/2) \sim 2.612 \quad (1.17)$$

at $T = T_c$. The thermal de Broglie length at the critical temperature is of the order of the average interparticle distance $n^{-1/3}$. The quantity $n\lambda_{th}^3$ is called the 'phase-space density'.

Weakly interacting BEC

Almost 70 years after its prediction, BEC was experimentally achieved in dilute alkali metal atomic gases by three independent research groups. Eric Cornell and Carl Wieman at JILA demonstrated a BEC with Rubidium (^{87}Rb) atoms [7], Wolfgang Ketterle achieved a BEC at MIT using sodium (^{23}Na) atoms [8], and Randall Hulet's group at Rice University created a BEC with Lithium (^7Li) atoms [9]. In contrast to the simplified model of an ideal Bose gas, wherein interparticle interactions are absent, these experimentally realized systems are governed by substantial interatomic

interactions. These interactions can be strongly repulsive at short distances, and also at large interatomic distances, where there is an attractive van der Waals force between the atoms. These can lead to the atoms binding strongly together into atomic clusters due to three-body collisions, in which one pair of atoms can form a bound state, while the excess kinetic energy is carried off by the third atom. However, in dilute gases, the rate of three-body collisions is substantially suppressed, allowing for reasonably long observation times in experiments. When the range of the interatomic forces (r_0) is significantly smaller compared to the average distance between particles ($d = n^{-1/3}$), i.e., $r_0 \ll d$, we can consider only pairwise interactions among particles, and simultaneous interactions involving three or more particles can be safely disregarded. The prevalent two-body interactions in such dilute atomic gases can be effectively modeled using s-wave scattering theory. Since the interactions only act on a very short length scale compared to typical interparticle separations, the pair interaction can be approximated by a Dirac delta function [25]:

$$V(\mathbf{r}_1 - \mathbf{r}_2) \simeq g\delta(\mathbf{r}_1 - \mathbf{r}_2), \quad (1.18)$$

g is characterized by the two-body s-wave scattering length a_s ,

$$g = \frac{4\pi\hbar^2 a_s}{m}. \quad (1.19)$$

The contact interaction can be tuned by varying the scattering length (a_s), which can be positive or negative depending on Feshbach resonances [122–124].

Gross-Pitaevskii equation

In a BEC comprising N atoms, the system involves numerous two-body interactions and is described by a full many-body Hamiltonian. However, it is difficult to solve the N -body problem, and the problem is often reduced to an effective single-particle description using the mean-field approach, commonly known as the Hartree-Fock approximation. In this framework, the many-body wavefunction $\hat{\Psi}$ is expressed as a product of identical single-particle states ψ of N bosons, replacing the detailed interactions with an average potential experienced by each atom. For the mean-field approach to be valid, the system must contain a large number of particles ($N \gg 1$) and the interactions must be dominated by low-energy scattering. As introduced in the previous section, N interacting bosons can be described using the following

many-body Hartree-Fock Hamiltonian,

$$\hat{H} = \int d\mathbf{r} \hat{\Psi}^\dagger(\mathbf{r}) \left[-\frac{\hbar^2}{2m} + V_T(\mathbf{r}) \right] \hat{\Psi}(\mathbf{r}) + \frac{1}{2} \int d^3\mathbf{r} d^3\mathbf{r}' \hat{\Psi}^\dagger(\mathbf{r}') \hat{\Psi}^\dagger(\mathbf{r}) V(\mathbf{r} - \mathbf{r}') \hat{\Psi}(\mathbf{r}') \hat{\Psi}(\mathbf{r}). \quad (1.20)$$

The basic idea of the mean-field approach is to separate the condensate contribution from the bosonic field operator. It was introduced by Bogoliubov in 1947 [125] and is known as the Bogoliubov approximation. It is equivalent to treating the macroscopic component of the field operator as a classical field,

$$\hat{\Psi}(\mathbf{r}, t) = \psi(\mathbf{r}, t) + \delta\hat{\Psi}(\mathbf{r}, t), \quad (1.21)$$

where $\psi(\mathbf{r}, t)$ is the expectation value of the field operator ($\langle \hat{\Psi}(\mathbf{r}, t) \rangle$), known as the order parameter or the macroscopic wave function of the condensate and $\delta\hat{\Psi}(\mathbf{r}, t)$ describes the non-condensate part. One can neglect the non-condensed component in dilute Bose gases at very low temperatures, and the field operator coincides exactly with the classical field ψ .

First, we write down the time evolution of the field operator using the Heisenberg equation,

$$i\hbar \frac{\partial}{\partial t} \hat{\Psi}(\mathbf{r}, t) = [\hat{\Psi}(\mathbf{r}, t), \hat{H}] = \left[-\frac{\hbar^2}{2m} \nabla^2 + V_T(\mathbf{r}) \int d^3\mathbf{r}' \hat{\Psi}^\dagger(\mathbf{r}', t) V(\mathbf{r}' - \mathbf{r}) \hat{\Psi}(\mathbf{r}, t) \right] \hat{\Psi}(\mathbf{r}, t). \quad (1.22)$$

In the case of dilute gases, only two-body collisions at a low energy scale are relevant, and the interatomic potential is replaced by an effective delta function potential as in Eq. (1.19). Replacing the field operator $\hat{\Psi}$ with its classical counterpart ψ and neglecting the $\delta\Psi$ terms we obtain,

$$i\hbar \frac{\partial}{\partial t} \psi(\mathbf{r}, t) = \left[-\frac{\hbar^2}{2m} \nabla^2 + V_T(\mathbf{r}) + g|\psi(\mathbf{r}, t)|^2 \right] \psi(\mathbf{r}, t). \quad (1.23)$$

This equation is known as the Gross-Pitaevskii equation (GPE) [126–128]. The GPE is valid in the regime when the s-wave scattering length (a_s) is much smaller than the average distance between the atoms and the total number of atoms in the condensate is much larger than one ($N \gg 1$). For a dilute Bose gas with repulsive interactions, the GPE is asymptotically exact in the limit of $N \rightarrow \infty, a_s \rightarrow 0$ with Na_s kept constant [129].

Now, we turn our attention to the discussion of BEC with dipolar interactions.

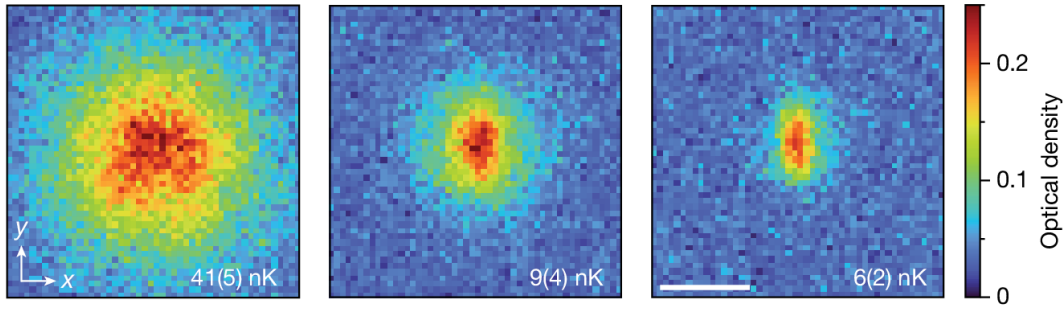


FIGURE 1.4: **BEC of dipolar NaCs molecules.** Absorption images of a thermal cloud (left), a partially condensed cloud (middle), and a quasi-pure BEC (right) after 17 ms of time-of-flight expansion. All the images are an average of 20 individual pictures. The figure was 'Reproduced with permission from Springer Nature' from [130].

Initially, BECs were achieved with alkali atoms, which have very small dipole moments to observe the effects of dipole-dipole interactions, e.g., the ^{87}Rb atom has a dipole moment of $1\mu_B$. In contrast, strong dipolar effects in BEC have been observed since the realization of BEC with Cr atoms[88]. Cr has a dipole moment of $6\mu_B$, and the dipole-dipole interaction is 36 times stronger compared to Rb. Later, BECs have been achieved with strong dipolar atoms of Dy [91], Er [89], and Europium (Eu) [131]. Recently, BEC with dipolar molecules has been realized by Sebastian Will's group at Columbia [130]. Fig. 1.4 shows the absorption image of a dipolar condensate with NaCs molecules from this experiment. Due to its long-range and anisotropic characteristics, dipole-dipole interactions introduce novel phenomena in the field of condensates.

1.5.2 Nonlocal Gross-Pitaevskii equation

As introduced earlier, the interaction between two dipolar bosons is described through the pseudopotential,

$$V(\mathbf{r} - \mathbf{r}') = \frac{4\pi\hbar^2 a_s}{m} \delta(\mathbf{r}) + \frac{C_{\text{dd}}}{4\pi} \frac{1 - 3 \cos^2 \theta}{r^3}, \quad (1.24)$$

where a_s is the s-wave scattering length and $a_{\text{dd}} = C_{\text{dd}}m/3\hbar^2$ characterizes the dipolar scattering length, for magnetic dipoles $a_{\text{dd}} = m\mu_0 d^2/12\pi\hbar^2$. The ratio of the dipolar and short-range scattering interaction is estimated through $\epsilon_{\text{dd}} = a_{\text{dd}}/a_s$. This expression for the potential results from the first-order Born approximation applied to a molecular potential of the dipole-dipole type dominating at long distance, plus a van der Waals potential dominating at short range. In principle, the s-wave scattering length may have a dependence on the dipolar interaction, $a_s = a_s(d)$, particularly for strong dipolar interactions and near shape resonances [98, 132–134]. The

most magnetic atom, Dy, shows a small correction to the a_s value [135], and the pseudopotential remains valid for weak dipolar interactions. Within the mean-field approximation, at a very low temperature, the GPE in Eq. (1.23) is modified to the following:

$$i\hbar \frac{\partial}{\partial t} \psi(\mathbf{r}, t) = \left[-\frac{\hbar^2}{2m} \nabla^2 + V_T(\mathbf{r}) + g|\psi(\mathbf{r}, t)|^2 + \frac{c_{\text{dd}}}{4\pi} \int d\mathbf{r}' \psi^*(\mathbf{r}', t) \frac{1 - 3 \cos^2 \theta}{|\mathbf{r} - \mathbf{r}'|^3} \psi(\mathbf{r}', t) \right] \psi(\mathbf{r}, t). \quad (1.25)$$

In the absence of dipolar interactions, the nonlinearity is local, given by $g|\psi(\mathbf{r})|^2$, and hence similar to that found in Kerr media in nonlinear optics. On the contrary, the long-range dipolar interaction introduces a non-local non-linearity. Interestingly, this links the physics of dipolar condensates with other nonlocal nonlinear systems, such as plasmas [136] and nematic liquid crystals [137].

Magnetostriction

In a nondipolar Bose gas, the shape of the condensate follows the geometry of the external harmonic trap. In contradiction, a dipolar gas behaves differently and tends to elongate along the dipole polarization axis. In a magnetic dipolar gas, the polarization direction is determined by an external magnetic field, and the interaction is maximally attractive along the same direction. Due to its attractive characteristics, the condensate is elongated along the dipolar axis. This effect is known as *magnetostriction*, and for an electric field, the effects are called electrostrictive effects.

In the Thomas-Fermi approximation, where kinetic energy is negligible in Eq. (1.23), the density of a nondipolar BEC takes an inverted parabolic shape. It's called the Thomas-Fermi (TF) radius and scales inversely with the trap frequencies, $R_i \propto 1/\omega_i$, $i = x, y, z$. In the case of a dipolar BEC, it retains the parabolic shape in the TF limit; however, the aspect ratio no longer reflects the aspect ratio of the trap [138, 139]. Experimentally, the phenomenon of magnetostriction was observed in a freely expanding BEC of Cr atoms [140].

Bogoliubov excitation spectrum

In the presence of the dipolar interactions, the excitation spectrum of a uniform 3D dBEC is given by [13, 36]:

$$\hbar\omega(\mathbf{k}) = \sqrt{\frac{\hbar^2 k^2}{2m} \left[\frac{\hbar^2 k^2}{2m} + 2gn_0(1 + \epsilon_{\text{dd}}(3 \cos^2 \theta_k - 1)) \right]}, \quad (1.26)$$

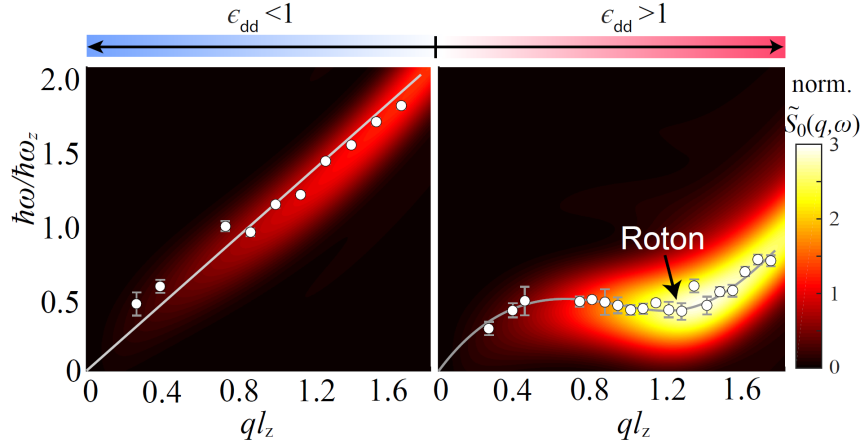


FIGURE 1.5: **Roton Minima of a dipolar BEC.** Excitation spectra for $\epsilon_{dd} < 1$ and $\epsilon_{dd} > 1$ for an Erbium dipolar BEC, axially elongated along y and the atomic dipoles point along z . Reprinted with permission from [141] ©2019, American Physical Society.

where n_0 is the density of the condensate, θ_k is the angle between the direction of excitation propagation and the dipole polarization. The dipolar contribution is simply given by the Fourier transform of the dipole-dipole interactions, defined as $V_{dd}(\mathbf{k}) = \frac{C_{dd}}{3}(3 \cos^2 \theta_k - 1)$, and yields an anomalous momentum dependence in the dispersion relation. For a contact-interacting gas, in the limit of $k \rightarrow 0$, the sound velocity is given by $c_0 = \sqrt{gn_0/m}$, and in the presence of dipolar interactions it acquires an direction dependence, $c(\theta_k) = c_0 \sqrt{1 + \epsilon_{dd}(3 \cos^2 \theta_k - 1)}$. Excitations propagating along the dipoles' direction ($\theta_k = 0$) have the highest sound velocity, whereas those propagating perpendicular to the plane ($\theta_k = \pi/2$) have the lowest velocity. The excitation spectra of a harmonically-trapped dBEC in the weak dipolar regime ($\epsilon_{dd} < 1$) have been experimentally probed using the standard two-photon Bragg spectroscopy method [39, 141]. The left panel of Fig. 1.5 shows the linear phonon-like spectra for a BEC with dipolar Er atoms.

For $\epsilon_{dd} > 1$, phonons ($k \rightarrow 0$) acquire imaginary frequencies, and the homogeneous 3D dipolar BEC is dynamically unstable. This is the so-called *phonon instability*, which leads to the collapse of the homogeneous system.

1.5.3 Roton minima

The dispersion relation in a harmonically-trapped dipolar BEC may become non-monotonous due to the momentum-dependence of the dipole-dipole interaction. Strikingly, in between the phonon dispersion ($\sim k$) at low k and the free particle spectrum ($\sim k^2$) at high momenta, the dispersion reaches a local minimum at a finite k , known as the *Roton* minima. Roton excitation was first observed in superfluid Helium [142, 143], where it originates due to the strong interparticle interactions. Although the

physics behind the roton is different in dBEC, since the minimum resembles the dispersion minimum found in helium, it's called the *roton-like* minimum.

The existence of roton minima in dBECs was theoretically predicted in semi-infinite trapping geometries, specifically systems confined along one [144] or two spatial directions while remaining unconfined in others [145]. The roton minimum arises due to the attractive nature of $V_{\text{dd}}(\mathbf{k})$ at large k . In these semi-infinite geometries, the confinement limits the attractive contribution of the dipolar interactions. The attractive contribution dominates over the repulsive part when the momentum (along an unconfined direction) exceeds the inverse of the characteristic confinement length, l_h . Thus, for excitations along the unconfined direction, $k \ll 1/l_h$ yields $V_{\text{dd}}(\mathbf{k}) > 0$ and for $k \geq 1/l_h$, $V_{\text{dd}}(\mathbf{k}) < 0$. Consequently, the dipolar interaction stiffens the dispersion relation in the phononic regime but bends it downwards at large k . Since the kinetic term dominates at very high k , the effect of $V_{\text{dd}}(\mathbf{k}) < 0$ is maximum at $k \sim 1/l_h$ and for appropriate s-wave scattering interactions the roton minimum forms at $k_{\text{rot}} \sim 1/l_h$. Experimentally, roton minima in dipolar Erbium atoms have been probed through investigations of instability dynamics or by utilizing Bragg spectroscopy [38, 141]. Fig. 1.5 shows the roton-minimum in a cigar-shaped trap geometry with the dipoles aligned along a tightly confining direction [141]. Recent experiments have realized roton excitations by a direct analysis of the in-situ density fluctuations in Dy BECs [146, 147]. Theoretical study has also explored the roton minima in a dipolar gas with tilted dipoles in a pancake-shaped trap [148].

A BEC, while stable in the phonon regime at low wavevectors, can exhibit instability at finite momenta. This occurs when the roton-like minimum in the excitation spectrum approaches zero energy, a phenomenon termed roton instability. The presence of such dynamical instability at finite momentum indicates that the system is prone to developing a density modulation with a finite wavelength, inversely related to the roton momentum. This instability mechanism is crucial, as it provides a pathway for the formation of density-modulated states and, ultimately, supersolids. A stable roton in dipolar condensates can be probed via Faraday patterns, and in particular, a roton minimum causes the wave number of the transient pattern created by periodic driving to be close to the inverse of the roton momentum [149, 150]. The latter leads to the predominant excitation of higher harmonics at low driving frequencies. Additionally, angular rotors are predicted in dipolar BECs, which may lead to the formation of unique biconcave, blood shell-shaped condensates [151].

1.5.4 Beyond mean-field: LHY corrections

In dBECs, the attractive component of the dipole-dipole interaction can lead to instability when it dominates over repulsive short-range interactions. Within the mean-field approximation, this manifests as a collapse of the condensate, signaled by a divergence in density ($n \rightarrow \infty$) and thus in energy in the many-body ground state.

This occurs due to the breakdown of the mean-field theory in the high-density regime, where quantum fluctuations present in the system become important. These quantum fluctuations come from the fluctuations of the vacuum of the excitations. Due to strong interactions between particles, quantum fluctuations yield corrections to the population of the BEC mode known as the *quantum depletion*, as well as corrections in the energy. Considering the population in the excited states (i.e., $k \neq 0$), the zero-point energy of the Bogoliubov quasiparticles shifts the ground state energy compared to the mean-field one. For a non-dipolar weakly interacting BEC, it was first calculated by Lee, Huang, and Yang [152, 153]. In the case of a homogeneous repulsive Bose gas, the correction to the energy reads [154, 155], $\Delta E = \frac{g}{2} \frac{N_0^2}{2V} \frac{128}{15\sqrt{\pi}} \sqrt{na_s^3}$, where N_0 is the number of atoms in the BEC of volume V and n is the density. This correction is the first-order correction to the mean-field, known as the LHY correction term. The presence of the dipolar interactions modifies the elementary excitation spectrum and hence the zero-point energy. For the dipolar BEC, this correction term is obtained as follows [156–158]:

$$\Delta E = V \frac{2\pi\hbar^2 a_s n^2}{M} \frac{128}{15} \sqrt{\frac{na_s^3}{\pi}} Q_5(\epsilon_{\text{dd}}), \quad (1.27)$$

where the function $Q_5(\epsilon_{\text{dd}}) = \int_0^\pi \frac{1}{2} \sin \theta d\theta [1 + \epsilon_{\text{dd}}(3 \cos^2 \theta - 1)]^{5/2}$. For a more detailed derivation, see Appendix A. The function Q_5 becomes imaginary at some angles for $\epsilon_{\text{dd}} > 1$, hence the energy. However, if the imaginary part is very small compared to the real part, one can ignore it and use Eq. (1.27). The correction to the chemical potential is given by $\Delta\mu = \frac{\partial \Delta E}{\partial \Delta N}$.

The effect of three-body collisions has been ignored here, which can drive the system into a solid configuration. However, experimental verification has proved the existence of the quantum gas phase and its long lifetime for systematic measurements of many relevant physical quantities.

Generalized Gross-Pitaevskii equation

The correction to the chemical potential due to the quantum fluctuations gives access to study the beyond-mean-field physics of the dipolar condensates. Within the local density approximation, which assumes that the density varies sufficiently slowly to

be calculated locally, for a given density n , the correction to the chemical potential is given by,

$$\Delta\mu(\mathbf{r}, t) = \frac{32gn(\mathbf{r}, t)^{(3/2)}}{3} \sqrt{\frac{a_s^3}{\pi}} Q_5(\epsilon_{\text{dd}}). \quad (1.28)$$

Adding this to the NLGPE (2.10), we obtain the following generalized Gross-Pitaevskii equation (gGPE),

$$i\hbar \frac{\partial}{\partial t} \psi(\mathbf{r}, t) = \left[-\frac{\hbar^2}{2m} \nabla^2 + V_{\text{T}}(\mathbf{r}) + g|\psi(\mathbf{r}, t)|^2 + \frac{c_{\text{dd}}}{4\pi} \int d\mathbf{r}' \psi^*(\mathbf{r}', t) \frac{1 - 3\cos^2\theta}{|\mathbf{r} - \mathbf{r}'|^3} \psi(\mathbf{r}', t) + \Delta\mu(\mathbf{r}, t) \right] \psi(\mathbf{r}, t). \quad (1.29)$$

This beyond mean-field equation is also known as the Extended Gross-Pitaevskii equation in the literature and plays a key role in studying the dipolar quantum droplets and supersolids.

1.5.5 Quantum droplets

One of the key consequences of physics beyond mean-field (BMF) approximation is the emergence of quantum droplets. While the attractive mean-field interactions can drive a condensate towards collapse, the LHY correction term provides an additional repulsive potential, which acts as an effective higher-order (in 3D, effective 5/2-body interaction) interaction term in the GPE. This leads to a stabilization mechanism, even in the absence of an external trap. By competing MF attraction and the BMF repulsion, the equilibrium between these two forces gives rise to a high-density liquid-like state.

This stabilization mechanism has a similarity with classical liquid states. In ordinary liquids, long-range attractive forces, such as van der Waals or covalent interactions, are balanced by a short-range repulsive core due to Pauli exclusion and electromagnetic interactions. This stabilises the liquid at a large density at which the repulsion becomes effective. Analogously, the stabilisation resulting from competing MF and BMF effects in strongly dipolar gases results in a liquid state, termed as *quantum droplet*. Quantum droplets are self-bound states, such as atomic nuclei [159] and helium droplets [160].

Quantum droplets were first predicted in Bose-Bose mixtures, by Petrov [161], where the stabilization mechanism is in between repulsive intra- and attractive inter-species interactions [162, 163]. In dipolar gases, the scattering length (a_s) can be tuned via Feshbach resonances, leading to the strongly dipolar-interacting regime, where the repulsive LHY interactions manifest in the formation of the droplets.

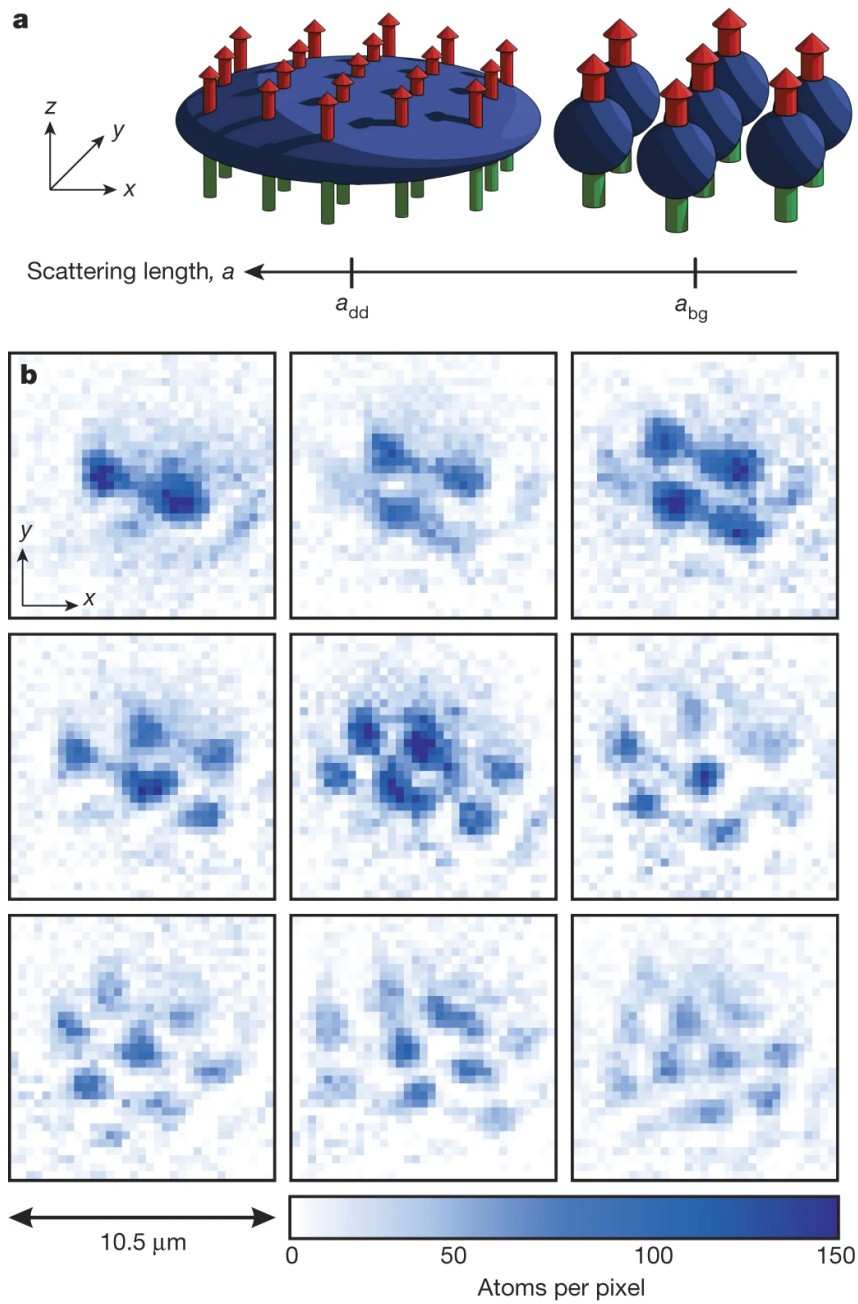


FIGURE 1.6: **Observation of dipolar quantum droplets.** (a) Schematic of the experimental procedure. Preparation of a strongly dipolar BEC of Dy atoms in a pancake-shaped trap and reducing the scattering length. (b) Droplet patterns observed through the in situ imaging method. The figure was 'Reproduced with permission from Springer Nature' from [70].

These droplets are denser than the MF-stable gaseous BEC, but remain significantly more dilute than classical liquids. The droplets are elongated along the dipole direction, due to the magnetostriction effect discussed above. The first experimental observation of droplets was realized with dipolar Dy atoms [40, 70]. Fig. 1.6 displays the formation of quantum droplets in a triangular pattern. Following that, there have been several theoretical works [164–167] on quantum droplets in dipolar BECs. Experiments have also studied collective modes and compressional characteristics of droplets with Er atoms [168].

The self-bound nature of the droplets draws a similarity with the *bright solitons* in a BEC [169]. Solitons, a hallmark of nonlinear theories, are localized wave packets that propagate without distortion due to a precise balance between nonlinearity and dispersion within their medium. In a non-dipolar BEC, a stable bright soliton is formed only in 1D [170] and is not possible to form in 2D or 3D due to the collapse of the BEC. But, in the presence of dipolar interactions, the existence of a stable 2D bright soliton was predicted [171–173]. A stable 3D soliton was also predicted in a Rydberg-dressed BEC [174].

Although both solitons and droplets are self-bound phases, the distinction arises from the stabilization mechanism. Bright solitons are stabilized by dispersive effects—originating from single-particle kinetic energy—along the unconfined spatial direction. In contrast, quantum droplets are stabilized by a repulsive force originating from quantum fluctuations, a phenomenon with a quantum many-body origin. The beyond-mean-field LHY corrections are crucial for the existence of a droplet. Furthermore, solitons typically exhibit a Gaussian density profile, whereas droplets display a flat-top, liquid-like shape. Interestingly, in quasi-one-dimensional (Q1D) geometries, the nature of quantum fluctuations can change, leading to a transition between droplet and soliton phases [175]. A smooth transition from bright solitons to quantum droplets has also been predicted in a gas of Bose-Bose mixture [176].

Notably, the coherence properties of the droplets have also been investigated, revealing that while individual droplets are phase-coherent, a collection of droplets can be either incoherent or, under certain conditions, form a phase-coherent state, leading to the formation of *supersolids*.

1.6 Supersolids

Supersolid is a counterintuitive phase of matter, which simultaneously features the contradictory properties of a superfluid’s perfect flow and of a solid’s rigid, crystalline structure [177]. Imagine a jar of jelly where the contents might exist either as

a liquid or in a crystalline state. A hypothetical supersolid jelly would, counterintuitively, exhibit a quantum mechanical superposition of both phases. To understand the definition of a supersolid, we briefly summarize the properties of a solid and a superfluid.

Order in a solid

In a crystalline solid, atoms or molecules are arranged in a regular, ordered structure, with each constituent occupying a specific site on a periodic lattice. Let the local particle density forming the crystal be denoted by $\rho(\mathbf{r})$. For a macroscopic crystal of volume V , the spatially averaged density is given by $\bar{\rho} \equiv \frac{1}{V} \int d^3r \rho(\mathbf{r})$. The deviation of the local density from its average is given by $\delta\rho(\mathbf{r}) \equiv \rho(\mathbf{r}) - \bar{\rho}$. In systems that preserve translational symmetry, such as gases or liquids, the local density is uniform throughout space, implying $\rho(\mathbf{r}) = \bar{\rho}$ and $\delta\rho(\mathbf{r}) = 0$. But, in a crystal, the translational invariance is broken and $\delta\rho(\mathbf{r})$ doesn't vanish, and ordering is expressed as follows:

$$\delta\rho(\mathbf{r}) = \delta\rho(\mathbf{r} + \mathbf{R}). \quad (1.30)$$

This holds for any vector \mathbf{R} connecting any two lattice sites of the crystal. The condition in Eq. (1.30) holds for a macroscopic sample, indicating a *long-range order* (LRO) in density. Broken translation invariance has the immediate macroscopic consequence of imparting to the system the well-known property of resistance to shear, which a fluid does not possess. It is important to note that Eq. (1.30) occurs in a solid spontaneously, exclusively as a result of interactions among elementary constituents. Such a spontaneous breaking of translation symmetry is an integral part of the definition of a supersolid.

Order in a superfluid

Superfluidity, the ability of quantum fluids to flow without friction, is one of the most spectacular phenomena occurring in quantum many-body systems. It was first discovered in Helium-4 by Kapitza [178] and independently by Allen and Misener [179] in 1937. Soon after that, Tisza introduced a phenomenological two-fluid model [180] that provides a conceptual basis for understanding superfluidity. It expresses the local density of the system as comprising two coexisting components:

$$\rho(\mathbf{r}) = \rho_s(\mathbf{r}) + \rho_n(\mathbf{r}). \quad (1.31)$$

The subscripts denote the superfluid and normal components of the fluid. The superfluid component is non-dissipative and carries no entropy, whereas the normal

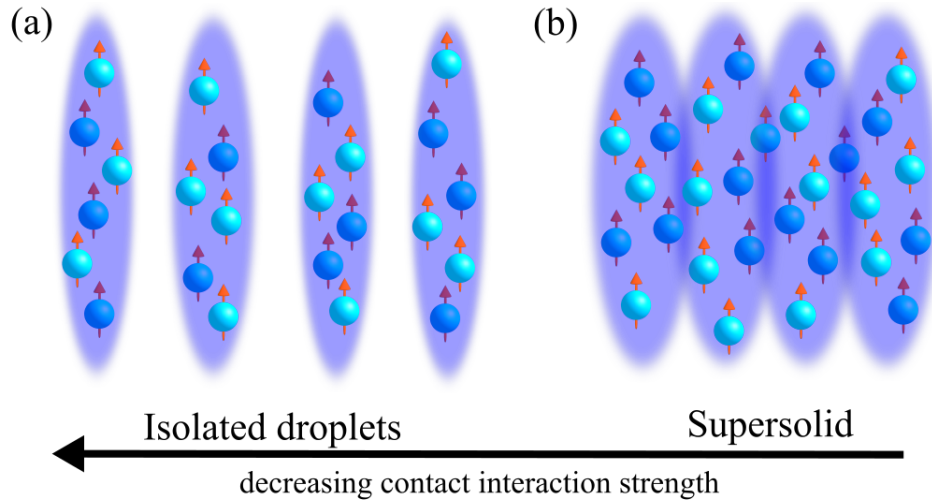


FIGURE 1.7: Schematic diagram of isolated droplets and supersolids.

component exhibits conventional fluid-like behavior. The superfluid component is free of entropy and is capable of maintaining perpetual flow, while the normal component experiences dissipation similar to ordinary fluids. The onset of superfluidity is captured through the increase in the superfluid fraction of the system, which is defined as $f_s = \rho_s/\bar{\rho}$. In a translationally invariant system, $\rho_s(T = 0) = \bar{\rho}$ and the superfluid fraction becomes unity, $f_s = 1$ as $T \rightarrow 0$. The superfluid fraction can be measured through the superfluid response of a system to a small perturbation.

In three-dimensional systems, superfluidity is intrinsically linked to condensation [181]. One can define the one-particle density matrix for a BEC as follows:

$$n(\mathbf{r}, \mathbf{r}') = \langle \hat{\psi}^\dagger(\mathbf{r}) \hat{\psi}(\mathbf{r}') \rangle. \quad (1.32)$$

Here $\hat{\psi}(\mathbf{r})(\hat{\psi}^\dagger(\mathbf{r}))$ is the field operator that annihilates (creates) a particle at position \mathbf{r} . In a Bose condensed system, the individual bosons overlap, and the particle at \mathbf{r} becomes indistinguishable from a particle at \mathbf{r}' . As a result, $n(\mathbf{r}, \mathbf{r}')$ doesn't vanish over a long distance $|\mathbf{r} - \mathbf{r}'|$, $n(r) \rightarrow n_0$ as $r \rightarrow \infty$, where n_0 is the condensate fraction, corresponding to the macroscopic occupation of the zero-momentum state. This persistence of coherence across long distances defines the off-diagonal long-range order (ODLRO). ODLRO indicates that the quantum state of the system remains unperturbed if a particle is removed from the system at \mathbf{r}' and added to it at \mathbf{r} .

Order in a supersolid

The supersolid is defined as a phase of matter in which both the LRO and ODLRO spontaneously occur and exist simultaneously. In such a phase, the superfluid component retains its characteristic ODLRO even within a periodic crystal structure. However, due to the broken translational symmetry introduced by the crystalline lattice, the superfluid fraction is reduced from unity, even when $T \rightarrow 0$.

The concept of supersolidity was first proposed in the context of solid helium in the 1960s [182, 183], with theoretical predictions suggesting that quantum crystals with defects could exhibit superfluid-like behavior at low temperatures [184–186]. The search for supersolidity in helium [187, 188] is still going on, but the first experimental realizations of supersolids have been achieved in ultracold quantum gases [189, 190], where a superfluid becomes solid. In 2019, dipolar Bose gases provided a major breakthrough, with three experimental groups reporting on the evidence of supersolidity with highly magnetic Dy and Er atoms [41, 71, 72]. In dipolar BEC, the formation of supersolidity is linked to the presence of roton-like minima at a finite momentum (k_{rot}). Softening of the roton minima can trigger an instability towards a modulated state characterized by a structure with a period $\propto k_{\text{rot}}^{-1}$.

An essential role in stabilizing this modulated state is played by quantum fluctuations, incorporated through the Lee-Huang-Yang (LHY) correction. By tuning the s-wave scattering length starting from a stable BEC, one can drive the system into a regime where the dipolar interaction dominates ($\epsilon_{\text{dd}} > 1$), and the repulsive quantum fluctuations prevent collapse. Appropriate geometries of the external harmonic confinements can trigger the roton instability in this regime, leading to the supersolid state [41, 71, 72, 191–193]. The emergence of supersolids is observed for a very narrow range of ϵ_{dd} . As ϵ_{dd} increases, coherence between droplets is lost, resulting in an incoherent droplet array. Fig. 1.7 shows a schematic diagram of supersolids and incoherent droplet arrays.

Experimentally, the supersolid state is identified by two primary signatures: The occurrence of modulated patterns is observed in gas absorption images, either in situ or in time-of-flight (TOF) images. The global phase coherence is confirmed from the stable, high-contrast interference pattern in time-of-flight images, differentiating supersolids from an incoherent array of droplets. Fig. 1.8 shows the evolution from in situ density distribution to time-of-flight interference of the phase-coherent droplet regime in a dipolar gas of Dy atoms [72]. The formation of multiple droplets from an initially single droplet configuration can be understood energetically: the anisotropic nature of dipole-dipole interactions imposes a preferred geometry, and fragmentation into multiple droplets can be energetically favorable when compressed along the long axis due to anisotropic repulsion.

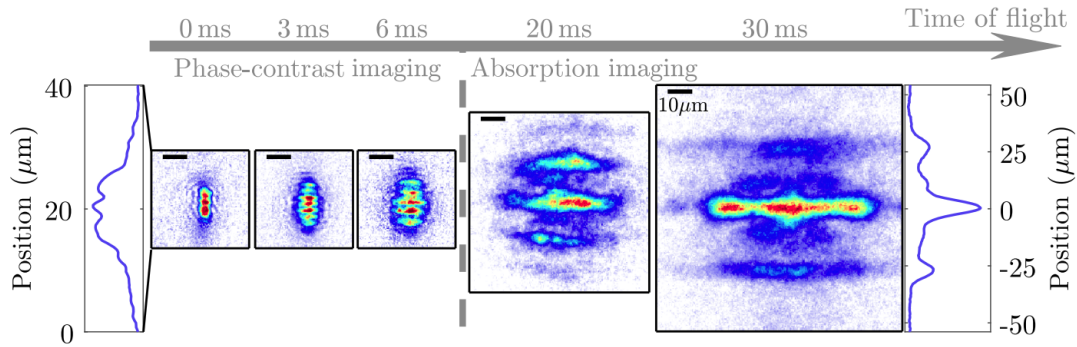


FIGURE 1.8: **Dipolar supersolids of Dysprosium atoms.** Evolution from in situ density distribution to time-of-flight interference. The left-hand side shows an exemplary in situ image together with the integrated density distribution for the phase-coherent droplet regime, revealing a clear density modulation. The right-hand side demonstrates the expansion dynamics for different times of flight. The figure is reprinted from [41] under the [Creative Commons Attribution 4.0 International license](#).

Signatures of supersolidity can also be obtained from the different dynamical properties of supersolids, e.g., sound propagation or response to an external rotation. Supersolids exhibit two distinct types of low-energy excitations: phonon modes associated with the coherent phase of the superfluid, and lattice vibrations corresponding to the crystalline structure. Those two kinds of sound waves are manifestations of the two spontaneously broken symmetries: global $U(1)$ phase symmetry and continuous translational symmetry, respectively. Each broken continuous symmetry gives rise to a corresponding Nambu–Goldstone mode. Several theoretical and experimental studies have investigated these two branches in a dipolar supersolid [194–198] as well as probed the lowest-lying Goldstone mode [199]. Analogous phenomena are found in other areas of physics, for example, in condensed matter physics, magnons are excitations that emerge in ferromagnets below the Curie point when a spontaneous magnetization breaks rotational symmetry. In high-energy physics, the spontaneous breaking of chiral symmetry is linked to the emergence of pions as collective excitations.

The formation of density modulation in supersolids hinders the superfluid flow along that direction, resulting in reduced superfluidity. Experimental measurements have demonstrated this reduced superfluidity based on the non-classical moment of inertia [200]. When a bucket of water is rotated, the water rotates with the vessel, contributing to the total moment of inertia. An ideal superfluid would completely decouple from a rotating container and exhibit zero moment of inertia, while a supersolid would only partially decouple. The resulting moment of inertia is smaller than the classical value but greater than zero. From the measured moment of inertia, the superfluid fraction comes out to be a finite value between zero and one, providing direct evidence of the superfluid nature of the dipolar supersolid. The reduced

superfluid fraction in a supersolid has also been measured using the Josephson effect [201].

While initial experiments primarily observed one-dimensional supersolid arrays, subsequent work has demonstrated the formation of two-dimensional structures [202–206]. Modifying the external harmonic trap geometry, recent experiments have observed the supersolid with linear as well as zig-zag [204] and hexagonal crystal structures [205]. In this thesis, we will explore the emergence of novel supersolid structures, not observed before in dipolar condensates.

Another very important feature of superfluidity can be proven from the existence of *quantized vortices* in rotating supersolids. In the following section, we discuss the theory of quantized vortices in detail.

1.7 Quantized Vortices

Vortex is fundamentally a region within a fluid characterized by a circulating or rotating flow, often manifesting as a hollow or circular structure. Everyday examples of vortices include the swirling water draining from the sink of a bathtub, water-spouts induced by strong winds over the sea, and atmospheric phenomena such as dust devils, tornadoes, hurricanes, and cyclones. In classical fluids like water and air, their flow is not frictionless, and vortices can be generated by perturbations, e.g., by the turbulent flow near an obstacle or by a temperature gradient. In contrast, in an ideal, frictionless fluid, vortices cannot terminate within the fluid medium: they either form a closed loop, or they start and end at the surface or at the container wall. This principle is particularly relevant for superfluids, where vortex lines can thus be generated only at the surface, or they nucleate as vortex rings inside the fluid, and they can disappear only through the surface or when a vortex loop shrinks to a point.

The study of vortices has been an active area of research for more than a century. The late 19th century marked a classical period in vortex dynamics, revealing significant characteristics such as the propagation of Kelvin waves along isolated vortex lines. Onsager (1949) [207] and Feynman (1955) [208] discovered an array of vortex lines with quantised circulation that thread the rotating superfluids. With this discovery, the age of quantum vortices began. Here, in this section, we briefly review the background theory of quantized vortices and discuss the properties of vortices in dipolar condensates and dipolar supersolids.

1.7.1 Hydrodynamic theory of vortices

Understanding the behavior of vortices often benefits from a foundation in hydrodynamic theory, since many notable features of vortices have a hydrodynamic origin. We begin with a brief review of the hydrodynamic theory of vortices.

Consider a fluid characterized by its mass density $\rho(\mathbf{r}, t)$, and velocity field $\mathbf{v}(\mathbf{r}, t)$ at position \mathbf{r} and time t . They obey the equation of continuity resulting from the conservation of mass:

$$\frac{\partial \rho}{\partial t} + \nabla \cdot (\rho \mathbf{v}) = 0. \quad (1.33)$$

For an ideal fluid, which is both inviscid and adiabatic (implying no thermal conduction), the evolution of the velocity field is governed by the Euler equation,

$$\frac{d\mathbf{v}}{dt} = \frac{\partial \mathbf{v}}{\partial t} + (\mathbf{v} \cdot \nabla) \mathbf{v} = -\frac{1}{\rho} \nabla p - \frac{1}{m} \nabla U, \quad (1.34)$$

where p , U , and m are the pressure, an external potential, and the mass of the constituent particle of the fluid. Since the entropy is conserved, $(1/\rho) \nabla p = dw$, where w is the enthalpy per unit mass, the Euler equation can be equivalently expressed as:

$$\frac{d\mathbf{v}}{dt} = \frac{\partial \mathbf{v}}{\partial t} + (\mathbf{v} \cdot \nabla) \mathbf{v} = -\nabla \left(w + \frac{U}{m} \right). \quad (1.35)$$

Using the identity, $(\mathbf{v} \cdot \nabla) \mathbf{v} = \nabla \left(\frac{1}{2} \mathbf{v}^2 \right) - \mathbf{v} \times (\nabla \times \mathbf{v})$, we obtain the fundamental equation for the ideal fluid:

$$\frac{\partial \mathbf{v}}{\partial t} - \mathbf{v} \times (\nabla \times \mathbf{v}) = -\nabla \left(\frac{1}{2} \mathbf{v}^2 + w + \frac{U}{m} \right). \quad (1.36)$$

For a stationary flow, where $\partial \mathbf{v} / \partial t = 0$, the preceding equation simplifies to:

$$(\mathbf{v} \cdot \nabla) \left(\frac{1}{2} \mathbf{v}^2 + w + \frac{U}{m} \right) = 0. \quad (1.37)$$

This result indicates that the quantity $\mathbf{v}^2/2 + w + \frac{U}{m}$ remains constant along a streamline, which is a curve whose tangent at any point aligns with the velocity vector at that point. This leads directly to Bernoulli's equation:

$$\frac{1}{2} \mathbf{v}^2 + w + \frac{U}{m} = \text{constant}. \quad (1.38)$$

In the specific case of an incompressible fluid where the mass density is constant, we can write $w = p/\rho$ in Eq. (1.38), obtaining

$$\frac{1}{2}\mathbf{v}^2 + \frac{p}{\rho} + \frac{U}{m} = \text{constant}. \quad (1.39)$$

The circulation of a fluid along a closed contour C is defined as the line integral of the velocity along C :

$$\Gamma \equiv \oint_C \mathbf{v} d\mathbf{r}. \quad (1.40)$$

Applying Stokes' theorem, the integral is converted into the surface integral over the area enclosed by C

$$\Gamma = \int_C \omega d\mathbf{S}, \quad (1.41)$$

where

$$\omega = \nabla \times \mathbf{v} = \text{rot} \mathbf{v} \quad (1.42)$$

is called *vorticity*. Eq. (1.41) shows that circulation gives the total vorticity of the enclosed area. Since $\text{div} \omega = 0$, the vortex can not appear or disappear in the system; it can only either form a closed loop or terminate at the fluid's boundary.

1.7.2 Quantized vortices in superfluids

The concept of quantized vortices arises from the fundamental principles of quantum mechanics applied to macroscopic systems that exhibit superfluidity or superconductivity, phases of matter characterized by dissipationless flow. In superfluids, this manifests as zero viscosity, while in superconductors, it corresponds to zero electrical resistance. The existence of a macroscopic wave function in these systems leads to the quantization of flow.

A superfluid, in particular, can be described by a macroscopic order parameter ψ , which is a complex-valued wave function. This order parameter can be decomposed into an amplitude and a phase component:

$$\psi(\mathbf{r}, t) = \sqrt{n(\mathbf{r}, t)} e^{i\phi(\mathbf{r}, t)}, \quad (1.43)$$

where $n(\mathbf{r}, t) = |\psi(\mathbf{r}, t)|^2$ is the superfluid density and $\phi(\mathbf{r}, t)$ is the phase of the order parameter. The mass density ρ and the current density \mathbf{j} are given by

$$\rho(\mathbf{r}, t) = m|\psi(\mathbf{r}, t)|^2, \quad (1.44)$$

$$\mathbf{j}(\mathbf{r}, t) = \frac{\hbar^2}{2im}(\psi^* \nabla \psi - \psi \nabla \psi^*) = \rho(\mathbf{r}, t) \frac{\hbar}{m} \nabla \phi(\mathbf{r}, t). \quad (1.45)$$

The superfluid velocity is defined as the ratio of the current density to the mass density

$$\mathbf{v}_s(\mathbf{r}, t) = \frac{\hbar}{m} \nabla \phi(\mathbf{r}, t). \quad (1.46)$$

Since the superfluid velocity is the gradient of a scalar function, its rotation vanishes identically:

$$\nabla \times \mathbf{v}_s = \text{rot} \mathbf{v}_s = 0. \quad (1.47)$$

This indicates that a superfluid is inherently irrotational. The quantization arises from the requirement that the order parameter $\psi(\mathbf{r}, t)$ must be single-valued, while traversing a closed loop around a region in the superfluid, the phase ϕ must return to its initial value plus an integer multiple of 2π . Putting the superfluid velocity in Eq. (1.41), we obtain the quantization of circulation:

$$\Gamma = \frac{\hbar}{m} \oint \nabla \phi d\mathbf{r} = kn(n = 0, \pm 1, \pm 2, \dots), \quad (1.48)$$

where,

$$k = \frac{h}{m}, \quad (1.49)$$

is defined as the quantum of circulation.

A quantized vortex is essentially a singularity (a "hole" or "core") in the superfluid, around which the phase winds by an integer multiple of 2π . The superfluid density goes to zero at the core of the vortex, as the phase is undefined there. The integer n in Eq. (1.48) is referred to as the winding number or charge of the vortex; a vortex with $|n| = 1$ (2) corresponds to a singly quantized (doubly quantized) vortex. The quantized vortex features a phase singularity that is characterized by the topological quantum number n . This discrete nature of circulation, governed by a topological quantum number n , fundamentally distinguishes quantized vortices from classical vortices, where Γ can vary continuously.

Quantized vortices have been experimentally observed and extensively studied in various rotating superfluid systems, including ^3He and ^4He superfluids, [209–211], as well as ultracold Bose and Fermi gases [212, 213]. Apart from the superfluid in the laboratories, the interior matter of neutron stars is hypothesized to exist in a superfluid state, threaded by quantised vortices due to the star's rotation [214, 215]. The theoretical framework of quantum vortices provides a compelling explanation for a rich variety of phenomena observed in pulsars.

1.7.3 Vortices in Bose-Einstein condensates

There is no unique relationship between BEC and superfluidity; for instance, an ideal Bose gas can undergo BEC without exhibiting superfluid properties, and a two-dimensional superfluid may exist without forming a BEC. Nevertheless, in many scenarios, BEC and superfluidity occur simultaneously. The manifestation of quantized vortices under rotation serves as a fundamental signature of superfluidity.

1.7.4 Experimental generation of vortices in BEC

Experimental observations in BECs with short-range interactions have revealed the emergence of vortices in various forms, including single vortices [216, 217], vortex lattices [212, 217–219], vortex rings [220], and vortex-antivortex pairs [221]. Vortices can be generated in a condensate in various ways.

- One of the most intuitive and elegant methods involves physically rotating the external trapping potential of the gas using off-center optical beams [217, 219] or anisotropic magnetic confinement [222, 223].
- Vortices can be directly "imprinted" onto the condensate by applying a spatially varying phase to the macroscopic wavefunction using tailored laser fields. Quantum vortices have been successfully generated using optical imprinting methods that employ either dynamic beam configurations [216] or static configurations with Laguerre-Gauss beams [224].
- Vortices may be nucleated by the motion of a small perturbation, for instance, a focused laser beam traversing the superfluid medium [221, 225], or by vigorously shaking the confining potential [226, 227]. If the perturbation exceeds a critical velocity, the superfluid flow breaks down, leading to vortex formation.
- The introduction of synthetic magnetic fields offers another avenue for generating vortices. This has been demonstrated [228] by implementing spin-orbit coupling potentials through the use of two Raman beams that have designated propagation directions and distinct frequency differences, effectively mimicking the Lorentz force on charged particles.
- Vortices can emerge in a merged condensate through the interference of isolated, phase-independent condensates arranged in a ring. This mechanism, where the individual phase distributions dictate the final circulation, was first shown with three BECs [229] and later extended to more condensates [230].

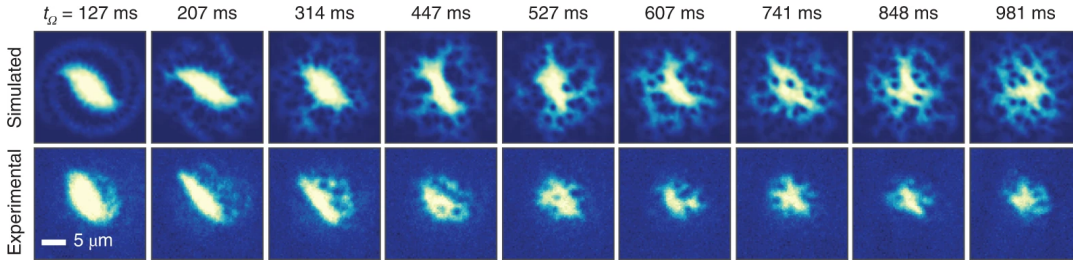


FIGURE 1.9: **Observation of vortices in a dipolar BEC.** The upper panel shows the simulated and the bottom panel shows the experimental images in a rotating dipolar BEC of Dy atoms. In each experimental run, the magnetic field is rotated anticlockwise at $\Omega = 0.74\omega_{\perp}$ for different rotation times. The initial condensed atom number is $N = 15,000$. The decreasing size of the cloud suggests a decrease in atom number. The figure is reused from [233] with the permission from F. Ferlaino.

- In systems with reduced dimensionality, such as two-dimensional superfluids, enhanced thermal fluctuations play a crucial role. The Berezinskii-Kosterlitz-Thouless (BKT) transition describes a continuous phase transition in two-dimensional systems, moving from a low-temperature superfluid to a high-temperature normal gas. As temperature rises, spatial correlations shift from algebraic to exponential decay. This change is driven by the unbinding of low-energy vortex-antivortex pairs, leading to a proliferation of free vortices. This phenomenon has been observed in both continuous [54, 231] and lattice systems [232].

These methods have primarily been explored in Bose gases characterized by short-range contact interactions. In the following, we focus on the vortex generation in dipolar condensates, where long-range, anisotropic interactions lead to qualitatively new behavior.

1.7.5 Quantized vortices in dipolar condensates

The anisotropic nature of dipolar interaction alters the properties of vortices compared to short-range interacting BECs [234]. Theoretical studies predict new features in the rotating dipolar gases; the anisotropic nature of dipolar interactions deforms vortex cores into elliptical or crater-like shapes and can also induce density ripples around the vortex core [235, 236]. The critical frequency required to nucleate vortices can also be affected by the dipolar interactions [237]; it can be either increased or decreased depending on the trap geometry, the orientation of the dipoles relative to the rotation axis, and the interplay with contact interactions. While a triangular (Abrikosov) lattice is typical for non-dipolar BECs, the anisotropic dipolar interactions can lead to the formation of other vortex lattice symmetries, such as a squared or striped lattice [238–240]. Dynamical instabilities can also be seeded in rotating dipolar condensates [241–243].

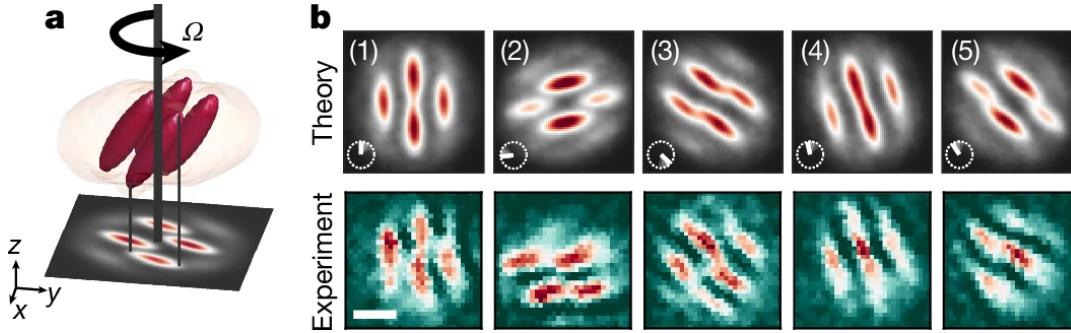


FIGURE 1.10: **Magnetostirring of a dipolar supersolid.**(a) Density isosurfaces and corresponding integrated 2D density of a four-droplet supersolid. (b) Column densities of a four-droplet supersolid state from theory (upper panel) and experiment (bottom panel) with $\Omega = 0.3\omega_{\perp}$ at different times: 1, 19, 43, 70, and 274 ms, labelled (1) to (5), respectively. The insets show the magnetic-field vector rotation in the xy plane with white lines. Experimental parameters: $B = 18.24(2)G$, $N = 7 \times 10^4$ and $(\omega_{\perp}, \omega_z) = 2\pi \times [50.5(3), 135(2)]\text{Hz}$. Illustrative simulation parameters: $a_s = 92.5a_0$, $N = 6 \times 10^4$ and $(\omega_{\perp}, \omega_z) = 2\pi \times [50, 135]\text{Hz}$. Scale bar, $5\mu_m$. The figure was 'Reproduced with permission from Springer Nature' from [244].

A recent experimental breakthrough in Innsbruck achieved the first direct observation of vortices in a dipolar Bose-Einstein condensate (BEC) of Dysprosium (Dy) atoms [233]. Fig. 1.9 illustrates the formation of these vortices within the dipolar condensate. They have used a novel method to rotate the dipolar gas. Key to their approach are two important features of dipolar BECs: i) Dipoles inherently align along the magnetic-field vector, which defines the polarization axis; ii) polarized gas elongates along its polarization axis through a process known as magnetostriction. By tilting the magnetic field into the plane of an otherwise cylindrically symmetric trap, asymmetry is induced in the dipolar BEC's density profile. Subsequently, rotating the tilted magnetic field around the trap center generated vortices, analogous to the mechanical rotation of the trap used for non-dipolar BECs. The realization of quantized vortices in a rotating dipolar BEC has opened up exciting new avenues for future research into rotating dipolar gases.

1.7.6 Quantized vortices in supersolids

Supersolid is a fascinating phase of matter, uniquely characterized by the simultaneous manifestation of both superfluid and solid properties. Unlike conventional superfluids, where the underlying macroscopic wavefunction is continuous and vortices can move freely, supersolids spontaneously break translational symmetry. This inherent density non-uniformity, occurring on scales comparable to the vortex core, fundamentally differentiates supersolids. As a result, supersolids exhibit a fascinating blend of rotational and irrotational behaviors, leading to a complex, multimode

response to external perturbations. When subjected to rotation, supersolids display intricate dynamics, with the presence of quantized vortices serving as a direct signature of their underlying superfluid characteristics.

Theoretical investigations have explored quantized vortices in different types of supersolids, including Rydberg-dressed [245] and dipolar supersolids [246–248]. These studies predict several distinctive features for such vortices, including a reduced angular momentum [246, 247], and unusual dynamics such as pinning and snaking due to the interaction with the crystals [245, 249]. Very recently, the ‘Magnetostirring’ methodology has been implemented to rotate a dipolar supersolid of Dy atoms, and quantized vortex lines manifest between the droplet crystal peaks [244]. Fig. 1.10 shows the rotation of a supersolid through the rotation of the external magnetic field. Rotating supersolids offer an intriguing platform to study broader physical phenomena, such as synchronization [250] and glitches in neutron stars [251]. In the last part of this thesis, we investigate the physics of rotating dipolar supersolids in detail.

1.8 Outline of the Thesis

In chapter 2, we present the setup of doubly dipolar Dysprosium (Dy) atoms and provide a theoretical framework for the doubly dipolar Bose-Einstein condensates (DDBEC). We introduce the Hamiltonian of a Dy atom subjected to both magnetic and electric fields. Due to the presence of a pair of quasi-degenerate states with opposite parity, an additional electric dipole moment is induced in Dy atoms, along with their permanent magnetic dipole moment. This chapter explores the highly anisotropic property of the doubly dipolar potential, which depends on the relative orientation and magnitude of the two dipole moments. We then introduce the Gross-Pitaevskii equation for a homogeneous doubly dipolar condensate and discuss the sound velocity in a homogeneous DDBEC. Subsequently, we obtain the Lee-Huang-Yang (LHY) correction term for the DDBEC, accounting for the quantum fluctuations within the system. Through the assumptions of a local-density approximation, we arrive at the generalized Gross-Pitaevskii equation (gGPE), which serves as a pivotal equation in the later chapters of the thesis. In the second part of this chapter, we describe the methodologies to explore finite temperature properties of the doubly dipolar Bose gas. We briefly review Feynman’s path integral formulation of quantum mechanics and proceed to describe the thermal density matrix within this representation. Following that, we discuss the worm algorithm and the measurement of various observables within PIMC simulations.

In chapter 3, we investigate the properties of a quantum droplet within DDBEC. We begin by examining the physics of self-bound quantum droplets. The precise control of tuning the relative angle between two dipole moments in DDBEC results in the emergence of a unique quasi-two-dimensional pancake quantum droplet, which is not observed in typical dipolar condensates. Through a Gaussian variational approach and numerically solving the generalized Gross-Pitaevskii equation, we illustrate a dimensional crossover from a self-bound, cigar-shaped droplet to a pancake droplet [45, 46]. In the second part of this chapter, we explore the finite temperature properties of doubly dipolar Bose gases using path integral Monte Carlo (PIMC) simulations [252]. We illustrate the ground state transition from a condensate to a pancake droplet in both PIMC and mean-field simulations, comparing these approaches. By computing the superfluid fractions from PIMC simulations, we reveal a highly anisotropic superfluid behavior of a quantum pancake droplet compared to a repulsive DDBEC. We then display the transitions from a thermal gas to a DDBEC and from a thermal gas to a pancake droplet as a function of temperature variation, noting that the latter occurs at a higher transition temperature. We also demonstrate the structural transition by varying the magnitude of the electric dipole moment.

In chapter 4, we study the formation of exotic droplet arrays and supersolids in harmonically-trapped DDBEC. We explore the ground-state phases of the DDBEC in two different harmonic trap configurations [46]. The interplay between doubly dipolar interactions, quantum fluctuations, and external confinement leads to supersolid-supersolid transitions and the formation of novel pancake supersolids. Furthermore, we indicate the appearance of modulated droplets, a unique feature of the DDBEC.

In chapter 5, we explore the formation of a dilute supersolid phase induced by the rotation of a dipolar quantum gas. In dipolar quantum gases, supersolids have been experimentally realized through the formation of high-density coherent droplet arrays, stabilized by repulsive quantum fluctuations. In this work, we present a theoretical prediction of the formation of supersolids in rotating dipolar Bose gases without relying on the stabilization from quantum fluctuations. We investigate the rotation of a cylindrically trapped magnetic dipolar condensate around an axis perpendicular to the dipole polarization axis. We consider the simultaneous rotation of the external trap and the external magnetic field to rotate the condensate. We investigate the ground states in a rotating frame and observe the emergence of spontaneous crystallization above a rotation frequency. Additionally, vortex lines emerge within the low-density regime, pinned between the crystal peaks. We also investigate the stability of the condensate under rotation by studying the real-time dynamics based on the truncated Wigner formalism using a nonlocal Gross-Pitaevskii equation. Finally, we explore the effect of the external trap geometry on the formation of this

vortex-stabilized supersolid state.

In chapter 6, we summarize the work of this thesis and provide an outlook for future research exploration.

Chapter 2

Doubly Dipolar Bose-Einstein Condensate: Setup and Methodologies

The content of this chapter is adapted from the research article, "Droplet arrays in doubly dipolar Bose-Einstein condensates" [46] and "Path integral Monte Carlo study of a doubly dipolar Bose gas" [252].

2.1 Introduction

Doubly dipolar quantum gases are novel ultracold atomic or molecular gases in which the constituent particles possess both magnetic and electric dipole moments. This is in contrast to typical dipolar quantum gases, where particles possess a significant dipole moment of only one type, either magnetic, as in highly magnetic atoms, or electric, as in polar molecules. The simultaneous presence of electric and magnetic dipolar interactions leads to significantly richer and more anisotropic long-range interactions compared to conventional singly dipolar gases. The unprecedented control and tunability of the relative orientations and strengths of these two distinct dipole moments offer the possibility to explore a rich landscape of novel quantum many-body phenomena. Such doubly dipolar quantum gases have attracted significant interest [44, 253–260] due to their potential application in diverse areas, including quantum simulation [261, 262], quantum computation [263, 264], high-precision tests of fundamental symmetries [265], and for the tuning of collisions and chemical reactions [266, 267]. Recent experimental realization of doubly dipolar quantum gases with Dy atoms [47] and LiCr molecules [268] signifies a crucial step forward in exploring this field. In this chapter, we present an overview of engineering the doubly dipolar interaction in Dy atoms, followed by a detailed discussion of the properties of the doubly dipolar potential. Subsequently, we provide the theoretical framework to describe the doubly dipolar Bose-Einstein condensates (DDBEC) and outline their

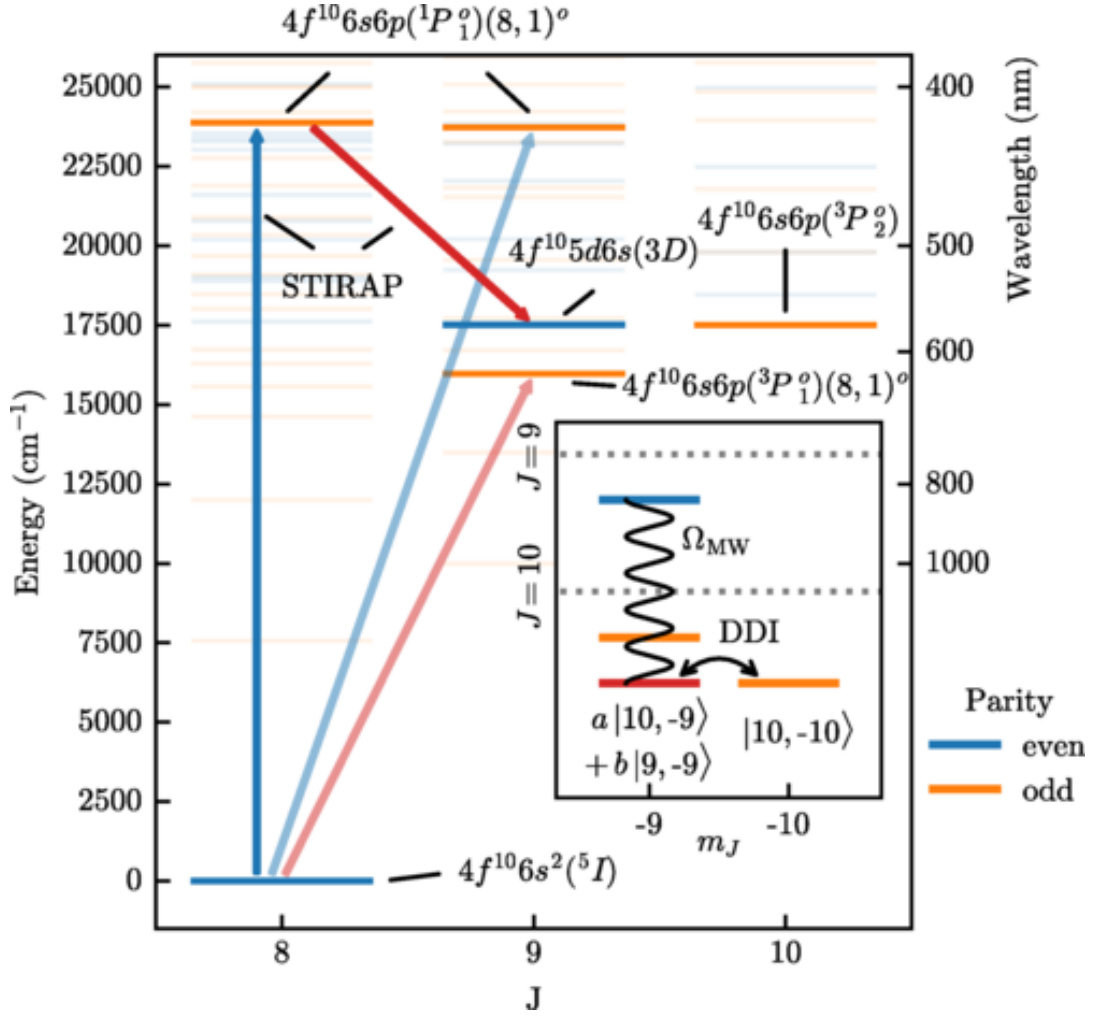


FIGURE 2.1: **Relevant atomic structures of Dy atom.** The figure was taken from [47] with permission from PHYSICAL REVIEW A 110, 023311 ©2024, American Physical Society.

key physical characteristics. Finally, we incorporate the contribution of quantum fluctuations through the inclusion of the Lee-Huang-Yang (LHY) correction term, offering a beyond-mean-field description of DDBEC.

2.2 Dysprosium Atoms under Magnetic & Electric Fields

2.2.1 The Dysprosium atom

Quantum gases made of atoms with multiple valence electrons and a non-zero orbital angular momentum in their electronic ground state, like magnetic Lanthanides (Lns), have emerged as promising candidates for studying strong dipolar phenomena. Notably, Dysprosium (Dy) was the first of these magnetic lanthanides to be cooled to quantum degeneracy [91, 92]. Dy has several special features that make it

particularly accessible for quantum-gas experiments. Dy possesses a wide range of naturally abundant isotopes, including several bosonic (^{164}Dy , ^{162}Dy) and fermionic isotopes (^{161}Dy , ^{163}Dy). The isotope variety provides a useful range and tunability of scattering properties: each isotope is characterized by a distinct background scattering length (a_s) and a unique Feshbach spectrum, the latter of which enables further control of a_s [269].

The electronic configuration of Dy, denoted as $[\text{Xe}]4f^{10}6s^2$, is characterised by a xenon-like core, an inner open 4f shell with 10 valence electrons, and a closed outer 6s shell. The partially filled subshell is fundamental to Dysprosium's unique magnetic properties. The ten 4f electrons are responsible for the large magnetic dipole moment. According to Hund's rules, these electrons will arrange themselves to maximize the total spin and then the total orbital angular momentum, leading to a large net magnetic moment. The magnetic dipole moment of Dy is $10\mu_B$ in its electronic ground state, which is the highest among all stable elements. The corresponding dipolar length for Dy is, $a_{\text{dd}} \simeq 131a_0$. Typically, $\varepsilon_{\text{dd}} = a_{\text{dd}}/a_s$ for Dy is of the order of 1, which makes it a very good candidate to study dipolar effects in quantum gases.

The atomic spectra of lanthanides are characterized by a rich set of $J \rightarrow J + 1$ optical transitions, transitions with broad, narrow, and ultra-narrow linewidths. Dysprosium exhibits strong electronic transitions in the visible range of the electromagnetic spectrum (e.g., around 421 nm and 626 nm). Such transitions can be used for optical manipulation and laser cooling, and are readily accessible with common lasers [270].

In summary, Dy possesses a favorable combination of atomic properties, including strong and accessible laser cooling transitions, isotopic abundance, and the presence of Feshbach resonances. These properties and their large magnetic dipole moment make Dy a prime candidate for creating and studying novel dipolar quantum gases.

2.2.2 Doubly dipolar interactions in Dy atoms

In this thesis, we investigate a particular realization of a doubly dipolar system using Dysprosium (Dy) atoms, based on the proposal outlined by Lepers. et al. in Ref. [44]. While our primary focus is on Dy atoms, it is important to highlight that similar physics can be explored in other doubly dipolar systems, such as those involving dipolar molecules.

Dy atoms are of particular interest due to their unique properties, which include a permanent magnetic moment and the ability to acquire an induced electric dipole moment when subjected to an external electric field. This unique characteristic arises due to the presence of a pair of quasi-degenerate states with opposite parity.

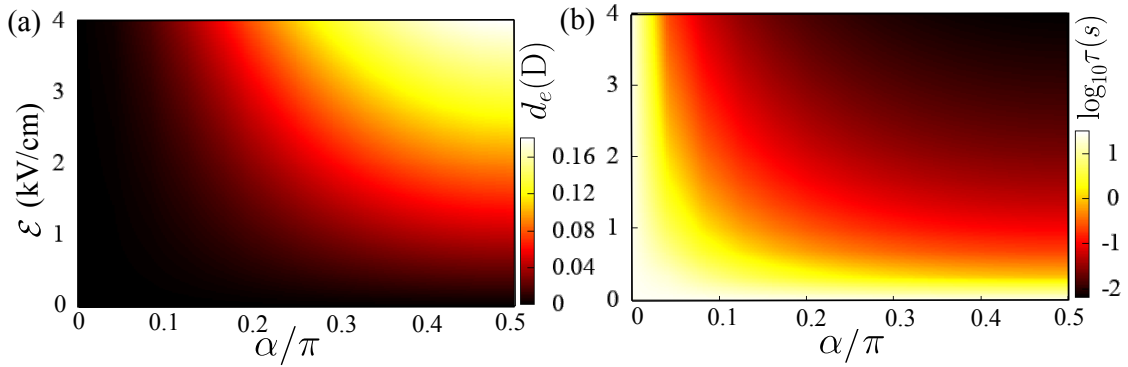


FIGURE 2.2: **Doubly dipolar Dysprosium.** (a) Electric dipole moment d_e and (b) lifetime τ of the $|S\rangle$ state of a Dy atom, as a function of the electric field strength \mathcal{E} and the angle α between the electric and magnetic fields for $\mathcal{B} = 100$ G.

These states, $|a\rangle$ (odd parity) and $|b\rangle$ (even parity), have total angular momenta $\{J_a = 10, J_b = 9\}$, and energies $\{E_a = 17513.33 \text{ cm}^{-1}, E_b = 17514.50 \text{ cm}^{-1}\}$. Within the electric-dipole approximation, the line-widths of the states are $\Gamma_a \approx 0$ (metastable) and $\Gamma_b = 2.98 \times 10^4 \text{ s}^{-1}$, respectively.

In our setup, we assume that the Dy atoms are subjected to uniform magnetic and electric fields. The magnetic field, $\mathbf{B} = \mathcal{B}\hat{z}$, is directed along z , setting the quantization axis and splitting the degeneracy of the energy levels E_a and E_b . The electric field, $\mathbf{E} = \mathcal{E}\hat{u}$ mixes the Zeeman sublevels of the states $|a\rangle$ and $|b\rangle$, which include $\{|M_a = -J_a\rangle, \dots, |J_a\rangle, |M_b = -J_b\rangle, \dots, |J_b\rangle\}$ respectively. This mixing induces an electric dipole moment along \hat{u} . For our analysis, we assume that \hat{u} lies on the xz plane forming an angle α with the z -axis. This relative angle plays a crucial role in the physics of doubly dipolar Bose gases.

Restricting to the subspace of both E_a and E_b , the Hamiltonian for a Dy atom is $\hat{H} = \hat{H}_B + \hat{H}_{\text{stark}}$ with

$$\hat{H}_B = \sum_{M_a} (E_a + \mu_B \mathcal{B} g_a M_a) |M_a\rangle \langle M_a| + \sum_{M_b} (E_b + \mu_B \mathcal{B} g_b M_b) |M_b\rangle \langle M_b|, \quad (2.1)$$

where $g_a = 1.3$ and $g_b = 1.32$ are the Landé g factors. The term \hat{H}_{stark} accounts for the interaction of the electric field with the Dy atom. The electric field strength is such that the lowest eigenstate of the atom is $|S\rangle = c_0 |M_a = -10\rangle + \sum'_i c_i |i\rangle$ with $\sum'_i |c_i|^2 / |c_0|^2 \ll 1$, where the sum \sum'_i is taken over all the magnetic sublevels except $|M_a = -10\rangle$, and c_i is the probability amplitude for finding the atom in the state $|i\rangle$. The summation \sum'_i has two contributions, one from the sublevels of $|a\rangle$ and the other from those of $|b\rangle$. Since $\Gamma_a \approx 0$, only the contributions from the sublevels $\{|M_b\rangle\}$ determine the lifetime of the stretched state $|S\rangle$, $\tau = (n_b \Gamma_b)^{-1}$, where n_b is the total population in $\{|M_b\rangle\}$ sublevels. The magnetic and electric dipole moments of a Dy

atom in $|S\rangle$ are, respectively:

$$d_m = -\mu_B \left(g_a \sum_{M_a=-J_a}^{J_a} |c_{M_a}|^2 M_a + g_b \sum_{M_b=-J_b}^{J_b} |c_{M_b}|^2 M_b \right), \quad (2.2)$$

$$d_e = -\frac{1}{\mathcal{E}} \sum_{M_a, M_b} c_{M_a}^* c_{M_b} \langle M_a | \hat{H}_{\text{stark}} | M_b \rangle + \text{c.c.}, \quad (2.3)$$

with

$$\begin{aligned} \langle M_a | \hat{H}_{\text{stark}} | M_b \rangle = & -\sqrt{\frac{4\pi}{3(2J_a+1)}} \langle a || \hat{d} || b \rangle \mathcal{E} \times \\ & Y_{1, M_a - M_b}^*(\alpha, 0) C_{J_b M_b, 1, M_a - M_b}^{J_a M_a}, \end{aligned} \quad (2.4)$$

where, $\langle a || \hat{d} || b \rangle = 8.16$ Debye is the reduced transition dipole moment, $Y_{l,m}(\theta, \phi)$ are the spherical harmonics and $C_{J_b M_b, 1, M_a - M_b}^{J_a M_a}$ are the Clebsch-Gordan coefficients.

Figure 2.2 depicts, for $\mathcal{B} = 100$ G, d_e and d_m for the state $|S\rangle$, as a function of \mathcal{E} and α . When $\alpha = 0$, the spherical harmonics, $Y_{1, M_a - M_b}^*(\alpha, 0)$ are non-zero only when $M_a = M_b$ and thus, the electric field couples pairs of sublevels with $M_a = M_b$. Since the state $|M_a = -10\rangle$ has no counterpart in the $\{|M_b\rangle\}$ subspace, the former is unaffected by the electric field. Hence, the electric dipole moment of the Dy atom in the state $|S\rangle$ vanishes for $\alpha = 0$. When α grows, the electric field couples $|M_a = -10\rangle$ with other $|M_b\rangle$ sublevels, reaching a maximum mixing for $\alpha = \pi/2$ (see Fig. 2.2 (a)). Therefore, for a given \mathcal{E} , d_e increases with α until $\alpha = \pi/2$. This comes at the cost of decreasing the lifetime of $|S\rangle$, as shown in Fig. 2.2 (b). For a range of experimentally realistic $\mathcal{E} = 0\text{-}4$ kV/cm, d_e varies from 0 to 0.16 Debye and the magnetic moment remains constant, $d_m \simeq 13 \mu_B$ (higher than ground-state Dy atoms), whereas the lifetime of $|S\rangle$ varies from 28 s (considering electric-quadrupole and magnetic-dipole transitions) to 10 ms [44].

2.2.3 Experimental realization of doubly dipolar Dy atoms

In a recent experiment [47] by Anich et al. in Innsbruck, the engineering of a doubly dipolar interaction in Dy atoms has been realized. Fig. 2.1 illustrates the energy levels and transitions in Dy that are relevant for creating and manipulating electromagnetic dipoles. In the experiment, the electric dipole moment in Dy atoms was engineered by coherently mixing two nearly degenerate atomic states of opposite parity using microwave (MW) radiation. These states are the $J = 10$ state from the $[Xe]4f^{10}6s6p$ and $J = 9$ state from $[Xe]4f^{10}5d6s$, separated by about 35 GHz in energy. Initially, the opposite parity states are populated by a Stimulated Raman Adiabatic Passage (STIRAP) technique, efficiently preparing the atoms without

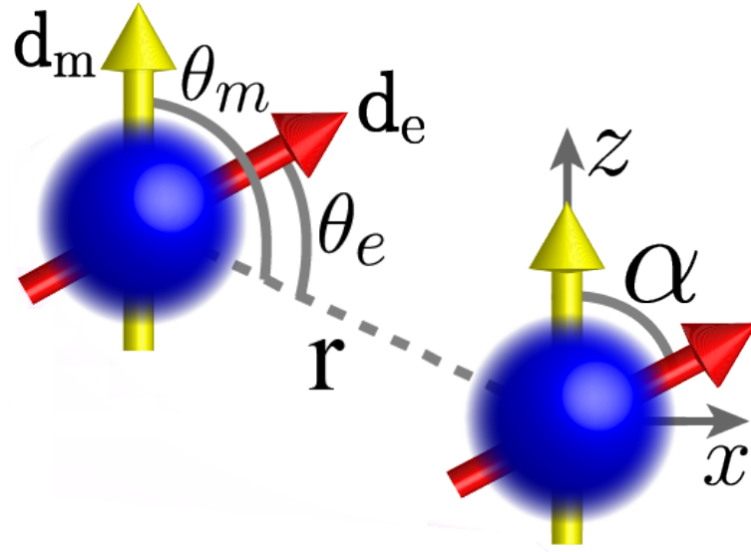


FIGURE 2.3: **Doubly dipolar particles.** Both electric (\mathbf{d}_e) and magnetic (\mathbf{d}_m) dipoles are assumed polarized on the xz plane, forming an angle α between them. The angle θ_m (θ_e) is the angle between \mathbf{d}_m (\mathbf{d}_e) and the vector joining the atoms, \mathbf{r} .

populating intermediate excited states. A linearly polarized MW field couples the $|10, -9\rangle$ and $|9, -9\rangle$ states and creates a dressed state, which is a coherent superposition of opposite-parity components. This mixing induces a finite electric dipole moment while maintaining the atom's large intrinsic magnetic dipole moment. By adjusting the magnetic field (Zeeman shift) and MW parameters (detuning and Rabi frequency), a degeneracy is induced between the microwave-dressed state and another nearby Zeeman sublevel, $|10, -10\rangle$. This establishes a degenerate isospin-1/2 system where both electric and magnetic dipole-dipole interactions are simultaneously active. The magnitude of the electric dipole moment in the dressed state can be tuned by controlling the MW field parameters. The mixing of the opposite parity states is also feasible through a DC electric field.

2.3 Doubly Dipolar Potential

Now, we study the properties of the doubly dipolar potential in detail. The doubly-dipolar interaction between two atoms is described as follows :

$$V_d(\mathbf{r}) = \frac{\mu_0 d_m^2}{4\pi} \frac{(1 - 3 \cos^2 \theta_m)}{|\mathbf{r}|^3} + \frac{d_e^2}{4\pi\epsilon_0} \frac{(1 - 3 \cos^2 \theta_e)}{|\mathbf{r}|^3}, \quad (2.5)$$

where μ_0 (ϵ_0) is the vacuum permeability (permittivity) and θ_m (θ_e) is the angle formed by the magnetic (electric) dipole moment with the vector \mathbf{r} joining the atoms (See Fig. 2.3). We define the $g_m = \mu_0 d_m^2 / 4\pi$, $g_e = d_e^2 / 4\pi\epsilon_0$ as the magnetic and electric dipole strengths, respectively.

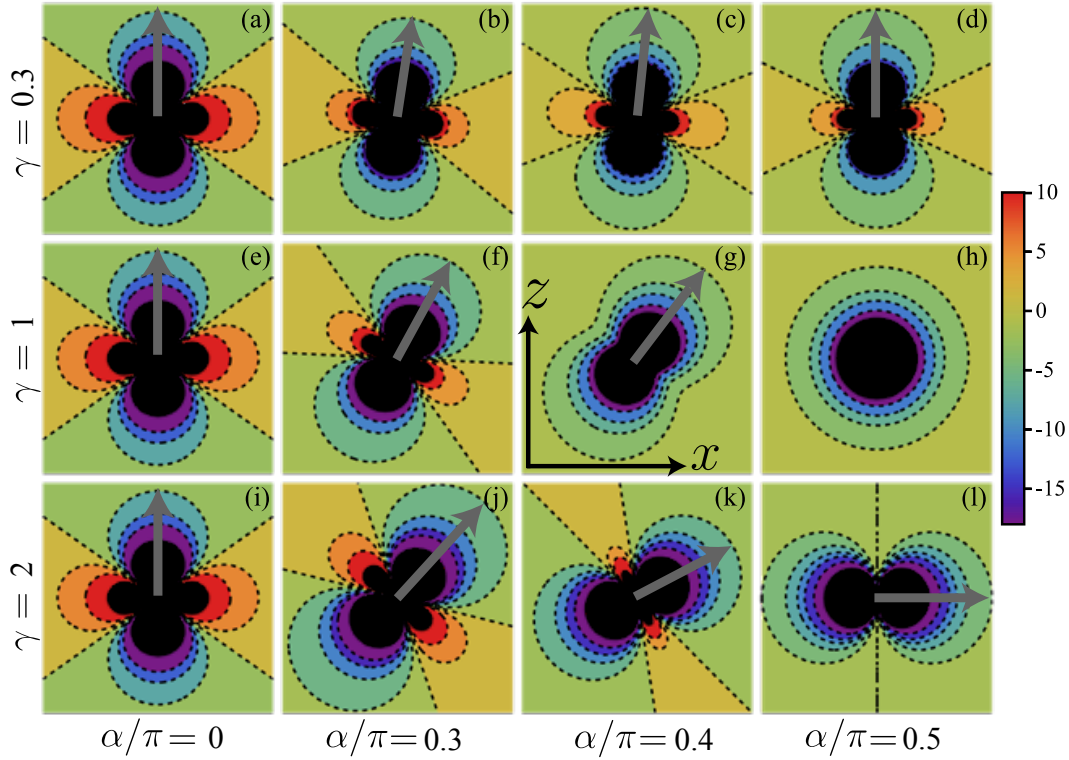


FIGURE 2.4: **Anisotropy of the doubly dipolar potential.** ($V_d^{y=0}(r, \theta)$) for different values of α and γ on the xz -plane. Grey arrows indicate the effective polarization axis determined by the polarization angle θ_p (Eq. (2.7)).

Whereas $V_d(\mathbf{r})$ is always repulsive along the y -axis, it is anisotropic on the xz -plane. This anisotropy is well characterized by the angular part of the dipolar potential on the xz -plane:

$$V_d^{y=0}(r, \theta) \propto \left[1 - 3 \frac{\cos^2 \theta + \gamma(\cos \theta \cos \alpha + \sin \alpha \sin \theta)^2}{1 + \gamma} \right], \quad (2.6)$$

where θ is the polar angle (xz coordinates have been transformed to the r, θ coordinates), and $\gamma = (d_e/d_m)^2/(\mu_0\epsilon_0)$ characterizes the relative strength between the electric and magnetic dipole moments. The ratio γ can be varied independently of α by tuning the external electric field, \mathcal{E} . From Eq. (2.6), we can realize that $V_d^{y=0}(r, \theta)$ exhibits non-trivial anisotropic properties despite being independent of the azimuthal angle. Interestingly, the anisotropic nature of $V_d^{y=0}(r, \theta)$ also depends on the ratio between the dipole moments through the parameter γ , not just on the orientation of the dipoles. In Fig. 2.4, we depict $V_d^{y=0}(\mathbf{r})$ for different α and γ . When $\alpha = 0$, we have the usual dipolar potential, attractive along z and repulsive along x [36]. As α increases up to $\pi/2$, the dependence of the potential on γ becomes more significant. For $\alpha = \pi/2$, when γ grows, the potential eventually inverts its anisotropy (last column of Fig. 2.4).

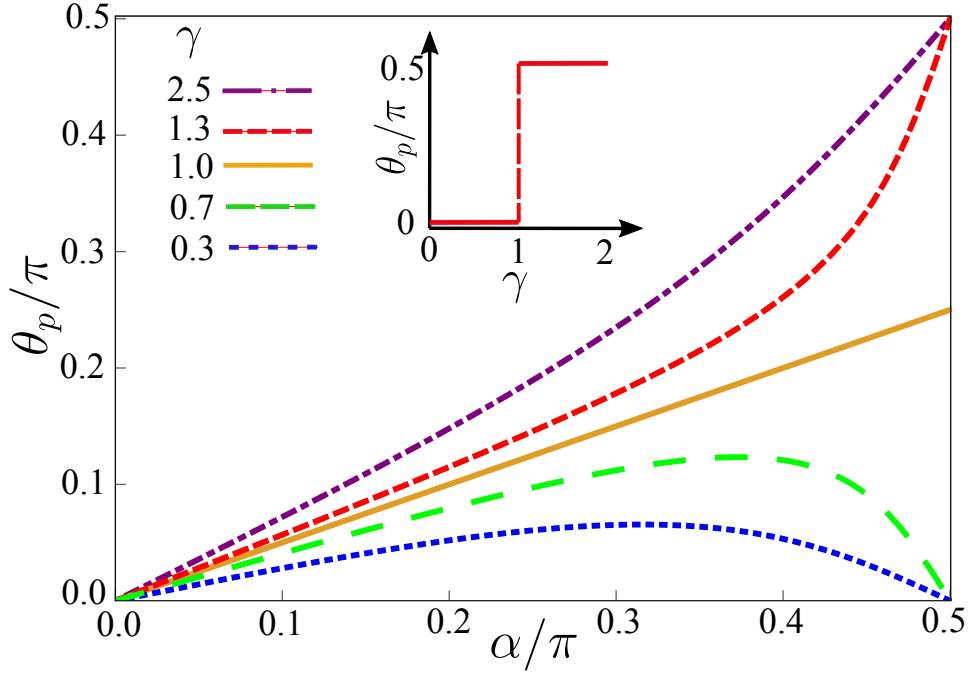


FIGURE 2.5: **Polarization angle.** Polarization angle θ_p as a function of α for different values of γ . The inset shows θ_p as a function of γ for $\alpha = \pi/2$, exhibiting a jump at $\gamma = 1$.

Despite this nontrivial anisotropy, it is possible to define an effective polarization axis, as illustrated by the arrows in Fig. 2.4. This axis corresponds to the direction where the doubly dipolar potential is maximally attractive. This direction lies on the xz plane, forming an angle

$$\theta_p(\alpha, \gamma) = \cos^{-1} \left[\frac{1}{\sqrt{2}} \sqrt{1 + \frac{1 + \gamma \cos 2\alpha}{\sqrt{1 + \gamma^2 + 2\gamma \cos 2\alpha}}} \right], \quad (2.7)$$

with the positive z -axis. As shown in Fig. 2.5, for a dominant magnetic dipole ($\gamma < 1$), θ_p increases with α , reaches a maximum $[\theta_p^{\max} = \cos^{-1} \left(\frac{1}{2} [1 + \sqrt{1 - \gamma^2}] \right)^{1/2}]$ at $\alpha = \frac{1}{2} \cos^{-1}(-\gamma)$ and then decreases back to zero at $\alpha = \pi/2$. On the contrary, for a dominant electric dipole ($\gamma > 1$), θ_p increases monotonously from zero to $\pi/2$. A linear relation, $\theta_p = \alpha/2$, holds for $\gamma = 1$. When $\alpha = \pi/2$ and $\gamma = 1$, θ_p is not defined due to the isotropic nature of the xz -interactions. Thus, θ_p exhibits a discontinuous behavior as a function of γ for $\alpha = \pi/2$, changing abruptly from zero to $\pi/2$ across $\gamma = 1$ (inset of Fig. 2.5). As discussed below, θ_p plays a key role in characterizing the anisotropic nature of the interactions and provides valuable insights into the overall behavior of the doubly dipolar system.

It can also be seen that, there exists a critical angle $\alpha_a = \frac{1}{2} \cos^{-1} \left[\frac{\gamma - 4(1 + \gamma^2)}{9\gamma} \right]$, above which the xz potential becomes purely attractive (see Figs. 2.4 (g), (h), and (l)). The angle α_a separates the regime between the purely attractive xz potential ($\alpha >$

α_a) with an anisotropic xz potential exhibiting both repulsive and attractive lobes. The attractive and repulsive lobes in the potential are separated by two intersecting straight lines satisfying $V_d^{y=0}(r, \theta) = 0$. Writing the equation for these straight lines as $z = m_{\pm}x$, where the slopes m_{\pm} can be found from the condition $V_d^{y=0}(r, \theta) = 0$ as,

$$m_{\pm} = -\frac{3\gamma \sin 2\alpha \pm \sqrt{2(4 - \gamma + 4\gamma^2 + 9\gamma \cos 2\alpha)}}{4 + \gamma + 3\gamma \cos 2\alpha}. \quad (2.8)$$

When the xz potential becomes purely attractive, the two lines merge into one, i.e., $m_+ = m_-$, and we obtain,

$$\alpha_a = \frac{1}{2} \cos^{-1} \left[\frac{\gamma - 4(1 + \gamma^2)}{9\gamma} \right]. \quad (2.9)$$

The region in the $\alpha - \gamma$ plane in which the potential $V_d^{y=0}(r, \theta)$ becomes purely attractive is shown as shaded in Fig. 2.6 (a). The potential remains anisotropic except when $\alpha = \pi/2$ and $\gamma = 1$. For this special case, the doubly dipolar potential becomes isotropic, $V_d^{y=0}(r, \theta) = -1/r^3$.

2.4 Doubly Dipolar BEC

At this juncture, we consider a gas consisting of N doubly dipolar Dy bosonic atoms of mass M with both electric and magnetic dipole moments, as schematically shown in Fig. 2.3. At very low temperatures, the system is described in the mean-field by a nonlocal Gross-Pitaevskii equation (NLGPE): $i\hbar\dot{\psi}(\mathbf{r}, t) = \mathcal{H}\psi(\mathbf{r}, t)$, where

$$\mathcal{H} = \frac{-\hbar^2 \nabla^2}{2M} + \int d^3r' \psi(\mathbf{r}', t) V(\mathbf{r} - \mathbf{r}') \psi(\mathbf{r}', t), \quad (2.10)$$

where $V(\mathbf{r}) = g\delta(\mathbf{r}) + NV_d(\mathbf{r})$ is the interaction potential. The parameter $g = 4\pi\hbar^2 a_s N/M$ determines the contact interaction strength, with a_s being the s -wave scattering length. To quantify the dipolar interactions in the condensate, we introduce the parameters $g_m = N\mu_0 d_m^2/4\pi$ and $g_e = Nd_e^2/4\pi\epsilon_0$, respectively, for quantifying the magnetic and electric dipole-dipole interaction strengths.

2.4.1 Bogoliubov excitations and sound velocity in a homogeneous doubly DBEC

In the following, we consider a condensate with uniform density n_0 . Assuming the homogeneous solution as, $\psi(\mathbf{r}, t) = \left[\sqrt{n_0} + u_k e^{-i(\mathbf{k}\cdot\mathbf{r} - \epsilon_k t/\hbar)} + v_k^* e^{i(\mathbf{k}\cdot\mathbf{r} - \epsilon_k t/\hbar)} \right] e^{-i\mu t/\hbar}$ in

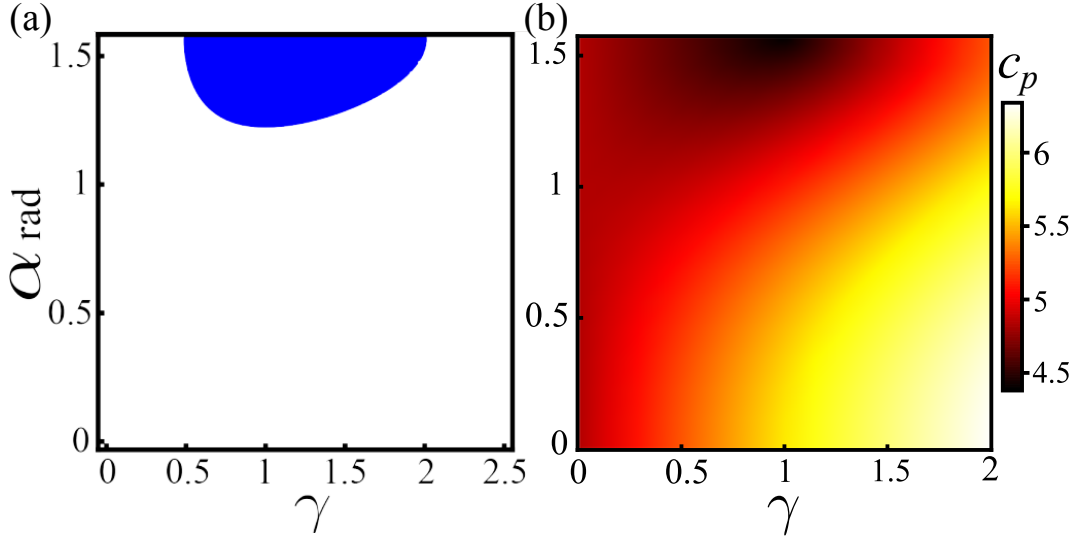


FIGURE 2.6: **Attractive doubly dipolar potential and sound velocity.** (a) The blue shaded part indicates the region in which the two-dimensional xz potential $V_d^{y=0}(r, \theta)$ becomes purely attractive. (b) The sound velocity c_p along the polarization axis as a function of γ and α . Up to a critical value of $\alpha = \alpha_a$, c_p increases monotonously with γ . For $\alpha > \alpha_a$, c_p shows a non-monotonous behavior as a function of γ with a minimum at $\gamma = 1$

NLGPE, where k is the quasi-momentum and μ is the chemical potential of the condensate, we obtain the dispersion law of elementary excitations as,

$$\varepsilon_k = \sqrt{\frac{\hbar^2 k^2}{2M} \left(\frac{\hbar^2 k^2}{2M} + 2g_m n_0 [\beta + \mathcal{F}(\theta_k, \phi_k, \alpha)] \right)}, \quad (2.11)$$

where $\beta = g/g_m$ and

$$\begin{aligned} \mathcal{F}(\theta_k, \phi_k, \alpha) &= \frac{4\pi\gamma}{3} \left[3(\cos \alpha \cos \theta_k + \sin \alpha \sin \theta_k \cos \phi_k)^2 - 1 \right] \\ &\quad + \frac{4\pi}{3} (3 \cos^2 \theta_k - 1). \end{aligned} \quad (2.12)$$

θ_k and ϕ_k are the angular coordinates in the momentum space. The phonons $\varepsilon_{k \rightarrow 0} = c(\theta_k, \phi_k) \hbar k$ determine both the superfluid nature and stability properties of the condensate, where

$$c(\theta_k, \phi_k) = [g_m n_0 (\beta + \mathcal{F}(\theta_k, \phi_k, \alpha)) / M]^{1/2}, \quad (2.13)$$

is the angle-dependent sound velocity. The stiffer phonons propagate along the effective polarization axis set by θ_p , whereas the softer ones reside in a plane or axis perpendicular to it. Note that exciting phonons with the wave vector along an axis creates density modulations in a plane perpendicular to it. The atoms in the plane perpendicular to the polarization axis experience stronger repulsive DDIs, and hence, the phonons with wave vectors along the polarization axis are stiffer.

Therefore, for dipoles polarized in the xz plane, the phonons propagating along the y -axis are always softer, which sets the stability criteria for the condensate, i.e., $c_y^2 = c^2(\pi/2, \pi/2) = c_m^2 \left[\beta - \frac{4\pi}{3}(1 + \gamma) \right] > 0$ with $c_m = \sqrt{g_m n_0 / M}$. Thus, a homogeneous DDBEC becomes unstable against local collapses if $\beta < \frac{4\pi}{3}(1 + \gamma)$. Though the instability condition is independent of α , the post-instability dynamics crucially depend on it. The sound velocity along the polarization axis (c_p) can be obtained by taking $\theta_l = \theta_p$ and $\phi_k = 0$ in Eq. (2.13), which provides us,

$$c_p = c_m \left(\beta + \frac{4\pi\gamma}{3} \left[3 \left(\cos \alpha \cos \theta_p + \sin \alpha \sin \theta_p \right)^2 - 1 \right] + \frac{4\pi}{3} (3 \cos^2 \theta_p - 1) \right), \quad (2.14)$$

which as a function of α and γ is shown in Fig. 2.6 (b). For small values of α , the polarization axis lies almost along the z -axis [$\theta_p \sim 0$, as seen in Fig. 2.4] and in the plane perpendicular to it (almost xy -plane), the dipoles exhibit repulsive interactions. Therefore, c_p increases monotonously with γ for small values of α . As α approaches $\pi/2$, we see that c_p shows a non-monotonous behavior as a function of γ with a minimum at $\gamma = 1$ [see top part of Fig. 2.6 (a)]. It can be understood from the fact that in the limit $\gamma \rightarrow 1$ and $\alpha \rightarrow \pi/2$, the potential $V_d^{y=0}(r, \theta)$ becomes purely attractive, easing the density modulations along at least one axis perpendicular to the polarization axis.

2.4.2 Lee-Huang-Yang correction

Using the dispersion in Eq. (2.11), we obtain the beyond mean field, Lee-Huang-Yang (LHY) correction to the ground state energy of the condensate as,

$$\Delta E = \frac{V}{2} \int \frac{d^3 q}{(2\pi)^3} \left[\varepsilon_q - \frac{\hbar^2 q^2}{2m} - nV_q + \frac{mn^2 V_q^2}{\hbar^2 q^2} \right],$$

where V is the volume and V_q is the Fourier transform of the total inter-atomic potential (both contact and dipolar potential). Then, the LHY correction of the chemical potential $\Delta\mu = \partial\Delta E/\partial N$ [156–158, 165, 167, 271, 272] and is obtained as,

$$\begin{aligned} \Delta\mu = & \frac{1}{3\pi^3 N} \left(\frac{Mn_0}{\hbar^2} \right)^{3/2} g_m^{5/2} \left[\frac{15}{8\sqrt{2}} \int d\Omega_k \int_0^\infty \frac{\hbar^3 k^2 dk}{(2mg_m n_0)^{3/2}} \times \right. \\ & \left(\frac{\hbar k}{\sqrt{2mg_m n_0}} \sqrt{\frac{\hbar^2 k^2}{2mg_m n_0} + 2[\beta + \mathcal{F}(\theta_k, \phi_k, \alpha)]} - \frac{\hbar^2 k^2}{2mg_m n_0} - \right. \\ & \left. \left. \beta - \mathcal{F}(\theta_k, \phi_k, \alpha) + \frac{2mg_m n_0 [\beta + \mathcal{F}(\theta_k, \phi_k, \alpha)]^2}{2\hbar^2 k^2} \right) \right], \quad (2.15) \end{aligned}$$

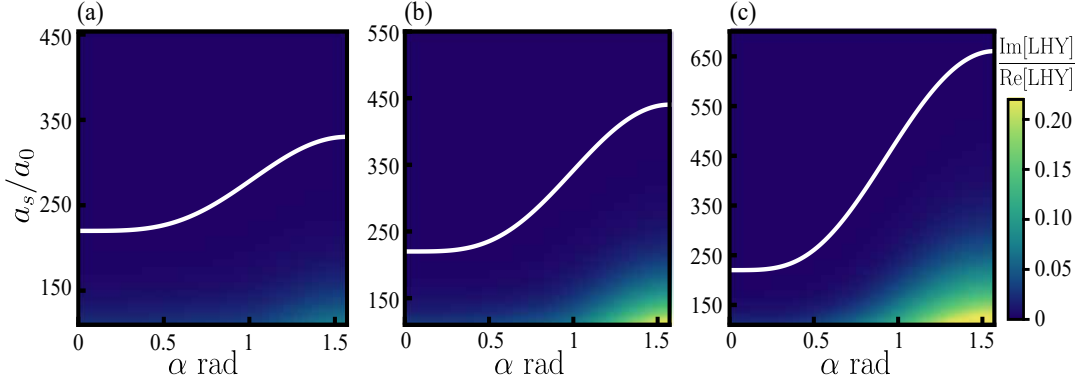


FIGURE 2.7: $\text{Im}[\Delta\mu]/\text{Re}[\Delta\mu]$ for homogeneous BEC for 3 different values of electric fields, (a) $\mathcal{E}=1.46$ Kv/cm, (b) $\mathcal{E}=2.66$ Kv/cm, (c) $\mathcal{E}=3.76$ Kv/cm for a fixed value of magnetic field $\mathcal{B}=100$ G. The boundary separates the stable and unstable regime determined from the stability criteria: $\beta - \frac{4\pi}{3}(1 + \gamma) > 0$

where $\int d\Omega_k = \int_0^{2\pi} d\phi_k \int_0^\pi d\theta_k \sin \theta_k$. After doing the integration over k , we get

$$\Delta\mu = \frac{1}{3\pi^3 N} \left(\frac{Mn_0}{\hbar^2} \right)^{3/2} g_m^{5/2} \int d\Omega_k [\beta + \mathcal{F}(\theta_k, \phi_k, \alpha)]^{\frac{5}{2}}. \quad (2.16)$$

The correction, $\Delta\mu$ becomes complex when $\beta < \frac{4\pi}{3}(1 + \gamma)$. The real part of $\Delta\mu$ is dominated by hard modes, whereas the unstable low-momentum excitations determine the imaginary part. Not very deep in the instability regime, $\text{Im}[\Delta\mu]/\text{Re}[\Delta\mu] \ll 1$ and $\text{Im}[\Delta\mu]$ can be disregarded. The ratio $\text{Im}[\Delta\mu]/\text{Re}[\Delta\mu]$ for a homogeneous BEC is shown in Fig. 2.7 for different values of the external electric field, \mathcal{E} at a fixed value of the magnetic field, $\mathcal{B}=100$ G. As one can see that, deep in the unstable regime $\text{Im}[\Delta\mu]/\text{Re}[\Delta\mu]$ has significant value, but as we approach the boundary between a stable and an unstable homogeneous BEC, $\text{Im}[\Delta\mu]/\text{Re}[\Delta\mu]$ is vanishingly small, and the $\text{Im}[\Delta\mu]$ can be neglected. Note also that for a finite-size condensate, $\text{Im}[\Delta\mu]$ is further suppressed by a low-momentum cut-off [165, 167, 272, 273].

2.4.3 Generalized Gross-Pitaevskii equation

The LHY correction given in Eq. (2.16) is repulsive in nature, and it also exhibits a density dependence of $n_0^{3/2}$. Due to this density dependence, the LHY correction becomes very significant at high densities, and in particular, halts the condensate collapse arising from the attractive interactions, leading to the formation of a quantum droplet, which we discuss in Chapter 3. By incorporating the LHY correction to the NLGPE using local density approximation [$n_0 \rightarrow n(\mathbf{r}, t)$] [157, 165–167, 271, 272, 274], we arrive at a generalized NLGPE:

$$i\hbar\dot{\psi}(\mathbf{r}, t) = (\mathcal{H} + \Delta\mu[n(\mathbf{r}, t)])\psi(\mathbf{r}, t). \quad (2.17)$$

Similar generalized GPE equations have been employed in singly-dipolar BECs and binary mixtures [40, 41, 71, 161–163, 168, 194], providing a good qualitative and, to a large extent, quantitative agreement with experiments. A better quantitative picture may, however, require going beyond the local-density approximation and/or the use of involved quantum Monte Carlo calculations [252, 275–280] which will be explored in the next section. We numerically solve Eq. (2.17) via imaginary time evolution to obtain the ground states of a doubly dipolar BEC. We have used the split-step Crank–Nicolson method for the imaginary-time propagation as detailed in Ref. [281]. Note that, for the generalized NLGPE to be valid, we require $\text{Im}[\Delta\mu]/\text{Re}[\Delta\mu] \ll 1$.

2.5 Path Integral Monte Carlo Simulation

Path integral quantum Monte Carlo (PIMC) is a methodology based on Feynman’s path integral theory, devised to accurately characterize the thermodynamic features of quantum systems at finite temperatures. PIMC has been fruitfully applied to a variety of bosonic systems, starting with ^4He [282] and continuing, more recently, with different ultracold atomic and molecular setups [272, 276, 277, 283–285]. In the following, we discuss the detailed background of the PIMC formalism and the PIMC algorithm.

Feynman’s path integral formulation presents an elegant approach to quantum mechanics that offers a different perspective from the traditional Schrödinger and Heisenberg formulations. Introduced by Richard P. Feynman in 1948 [286], the underlying idea of this formulation is the sum of all possible trajectories a quantum particle can take between two points, weighted by a phase factor derived from the classical action.

2.5.1 Classical action and Lagrangian

In classical mechanics, the trajectory of a particle is described using Hamilton’s principle of least action. The classical path traversed by a particle between two points in time is the one that extremizes the action S . The action is defined in terms of the Lagrangian, $L(\mathbf{q}, \dot{\mathbf{q}}, t)$:

$$S[\mathbf{q}(t)] = \int_{t_i}^{t_f} L(\mathbf{q}, \dot{\mathbf{q}}, t) dt. \quad (2.18)$$

Here, $\mathbf{q}(t)$ denotes the vector of the generalized coordinates of the particle, and $\dot{\mathbf{q}}(t)$ is the corresponding velocity vector. The Lagrangian is given by $L(\mathbf{q}, \dot{\mathbf{q}}, t) = T - V$, where T is the kinetic energy and V is the potential energy.

The classical trajectory is the one that makes the action stationary ($\delta S = 0$), leading to the Euler-Lagrange equation:

$$\frac{d}{dt} \left(\frac{\partial L}{\partial \dot{\mathbf{q}}} \right) - \frac{\partial L}{\partial \mathbf{q}} = 0.$$

This leads to the equations of motion for the system. If the initial conditions at t_i are known, one can determine the position and the velocity of the particle at any later time t_f by solving the Euler-Lagrange equation. This uniquely determines the trajectory $\mathbf{q}(t)$ which the particle follows and for which one computes the action $S(\mathbf{q})$.

2.5.2 Quantum path integral

Heisenberg's uncertainty principle posits that within the realm of quantum mechanics, it is fundamentally impossible to simultaneously determine both the position and the velocity (or momentum) of a particle. The central quantity is the transition amplitude of the time-evolution operator between localized states of the particles, from $|\mathbf{q}_i, t_i\rangle$ at time t_i to state $|\mathbf{q}_f, t_f\rangle$ at time t_f :

$$\langle \mathbf{q}_f, t_f | \mathbf{q}_i, t_i \rangle = \langle \mathbf{q}_f | \hat{U}(t_f, t_i) | \mathbf{q}_i \rangle. \quad (2.19)$$

We can express the time-evolution operator as follows:

$$\hat{U}(t_f, t_i) = \exp \left[-\frac{i}{\hbar} \int_{t_i}^{t_f} dt' \hat{H}(t') \right], \quad (2.20)$$

where $\hat{H}(t) \equiv H(\mathbf{q}, \mathbf{p}, t)$ is the Hamiltonian operator.

In the coordinate space, we can write

$$\langle \mathbf{q}_f, t_f | \mathbf{q}_i, t_i \rangle \equiv \mathcal{N} \int_{\mathbf{q}_i}^{\mathbf{q}_f} \mathcal{D}\mathbf{q} \exp \left[\frac{i}{\hbar} S[\mathbf{q}(t)] \right]. \quad (2.21)$$

Eq. (2.21) expresses the path-integral representation of the quantum-mechanical transition amplitude in the coordinate space. This involves weighing every trajectory $\mathbf{q}(t)$ with the phase factor $e^{iS[\mathbf{q}(t)]/\hbar}$ followed by summing over all possible trajectories in the coordinate space. This framework provides a powerful understanding of how quantum systems explore all possible configurations simultaneously and how interference between different paths leads to quantum phenomena. The crucial aspect in evaluating the individual trajectories lies in determining the magnitude of the action along a given trajectory relative to Planck's quantum of action \hbar . In the limit of $\hbar \rightarrow 0$, the ratio $S[\mathbf{q}(t)]/\hbar$ becomes arbitrarily large, leading to rapid oscillations of the phase factors away from the classical trajectory. The contribution of these

trajectories in the path integral cancels mutually. In contrast, in the vicinity of the classical trajectory, the action is stationary, and the phase factors remain nearly identical. Hence, the limit $\hbar \rightarrow 0$ corresponds to the classical limit, where the behavior of the system is dominated by the classical trajectory.

2.5.3 Thermal density matrix

The path integral formulation is a powerful approach to understanding the thermal equilibrium properties of a quantum system. Here, we discuss the thermal density matrix, which describes the quantum state of a system at a finite temperature T and can be expressed as a sum over all possible paths that the system can take, weighted by a phase factor [282, 286, 287].

We assume a canonical ensemble where the system has fixed volume V , the number of particles N , and temperature T . For a Hamiltonian \mathcal{H} , the bulk thermodynamic quantities can be determined from the quantum-statistical partition function,

$$Z = \sum_n e^{-E_n/K_B T} = \sum_n e^{-\beta E_n}. \quad (2.22)$$

In operator notation, we can write, $Z = \text{Tr}(e^{-\beta \mathcal{H}})$. Where the operator $\rho = e^{-\beta \mathcal{H}}$ is the density matrix. In our notation, the density matrix is not normalized by the partition function. If ϕ_i are the eigenstates of the Hamiltonian, the equilibrium value of an observable O can be expressed as,

$$\langle O \rangle = Z^{-1} \sum_n \langle \phi_n | O | \phi_n \rangle e^{-\beta E_n} = \text{Tr}(O\rho)/Z. \quad (2.23)$$

These traces can be performed on any complete basis; however, we shall exclusively utilize a position basis. The coordinate space density matrix is

$$\rho(\mathbf{R}, \mathbf{R}'; \beta) = \langle \mathbf{R} | e^{-\beta \mathcal{H}} | \mathbf{R}' \rangle = \sum_n \phi_n^*(\mathbf{R}) \phi_n(\mathbf{R}') e^{-\beta E_n}, \quad (2.24)$$

where $\mathbf{R} = \mathbf{r}_1, \dots, \mathbf{r}_N$ and \mathbf{r}_i is the coordinate of the i -th particle. This notation indicates generic off-diagonal elements of the density matrix, defined as $\rho_{i,j}$. Two sets of equal coordinates represent the diagonal elements, $\rho(\mathbf{R}, \mathbf{R}; \beta)$. For a three-dimensional system $\rho(\mathbf{R}, \mathbf{R}'; \beta)$ is a function of $6N+1$ variables. In the coordinate basis representation, the expectation value of O becomes,

$$\langle O \rangle = \frac{1}{Z} \int d\mathbf{R} d\mathbf{R}' \rho(\mathbf{R}, \mathbf{R}'; \beta) \langle \mathbf{R} | O | \mathbf{R}' \rangle, \quad (2.25)$$

and the partition function is given by,

$$Z = \int d\mathbf{R} \rho(\mathbf{R}, \mathbf{R}; \beta). \quad (2.26)$$

The thermal density matrix possesses the convolution property, which establishes a relationship between the density matrix of a composite system and those of its constituent subsystems. This precise and straightforward property of density matrices is the foundation for the path-integral method. The product of two density matrices is a density matrix,

$$e^{-\beta_1 \mathcal{H}} e^{-\beta_2 \mathcal{H}} = e^{-(\beta_1 + \beta_2) \mathcal{H}} = e^{-\beta \mathcal{H}}. \quad (2.27)$$

In the coordinate basis, the convolution can be written as

$$\rho(\mathbf{R}, \mathbf{R}'; \beta) = \int d\mathbf{R}_1 \rho(\mathbf{R}, \mathbf{R}_1; \beta_1) \rho(\mathbf{R}_1, \mathbf{R}'; \beta_2). \quad (2.28)$$

We have written the expression for $\beta \mathcal{H}$ as $\beta_1 \mathcal{H} + \beta_2 \mathcal{H}$, and subsequently decomposed the exponential function. One can do it given that β represents a numerical value and \mathcal{H} commutes with itself.

Discrete path integrals

The path-integral formula for the many-body density matrix is obtained by using the product property M times, which gives the expression for the density matrix at a temperature T in terms of density matrices at temperature MT :

$$e^{-\beta \mathcal{H}} = \left(e^{-\tau \mathcal{H}} \right)^M, \quad (2.29)$$

In the coordinate representation,

$$\rho(\mathbf{R}_0, \mathbf{R}_M; \beta) = \int \dots \int d\mathbf{R}_1 d\mathbf{R}_2 \dots d\mathbf{R}_{M-1} \rho(\mathbf{R}_0, \mathbf{R}_1; \tau) \rho(\mathbf{R}_1, \mathbf{R}_2; \tau) \dots \rho(\mathbf{R}_{M-1}, \mathbf{R}_M; \tau), \quad (2.30)$$

where we introduce the time step $\tau = \beta/M$. For finite M values, we have a discrete-time path. For the limit, $M \rightarrow \infty$, one has a continuous path. It is important to note that Eq. (2.30) is exact for any $M \geq 1$. For more details on the validity of Eq. (2.30), please refer to Appendix B.1.

We can write the free particle propagator for a single free particle as follows,

$$\rho_{\text{free}}(\mathbf{R}, \mathbf{R}_1; \tau) = \frac{1}{\Lambda_\tau^d} e^{-\frac{\pi(\mathbf{R} - \mathbf{R}_1)^2}{\Lambda_\tau^2}}, \quad (2.31)$$

where $\Lambda_\tau = \sqrt{4\pi\lambda\tau}$ is the thermal de Broglie wavelength at the temperature set by the imaginary time step τ . Using the free particle propagator, we arrive at the discrete path-integral expression for the density matrix in the primitive approximation:

$$\rho(\mathbf{R}_0, \mathbf{R}_M; \beta) = \int d\mathbf{R}_1 \dots d\mathbf{R}_{M-1} \left(\frac{1}{\Lambda_\tau^d} \right)^M \exp \left(-\frac{\pi}{\Lambda_\tau^2} \sum_{j=1}^M [(\mathbf{R}_{j-1} - \mathbf{R}_j)^2 + \tau V(\mathbf{R}_j)] \right). \quad (2.32)$$

This expression relates the thermal density matrix at any temperature to integrals over the path $\mathbf{R}_1 \dots \mathbf{R}_{M-1}$ similar to a classical Maxwell-Boltzmann function. This is a quantum-classical mapping of the Feynman path integral formulation of quantum statistical mechanics.

Path-integral notation

The collection $(\mathbf{R}_0, \dots, \mathbf{R}_M)$ represents N discrete worldlines in imaginary time from 0 to β . $\tau \equiv \beta/M$ is the time step, and a single \mathbf{R}_j represents the positions of all particles on the j -th time slice. $\mathbf{R}_j = (\mathbf{r}_j^0, \dots, \mathbf{r}_j^N)$. \mathbf{r}_j^i is called a *bead* and denotes the position of the i -th particle on the j -th time slice. The propagator, $\rho(\mathbf{r}_{j-1}^i, \mathbf{r}_j^i; \tau)$ that connects the two beads of consecutive time slices is called a *link*. The action of a link is defined as minus the logarithm of the exact density matrix:

$$S^j \equiv S(\mathbf{R}_{j-1}, \mathbf{R}_j; \tau) \equiv -\ln[\rho(\mathbf{R}_{j-1}, \mathbf{R}_j; \tau)]. \quad (2.33)$$

There will be contributions to S^j coming from each term of the Hamiltonian. Separating out the kinetic and the potential part, we can write the free action,

$$S_{\text{free}} = \sum_{j=1}^M \left[\ln \Lambda_\tau^d + \frac{\pi}{\Lambda_\tau^2} (\mathbf{R}_{j-1} - \mathbf{R}_j)^2 \right]. \quad (2.34)$$

Within the primitive approximation, we can express the primitive action,

$$S_{\text{primitive}} = \sum_{j=1}^M \left[\ln \Lambda_\tau^d + \frac{\pi}{\Lambda_\tau^2} (\mathbf{R}_{j-1} - \mathbf{R}_j)^2 + \tau V(\mathbf{R}_j) \right]. \quad (2.35)$$

Since the exact density matrix is symmetric, we can rearrange the terms in the integral and write the primitive action in a symmetrized form:

$$S_{\text{primitive}} = \sum_{j=1}^M \left[\ln \Lambda_\tau^d + \frac{\pi}{\Lambda_\tau^2} (\mathbf{R}_{j-1} - \mathbf{R}_j)^2 + \tau \frac{V(\mathbf{R}_{j-1}) + V(\mathbf{R}_j)}{2} \right]. \quad (2.36)$$

Interaction potentials

In addition to the external potential $V(\mathbf{R})$, the potential term may include interaction potentials, $U(\mathbf{R})$. These interaction potentials are addressed using the primitive approximation, similar to the treatment of external potentials. Generically, we can write the density matrix,

$$\rho(\mathbf{R}, \mathbf{R}'; \tau) = \rho_{\text{free}}(\mathbf{R}, \mathbf{R}'; \tau) \rho_{\text{pot}}(\mathbf{R}, \mathbf{R}'; \tau). \quad (2.37)$$

In the primitive approximation and due to the interaction potential between the pair of particles (i, j) , we have:

$$\rho_{\text{pot}}(\mathbf{R}, \mathbf{R}'; \tau) = \prod_{i < j} e^{-\tau \frac{u(\mathbf{r}_{ij}) + u(\mathbf{r}'_{ij})}{2}}. \quad (2.38)$$

The classical isomorphism

The path-integral formulation expressed in Eq. (2.32) can be constructed as a classical configuration integral, where the action plays a role similar to classical potential energy. In this analogy, the kinetic link action corresponds to a spring potential connecting beads representing the same atom in successive time slices. The system forms a classical chain of M beads linked by harmonic springs, resembling a "ring polymer".

Quantum statistics: Bose symmetry

The density matrices discussed till now have been appropriate for distinguishable particles, which follow Boltzmann statistics. The density matrix of indistinguishable particles (bosons or fermions) needs to be modified compared to Boltzmann particles. Here, we introduce the bosonic density matrix,

$$\rho(\mathbf{R}, \mathbf{R}'; \beta) = \frac{1}{N!} \sum_{\mathcal{P}} \rho_D(\mathbf{R}, \mathcal{P}\mathbf{R}'; \beta), \quad (2.39)$$

where ρ is the bosonic density matrix and ρ_D is the density matrix for the distinguishable particles. \mathcal{P} is the permutation operator, which reshuffles particle coordinates in all possible ways. The Hamiltonian for Bose systems is symmetric under particle exchange; all states are either even or odd with respect to a permutation. A bosonic simulation involves a random walk through both the path and permutation spaces. In fermionic systems, an additional \pm factor arises, contingent upon the selection of permutation. From a numerical perspective, this poses issues because positive and

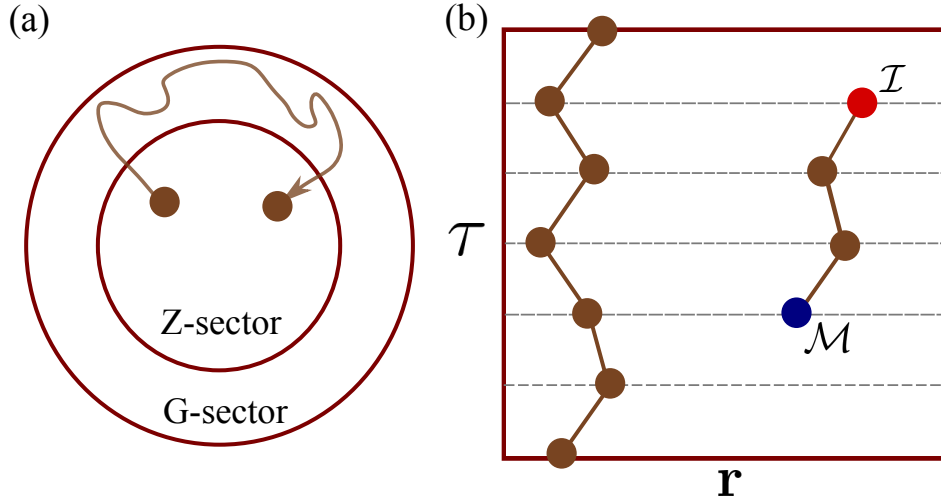


FIGURE 2.8: **Worm Algorithm.** (a) Schematic representing a walk in the configuration space, where the walker takes a detour in the G-sector to reach a point in the Z-sector more easily. (b) A configuration in the G-sector with one closed worldline and a worm. The head (Ira) and tail (Masha) are labelled by \mathcal{I} and \mathcal{M} .

negative contributions to the density matrix lead to increased variance and slower convergence when calculating thermodynamic averages. In this study, we will focus solely on bosonic systems.

The partition function for the Bose systems has the form,

$$Z = \frac{1}{N!} \sum_{\mathcal{P}} \int d\mathbf{R} \rho_D(\mathbf{R}, \mathcal{P}\mathbf{R}; \beta). \quad (2.40)$$

Paths are allowed to close on any permutation of their initial positions. The partition function includes contributions from all possible $N!$ closures. Within the classical isomorphic framework, ring polymers are capable of 'cross-linking.' A two-atom system consisting of M links can manifest in two distinct permutation states: either as two independent ring polymers, each comprised of M links, or as a singular, larger polymer containing $2M$ links.

2.5.4 Worm algorithm

An accurate investigation of bosonic systems requires the comprehensive sampling of all possible particle permutations, which are crucial for understanding quantum statistics like Bose-Einstein condensation and superfluidity. Traditional Monte Carlo methods, which permute particles while keeping their "worldlines" closed, struggle with repulsive or hard-core interactions. This leads to inefficient sampling and makes it difficult to generate the long exchange cycles needed to understand superfluidity, especially with many particles. This issue, known as critical slowing down, means

the entire configuration space can't be explored in a reasonable time, worsening exponentially with the number of particles.

To deal with this critical slowing down phenomenon, a new algorithm, "worm algorithm" (WA), was introduced, initially in the discrete spatial variation of PIMC [288] and afterwards in the continuous version [289, 290]. A fundamental aspect of the WA is that it operates in an extended configurational space, containing both closed world-line configurations (henceforth referred to as Z or diagonal configurations), contributing to the partition function Z, as well as configurations containing one open line (worm). The latter configurations contribute to the one-particle Green function; below, they are referred to as G (or off-diagonal) configurations. Fig. 2.8 (a) illustrates the fundamental concept. The WA involves the principle that paths can open, evolve, and later close, changing permutations in the process. Figure 2.8 (b) provides an example of a configuration within the G-sector. For historical reasons, the tail of the worm, i.e., the first bead, is called Masha \mathcal{M} and the head or last bead is called Ira \mathcal{I} . Please refer to Appendix B for a more detailed discussion on the PIMC algorithm, Monte Carlo techniques, and various Monte Carlo moves.

2.5.5 Measurement of observables

Once the sampling of the configuration is completed, the only thing that remains is to extract physical properties from the configurations. We can compute the equilibrium values of thermodynamic observables in the form of the partition function as shown in (2.23). We can express the thermodynamic average of an observable O in the most generic case as follows,

$$\langle O \rangle = \int d\mathbf{R}d\mathbf{R}' \rho(\mathbf{R}, \mathbf{R}'; \beta) \langle \mathbf{R} | O | \mathbf{R}' \rangle. \quad (2.41)$$

Certain observables, such as density and potential energy, which depend solely on particle positions, are readily accessible. Conversely, other quantum observables require extensive analysis to understand their manifestation within the polymer space. For a simple example, we show the measurement of the particle density here.

Particle density

The spatial density distribution $n(\mathbf{r})$ of a system reveals interesting features of the system. The density can be evaluated by summing the positions of all beads at each simulation step and subsequently averaging over the ensemble. Owing to the system's invariance along the imaginary time axis, we can further enhance statistical efficiency by averaging across all time slices within a single configuration, thereby significantly accelerating the convergence rate of the density estimator:

$$n(\mathbf{r}) = \frac{1}{M} \sum_i^N \sum_j^M \left\langle \delta(\mathbf{r} - \mathbf{r}_j^i) \right\rangle. \quad (2.42)$$

To perform this calculation in continuous space, one typically establishes a grid and computes the integral within each cell.

Similarly, observables like structure factor, total energy, superfluid fraction, condensate fraction, etc., are accessible through the PIMC simulations.

2.5.6 Model for the doubly dipolar Bose gas

In this thesis, we explore the finite temperature properties of the doubly dipolar Bose gas using PIMC simulations. The quantum mechanical many-body Hamiltonian describing the system reads

$$\mathcal{H} = \sum_{i=1}^N \left[\frac{\mathbf{p}_i^2}{2m} + V(\mathbf{r}_i) \right] + \sum_{i<j} U(\mathbf{r}_i - \mathbf{r}_j), \quad (2.43)$$

where $\mathbf{r}_i = (x_i, y_i, z_i)$ is the position of the i -th atom of momentum \mathbf{p}_i , $V(\mathbf{r})$ is the external harmonic trap. The two-body interaction potential U in Hamiltonian (2.43) yields

$$U(\mathbf{r}_i - \mathbf{r}_j) = U_{\text{hard}}(r) + U_{\text{DDI}}(\mathbf{r}_i - \mathbf{r}_j), \quad (2.44)$$

where $r = |\mathbf{r}_i - \mathbf{r}_j|$. $U_{\text{hard}}(r) = \infty$ for $r < a_s$ and $U_{\text{hard}}(r) = 0$ for $r > a_s$, a_s being the two-body s-wave scattering length. U_{DDI} is related to the DDI, which reads

$$U_{\text{DDI}}(\mathbf{r}_i - \mathbf{r}_j) = g_m \frac{(1 - 3 \cos^2 \theta_m)}{r^3} + g_e \frac{(1 - 3 \cos^2 \theta_e)}{r^3}, \quad (2.45)$$

where $g_m = \mu_0 d_m^2 / 4\pi$, $g_e = d_e^2 / 4\pi\epsilon_0$.

PIMC simulations have been extensively applied to three-dimensional dipolar Bose gases, employing various strategies to handle the unique nature of their interactions. An early approach was proposed by Nho and Landau [284], who utilized the Cao-Berne propagator [291] to account for the short-range contact interaction, while treating the long-range dipolar component within the primitive approximation. This methodology was later examined in detail by Saito [272], who investigated the influence of introducing a short-range cutoff in the $1/r^3$ term, and provided systematic benchmarks for its applicability. An alternative PIMC strategy involves representing the contact interaction through a smooth potential, such as a Lennard-Jones potential, and then treating all interactions, including the dipolar component, with the primitive approximation [277, 285]. PIMC has also been instrumental in investigating the behavior of purely repulsive dipoles in two-dimensional systems [283, 292–295].

In general, dipolar interactions introduce two primary numerical challenges. First, their long-range nature results in a computational cost that scales as $O(N^2)$. Second, the anisotropy of the interaction, combined with its divergence at $r = 0$, necessitates the use of a large number of time slices to achieve convergence within the primitive approximation. In this work, we employ the scheme proposed by Saito [272], suitably adapted to treat the doubly dipolar interaction. In this way, the density matrix reads

$$\rho(\mathbf{R}^m, \mathbf{R}^{m+1}; \tau) = \rho_{\text{free}}(\mathbf{R}^m, \mathbf{R}^{m+1}; \tau) \times \left[\prod_{i < j} \rho_{\text{CB}}(\mathbf{r}_{ij}^{(m)}, \mathbf{r}_{ij}^{(m+1)}; \tau) \right] e^{-\tau U_{\text{DDI}}(\mathbf{R}^m)}. \quad (2.46)$$

The first term of the right side of Eq. 2.46 represents the free-particle density matrix:

$$\rho_{\text{free}}(\mathbf{R}^m, \mathbf{R}^{m+1}; \tau) = \frac{1}{(4\pi\lambda\tau)^{3/2}} e^{-\tau \frac{(\mathbf{R}^m - \mathbf{R}^{m+1})^2}{4\lambda\tau}}, \quad (2.47)$$

where m is a given time slice, $\lambda = \frac{\hbar^2}{2m}$. The second term corresponds to the Cao-Berne propagator [291]

$$\rho_{\text{CB}}(\mathbf{r}, \mathbf{r}', \tau) = 1 - \frac{a_s(r + r' - a_s)}{rr'} e^{-\frac{(r - a_s)(r' - a_s)(1 + \cos \widehat{rr'})}{2\tau\lambda_r}}. \quad (2.48)$$

where $\lambda_r = \frac{\hbar^2}{2m} + \frac{\hbar^2}{2m'}$. Finally, we define the exponential argument of the third term as

$$U_{\text{DDI}}(\mathbf{R}^m) = \sum_{i < j} U_{\text{DDI}}(\mathbf{r}_i^{(m)} - \mathbf{r}_j^{(m)}). \quad (2.49)$$

To enable the study of large particle numbers in our simulations, up to $N = 2000$, we perform calculations on a high-performance computing cluster. We achieve a significant speed-up by parallelizing the computation of the interaction terms. This parallelization is crucial for efficiently handling the computational cost associated with long-range interactions, while simultaneously ensuring the convergence in the discretization of imaginary time.

Here, we discuss in detail the derivation of energy and the superfluid fraction of the system from the PIMC simulations.

Energy

Calculating the potential energy in a quantum system is straightforward, since it is diagonal in configuration space. However, determining the kinetic energy presents a greater challenge. The total energy estimator can be directly derived from the density matrix using its thermodynamic definition:

$$\langle E \rangle = -\frac{\partial \ln Z}{\partial \beta} = -\frac{1}{Z} \frac{\partial Z}{\partial \beta} = \frac{1}{Z} \frac{\partial}{\partial \beta} \int d\mathbf{R} \rho(\mathbf{R}, \mathbf{R}; \beta). \quad (2.50)$$

To illustrate, we first consider the energy for a single particle. The expression for the total energy is given by:

$$\langle E \rangle = \frac{1}{Z} \int d\mathbf{r}_0 d\mathbf{r}_1 \dots d\mathbf{r}_{M-1} \left(\sum_{j=0}^{M-1} \frac{\partial}{\partial \beta} S_j(\mathbf{r}_j, \mathbf{r}_{j+1}) \right) e^{-S(\mathbf{r}_0, \mathbf{r}_1, \dots, \mathbf{r}_{M-1})}. \quad (2.51)$$

with M being the total number of time slices. For a single particle in the primitive approximation, the energy is obtained as follows [296]:

$$\langle E \rangle = \left\langle \frac{d}{2\tau} - \sum_{j=0}^{M-1} \frac{(\mathbf{r}_j - \mathbf{r}_{j-1})^2}{4M\lambda\tau^2} + \frac{1}{M} \sum_j V(\mathbf{r}_j) \right\rangle. \quad (2.52)$$

Here, d is the spatial dimension, $\tau = \beta/M$, and $\lambda = \hbar^2/2m$. The value of the estimator can be negative sometimes, although the average is always positive.

For a more generalized scenario involving multiple bosons and a more complex interaction potential, such as in Eq. (2.45), the energy is obtained as:

$$E = \left\langle \frac{Nd}{2\tau} - \frac{1}{4\lambda\tau^2 M} \sum_{j=1}^M (\mathbf{R}_j - \mathbf{R}_{j+1})^2 - \frac{1}{M} \sum_{j=1}^M \frac{\partial \ln \rho_{\text{pot}}(\mathbf{R}_j, \mathbf{R}_{j+1}, \tau)}{\partial \tau} \right\rangle. \quad (2.53)$$

This result allows for a clear physical interpretation. The first term corresponds to the well-known *equipartition theorem* for the kinetic energy of an ideal gas. e.g. $E_{\text{kin}} = 3Nk_B T/2$ in a three-dimensional system. The second term represents a quantum correction to the kinetic energy; this term vanishes in the classical limit where $M=1$. The last term corresponds to the contribution to the potential energy. The kinetic energy becomes small when the beads are far apart from each other. It shows that worldlines in imaginary time that combine to form a configuration do not represent real physics, i.e., do not correspond to any real-time propagation, and are only a convenient representation of the quantum mechanical path integral structure. For the sake of brevity, $\rho_{\text{pot}}(\mathbf{R}^m, \mathbf{R}^{m+1}, \tau)$ represents the interacting part of the density matrix, that is, the second and third terms of Eq. (2.46).

Superfluid fraction: area estimator

Superfluidity, the ability of a quantum fluid to flow without friction, is one of the most spectacular phenomena occurring in quantum many-body systems. It was first discovered in Helium-4 by Kapitza [178] and independently by Allen and Misener [179] in 1937. Within the framework of PIMC, which utilizes the path integral formulation

of quantum mechanics, such intrinsically quantum phenomena can be quantitatively analyzed through first-principles calculations.

The phenomenological two-fluid model [180] provides a conceptual basis for understanding superfluidity, treating the system as comprising two coexisting components: a superfluid component of density ρ_s and a normal one of density ρ_n . These components collectively contribute to the total fluid density:

$$\rho = \rho_n + \rho_s, \quad (2.54)$$

where $\rho = M/V$ is the mass density, M being the total mass and V the volume. The superfluid fraction is then defined as the ratio of the superfluid density to the total density:

$$f_s = \frac{\rho_s}{\rho}. \quad (2.55)$$

Superfluidity is experimentally characterized by the response of a system to movements of its boundaries. Landau's theoretical analysis of the rotating bucket experiment provided a foundational understanding, predicting an anomalous relationship between the energy required to spin a bucket of superfluid helium and its moment of inertia. Suppose one measures the work needed to bring a container filled with helium to a steady rotation rate. A normal fluid in equilibrium will rotate rigidly with the walls. On the other hand, a superfluid will stay at rest if the walls rotate slowly, so that a smaller energy is needed to spin up the container. The liquid that stays at rest is the superfluid. This behavior leads to a reduction in the total moment of inertia compared to a classical fluid under identical conditions. Consequently, the superfluid fraction can be quantitatively expressed as:

$$f_s = 1 - \frac{I}{I_{cl}}, \quad (2.56)$$

where I is the measured moment of inertia, which only the normal component contributes to, while I_{cl} is the classical moment of inertia, which is the one the same mass of fluid would have if it behaved classically. Thus, superfluidity can be understood as a linear response to an imposed rotation, analogous to electrical conductivity as a response to an applied voltage.

Within the framework of linear perturbation theory, the change in the moment of inertia can be linked to the variance of the angular momentum operator. In the path-integral formalism, this variance is expressed through the area enclosed by the polymer paths of the particles. Following the formulation by Sindzingre et al. [297],

the superfluid fraction in a plane parallel to the axis k is given by,

$$f_s^{(k)} = \frac{4m^2}{\hbar^2 \beta I_{\text{cl}}^{(k)}} \left(\langle A_k^2 \rangle - \langle A_k \rangle^2 \right), \quad (2.57)$$

where A_k denotes the total projected area of the particle paths onto the plane perpendicular to the k -axis, which can be written in terms of particle positions as :

$$A_k = \frac{1}{2} \sum_{i=1}^N \sum_{j=0}^{M-1} (\mathbf{r}_i^j \times \mathbf{r}_i^{j+1})_k, \quad (2.58)$$

with \mathbf{r}_i^j representing the position of the i -th particle on the j -th time slice. The corresponding classical moment of inertia around the k -axis is given by,

$$I_{\text{cl}}^{(k)} = m \sum_{i=1}^N \sum_{j=0}^{M-1} \mathbf{r}_i^{(j)} \cdot \mathbf{r}_i^{(j+1)}. \quad (2.59)$$

For an extensive discussion on these calculations, one can refer to [298].

Chapter 3

Quantum Droplet in Doubly Dipolar Bose-Einstein Condensates

The content of this chapter is adapted from the research articles, "Droplet arrays in doubly dipolar Bose-Einstein condensates" [46] and "Path integral Monte Carlo study of a doubly dipolar Bose gas" [252].

3.1 Introduction

The formation of liquid droplets is a phenomenon observed across diverse physical systems, ranging from classical fluids to superfluid helium to atomic nuclei. These droplets originate from a fundamental competition between attractive and repulsive forces that collectively determine the system's energetic stability. In the realm of ultracold quantum gases, quantum droplets arise from an analogous interplay between mean-field interactions and beyond-mean-field quantum fluctuations. These quantum droplets have been extensively explored in dipolar Bose-Einstein condensates (DBECs) [40, 168] and binary Bose mixtures [161–163].

In dipolar BECs, the anisotropic and long-range nature of dipole-dipole interactions leads to a rich variety of phenomena, including roton-like excitations [141]. The partially attractive character of the dipolar interactions can induce instability in dipolar gases. However, experiments have revealed the importance of beyond-mean-field effects in stabilizing the dipolar gases, leading to the formation of self-organized and self-bound structures in dipolar condensates [299]. In this chapter, we explore the formation of self-bound quantum droplets in doubly dipolar BEC. Self-bound quantum droplets may undergo a dimensional crossover from a quasi-one-dimensional (Q1D) to a quasi-two-dimensional (Q2D) regime as a function of the angle between the external electric and magnetic fields without modifying the external confinement.

Thermal fluctuations also play an essential role in the physics of the quantum droplets. Exploring finite-temperature effects requires methods beyond mean-field theory, and path integral Monte Carlo (PIMC) has been successfully employed for

such studies [272, 276, 277, 283–285]. In addition, PIMC has already proven to be an accurate method to describe the ground state limit of both weakly and strongly interacting bosonic systems [294, 295, 300–303]. Concerning dipolar BECs systems, PIMC has been instrumental in investigating key macroscopic properties such as the superfluid and condensate fraction [283, 304] (including their critical temperatures [305–307]), and pair correlation functions [308]. Additionally, PIMC furnishes a correct description of the supersolid phase in quantum droplet systems [303, 309, 310], self-bound liquid in binary Bose mixtures [311], and Bose glasses too [312–314].

In this chapter, we employ first-principles Path Integral Monte Carlo (PIMC) methods to thoroughly investigate the properties of trapped doubly dipolar Bose gases. Our initial analyses confirm the emergence of a pancake quantum droplet at low temperatures, corroborating earlier mean-field calculations. In the regime of weak doubly dipolar interactions, our first-principles PIMC results align well with predictions from the generalized Gross-Pitaevskii equation (gGPE). However, this agreement diminishes in the strong interaction limit. Here, PIMC, by inherently accounting for quantum fluctuations, accurately describes the strongly interacting doubly dipolar regime, whereas the gGPE, a mean-field approach, falls short. We also provide a comprehensive characterization of the system’s quantum behavior across a broad range of parameters. Notably, when the system forms a droplet, its superfluid fraction exhibits anisotropic behavior, a stark contrast to typical Bose gas systems. Intriguingly, we observed that the transition temperature from a thermal gas to a droplet state is higher than that from a thermal gas to a repulsive Bose-Einstein condensate, underscoring the enhanced robustness of the droplet phase against thermal fluctuations. Furthermore, we investigated the anisotropic behavior of the superfluid fraction during the structural transition from a pancake to a cigar-shaped droplet, induced by varying the ratio of electric and magnetic dipole interaction strengths.

These findings provide strong theoretical support for the experimental realization of stable doubly dipolar Bose–Einstein condensates using dysprosium atoms.

3.2 Self-Bound Quantum Droplet

Self-bound quantum droplets are a novel many-body quantum state that remains bound without external confinement. In dipolar BEC, these arise due to the interplay between attractive dipole-dipole interactions and repulsive quantum fluctuations. These droplets are stabilized against mean-field collapse due to beyond-mean-field effects and exhibit liquid-like behavior in an ultradilute regime. Self-bound droplets have been extensively studied and experimentally observed in magnetic dipolar condensates [40] and atomic mixtures [162].

Similarly, a doubly dipolar BEC is unstable against collapse if the attractive part of the doubly dipolar potential dominates the repulsive contact interactions. The Lee-Huang-Yang (LHY) correction introduced in chapter 2 plays a crucial role in stabilizing a collapsing DDBEC. Once the repulsive LHY correction is significant, it prevents the collapse and stabilizes the condensate into a self-bound quantum droplet [45]. In the following, we analyze the physics of a single self-bound droplet in a doubly dipolar condensate.

3.2.1 Variational analysis

We investigate the properties of self-bound quantum droplets using two distinct methodologies: direct numerical simulation of the generalized GPE (2.17), and a variational analysis. The variational approach provides a powerful framework for estimating the equilibrium widths of a BEC by minimizing the system's energy for a chosen trial wavefunction [315]. Typically, a Gaussian ansatz is employed, and the resulting Euler-Lagrange equations yield insights into the condensate's properties. Here we use a time-dependent variational Gaussian ansatz:

$$\psi(\mathbf{r}, t) = \frac{1}{\pi^{3/4} \sqrt{L'_x L'_y L'_z}} \exp \left[-\frac{x'^2}{2L_x'^2} - \frac{y^2}{2L_y^2} - \frac{z'^2}{2L_z'^2} + ix'^2 \beta_x + iy^2 \beta_y + iz'^2 \beta_z + ix'z' \beta_{xz} \right], \quad (3.1)$$

where we have used the following rotation matrix for the argument in the ansatz,

$$\begin{bmatrix} x' \\ y' \\ z' \end{bmatrix} = \begin{bmatrix} \cos \theta & 0 & -\sin \theta \\ 0 & 1 & 0 \\ \sin \theta & 0 & \cos \theta \end{bmatrix} \begin{bmatrix} x \\ y \\ z \end{bmatrix} \quad (3.2)$$

We take such a generalized ansatz as the condensate is expected to tilt away from the z -axis when α is varied. Here, $\{L_{x,y,z}, \beta_{x,y,z}, \beta_{xz}, \theta\}$ are variational parameters. The

angle θ determines the droplet orientation in the xz -plane and the parameters, L'_x, L_y , and L'_z are the droplet widths along x', y , and z' directions, respectively. Employing Eq. (3.1) in the Lagrangian density describing a doubly DBEC,

$$\begin{aligned} \mathcal{L} = & \frac{i\hbar}{2} (\psi\dot{\psi}^* - \dot{\psi}\psi^*) + \frac{\hbar^2}{2m} |\nabla\psi|^2 + \frac{g}{2} |\psi|^4 + \\ & \frac{1}{2} |\psi|^2 \int d^3r' V_d(r-r') |\psi(r')|^2 + \frac{2M^{3/2}}{15\pi^3\hbar^3 N} g_m^{5/2} |\psi|^5 \times \\ & \int d\Omega_k [\beta + \mathcal{F}(\theta_k, \phi_k, \alpha)]^{5/2}, \end{aligned} \quad (3.3)$$

where the function $\mathcal{F}(\theta_k, \phi_k, \alpha)$ is defined in Eq. (2.12). We obtain the Lagrangian $L = \int d^3r \mathcal{L}$, and the corresponding Euler-Lagrange equations of motion,

$$\frac{d}{dt} \left(\frac{\partial L}{\partial \dot{Q}} \right) - \frac{\partial L}{\partial Q} = 0, \quad (3.4)$$

for the dynamical variables $Q \in \{L_{x',y,z'}, \beta_{x',y,z'}, \beta_{x'z'}, \theta\}$. Using the equations of motion of β variables,

$$\beta_{x'z'} = \frac{M}{\hbar} \left(\frac{L_z'^2 - L_x'^2}{L_z'^2 + L_x'^2} \right), \quad (3.5)$$

$$\beta_{i \in \{x', y, z'\}} = \frac{M \dot{L}_i}{2\hbar L_i}. \quad (3.6)$$

and the transformation $L \rightarrow L - \frac{d}{dt} \left(\frac{\hbar}{2} \sum_i \beta_i L_i^2 \right)$, we finally arrive at the Lagrangian

$$\begin{aligned} L = & \frac{\hbar^2}{4M} \left(\frac{1}{L_x'^2} + \frac{1}{L_y^2} + \frac{1}{L_z'^2} \right) - \frac{M}{4} (\dot{L}_x'^2 + \dot{L}_y^2 + \dot{L}_z'^2) - \\ & \frac{M}{4} \frac{(L_x'^2 - L_z'^2)^2}{(L_x'^2 + L_z'^2)} \dot{\theta}^2 + \frac{g}{2(2\pi)^{3/2} L_x' L_y L_z'} + \\ & \frac{g_m}{2} \int \frac{d^3k}{(2\pi)^3} \mathcal{F}(\theta_k, \phi_k, \alpha) n^2(k) + \\ & \left(\frac{2}{5} \right)^{5/2} \frac{(M/\hbar)^{3/2} g_m^{5/2}}{3N\pi^{21/4}} \frac{\int d\Omega_k [\beta + \mathcal{F}(\theta_k, \phi_k, \alpha)]^{5/2}}{(L_x' L_y L_z')^{3/2}}. \end{aligned} \quad (3.7)$$

The equations of motion for the widths and the angle θ are, respectively, obtained as,

$$M\ddot{L}_i = -\frac{\partial V_{\text{eff}}}{\partial L_i}, \quad (3.8)$$

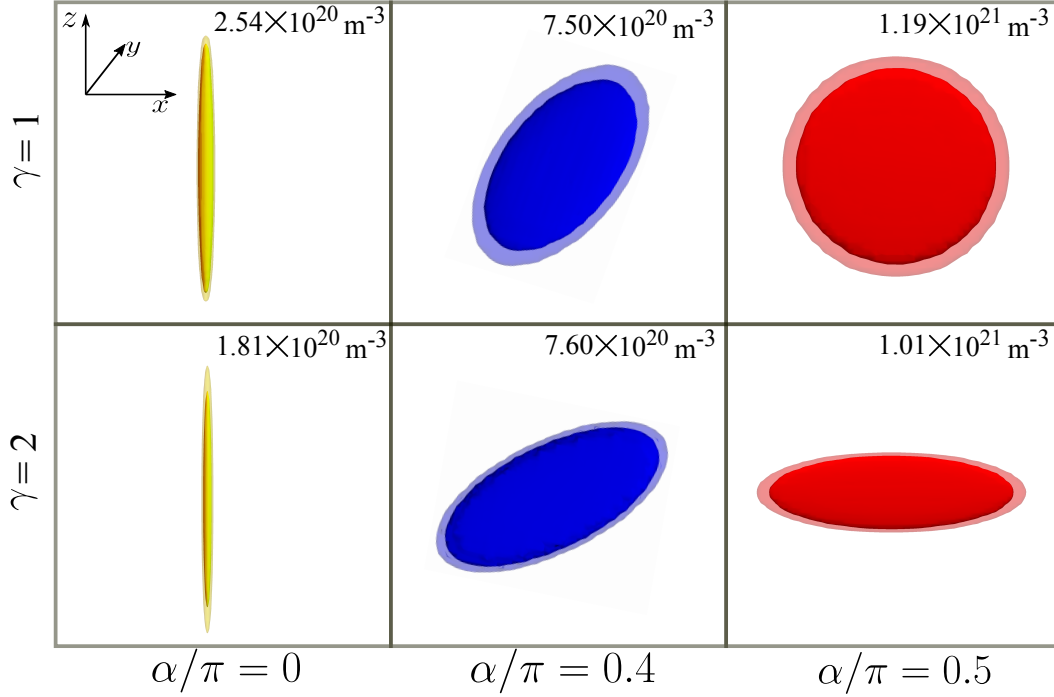


FIGURE 3.1: **Self-bound droplets.** The density isosurface ($|\psi(r)|^2$ at a particular value) of the ground states of the self-bound droplets obtained via imaginary time evolution of Eq. (2.17) for $N = 2000$ Dy atoms at $\alpha/\pi = 0, 0.4$, and 0.5 . Along each row (column) $\gamma(\alpha)$ is fixed. We have taken $a_s = 200a_0$ for $\gamma = 1$, and $a_s = 222a_0$ for $\gamma = 2$. The peak density of the droplet is provided at the top for each case. We observe a structural transformation from a cigar to a pancake shape as a function of α for $\gamma = 1$.

and

$$\frac{(L_x'^2 - L_z'^2)^2}{(L_x'^2 + L_z'^2)} M \ddot{\theta} = -\frac{\partial}{\partial \theta} \left(g_m \int \frac{d^3k}{(2\pi)^3} \mathcal{F}(\theta_k, \phi_k, \alpha) n^2(k) \right), \quad (3.9)$$

where the V_{eff} is defined as,

$$\begin{aligned} V_{\text{eff}} = & \frac{\hbar^2}{2M} \sum_i \frac{1}{L_i^2} - \frac{M}{2} \frac{(L_x'^2 - L_z'^2)^2}{(L_x'^2 + L_z'^2)} \dot{\theta}^2 + \frac{g}{(2\pi)^{3/2} L_x' L_y' L_z'} + \\ & g_m \int \frac{d^3k}{(2\pi)^3} \mathcal{F}(\theta_k, \phi_k, \alpha) n^2(k) \\ & + 2 \left(\frac{2}{5} \right)^{5/2} \frac{(M/\hbar)^{3/2} g_m^{5/2} \int d\Omega_k [\beta + \mathcal{F}(\theta_k, \phi_k, \alpha)]^{5/2}}{3N\pi^{21/4} (L_x' L_y' L_z')^{3/2}}. \end{aligned} \quad (3.10)$$

In the RHS of Eq. (3.9), θ dependence appears through the density $n(k)$, in the momentum space. At the equilibrium, the first derivative of the dynamical variables vanishes, providing us the widths ($L_{i \in x', y', z'}^0$) and orientation (θ^0) of the ground state droplet. Both the equilibrium widths and the orientation (θ^0) of the droplet can be obtained by minimizing the effective potential, V_{eff} . As expected, the equilibrium

orientation is given by $\theta^0 = \theta_p$, the same as that provided in Eq. (2.7). In general, we find that the variational results are in excellent agreement with the numerical results obtained from solving the generalized GPE in Eq. (2.17).

3.2.2 Anisotropic properties of a self-bound droplet

In the following, we discuss how the anisotropic features of the doubly dipolar potential introduced in Chapter 2 influence the structure of the self-bound droplet. In Fig. 3.1, we illustrate the 3d density isosurface plots of the droplet ground states, corresponding to selected potential surfaces presented in Fig. 2.4, as a function of γ and α . We consider $N = 2000$ Dy atoms, and tune the s-wave scattering length appropriately to obtain a stable droplet depending on the values of γ . The widths of the droplet, both $L_{\alpha \in x', y, z'}^0$ and $L_{\alpha \in x, y, z}^0$ are shown in Fig. 3.2 as a function of α for different γ . While the width along y remains the same between both coordinate systems, the widths along x and z are related via the following transformation:

$$\begin{aligned} L_{x'}^2 &= L_x^2 \cos^2 \theta_p + L_z^2 \sin^2 \theta_p - 2 \sin 2\theta_p \langle xz \rangle, \\ L_{z'}^2 &= L_x^2 \sin^2 \theta_p + L_z^2 \cos^2 \theta_p + 2 \sin 2\theta_p \langle xz \rangle. \end{aligned} \quad (3.11)$$

At $\alpha = 0$, we have a cigar droplet with $L_x^0 = L_y^0 \ll L_z^0$, irrespective of the value of γ . As α increases, the effective attractive interaction along the x -axis increases, causing an increment in L_x^0 with a decrement in both L_y^0 and L_z^0 as shown in Fig. 3.2. Since the droplet's width along both y and z axes decreases, the density at the centre of the droplet increases with α for a fixed γ .

For small γ and independently of the value of α , the effective polarization axis lies along the z -axis or closer to it [see the upper row of Fig. 2.4]. It implies that the droplet is mostly elongated along the z -axis for small γ values, which is further verified by the imaginary time evolution of Eq. (2.17). For $\gamma < 1$, the magnetic dipole moment is always dominant, and the width along the z -axis is the largest for any α .

As γ increases, the effect of the electric dipole interactions becomes crucial, and the effect of varying α becomes more prominent. In particular, the axis of the droplet gets tilted away from the z -axis significantly, along with structural modifications. For example, with $\gamma = 1$ [see the upper row in Fig. 3.1], varying α from zero to $\pi/2$, the droplet gets tilted and also transforms from a cigar to a pancake-shaped condensate. The corresponding width modifications are shown in Figs. 3.2 (a) and 3.2 (b). At $\alpha = 0$, we have a cigar droplet with $L_x^0 = L_y^0 \ll L_z^0$ and at $\alpha = \pi/2$ rad, the droplet is pancake shaped with $L_x^0 = L_z^0 \gg L_y^0$. For fixed interaction strengths, the pancake

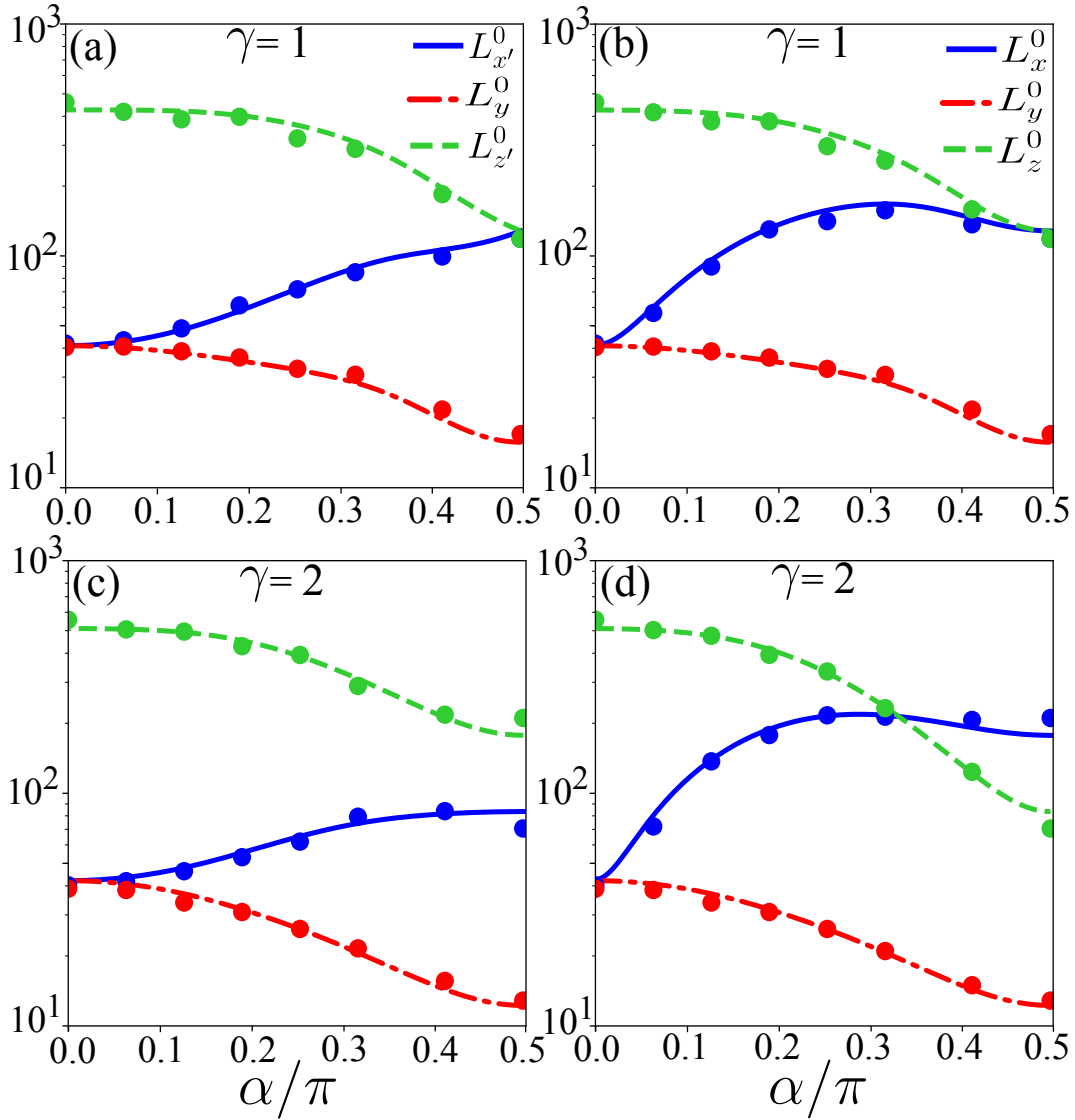


FIGURE 3.2: **Droplet widths.** Equilibrium widths of the droplets of Dy atoms as a function of α for different γ values and all other parameters are the same as Fig. 3.1. We plot $L_{\alpha \in \{x', y, z'\}}^0$ on the left and $L_{\alpha \in \{x, y, z\}}^0$ on the right. We show the results from both the numerical results (solid points) and the variational calculations (solid and dashed lines) methods, which show very good agreement.

droplet ($\alpha = \pi/2$) is denser than the cigar droplet ($\alpha = 0$). At large values of γ [see the bottom row in Fig. 3.1 for $\gamma = 2$], as a function of α , the droplet axis rotates up to a maximum of $\pi/2$ rad without non-trivial structural variations. It changes the long axis of the cigar from the z axis to the x axis. This is because the polarization axis approximately follows the dominant electric dipole vector for large values of γ . The α -dependence on the droplet's widths for a sufficiently large γ is shown in Figs. 3.2 (c) and 3.2 (d). Because of the $\pi/2$ rotation of the droplet's axis, we have $L_{x'}^0 = L_z^0$ and $L_{z'}^0 = L_x^0$ at $\alpha = \pi/2$, resulting in a crossing between L_x^0 and L_z^0 [see Fig. 3.2 (d)].

As seen in Fig. 3.1, the droplet undergoes a structural transformation from a

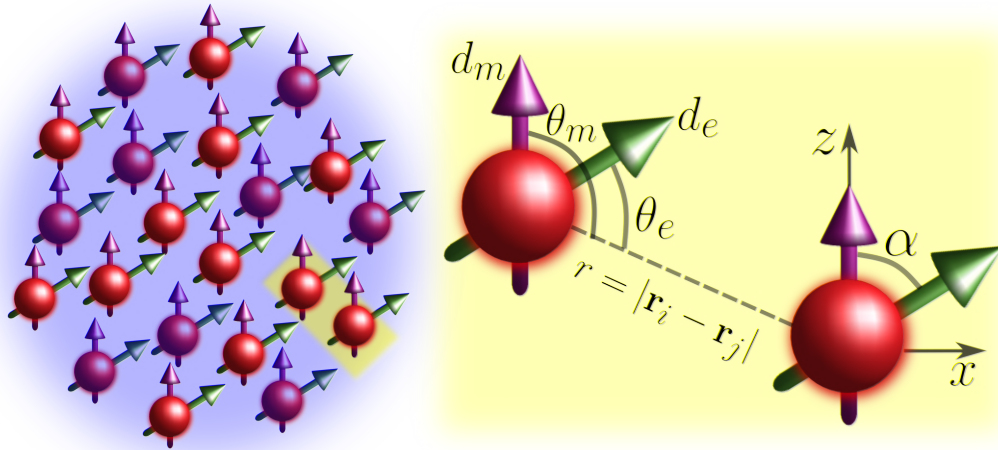


FIGURE 3.3: **Doubly dipolar gas.** Schematic diagram showing Doubly dipolar Bose gas consisting of N Dy atoms confined in an external harmonic trap, see Section 2.5.6. The atoms have both magnetic (d_m) and electric dipole moment (d_e), the magnetic dipole moment is fixed along the z -axis, and the electric dipole moment is assumed to be polarized in the xz -plane, forming an angle α with the z -axis. The angle $\theta_m(\theta_e)$ is the angle between $d_m(d_e)$ and the vector joining the two atoms, $r = |\mathbf{r}_i - \mathbf{r}_j|$.

cigar to a pancake while varying either α (upper row) or γ (last column). So far, only cigar-shaped droplets have been observed in the experiments of dipolar condensates [40, 168, 299]. Doubly dipolar interaction opens the interesting possibility of a controllable modification of quantum droplets from cigar to pancake-shaped. A detailed analysis of the widths and the modes (see Ref. [45]) reveals that more than just a structural crossover, there exists an actual dimensional crossover from the Q1D to Q2D droplet as a function of α .

3.3 Doubly Dipolar Bose Gas at Finite Temperatures

Here, we explore the finite temperature properties of the doubly dipolar Bose gas and the pancake droplet through first-principle calculations. We consider a gas of N doubly dipolar dysprosium (Dy) bosonic atoms of mass m confined in a cigar-shaped harmonic trap of potential $V(\mathbf{r}) = m(\omega_x^2 x^2 + \omega_y^2 y^2 + \omega_z^2 z^2)/2$, where ω_q is the trap frequency along the q th-direction. The atoms possess both magnetic and electric dipole moments polarized by external magnetic and electric fields, respectively. The quantum mechanical many-body Hamiltonian describing the system reads

$$\mathcal{H} = \sum_{i=1}^N \left[\frac{\mathbf{p}_i^2}{2m} + V(\mathbf{r}_i) \right] + \sum_{i<j} U(\mathbf{r}_i - \mathbf{r}_j), \quad (3.12)$$

where $\mathbf{r}_i = (x_i, y_i, z_i)$ is the position of the i -th atom of momentum \mathbf{p}_i . The two-body interaction potential U in Hamiltonian (3.12) yields

$$U(\mathbf{r}_i - \mathbf{r}_j) = U_{\text{hard}}(r) + U_{\text{DDI}}(\mathbf{r}_i - \mathbf{r}_j), \quad (3.13)$$

where $r = |\mathbf{r}_i - \mathbf{r}_j|$. $U_{\text{hard}}(r) = \infty$ for $r < a_s$ and $U_{\text{hard}}(r) = 0$ for $r > a_s$, a_s being the two-body s -wave scattering length. U_{DDI} is related to the DDI, which reads

$$U_{\text{DDI}}(\mathbf{r}_i - \mathbf{r}_j) = g_m \frac{(1 - 3 \cos^2 \theta_m)}{r^3} + g_e \frac{(1 - 3 \cos^2 \theta_e)}{r^3}, \quad (3.14)$$

where $g_m = \mu_0 d_m^2 / 4\pi$, $g_e = d_e^2 / 4\pi\epsilon_0$, while d_m (d_e) is the magnetic (electric) dipole moment of the atoms, moreover μ_0 (ϵ_0) is the vacuum permeability (permittivity). θ_m and θ_e are the angles formed by the magnetic and electric dipole vectors with the radial vector \mathbf{r} joining the two dipoles, and α is the relative angle between the two dipole moments as shown in Figure 3.3. In addition, we define $\gamma = g_e / g_m$ as the ratio that identifies the relative strength between electric and magnetic dipole moments.

In this chapter, we assume that the external magnetic field is directed along the z -axis, and hence, the direction of the magnetic dipole moment. The external electric field instead varies in the xz -plane, inducing a tunable electric dipole moment. The latter forms an angle α with the z -axis (see Figure 3.3). Both α and γ can be varied by tuning the external electric field for a range of experimentally feasible values [44, 46]. Since dipoles are polarized in the xz -plane only, the DDI always results in repulsion along the y -axis and is anisotropic in the xz -plane.

Here we study the thermodynamic features of the system at finite temperatures using the PIMC methodology described in the previous section. The methodology introduced here is capable of precisely estimating the chief quantities of interacting bosonic systems. In the following, we are interested in calculating the system's energy and its superfluid fraction; both cases are going to be evaluated at $T > 0$ and in the limit of zero temperature.

3.3.1 Ground state transition

In this section, we analyze the ground state passage of the doubly dipolar Bose gas from a BEC to a pancake droplet by employing the PIMC method and the gGPE (Eq. (2.17)) simulations. It is also interesting to compare the two methodologies under the variation of the short-range interaction, and in particular, decreasing the s -wave scattering length makes dipolar interactions very dominant.

Regarding PIMC, we consider a doubly dipolar Bose gas of $N = 1024$ Dy atoms described by Hamiltonian (3.12) and confined in a prolate trap elongated along the

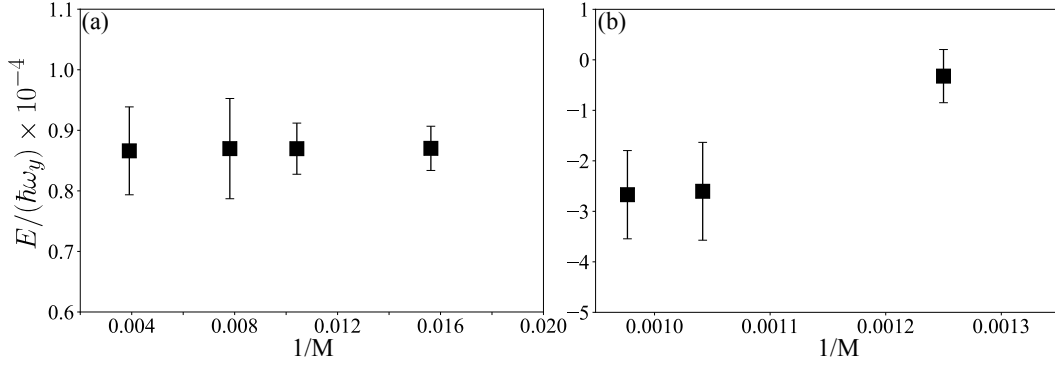


FIGURE 3.4: **Convergence with time slices.** The total energy of the ground state vs. inverse of time slices from the PIMC simulations in (a) BEC regime, $a_s = 260a_0$ with $M = 64, 96, 128, 256$ slices and, (b) in the pancake droplet regime, $a_s = 200a_0$ with $M = 800, 960, 1024$ slices. PIMC simulations have been performed for $N = 1024$ Dy atoms under the external trap, $\omega_{x,y,z} = 2\pi \times (75, 25, 75)$ Hz for $\alpha = \pi/2$, and $\gamma = 1$.

y -axis, with $\omega_{x,y,z} = 2\pi \times (75, 25, 75)$ Hz. Here, the magnetic and electric dipole moments are assumed to be oriented perpendicular to each other in the xz -plane, thus having $\alpha = \pi/2$, and their magnitudes are chosen to result in $\gamma = 1$. Ground state properties are obtained by extrapolating to the limit of zero temperature, that is, lowering the temperature until the observables (in this case, energy and superfluid fraction) do not change on further decreasing T . We first inspect the ground state energy of the system by varying a_s . For $a_s \gtrsim 222a_0$ the repulsive short-range interaction dominates, the system resulting in a stable low-density BEC ground state. For lower scattering lengths, where the attractive part of the DDI in Eq. (3.14) dominates over the repulsive short-range one, U_{hard} , the ground state of the system manifests as a pancake droplet.

Regarding the energy from PIMC, its estimator relies heavily on the approximation of the density matrix. Thus referring to the Eq. 2.46, the total energy reads

$$\langle \mathcal{H} \rangle = \left\langle \frac{3N}{2\tau} - \frac{1}{4\lambda\tau^2 M} \sum_{m=1}^M (\mathbf{R}^m - \mathbf{R}^{m+1})^2 - \frac{1}{M} \sum_{m=1}^M \frac{\partial \ln \rho_{\text{pot}}(\mathbf{R}^m, \mathbf{R}^{m+1}, \tau)}{\partial \tau} \right\rangle, \quad (3.15)$$

$\langle \dots \rangle$ denotes the statistical mean values of the estimator.

Convergence with time slices

We provide a figure (See Figure 3.4) demonstrating the convergence of total energy with the number of time slices in both the BEC and pancake droplet regimes.

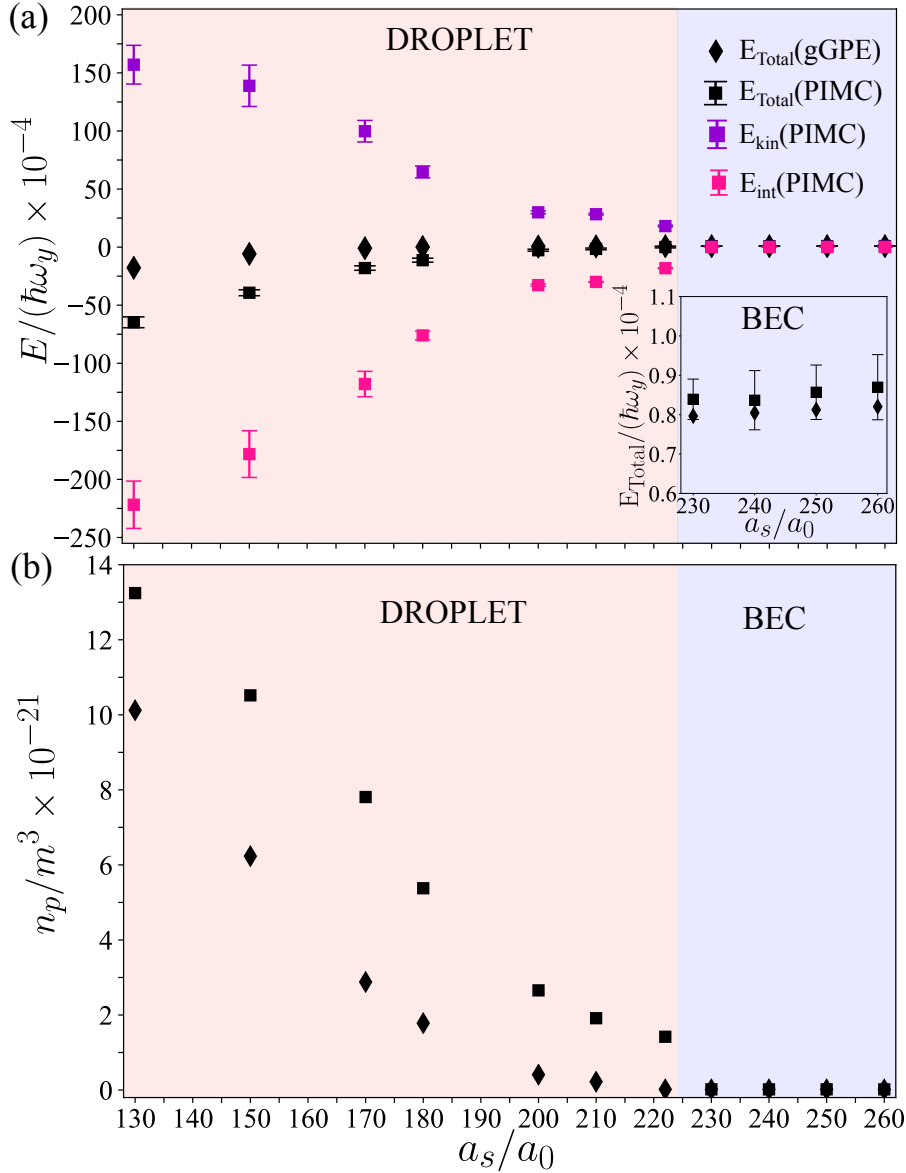


FIGURE 3.5: **PIMC vs gGPE.** (a) Energy comparison from the ground state of gGPE (diamond) and PIMC (squares). The total energy is shown in black, the energy contribution in PIMC arising from short-range interactions and long-range DDI is shown in pink, and the kinetic term is illustrated in violet. The inset shows the total energies in the BEC regime. (b) Peak density comparison from the ground state of gGPE (diamonds) and PIMC (squares). PIMC simulations have been performed for $N = 1024$ Dy atoms under the external trap, $\omega_{x,y,z} = 2\pi \times (75, 25, 75)$ Hz, see main text. The blue and red backgrounds denote the BEC and the droplet regime, respectively.

Figure 3.4 (a) illustrates the ground-state energy of the condensate with the inverse of the number of time slices for $a_s = 260a_0$. The energy doesn't change significantly with the increasing values of $M = 64, 96, 128, 256$, indicating convergence with the number of time slices. All the results in the manuscript in the BEC regime are shown from the simulations with $M = 128$ slices.

In the droplet regime, for small M values, the energy is quite noisy with the Monte Carlo steps and does not converge well. Hence, although computationally very extensive, we have performed the PIMC simulations with a high number of time slices to achieve better convergence.

Figure 3.4 (b) shows the ground-state energies from the simulations with $M = 800, 960, 1024$, number of time slices for $a_s = 200a_0$, demonstrating the convergence with increasing M . The results presented in the thesis for the droplet regime are based on the simulations with $M = 1024$ slices.

PIMC vs gGPE comparison

The beyond-mean-field, gGPE is solved at $T = 0$ via imaginary time evolution, see Eq. 2.17. Figure 3.5 (a) depicts this observable computed by using both PIMC and gGPE methods. Regarding the total energy (E_{total} , black points), PIMC and gGPE display a substantially concordant trend between them. For $a_s \gtrsim 222a_0$, the ground-state is a stable low-density BEC ground state. As expected, in this region, the energy calculations through gGPE exhibit a close agreement with the statistically *exact* PIMC simulations compared to the droplet regime for lower scattering lengths. The *transition* from a BEC to a pancake droplet is observed consistently around $a_s \approx 222a_0$ as witnessed in PIMC.

The appearance of the droplet regime from a BEC state is also captured well by analyzing the peak density behavior. A sharp increase in the peak density is evident as the system gets into the droplet regime. The peak density of the droplet rises with a decrease in the scattering length, PIMC and gGPE exhibiting a qualitatively similar pattern as shown in Figure 3.5 (b). The values obtained from PIMC indicate a sharper jump of this quantity around $222a_0$. A similar trend is observed in the total energy, as illustrated in Figure 3.5 (a), where gGPE shows a smoother behavior in the droplet regime. Regarding the PIMC findings, the sharp drop of E_{int} supports the analysis done in Figure 3.5 (b), indicating the presence of a structure dominated by the DDI.

The droplet regime features a clear growth of the E_{kin} terms computed from PIMC, violet points in Figure 3.5 (a). This shows the quantum fluctuations are indeed significant in the regime dominated by strong attractive DDI (low a_s). As discussed previously, the introduction of the repulsive LHY correction acts to stabilize the condensate against collapse and form a pancake quantum droplet. However, it should be remembered that LHY only remains a first-order correction to the mean-field theory (one-loop term). It, therefore, can never account for all the terms that characterize quantum fluctuations as PIMC can properly. Furthermore, PIMC provides an accurate estimate of the effects of DDI in the strongly dipole-dominated regime. These

explain the mismatch of energy between the mean-field calculations and the PIMC simulations in the droplet region.

3.3.2 Superfluid fraction across BEC-droplet transition

The superfluid phase can be characterized by the response of the fluid to a small external rotation [297]. While a normal fluid in equilibrium will rotate rigidly with the walls, a superfluid will stay at rest if the walls rotate slowly. The superfluid fraction, f_s , can be accurately estimated in a PIMC simulation by calculating the ratio of the moment of inertia of the system to that of the classical moment of inertia [282].

In this section, we evaluate f_s by sampling the well-established “area estimator” [297]. This method draws a direct connection between the area enclosed by tangled paths of polymers in a finite system and the reduction of the moment of inertia of the particles compared to the classical case. We inspect the superfluid fraction along three orthogonal axes ($k = x, y, \text{ and } z$). When doing so, the formula for $f_s^{(k)}$ reads:

$$f_s^{(k)} = \frac{4m^2}{\hbar^2 \beta I_{\text{cl}}^{(k)}} \left(\langle A_k^2 \rangle - \langle A_k \rangle^2 \right), \quad (3.16)$$

The full details of the derivation have been discussed in the previous chapter 2. We compute the superfluid fraction across the BEC-to-droplet transition via PIMC simulations employing area estimator methods as defined in Eqs. (2.57), (2.58), and (2.59). The upper panel of Figure 3.6 illustrates the ground state limit superfluid fraction along the three orthogonal directions (x, y, z) with varying short-range interactions. The density distributions obtained from PIMC simulations are visually represented through isodensity plots in the lower panel of Figure 3.6.

For higher values of a_s , the condensate represents the ground state of the system, which has a three-dimensional cigar shape elongated along the y -axis (see Figure 3.6 (c)), determined by the underlying trap geometry. The superfluid fraction values computed in the condensate regime at $T = 5 \text{ nK}$, are finite in all three directions, with f_s^y reaching unity and f_s^x and f_s^z having lower values. The anisotropy in the superfluidity is due to the anisotropic external harmonic trap applied to confine the doubly dipolar gas. The high values of the superfluid fraction indicate the inherent superfluid nature and the quantum coherence present in the DDBEC.

With decreasing a_s , the superfluid fraction shows a drastic change and becomes highly anisotropic. In this regime, the interaction is dominated by the strong DDI, which is purely attractive in the dipole plane (xz) and repulsive perpendicular to the

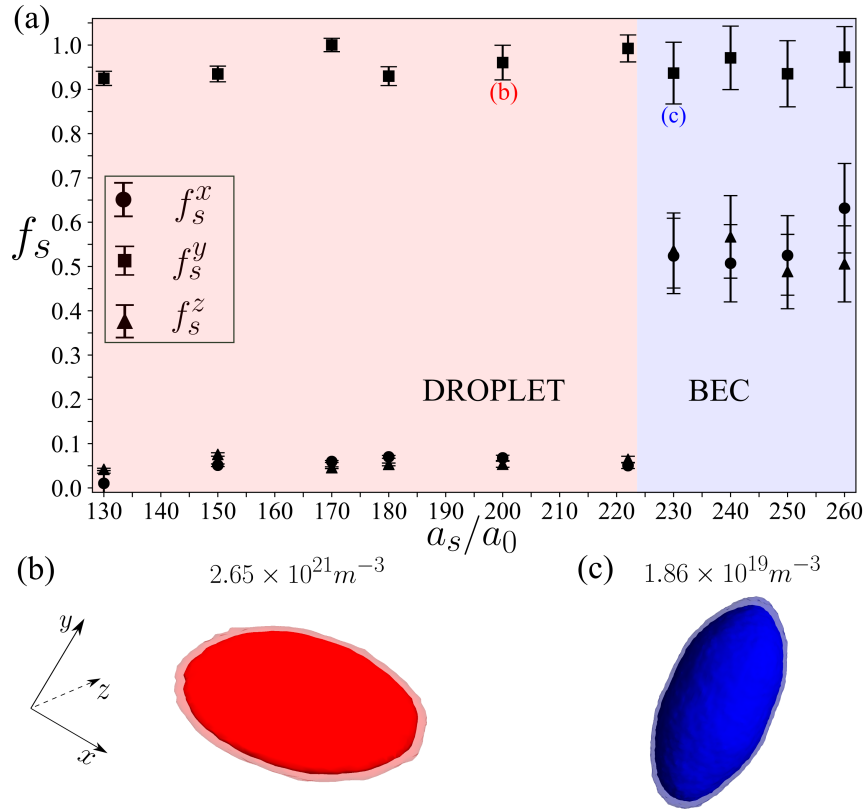


FIGURE 3.6: **Superfluid properties.** (a) Superfluid fraction across BEC to droplet transition along three orthogonal directions (x, y, z) with varying scattering length a_s for $\alpha = \pi/2$, and $\gamma = 1$, for a trap frequency, $\omega_{x,y,z} = 2\pi \times (75, 25, 75)$ Hz. The blue and red backgrounds denote the BEC and the droplet regime, respectively. We show the 3d density isosurfaces obtained via PIMC simulations, for (b) a pancake droplet ($a_s/a_0=200$), (c) a cigar-shaped BEC ($a_s/a_0=230$). The peak densities for each case are provided at the top. The PIMC simulations are done for $N = 1024$ Dy atoms.

dipole plane (y -axis). The attractive DDI forms a quasi-two-dimensional pancake-shaped droplet extending in the xz -plane (see Fig. 3.6 (b)), which emerges as the ground state of the system. Due to the highly anisotropic shape, the pancake droplet shows distinct superfluid responses to a small external rotation around different axes. Along the direction perpendicular to the dipole plane, the superfluid fraction reaches unity, while its values are greatly suppressed within the dipole plane. At a temperature of $T = 10$ nK, $f_s^{(y)}$ achieves around 100% superfluidity, and we extrapolate these values to lower temperatures. The anisotropy of the superfluidity in this regime is entirely dictated by the anisotropic DDI, with minimal influence from external trap geometry. Similar to the DDBEC, the superfluid fraction emphasizes the intrinsic superfluid nature of the doubly dipolar pancake droplet.

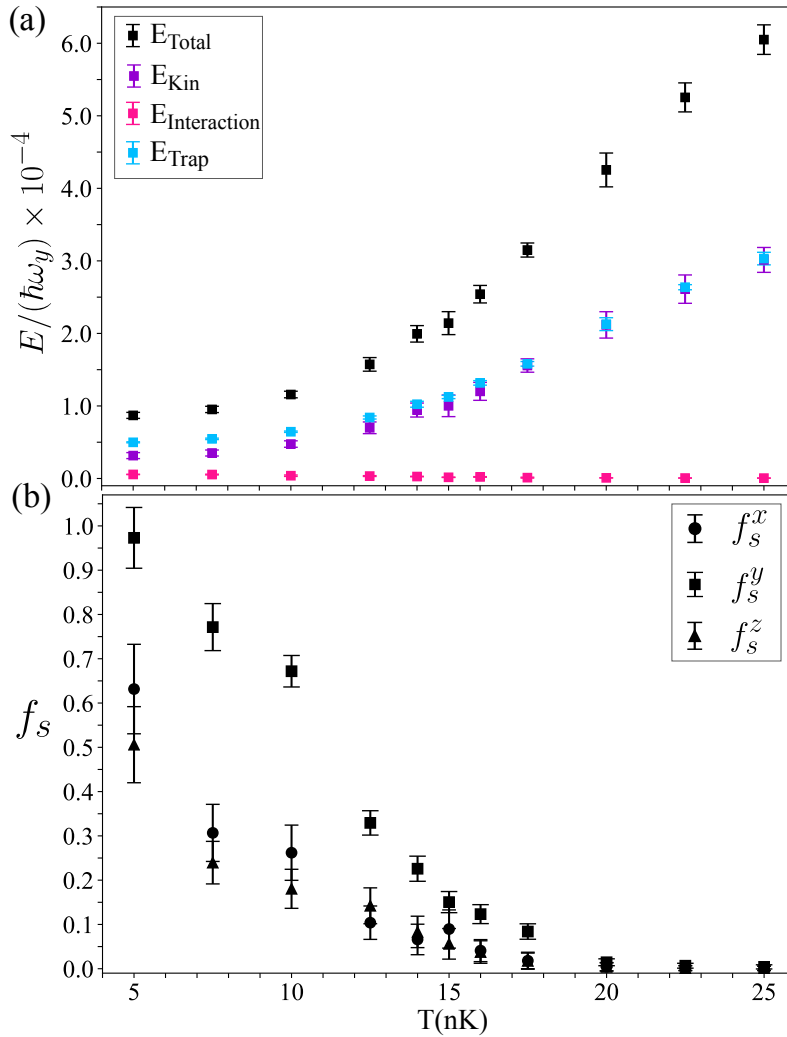


FIGURE 3.7: **Thermal gas to DDBEC transition.** (a) Energy variation with temperature for a doubly dipolar condensate at $a_s/a_0 = 260$. The total energy is shown in black, the energy contributions arising from short-range interactions and long-range DDI are shown in pink, and the energy contributions from the kinetic term and external harmonic trap are illustrated in violet and skyblue, respectively. (b) Superfluid fraction along the transition from a thermal gas to a doubly dipolar condensate. The PIMC simulations are done for $N = 1024$ Dy atoms for an external harmonic trap, $\omega_{x,y,z} = 2\pi \times (75, 25, 75)$ Hz.

3.3.3 Doubly dipolar gas with varying temperatures

In this section, we study the properties of the doubly dipolar condensate and the pancake droplet with temperature variations.

Thermal gas to DDBEC transition

As discussed in previous sections, at high scattering lengths, the doubly dipolar gas resides in a weak DDI regime. We compute the energy and the superfluid fraction across the passage from a thermal gas to a repulsive doubly dipolar condensate.

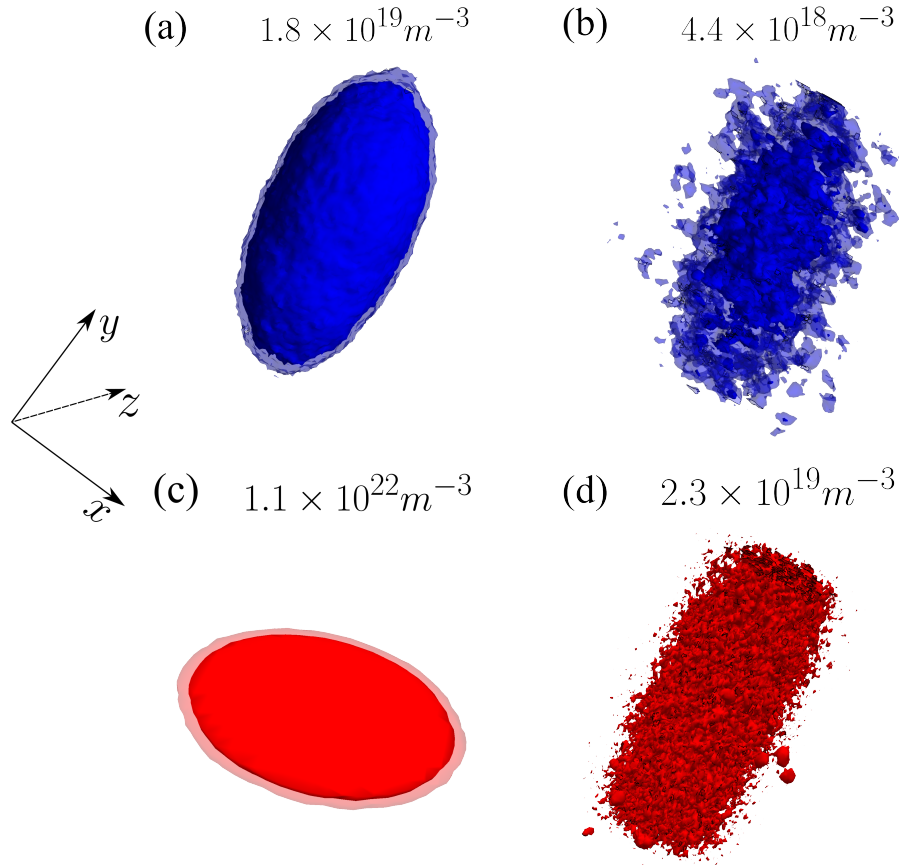


FIGURE 3.8: **Density plots.** The 3D isodensity surfaces are shown across the thermal gas to DDBEC and a pancake droplet transition. (a) cigar-shaped superfluid DDBEC ($T = 5$ nK) and (b) a thermal gas ($T = 25$ nK) at $a_s = 260a_0$. (c) A superfluid pancake droplet ($T = 5$ nK), and (d) a cigar-shaped thermal gas ($T = 40$ nK) at $a_s = 170a_0$. The peak densities for each case are provided at the top. The PIMC simulations are done for $N = 1024$ Dy atoms for an external harmonic trap, $\omega_{x,y,z} = 2\pi \times (75, 25, 75)$ Hz.

At high temperatures, the thermal fluctuations dominate and the system describes a simple thermal gas, without displaying any coherence between the particles. The pronounced thermal fluctuations result in a high value of the kinetic energy as shown in Figure 3.7 (a). The detailed energy analysis shows that the energy due to the harmonic trap is much higher compared to the interaction energy, resulting in a cigar-shaped geometry of the thermal gas dictated by the prolate trap geometry (see Figure 3.8 (b)). As the temperature diminishes, the thermal fluctuations decrease, and below a critical temperature, the thermal gas undergoes a transition to a condensed state. The transition is captured through a sharp increase in the superfluid fraction value around $T = 18$ nK (See Figure 3.7 (b)). Superfluidity increases in all three orthogonal directions as temperature decreases and reaches 100% superfluidity along the y -direction at lower temperatures. In this repulsive BEC regime, the role of the doubly dipolar interaction is minimal, and the anisotropy of superfluidity is attributed to the anisotropic trap geometry. At lower temperatures where thermal fluctuations

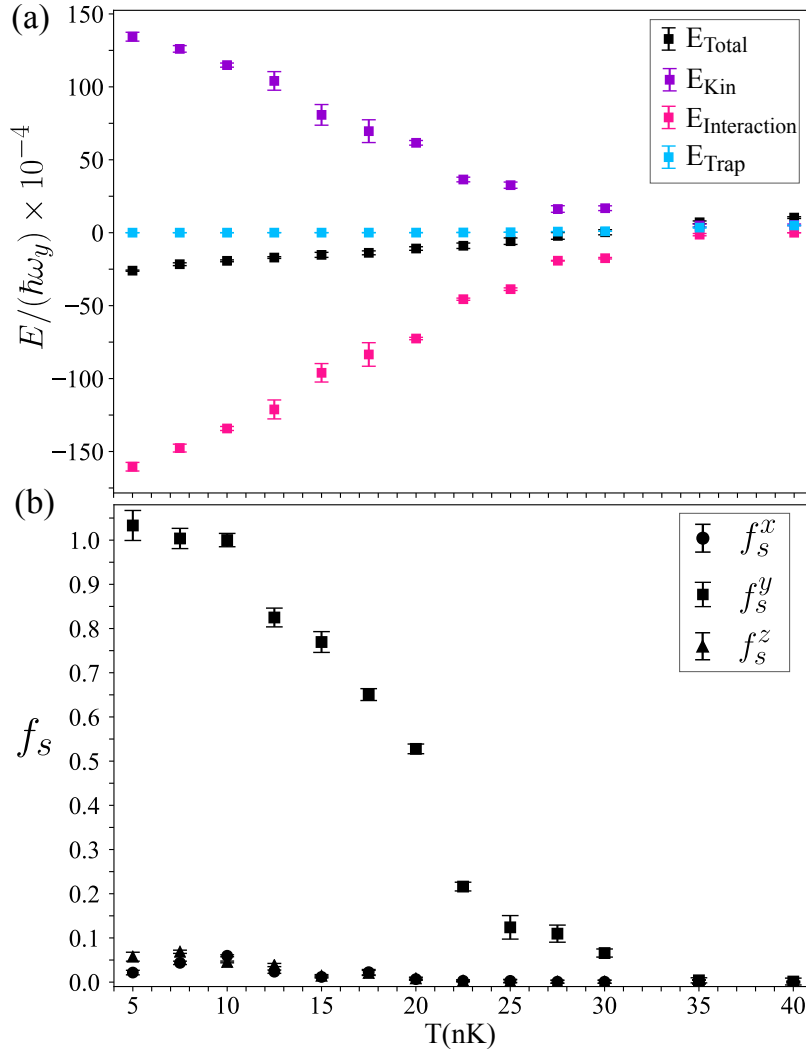


FIGURE 3.9: **Thermal gas to a pancake droplet transition** (a) Energy variation with temperature for a pancake droplet at $a_s/a_0 = 170$. The total energy is shown in black, the energy contributions arising from short-range interactions and long-range DDI are shown in pink, and the energy contributions from the kinetic term and external harmonic trap are illustrated in violet and skyblue, respectively. (b) Superfluid fraction along the transition from a thermal gas to a superfluid pancake droplet along three orthogonal directions (x, y, z). The PIMC simulations are done for $N = 1024$ Dy atoms for an external harmonic trap, $\omega_{x,y,z} = 2\pi \times (75, 25, 75)$ Hz.

are negligible, the system converges toward its ground state, with the total energy exhibiting minimal variation. Figure 3.8 (c) illustrates an isodensity plot of a superfluid cigar-shaped condensate at $T = 5$ nK.

Thermal gas to pancake droplet transition

In the low scattering length regime, the doubly dipolar gas is dominated by the strong DDI, where the quantum fluctuations present in the system play a pivotal role. We

investigate the interesting transition from a thermal gas to a quantum pancake droplet with varying temperatures.

As expected, at high temperatures, thermal fluctuations are strong and we observe a cigar-shaped thermal gas (see Figure 3.9 (d)). As the temperature decreases, the attractive DDI and the quantum fluctuations become prominent, leading to the transition from the thermal gas to a quasi-2D pancake droplet. Figure 3.9 (a) shows the energy computed from PIMC simulations across this transition. The high quantum fluctuations at low temperatures are reflected in the increase of the kinetic energy of the system, while the total energy decreases due to diminished thermal fluctuations and an increase in the attractive component of the DDI. The effect of the external trap is minimal in this regime, which indicates the pancake droplet is effectively self-bound due to the DDI.

The behavior of superfluidity across the temperatures is illustrated in Figure 3.9 (b). The rise in the superfluid fraction around $T = 30$ nK signals the formation of the quantum droplet. Upon entering the droplet regime, f_s^y increases steadily and reaches 100% superfluidity around 10 nK, while $f_s^{x,z}$ remains suppressed throughout due to the anisotropic DDI. The iso-density plot of a superfluid pancake droplet is shown in Figure 3.8 (c). Notably, we observe that the transition temperature from the thermal gas to the droplet is higher than that of the thermal gas to a condensate transition. This shows that the doubly dipolar potential alters the critical temperature for the condensation in the Bose gas. With decreasing a_s value, the increasing attractive nature of DDI shifts the critical temperature to a higher value, a similar phenomenon observed in dipolar Bose gases [50]. The pancake droplet demonstrates prolonged superfluidity across a broader temperature range compared to the condensate, which shows that the droplet is more robust against thermal fluctuations.

Our study reveals that the doubly dipolar condensate and the pancake droplet are stable against finite temperature fluctuations, which paves the way toward the experimental realization of DDBEC.

3.3.4 Structural transition with varying electric dipole moment

At this point, we study the characteristics of the doubly dipolar Bose gas by manipulating the relative strength, γ , between the electric and magnetic dipole moments at a fixed scattering length. γ can be varied by varying the magnitude of the electric dipole moment with the help of the external electric field [44]. The relative angle between the two dipole moments, α , is kept constant at $\pi/2$.

The PIMC simulations with varying γ reveal the BEC to droplet transition and the structural transition from a quasi-2D pancake to a quasi-1D cigar droplet. The superfluid behavior throughout this transition is illustrated in Figure 3.10 (a). When

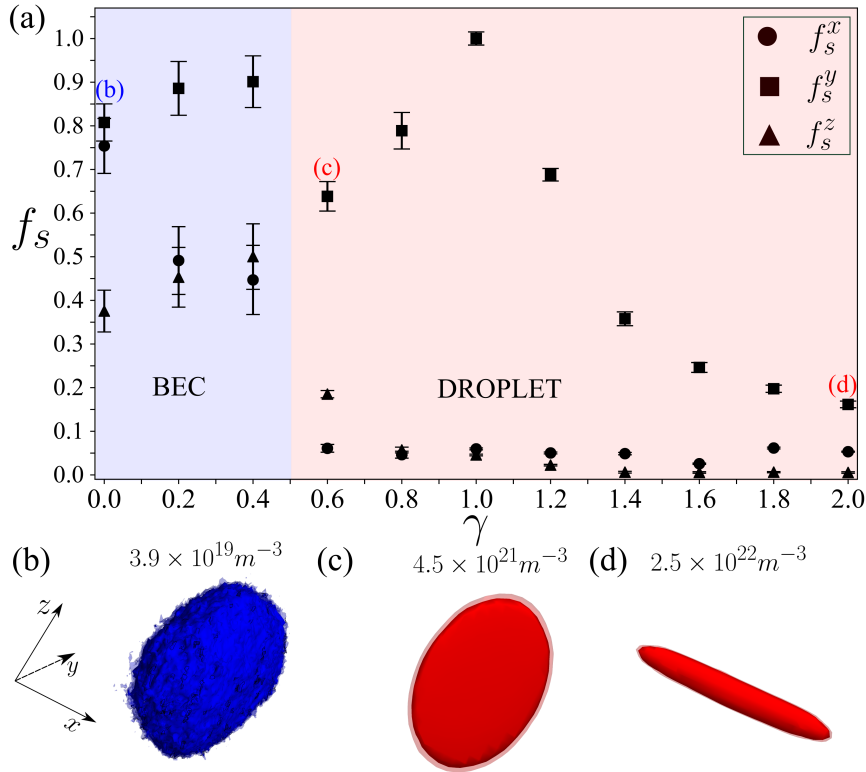


FIGURE 3.10: **Structural transition.** (a) Superfluid fraction across the structural transition from a BEC to a quasi-2D pancake droplet to a cigar droplet along three orthogonal directions (x, y, z) with increasing γ , for a constant $\alpha = \pi/2$ at scattering length, $a_s = 170a_0$. The 3D isodensity plots are shown for (b) BEC at $\gamma = 0$, (c) anisotropic pancake droplet at $\gamma = 0.6$, (d) cigar droplet elongated along the x -axis at $\gamma = 2$. The peak densities for each case are provided at the top. The PIMC simulations are done for $N = 1024$ Dy atoms for an external harmonic trap, $\omega_{x,y,z} = 2\pi \times (75, 25, 75)$ Hz. The blue and red backgrounds denote the BEC and the droplet regime, respectively.

$\gamma = 0$, DDI solely involves magnetic dipoles pointing along the z -direction. The repulsive short-range interaction dominates over the attractive DDI and forms a repulsive BEC (see Figure 3.10 (b)). Since the trap is weaker along y , the condensate is elongated in y , and the width of the condensate along z is greater than along x , due to the maximum attraction of DDI along z . The superfluid fraction exhibits finite values in all three orthogonal directions, with $f_s^{x,y}$ having higher values than f_s^z . With the introduction of γ and the associated electric dipole moment, attractive interactions along the x -direction come into play. In the BEC regime for $\gamma > 0$, f_s^y surpasses $f_s^{x,z}$ due to attractive DDI in the xz -plane. As γ increases further, the attractive DDI dominates over the short-range interactions, leading to the emergence of a quasi-2D pancake droplet. The pancake droplet is anisotropic for $\gamma \neq 1$, it is elongated along z for $\gamma < 1$ as shown in Figure 3.10 (c). For $\gamma = 1$, where DDI is radially symmetric in the xz -plane, an isotropic pancake is formed, see Figure 3.8 (c). Superfluidity is high perpendicular to the dipole plane for the pancake droplets and suppressed in

the dipole plane. f_s^y reaches around unity for an isotropic pancake droplet. For γ values much higher than one, the electric dipole moment dominates over the magnetic dipole moment, and DDI is maximally attractive along the x -axis. The droplet undergoes a structural transition from the pancake to a cigar shape elongated along the x -axis (see Figure 3.10 (d)). Superfluidity (f_s^y) decreases with the dimensional crossover from a quasi-2D to quasi-1D geometry. In this tightly confined configuration, the system can not support a rotational flow in the same way as the quasi-2D geometry and is forced to move almost like a rigid body. Consequently, the moment of inertia approaches the classical value, and the superfluid fraction is strongly reduced. This geometric constraint is further reinforced by the enhanced phase fluctuations inherent to effectively one-dimensional systems, which diminish long-range phase coherence. This study highlights that the superfluid characteristics of DDBEC can be manipulated through the application of an external field.

3.4 Conclusion

In this chapter, we have implemented first-principles numerical simulations to study the properties of a doubly dipolar Bose gas. Employing PIMC, we observe the transition from a repulsive BEC to a quantum pancake droplet at low temperatures and conduct a comparative study of the same at $T = 0$ using the gGPE in the mean-field framework. While PIMC and gGPE results align well in weak DDI regimes, PIMC correctly estimates dipolar as well as quantum fluctuation effects in a strong DDI regime. We have investigated the superfluid behavior based on rotational responses as a function of scattering lengths and temperatures. We observe a highly anisotropic superfluid fraction in the pancake droplet regime, attributed to the anisotropic nature of the doubly dipolar interaction. The direction-dependent superfluid fraction may be experimentally measured based on the system's non-classical rotational inertia [200]. The anisotropies in the superfluid fractions might also be observed in usual magnetic dipolar BECs or in non-dipolar BECs confined within highly anisotropic traps, paving the way for a comprehensive investigation in future studies. Notably, we observe that the temperature of passage from a thermal gas to the pancake droplet is higher than that of the transition to a BEC, showcasing the robustness of the pancake droplet against thermal fluctuations. Modulating the relative strength between the two dipole moments influences the structural and superfluid properties of the quantum droplet.

In this study, we have considered the doubly dipolar bosons confined within a cigar-shaped trap, which reveals the interesting transition from a cigar-shaped BEC to a pancake-shaped droplet due to the interplay between the trap and the anisotropic

DDI. Due to convergence issues, simulating a self-bound droplet using the PIMC method becomes difficult, and a detailed study on self-bound droplets can be explored in future work. Also, our current focus has been on a single pancake droplet, although by altering the trap geometry or number of atoms, multiple pancake droplets can be realized. Future investigation of superfluidity between the droplets will provide insights into novel pancake supersolids predicted in the mean-field work [46]. Exploring the finite temperature properties of pancake supersolids will also be the subject of future studies. Our study confirms a stable DDBEC at finite temperature and paves the way toward its experimental realization.

Chapter 4

Droplet Arrays and Supersolids in Doubly Dipolar Bose-Einstein Condensates

The content of this chapter is adapted from a part of the research article "Droplet arrays in doubly dipolar Bose-Einstein condensates" [46].

4.1 Introduction

Supersolid is a fundamental phase of matter characterized by the frictionless flow of a superfluid with the crystal-like periodic density modulation of a solid [177, 186]. This unique phase spontaneously breaks two continuous symmetries: the global phase coherence, which accounts for superfluidity, and the translational invariance resulting in a crystal structure. Originally predicted in solid helium [182, 184, 185], the first experimental realizations of supersolids have been achieved in ultracold quantum gases [189, 190]. In particular, dipolar quantum gases [13, 36] have been instrumental in exploring the supersolid characteristics, including spontaneous density modulation [41, 71, 72, 204], the existence of goldstone modes [198, 199] and Josephson-like dynamics [201, 316]. The formation of density modulation in supersolids hinders the superfluid flow along that direction, resulting in reduced superfluidity. Experimental measurements have demonstrated this reduced superfluidity based on the non-classical moment of inertia [200] and the Josephson effect [201]. The presence of quantized vortices provides unambiguous evidence of superfluidity in supersolids. Dipolar supersolids are usually obtained by triggering the roton instability [38]. At very low temperatures, the transition from a BEC to a supersolid is achieved by quenching the s-wave scattering length [41, 71, 72, 191–193], where the repulsive quantum fluctuations [157, 158] play a crucial role in stabilizing the condensate. Heating a dipolar superfluid can also induce a phase transition to a supersolid state [58, 317] due to the effect of thermal fluctuations.

In this chapter, we explore the formation of supersolids in a doubly dipolar BEC. We demonstrate that manipulating the relative angle between the two dipole moments can create novel scenarios for quantum droplet arrays in doubly dipolar condensates. These scenarios include a density-modulated single droplet ground state, supersolid-supersolid transitions, and the potential formation of an array of pancake-shaped quantum droplets.

4.2 Droplet Arrays and Supersolids

In contrast to homogeneous systems, where single quantum droplet formation is typically favored, the presence of an external harmonic confinement can result in the emergence of multi-droplet ground states, a phenomenon observed in condensates of magnetic dipolar atoms. Under proper conditions, these droplets may keep mutual phase coherence, leading to the formation of dipolar supersolids [41, 72, 204, 206]. Here, we investigate the novel possibilities opened by the doubly dipolar potential in the context of droplet arrays and supersolids, broadening the landscape of accessible quantum phases.

In the following, we consider a doubly dipolar Dy condensate of $N = 35000$ atoms in a magnetic field of $\mathcal{B} = 100$ G and an electric field $\mathcal{E} = 2.68$ kV/cm. These field strengths are experimentally convenient, and the electric dipole moment or γ varies with α accordingly, as shown in Fig. 2.2, with $\gamma = 1$ when $\alpha = \pi/2$. The lifetime of the stretched state $|S\rangle$, introduced in Chapter 2, varies from 28 s at $\alpha = 0$ to 58 ms at $\alpha = \pi/2$ for the chosen parameters. These lifetimes are experimentally sufficient to observe the physics discussed in this section. As mentioned in previous chapters, the effective polarization axis of the doubly dipolar potential is assumed to lie on the xz plane. The geometry of the external trapping potential, specifically the relative confinement strengths along and perpendicular to the polarization axis, plays a decisive role in determining the ground state of droplets and supersolids in DD BEC. In the following, we discuss separately the cases of weaker confinement on the dipole polarization plane and orthogonal to it. We explore the emergent ground states for the different trap geometries by solving the generalized GPE (2.17) in imaginary time evolution.

4.3 Weaker Confinement on the Dipole Plane

Figure 4.1 illustrates the possible ground states as a function of the angle between two dipole moments (α) and the scattering lengths (a_s) for the case of weaker confinement on the dipole plane. We consider $N = 35000$ atoms in a trap elongated

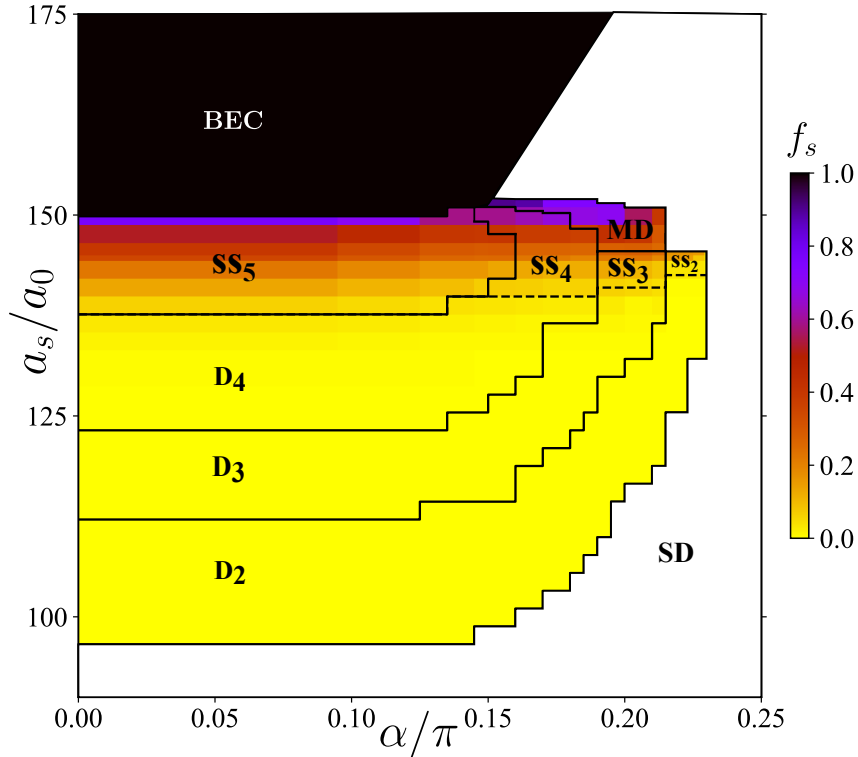


FIGURE 4.1: **Droplet arrays and supersolids.** Ground-state phase diagram as a function of α and a_s for $\omega_{x,y,z} = 2\pi \times (18.5, 53, 81)$ Hz, $N = 35000$, $\mathcal{B} = 100$ G and $\mathcal{E} = 2.68$ kV/cm. The incoherent (supersolid) arrays with n droplets are denoted as D_n (SS_n). The color bar shows the superfluid fraction f_s of the multi-droplet states. Solid lines separate states with different numbers of droplets, whereas dashed lines separate supersolid and incoherent arrays with the same droplet number. MD is the region where we observe a density-modulated droplet, and SD is the regime for a single droplet. To distinguish between BEC and SD, the superfluid fraction is not shown in the SD region.

along x , with $\omega_{x,y,z} = 2\pi \times (18.5, 53, 81)$ Hz. This specific trap geometry has been employed in the experiments of magnetic dipolar supersolids [41]. We observe the emergence of various ground states in the whole parameter regime and in the phase diagram, incoherent (supersolid) droplet arrays are labelled as D_n (SS_n), where n stands for the number of droplets.

4.3.1 Physics of magnetic dipolar condensates

We begin by discussing the physics for the case when $\alpha = 0$ and $\gamma = 0$. In this configuration, the ground state properties are determined solely by the magnetic dipole moment, which is polarized along the z -axis, and the system exhibits behavior analogous to that observed in conventional magnetic dipolar condensates. When decreasing a_s , the ground-state transitions from an unmodulated (denoted as BEC) regime to a supersolid and eventually to incoherent droplets [41, 71, 72]. At larger values of a_s , the repulsive scattering interaction dominates over the dipolar interactions, and

we observe the formation of a repulsive condensate elongated along the x -axis (the weaker confinement axis). Conversely, for lower a_s , the dipolar interactions become increasingly dominant, leading to the formation of supersolids, incoherent droplets, and eventually to a single one (SD regime). Fig. 4.3 (b) shows the density plot of supersolid with 5 droplets (SS₅) in the xz plane, the droplets are cigar-shaped and elongated along the z axis, consistent with the polarization of the magnetic dipoles. Here, we discuss in detail how we obtain the phase boundaries, differentiate between BEC and supersolid phase, and the different droplet states.

4.3.2 Finding the phase boundaries

Leggett's upper-bound for superfluid fraction:

To distinguish between incoherent droplets and supersolids, we employ Leggett's upper bound of the superfluid fraction [186]:

$$f_s = (2L)^2 \left[\int_{-L}^L dq \tilde{n}(q) \int_{-L}^L \frac{dq}{\tilde{n}(q)} \right]^{-1}, \quad (4.1)$$

where q is the coordinate along which the droplet array is formed, and $\tilde{n}(q)$ is the column density obtained after integrating over the other two axes. The length $2L$ encloses the central region, where droplets form. For a mean-field stable condensate (BEC regime) and an unmodulated single droplet (SD regime), $f_s = 1$, whereas $f_s \sim 0$ for an incoherent droplet array (D_n) with $n > 1$. Intermediate f_s values characterize the supersolid regime. We employ the criterion $f_s > 0.1$ to identify a regime as supersolid. We have shown the f_s value for all the parameters in the ground state phase diagram (Fig. 4.1). Fig 4.2 (b) shows the f_s value for $\alpha = 0$ with varying a_s . f_s decreases from unity to a finite value as the ground state gets transitioned from a BEC to a supersolid regime, and gradually it goes to 0 in the incoherent droplet array regime.

Contrast:

The transition from BEC to supersolid to an isolated array of droplets can also be characterized with the help of density contrast [202, 318, 319] defined by,

$$C = \frac{n_{\text{peak}} - n_{\text{min}}}{n_{\text{peak}} + n_{\text{min}}}, \quad (4.2)$$

where n_{peak} and n_{min} are the maximum and minimum densities along the direction of the droplet arrays. C changes from zero for the BEC state to a finite value for the supersolid state. C becomes unity for the array of isolated droplets. The contrast and superfluid fraction values complement each other, as demonstrated in Fig. 4.2 (b) for

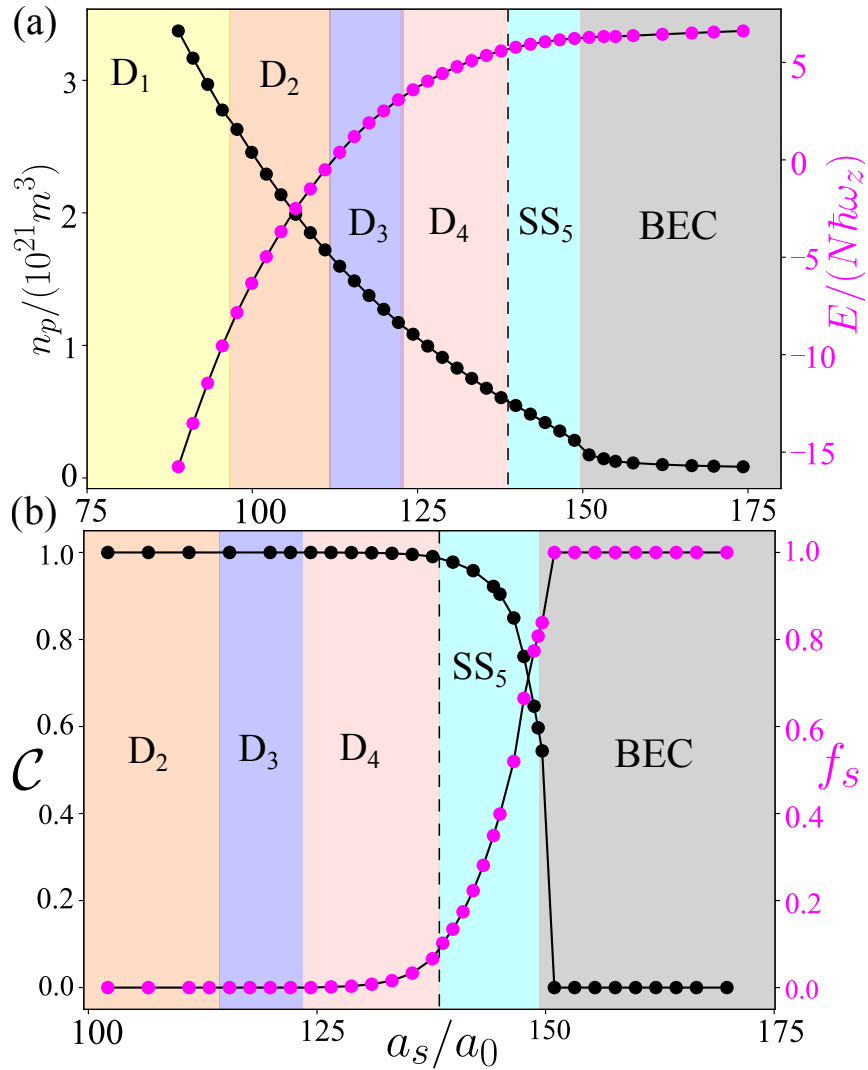


FIGURE 4.2: **Ground state transitions.** (a) The peak density, n_p (black) and the ground state energy per atom (magenta) as a function of a_s for $\alpha = 0$. (b) The contrast, C (black) and the superfluid fraction, f_s (magenta) as a function of a_s for $\alpha = 0$. The solid lines are a guide to the eye. All other parameters are the same as used in Fig. 4.1.

$\alpha = 0$ with varying scattering lengths. The f_s and C both go to zero for the incoherent droplet arrays, as there is no global phase coherence between the droplet peaks.

Ground state Energy:

We search for the ground state of the system for a set of α and a_s values, starting with different initial wave functions. We calculate the total energy of the system from each different initial wavefunction and find the lowest energy state [166, 203]. The total energy of the system is expressed through the following,

$$E = \int d^3r \frac{\hbar^2}{2m} |\nabla\psi|^2 + \int d^3r \frac{m}{2} (\omega_x^2 x^2 + \omega_y^2 y^2 + \omega_z^2 z^2) |\psi|^2 + \frac{g}{2} \int d^3r |\psi|^4 + \frac{1}{2} \int d^3r |\psi(r)|^2 \int d^3r' V_d(r-r') |\psi(r')|^2 + \frac{2}{5} \gamma_{QF} \int d^3r |\psi|^5,$$

where the first and second terms represent the kinetic and external potential energies, respectively. The third term accounts for the scattering energy, with $g = \frac{4\pi\hbar^2 N a_s}{m}$. The last two terms are the doubly dipolar interaction and the quantum fluctuation contribution to the total energy.

In the parameter regime we have investigated, numerous metastable states exist with nearly degenerate energies. Different droplet configurations may get energetically close for certain values of α and a_s . The imaginary time evolution need not necessarily converge to the ground state and may exhibit a dependence on the initial state. We do an exhaustive search for the ground state by considering various initial states, consisting of a variable number of Gaussians placed in distinct configurations. In the vicinity of some phase boundaries, configurations containing n and $n+1$ numbers of droplets often differ in energy by only a few Hertz per atom. We choose the low-energy configuration as the ground state among the different final states. We have decided the phase boundary following a similar procedure for all the α and a_s values. Due to the cigar-shaped geometry of the trap, finding the ground state is relatively easy in our case. For the interaction parameters we consider, the ground state droplet array is always along the direction of weaker confinement. A trap with comparable frequencies in all directions can pose more difficulty in finding the true ground state.

Fig. 4.2 (a) shows the ground state energies per atom for $\alpha = 0$ with varying scattering lengths. At larger values of a_s , the repulsive scattering interaction makes the total energy positive. With decreasing a_s , the DDI becomes dominant and the energy becomes negative due to the attractive contribution of the doubly dipolar interactions. Within the BEC regime, the energy exhibits a gradual variation; however, at the BEC-supersolid transition, a more rapid decrease in energy is observed, which becomes even more pronounced in the droplet regime.

Peak Density:

The peak density of a condensate serves as a key indicator for the transition from a BEC to droplets or a supersolid state. A sharp increase in the peak density marks the onset of the high-density droplet phase. Fig. 4.2 (a) demonstrates the peak density as a function of a_s for $\alpha = 0$. It is possible to distinguish arrays with odd and even numbers of droplets via the density at the trap centre. There is a droplet at the trap centre for odd cases, whereas the central density is nearly zero for even cases.

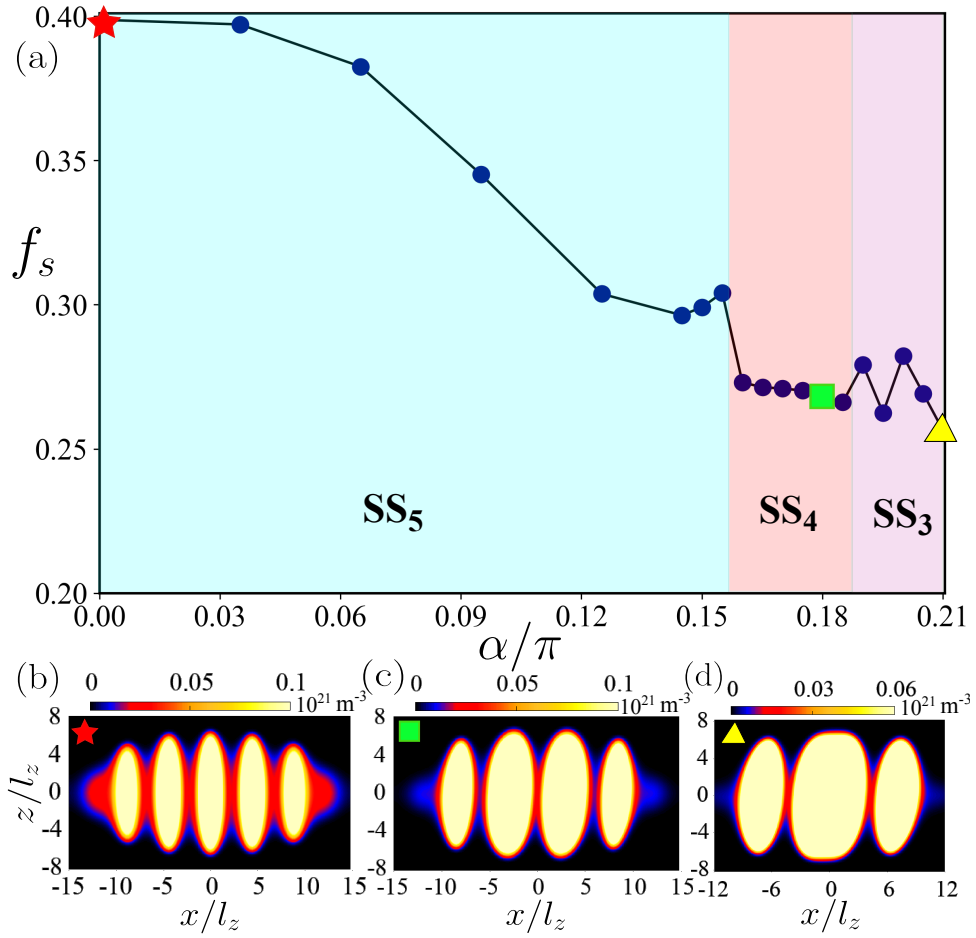


FIGURE 4.3: **Supersolid-supersolid transitions.** Superfluid fraction f_s as a function of α for $a_s = 145a_0$. The other parameters are the same as in Fig. 4.1. (b)-(d) show supersolid densities ($|\psi(x, y = 0, z)|^2$) at $\alpha/\pi = 0$ (SS_5), 0.18 (SS_4), and 0.21 (SS_3), respectively.

4.3.3 Supersolid-supersolid transition

Now we focus on the behaviour of the ground state phases as the electric dipole moment is tilted towards x , i.e., α is increased. The phase diagram remains unchanged for $\alpha \lesssim 0.12\pi$, since the magnitude of the electric dipole moment is very small (see Fig. 2.2 (a)).

In contrast, the phase diagram is radically altered for larger α . As the electric dipole moment becomes substantial, the ground states exhibit a non-trivial dependence on α . In particular, it is also possible to observe transitions between different droplet arrays by varying α . For a fixed a_s value, while for smaller α , results in multidroplet ground states, with increasing α , the attractive region in the xz -plane of the doubly dipolar potential gets augmented, and the attraction along the x -axis increases. Now, there is an interplay between the weaker trap along the x and the increasing attraction of DDI in the same direction. This leads to a decrease in the number of droplets with increasing α and eventually to a large single droplet as the ground state.

Remarkably, the ground state may undergo a transition between supersolid phases with a different number of droplets as a function of α . These transitions can occur while keeping a significant superfluid fraction, maintaining the superfluidity between the droplet peaks. Fig. 4.3 demonstrates such transition for $a_s = 145a_0$. Note as well that due to the interplay between the trapping potential and the doubly dipolar potential, the droplets that form the supersolids get tilted and take atypical shapes with varying α (see Figs. 4.3 (b-d)). The transition between supersolids with different droplet crystal structures is so far a unique scenario in the physics of dipolar condensates.

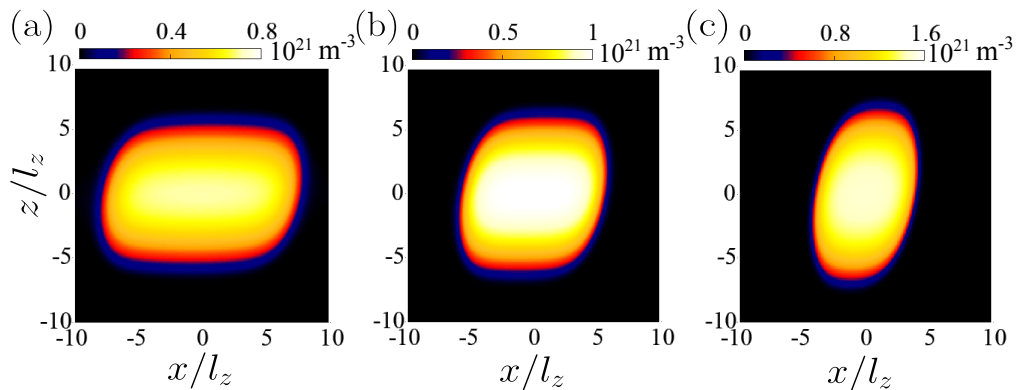


FIGURE 4.4: **Single droplet.** Droplet density $[|\psi(x, y = 0, z)|^2]$ in the xz plane for $\alpha/\pi = 0.25$, and $a_s/a_0 = 155$ (a), 146 (b), and 135 (c). The other parameters are the same as in Fig. 4.1. The droplet acquires a rectangular cuboid shape with its aspect ratio controlled by a_s .

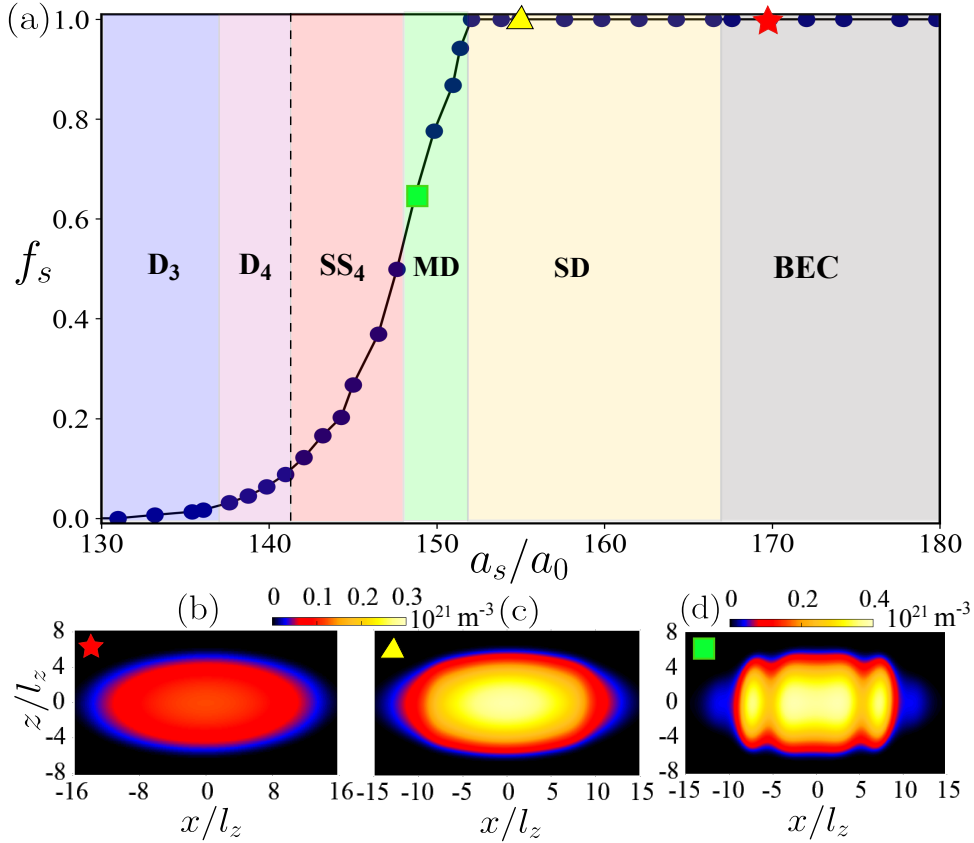


FIGURE 4.5: **Modulated droplet.** Superfluid fraction f_s as a function of a_s for $\alpha/\pi = 0.18$. The other parameters are the same as in Fig. 4.1. The dashed line separates supersolid and incoherent arrays with the same droplet number. (b)-(d) show the densities $|\psi(x, y = 0, z)|^2$. Upon decreasing a_s , the BEC phase (depicted in (b) for $a_s = 170a_0$) transitions into a single droplet (shown in (c) for $a_s = 155a_0$), which develops density modulations (as seen in (d) for $a_s = 149a_0$).

4.3.4 Single droplet and density-modulated droplets

Here we discuss the single droplet regime in more detail. For a sufficiently large $\alpha \gtrsim 0.15\pi$, the mean-field stable condensate transitions for decreasing a_s into a single droplet (see Fig. 4.5), resembling the situation found in usual dipolar condensates for a small-enough particle number [168]. For higher a_s , the droplet is elongated along the x axis due to the weaker confinement of the trap in the x axis. For $\alpha \gtrsim 0.23\pi$, the single droplet remains the ground-state when further decreasing a_s . However, the droplet shape may depart very significantly from the typical elongated form found in usual dipolar condensates. The interplay between the external confinement and the doubly dipolar potential causes shearing and tilting, leading to rectangular cuboid shapes, with an aspect ratio controlled by a_s (see Fig. 4.4).

The situation is very different for $0.15\pi \lesssim \alpha \lesssim 0.23\pi$, where the single droplet acquires a density modulation for decreasing a_s due to the roton-like softening of the lowest droplet mode along the x -axis [320]. The density-modulated state arises

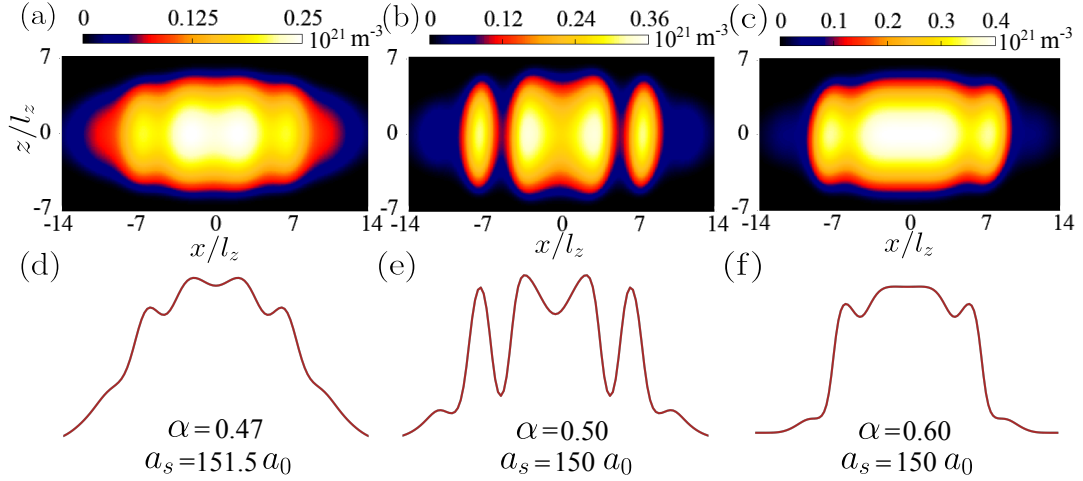


FIGURE 4.6: **Various kinds of modulated droplets.** Different modulated droplet states of doubly dipolar droplets. The densities $|\psi(x, y = 0, z)|^2$ (upper row) and $|\psi(x, y = 0, z = 0)|^2$ (bottom row) for the doubly dipolar BEC with all other parameters same as in Fig. 4.1. The corresponding value of α and a_s is provided at the bottom of each column. (a) resembles an arrested coalescence (AC) state of four droplets, in (b) the two inner droplets are in the AC state, and in (c) a central big droplet is almost merged with the two smaller outer droplets.

because of the combined effect of droplet tilting due to the additional electric dipole moment and the Q1D geometry of the harmonic trap, which causes the droplets to overlap. We observe the emergence of various kinds of these modulated droplet states in the parameter regime. These states resemble the form of arrested coalescence, which means they are not entirely coalesced. This partial coalescence leads to novel types of density-modulated droplets. Fig. 4.6. (a), (b) show two or more droplets in the form of arrested coalescence, and Fig. 4.6. (c) the two central droplets are in a state of partial coalescence and are weakly coupled to each outer droplet. The results indicate that such states can be easily observed and controlled in doubly dipolar BECs. A similar state is predicted in the usual dysprosium condensate [71, 201], but with different trap frequencies. The modulated-droplet state has comparatively higher superfluid fraction values than the usual supersolid (SS_n) phases.

When further decreasing a_s (see Fig. 4.5 (a)), this modulated-droplet (MD) supersolid ground-state evolves into a droplet supersolid and then into an incoherent droplet array, with a decreasing number of droplets until reaching a single-droplet solution. Below, we explore the roton minima in the excitation spectrum of DDBEC in more detail.

4.3.5 Quasi one-dimensional DDBEC

Since we have used an anisotropic external harmonic trap in our study, which is strongly confined in two directions, we approximate the trapped condensate as a quasi-one-dimensional (Q1D) condensate along the weaker trap direction (x -axis in this case). Any external trapping along the axial (x) direction is neglected, and a strong harmonic trapping potential is imposed in the radial (y and z) directions. The dipoles are polarized in the xz plane, with the magnetic dipoles always polarized in z and the electric dipole polarization varying in the xz plane. We can express the 3D wavefunction in a separable form as $\psi(\mathbf{r}) = \phi_\rho(y, z)\psi(x)$, where,

$$\phi_\rho(y, z) = \frac{1}{\sqrt{\pi L_y L_z}} \exp\left(-\left(\frac{y^2}{2L_y^2} + \frac{z^2}{2L_z^2}\right)\right), \quad (4.3)$$

represents the ground state of the harmonic oscillator of the radial confinement. Employing the above factorization and integrating out the radial directions, we obtain the Q1D generalized GPE along the axial direction :

$$i\hbar \frac{\partial \psi(x, t)}{\partial t} = \left[-\frac{\hbar^2}{2M} \frac{\partial^2}{\partial x^2} + \frac{g}{2\pi L_y L_z} |\psi(x, t)|^2 + \frac{4\pi g_m}{3} \int \frac{dk_x}{2\pi} e^{ik_x x} V^{1d}(k_x) n(k_x) + \frac{2}{5\pi^{3/2}} \frac{\Delta\mu}{(L_y L_z)^{3/2}} \right] \psi(x, t), \quad (4.4)$$

where $n(k_x)$ is the Fourier transform of the density $|\psi(x)|^2$ and the Q1D doubly dipolar interaction is expressed as follows:

$$V^{1D}(k_x) = \int_{-\infty}^{\infty} dk_z e^{-\frac{1}{2}k_z^2 L_z^2} \left[-\frac{\sqrt{2\pi}}{L_y} (1 + \gamma) + 3\pi \frac{e^{\frac{1}{2}(k_x^2 + k_z^2)L_y^2}}{\sqrt{k_x^2 + k_z^2}} \operatorname{erfc}\left[\frac{\sqrt{k_x^2 + k_z^2} L_y}{2}\right] (k_z^2 + \gamma(k_z \cos \alpha + K_x \sin \alpha)^2) \right], \quad (4.5)$$

where $\operatorname{erfc}(q) = (1 - \frac{2}{\sqrt{\pi}} \int_0^q e^{-t^2} dt)$ is the complementary error function.

Effective Q1D excitation spectrum

The collective excitations of the system can be expressed in terms of the Bogoliubov quasiparticles, with the excitation spectrum obtained by solving the Bogoliubov-de Gennes (BdG) equations. The BdG equations are derived by linearizing the time-dependent GPE (2.17) for a small perturbation around the stationary state.

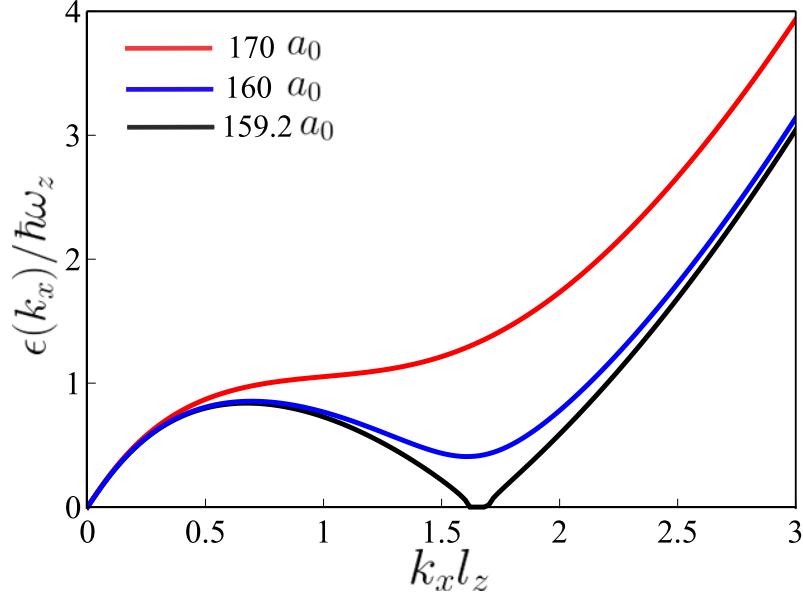


FIGURE 4.7: **Roton Minima.** The effective Q1D excitation spectrum is plotted for $\alpha/\pi = 0.18$ with varying scattering lengths, $a_s/a_0 = 170$ (red), 160 (blue), and 159.2 (black). The roton minimum softens around $a_s = 159.2a_0$, indicating the formation of spontaneous density modulation.

To obtain the effective Q1D excitation spectrum, we employ the same shape approximation [321] for the quasiparticle excitations, and integrate out $\phi_\rho(x, z)$ from the 3D BdG equations. For a uniform condensate along the y axis, excitations can be chosen as plane waves. Solving the BdG equations, the dispersion relation along k_x is obtained as follows [274, 318],

$$\epsilon(k_x) = \sqrt{\frac{\hbar^2 k_x^2}{2M} \left[\frac{\hbar^2 k_x^2}{2M} + 2 \left(\frac{gn_0}{2\pi L_y L_z} + \frac{4\pi g_m n_0}{3} V^{1d}(k_x) + \frac{2}{5\pi^{3/2}} \frac{\Delta\mu n_0^{3/2}}{(L_y L_z)^{3/2}} \right) \right]}, \quad (4.6)$$

where n_0 is the linear density along the x -axis.

Fig. 4.7 shows the Q1D excitation spectrum for $\alpha/\pi = 0.18$ for various scattering lengths, where we have used the widths along the $y(L_y)$ and $z(L_z)$ axes from the corresponding 3D numerics, as well as the n_0 is taken as the peak linear density along x -axis of the condensate obtained from the imaginary time evolution. For higher values of a_s in the BEC regime, a roton minimum is observed in the spectrum. With increasing the effect of DDI, the roton mode softens, i.e., the energy goes to zero at a finite momentum. The softening of the roton indicates the emergence of density modulation in the condensate.

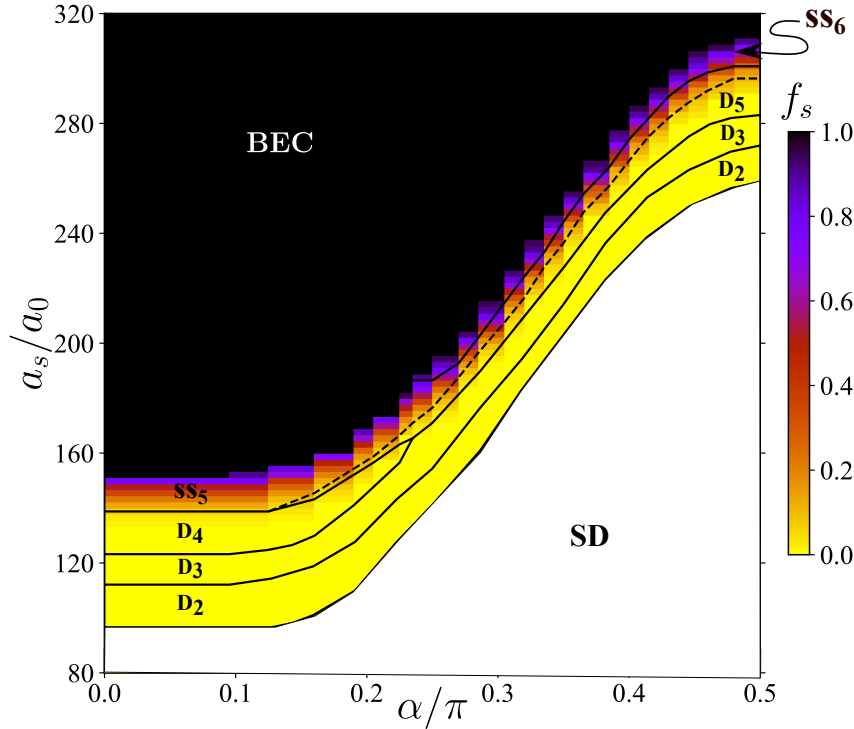


FIGURE 4.8: **Droplet arrays and supersolids.** Ground-state phase diagram as a function of α and a_s for $\omega_{x,y,z} = 2\pi \times (53, 18.5, 81)$ Hz. The other parameters are the same as in Fig. 4.1. The color bar shows the superfluid fraction f_s of the multi-droplet states. Solid lines separate states with different numbers of droplets, whereas dashed lines separate supersolid and incoherent arrays with the same droplet number.

4.4 Weak Confinement Perpendicular to the Dipole Plane

In this section, we investigate how just changing the external harmonic trap affects the ground states of doubly dipolar condensates. Here, the trap geometry, the number of atoms, and the electric and magnetic field strengths remain the same, except that the trap frequencies along the x and y axes are interchanged compared to the previous case in 4.3. We consider $\omega_{x,y,z} = 2\pi \times (53, 18.5, 81)$ Hz, the weaker confinement is along the y -axis, and the dipoles remain oriented in the xz -plane. In usual dipolar condensates with dipoles polarized along the z -axis, an interchange between the trap frequencies along the x and y axes leaves the condensate properties unchanged. However, it may have drastic effects on doubly dipolar condensates, as discussed here.

As shown in Fig. 4.8, for $\alpha \lesssim 0.12\pi$, the phase diagram remains the same as in the previous case since the electric dipole moment is small, and the trap frequency along z (the magnetic dipole direction) is unchanged. We see the identical transitions: $\text{BEC} \rightarrow \text{SS}_5 \rightarrow \text{D}_4 \rightarrow \text{D}_3 \rightarrow \text{D}_2 \rightarrow \text{D}_1$ when a_s is decreased for small α values. In

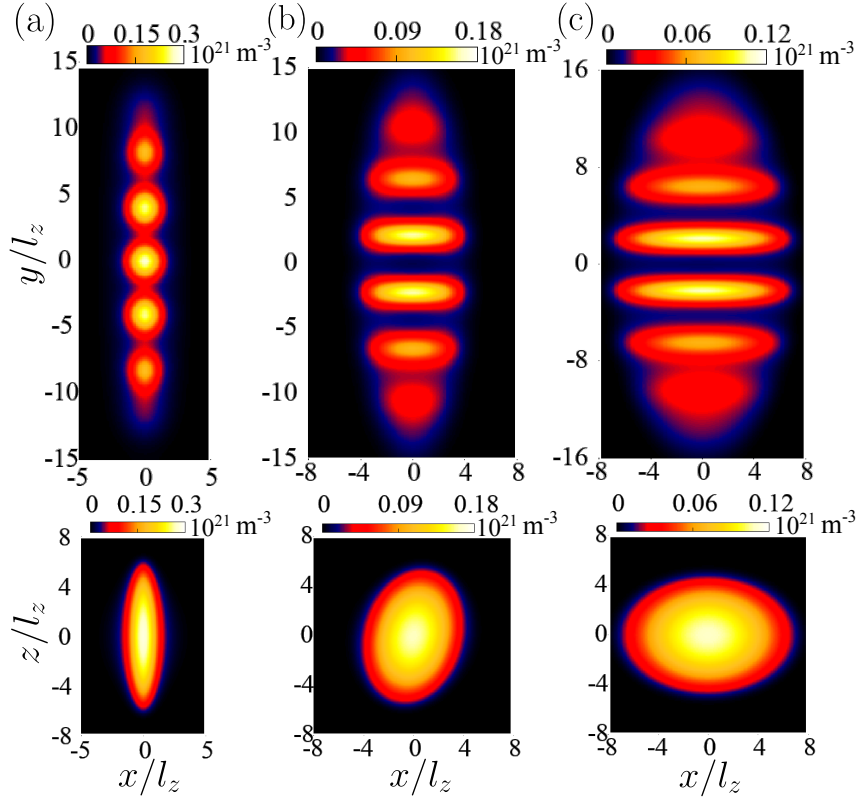


FIGURE 4.9: **Exotic supersolids in DDBEC.** Supersolid states for different relative orientations (α) between the two dipole moments. The upper row shows the density $|\psi(x, y, z = 0)|^2$ in the xy plane, and the bottom row shows the density $|\psi(x, y = 0, z)|^2$ in the xz plane. (a) is for $\alpha = 0$ and $a_s = 149a_0$, which shows a supersolid formed by cigar droplets. (b) is $\alpha = \pi/4$ and $a_s = 187a_0$, displaying a supersolid tilted droplets. (c) is $\alpha = \pi/2$ and $a_s = 306a_0$, we have a supersolid of pancake droplets. In (a), there are 5 droplets, whereas in (b) and (c), there are six droplets.

this case, the droplet array is formed along the y axis since that is the weaker trap direction.

4.4.1 Pancake supersolids

In contrast, for larger α , the phase diagram drastically departs from that of Fig. 4.1. As α increases to $\sim 0.12\pi$, the electric dipole moment becomes significant, and the explicit dependence of trap frequencies along each axis on the phase diagram becomes visible. We see a maximum of six droplets compared to five in the previous case. It is because the droplet width along the y -axis becomes increasingly smaller for larger electric dipole moment, which helps to accommodate more droplets along the y -axis. Another feature is that the transition between different droplet arrays occurs irrespective of α . The multi-droplet states always form in this case, since the increasing attraction of the DDI and the weaker trap axis are in the perpendicular direction and do not compete with each other. The transitions move to larger values

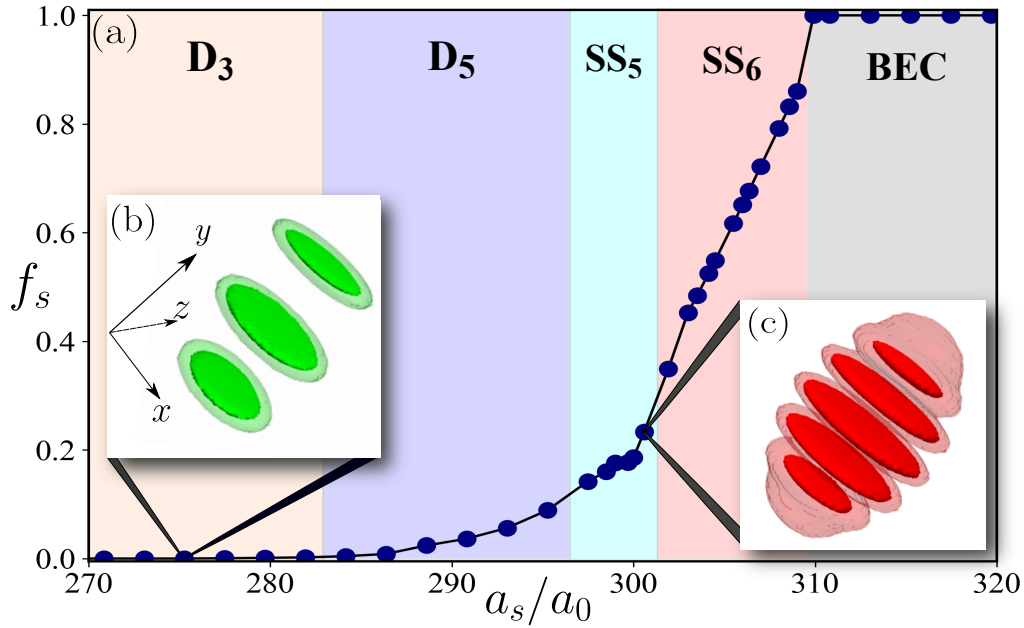


FIGURE 4.10: **Pancake supersolids.** Superfluid fraction f_s as a function of a_s for $\alpha/\pi = 0.5$. The other parameters are the same as in Fig. 4.8. Insets (b) and (c) illustrate, respectively, the case of an incoherent and supersolid pancake droplet array.

of a_s , but their nature remains unaltered. Notably, above a critical $\alpha \sim 0.25\pi$, SS_6 emerges but D_4 disappears. It also implies that above a critical a_s , increasing α , we get $BEC \rightarrow SS_6$ transition, and below the critical a_s , we observe $BEC \rightarrow SS_5$ transition. In our numerics, we have observed that for $\alpha > 0.22\pi$, in the vicinity of the transition region between D_5 and D_3 , the difference in the average energy per particle with D_4 is of the order of a Hertz. The latter implies that even though we do not observe D_4 as the ground state for $\alpha > 0.22\pi$, it is quasi-degenerate with D_5 and D_3 in the transition region. It can be experimentally challenging to resolve between these three states using this trap.

The doubly dipolar interaction offers the novel possibility to realize exotic supersolid states in this trap geometry. The supersolids are most probable to be found near the BEC-droplet array transition regions. In Fig. 4.9, we show the supersolids observed at three different α . The value of a_s is adjusted accordingly for each α . The top row shows the density in the xy -plane, and the bottom shows the same in the xz -plane. For $\alpha = 0$, it is composed of five cigar droplets as shown in Fig. 4.9 (a) and is also the case of usual dipolar condensates. Fig. 4.9 (b) and 4.9 (c) show the examples of novel supersolids emerging in DDBEC. Fig. 4.9 (b) demonstrates the emergence of a supersolid state with tilted droplets, and also the droplets start to look more quasi-2D-like.

Most remarkably, droplets become pancake-shaped on the xz -plane for $\alpha > 0.4\pi$.

As a result, doubly dipolar condensates offer the unique possibility of realizing arrays of pancake droplets, as illustrated in Fig. 4.10 for the case of $\alpha/\pi = 0.5$. Upon decreasing a_s , the unmodulated BEC phase undergoes a transition to a pancake supersolid (SS_6), followed by a pancake supersolid-supersolid ($SS_6 - SS_5$) transition. Eventually, it becomes an incoherent array of pancake droplets (D_5), and a further decrease in a_s leads to arrays with fewer droplets. The emergence of the pancake droplets is a unique scenario for the doubly dipolar condensates.

4.5 Conclusion

The interplay between doubly dipolar interactions and harmonic confinement leads to novel possibilities for quantum droplet arrays. The relative orientation between the electric and magnetic dipole moments constitutes a novel control parameter that may be employed to drive intriguing scenarios, such as modulated droplets and supersolid-supersolid transitions. Moreover, changing the relative angle allows, without changing the external confinement, transitioning from an array of cigar-shaped droplets, as those of usual dipolar condensates, to a novel array of pancake droplets. Although we have focused on one-dimensional droplet arrays, two-dimensional arrangements open new possibilities for other forms of supersolids and density patterns, as explored in the usual dipolar condensates [202–204, 206, 319]. The fascinating physics of two-dimensional quantum-stabilized doubly dipolar condensates will be the subject of future studies.

Chapter 5

Rotation-induced Supersolidity in Dipolar Bose Gases

The content of this chapter is adapted from an ongoing project, with the manuscript "Dilute supersolids in rotating dipolar Bose-Einstein Condensates" under preparation.

5.1 Introduction

A supersolid is a quantum phase of matter in which superfluid and crystalline properties coexist due to the spontaneous breaking of global $U(1)$ and translational symmetries [177]. Several variants of supersolids have been discovered over the last decade. For instance, stripe supersolids have been observed in spin-orbit coupled Bose-Einstein condensates (BECs) [189]. One-dimensional supersolids, characterized by density modulations along a specific axis, are found in a BEC coupled to two cavity modes [190], photonic-crystal polariton condensates [322], and in dipolar condensates [41, 71, 72]. Furthermore, two-dimensional supersolids have also been discovered in dipolar BECs [204, 205]. More exotic supersolids, from honeycomb to pancake ones, are predicted to exist in dipolar condensates [46, 202, 203, 323, 324]. The existence of supersolids is attributed to the instability of finite-momentum roton-like excitations in the Bogoliubov spectrum, which leads to crystallization in the system, transforming from a purely superfluid state [147, 245, 325].

Dipolar supersolids are realized as coherent arrays of self-assembled quantum droplets [13, 326, 327]. These droplets are clusters of bosons formed due to the interplay between effective mean-field attractive interactions and repulsive quantum fluctuations in the presence of a harmonic potential [45, 168, 252, 299]. Quantum fluctuations introduce density-dependent corrections that go beyond mean-field theory, known as Lee-Huang–Yang (LHY) corrections to the Gross-Pitaevskii equation governing the properties of dipolar bosons at very low temperatures [158]. The repulsive LHY correction is crucial for stabilizing each droplet against collapse [167]. The

emergence of supersolids is confirmed by the phase coherence among the droplets [41, 71, 72], the existence of Goldstone modes related to the spontaneous breaking of gauge and translational symmetries [194, 198, 199], and a reduced moment of inertia [200].

On the other hand, rotating a trapped dipolar BEC accommodates various forms of quantized vortices and vortex lattice geometries [234, 235, 237–240, 328–330]. Initial analyses of rotating dipolar condensates were based on time-dependent harmonic potentials. Recently, several studies have focused on injecting angular momentum into dipolar condensates by rotating the dipole polarization using time-dependent magnetic fields [242, 331]. The first experimental demonstration of quantized vortices in a dipolar BEC was achieved using highly magnetic dysprosium (Dy) atoms, under the rotation of dipole polarization, which they termed as magnetostirring [233]. The experiment was conducted in a cylindrically symmetric trap, where the rotation of the condensate about the trap axis was facilitated by magnetostriction resulting from anisotropic dipole-dipole interactions. The magnetostirring also results in an elongation of the condensate, with the degree of elongation increasing with the rotation frequency. The experiment also revealed the formation of vortex stripes when dipolar interactions are strong.

Very recently, rotating a supersolid via magnetic stirring and the subsequent formation of vortices have also been demonstrated experimentally [244]. This finding further confirms the superfluid characteristics of the droplet crystals. The vortices in supersolids, which are formed in the low-density regions between the droplets, exhibit different properties compared to their pure superfluid counterparts [246, 247, 249]. For instance, the angular momentum is lower than the expected value of \hbar due to the reduced superfluidity in the system, along with significant modifications in the vortex core structure caused by nearby droplets. Other notable differences include a considerably lower critical velocity for vortex nucleation and a steady increase in the number of vortices as the driving frequency surpasses a certain threshold.

In this chapter, we discuss the response of a dipolar condensate subjected to simultaneous rotation of a harmonic potential and the dipole orientation. We focus on a cigar-shaped condensate, with the rotation axis oriented perpendicular to both the trap's symmetry axis and the dipole polarization. Solving the GPE in a rotating frame, we demonstrate a ground state transition from a BEC to a supersolid phase accompanied by the formation of vortex lines. Crucially, these supersolids don't rely on LHY interactions and are stabilized by the emergence of vortices. In addition, rotational effects give rise to a supersolid–supersolid transition within the ground state. Furthermore, we study the stability of the system under real-time dynamics incorporating noise to the ground state via the truncated Wigner formalism. Finally, we also

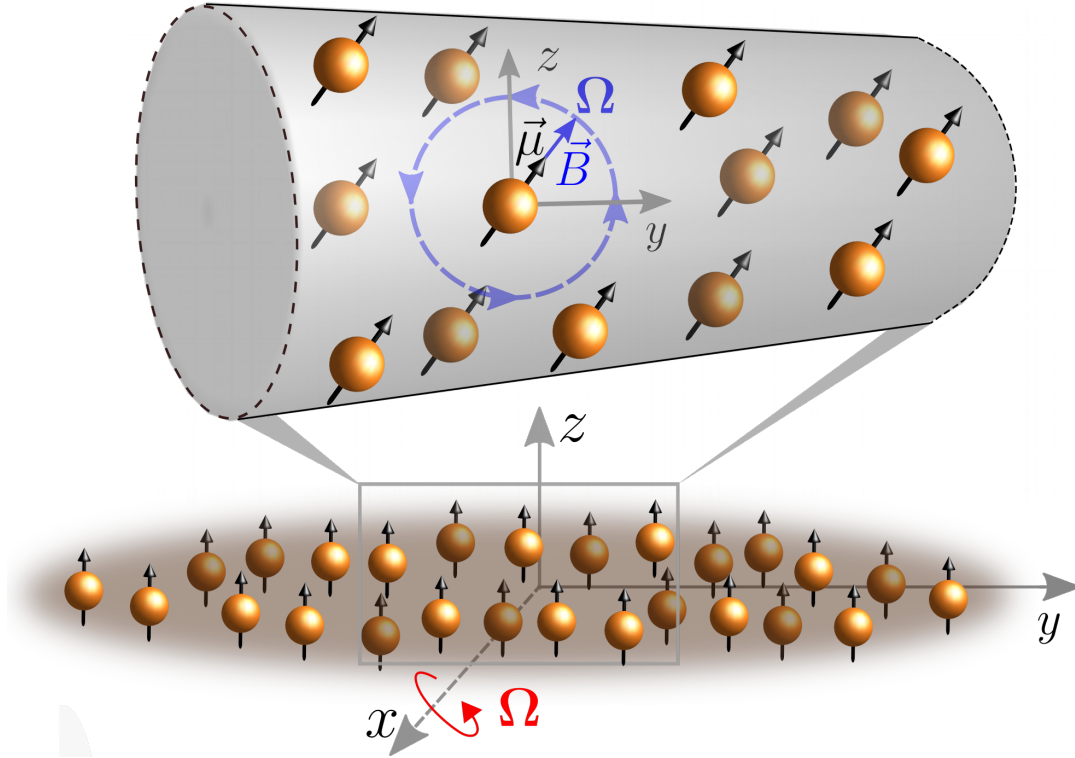


FIGURE 5.1: Schematic diagram showing the rotation of a cigar-shaped dipolar Bose gas. Dipolar atoms are in a magnetic field and a trap, both rotating about the x -axis with a frequency Ω . The dipoles are always polarized along the rotating magnetic field.

explore how the trap geometry influences the ground-state transition by examining variations from cigar to spherical configurations.

5.2 Dipolar Bose Gas in a Rotating Frame

We study the rotation of a dipolar Bose-Einstein condensate consisting of N atoms of mass m and magnetic dipole moment μ confined within an external harmonic trap. The dipole moments are aligned along an externally applied uniform magnetic field. We employ the rotation of both the external harmonic trap and the magnetic field around the x axis to rotate the gas. The time-dependent external harmonic trap potential is expressed as [332–334], $V^T(\mathbf{r}, t) = m/2(\omega_x^2 x^2 + \omega_y^2 (y \cos(\Omega t) + z \sin(\Omega t))^2 + \omega_z^2 (z \cos(\Omega t) - y \sin(\Omega t))^2)$, where \mathbf{r} is the coordinate of the rotating frame. The rotating magnetic field is expressed as, $\mathbf{B}(t) = \mathcal{B}\hat{\mathbf{e}}(t) = \mathcal{B}(z \cos(\Omega t) - y \sin(\Omega t))$. We assume the frequency of rotation is sufficiently slow such that the rotation is adiabatic. The rotation frequency is much lower compared to the Larmor frequency of the system, $\Omega \ll \omega_L = \mu\mathcal{B}/\hbar$. The magnetic dipoles follow the rotating magnetic field $\mathbf{B}(t)$ adiabatically [243, 335] and the dipoles are aligned along $\hat{\mathbf{e}}(t)$. In

experiments with dipolar Bose gases, the magnetic field can be rotated using the ‘Magnetostirring’ method [233, 336].

In the regime of very low temperatures, the system is aptly described in mean-field terms by a time-dependent non-local Gross-Pitaevskii equation,

$$i\hbar \frac{\partial}{\partial t} \psi(\mathbf{r}, t) = \mathcal{H}(\mathbf{r}, t) \psi(\mathbf{r}, t), \quad (5.1)$$

where the time-dependent Hamiltonian is expressed as [334, 337, 338],

$$\mathcal{H}(\mathbf{r}, t) = \frac{-\hbar^2 \nabla^2}{2m} + V^T(\mathbf{r}, t) + g|\psi(\mathbf{r})|^2 + \int d^3 r' V_d(\mathbf{r} - \mathbf{r}', t) |\psi(\mathbf{r}', t)|^2. \quad (5.2)$$

The parameter $g = 4\pi\hbar^2 a_s N/M$ determines the contact interaction strength, with a_s being the s -wave scattering length. The time-dependent dipolar interaction is given as,

$$V_d(\mathbf{r}, t) = \frac{\mu_0 \mu^2 (1 - 3 \cos^2 \theta(t))}{4\pi |\mathbf{r}|^3}, \quad (5.3)$$

where μ_0 is the vacuum permeability and $\cos^2(\theta(t)) = [\hat{\mathbf{e}}(t) \cdot \mathbf{r}]^2$.

5.2.1 GPE in the rotating frame

Following a unitary transformation, $\psi_{\text{Rot}}(\mathbf{r}, t) = \hat{U}^\dagger(\Omega t) \psi(\mathbf{r}, t)$, we obtain the time-independent Hamiltonian in the rotating frame, which allows us to write the GPE in the rotating frame as follows (see Appendix C for details),

$$i\hbar \frac{\partial}{\partial t} \psi_{\text{Rot}}(\mathbf{r}, t) = \left[\frac{-\hbar^2 \nabla^2}{2M} + \frac{m}{2} (\omega_x^2 x^2 + \omega_y^2 y^2 + \omega_z^2 z^2) + g |\psi_{\text{Rot}}(\mathbf{r}, t)|^2 + \int d^3 r' V_d(\mathbf{r} - \mathbf{r}') |\psi_{\text{Rot}}(\mathbf{r}', t)|^2 - \Omega L_x \right] \psi_{\text{Rot}}(\mathbf{r}, t), \quad (5.4)$$

where $\psi_{\text{Rot}}(\mathbf{r}, t)$ is the condensate wave function in the rotating frame satisfying $\int d^3 r |\psi_{\text{Rot}}(\mathbf{r}, t)|^2 = 1$. The external harmonic trap is static in the rotating frame, and the dipoles are always aligned along the z axis of the rotating frame. L_x corresponds to the x component of the angular momentum due to rotation about the x axis. We introduce dimensionless parameters, $\tilde{g} = g/\hbar\omega l_z^3$, $\tilde{g}_d = N\mu_0\mu^2/4\pi\hbar\omega l_z^3$, to quantify the interactions strengths, where $l_z = \sqrt{\hbar/m\omega}$. We numerically solve Eq. 5.4 via imaginary-time evolution to obtain the ground states of the system in the rotating frame.

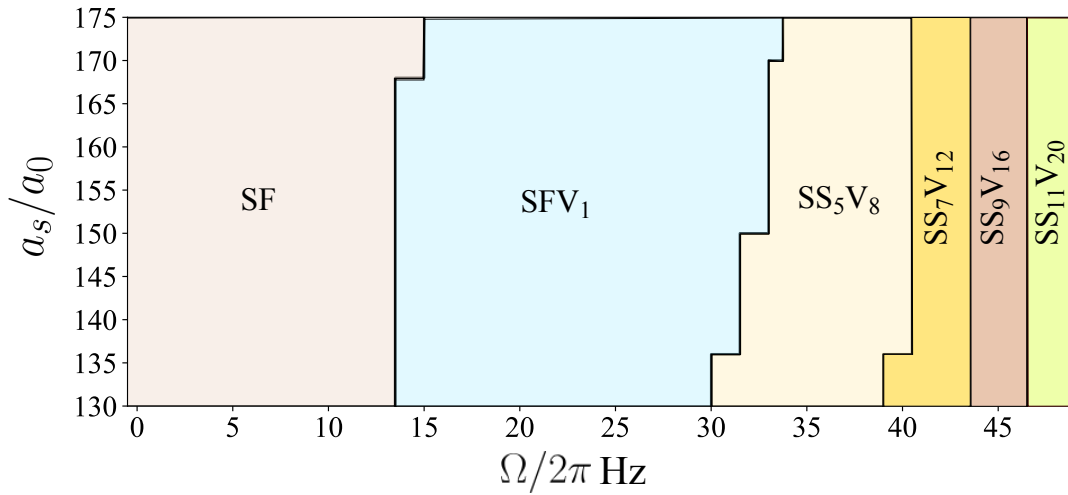


FIGURE 5.2: **Ground state phases.** Ground-state phase diagram as a function of the scattering length (a_s) and the rotation frequency (Ω). The light orange and cyan regimes denote the BEC and the BEC with a single vortex phase, respectively. The super-solid vortex phases with n crystal peaks and j no. of vortices are denoted as SS_nV_j . The results are demonstrated for $N = 30000$ Dy atoms with external trap frequencies, $(\omega_x, \omega_y, \omega_z) = 2\pi \times (150, 50, 150)$ Hz.

5.3 Ground-state Phases in the Rotating Frame

In this section, we investigate the ground-state properties of a harmonically-trapped dipolar Bose gas under rotation. In particular, our focus is on the rotation of a cigar-shaped dipolar condensate about an axis perpendicular to its dipole polarization direction.

We consider a condensate of $N = 30000$ magnetic dipolar Dy bosons confined within a cylindrical trap elongated along the y axis. We have considered an external trap, with $\omega_x = \omega_z = \omega$ and $\omega_y = \omega/\lambda$, with $\lambda \gg 1$, indicating the cigar geometry of the trap. Each boson has a mass m and magnetic dipole moment d . In the laboratory frame, the dipoles are polarized along the z direction (see Fig. 5.1), following the direction of the applied magnetic field along the same. We consider the rotation of the gas about the x axis, which is perpendicular to the dipole polarization direction. Both the harmonic trap and the magnetic field are rotated to rotate the gas, as discussed in the previous section. The dipoles will follow the rotating magnetic field and are always polarized along the z axis of the rotating frame. We obtain the ground state of the system in the rotating frame by solving the rotating frame GPE Eq. (5.4) in imaginary time evolution. In this chapter, we choose the interaction strengths, \tilde{g} and \tilde{g}_d , such that we are in a regime where the corrections to the chemical potential from the quantum fluctuations or the Lee-Huang-Yang (LHY) corrections can be neglected.

5.3.1 Ground-state phases

Figure 5.2 illustrates the various ground states of the rotating dipolar condensate as a function of the s-wave scattering length (a_s) and the rotation frequency (Ω). We observe the emergence of three different ground states in the parameter regime: i) Superfluid (SF), ii) Superfluid with vortex lines (SFV), and iii) Supersolid with vortex lines (SSV).

Searching for the ground state:

We search for the ground state of the system, starting with different initial wave functions. We have used three-dimensional Gaussian wavefunctions as the ansatz for $\Omega = 0$ and smaller Ω values. For $\Omega \neq 0$, in particular, we have imprinted a vortex line at the centre of the ground-state wave function and used the following ansatz for the initial wave function [339] :

$$\psi = \psi_0(\mathbf{r}) \frac{(y + iz)}{\sqrt{y^2 + z^2}}, \quad (5.5)$$

where ψ_0 is the ground-state wave function at $\Omega = 0$. From this ansatz, it is straightforward to see that ψ and ψ_0 have the same density profile, but ψ has an imprinted velocity field, which is irrotational everywhere except at the vorticity line (x axis). We calculate the total energy of the system from each different initial wavefunction and find the lowest energy state. The total energy of the system in the rotating frame is expressed through the following,

$$E = \int d^3r \frac{\hbar^2}{2m} |\nabla\psi|^2 + \int d^3r \frac{m}{2} (\omega_x^2 x^2 + \omega_y^2 y^2 + \omega_z^2 z^2) |\psi|^2 + \frac{g}{2} \int d^3r |\psi|^4 + \frac{1}{2} \int d^3r |\psi(r)|^2 \int d^3r' V_d(r-r') |\psi(r')|^2 - \Omega \int d^3r \psi^* L_x \psi. \quad (5.6)$$

In the parameter regime we have explored, numerous metastable states exist with nearly degenerate energies. Near the phase boundaries, different configurations may get energetically close. We do an exhaustive search for the ground state by considering various initial states, and choose the low-energy configuration as the ground state among the different final states.

The different phases

For small values of Ω , the system converges to a vortex-free configuration that corresponds to the ground state. At $\Omega = 0$, due to the higher value of the short-range

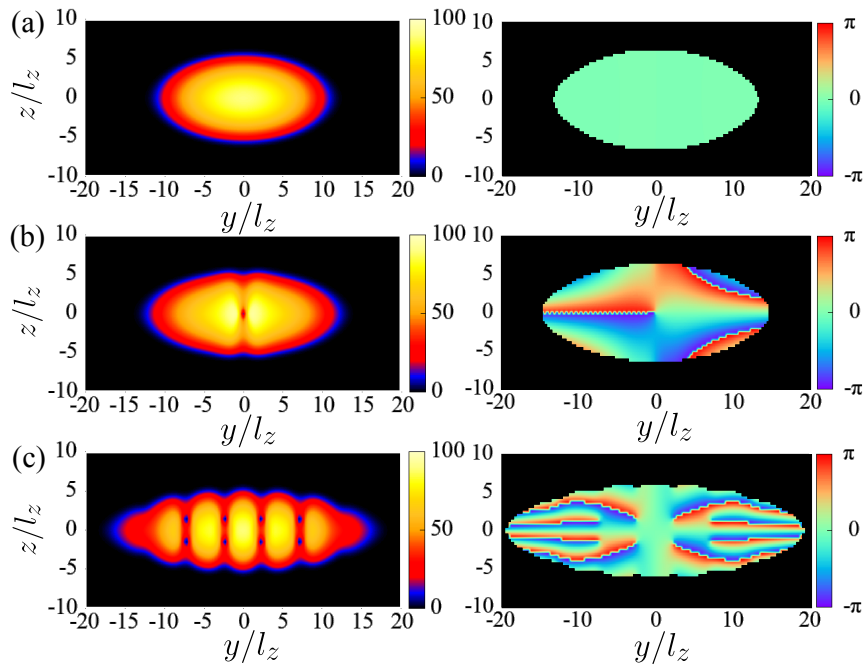


FIGURE 5.3: **Ground state transitions.** Left column: The density plots in the yz plane, $|\psi_{\text{Rot}}(x=0, y, z)|^2$ of ground states from GPE simulations for different Ω values at $a_s = 136a_0$. (a) $\Omega = 0$, BEC elongated along the y direction, (b) $\Omega/2\pi = 24$ Hz, BEC with a vortex line at the center, (c) $\Omega/2\pi = 40$ Hz, supersolid with vortex lines between the density peaks. Right column: phase profile ($\arg[\psi_{\text{Rot}}(x=0, y, z)]$) of the wavefunction in the yz plane. All other parameters are the same as Fig. 5.2.

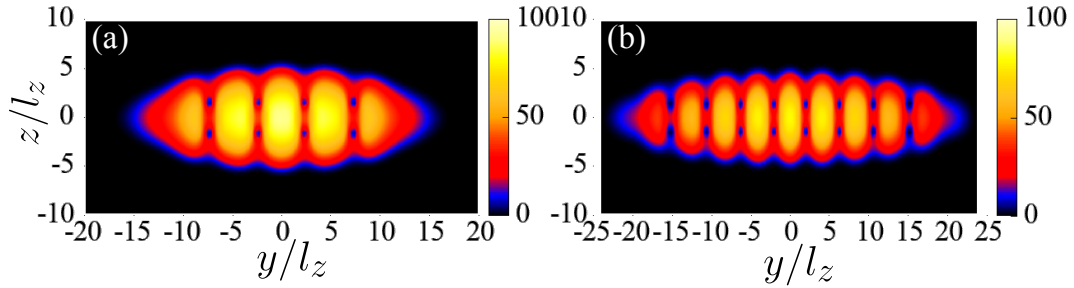


FIGURE 5.4: **Supersolid-supersolid transition.** The density plots in the yz plane, $|\psi_{\text{Rot}}(x = 0, y, z)|^2$ of ground states from GPE simulations for different Ω values at $a_s = 136a_0$. (a) $\Omega = 36$ Hz, SSV state with 5 density lobes and 8 vortices. (b) $\Omega/2\pi = 45$ Hz, SSV state with 9 density lobes and 16 vortices. All other parameters are the same as Fig. 5.2.

scattering interactions, the repulsive interactions dominate over the attractive dipolar interactions, and a repulsive BEC manifests as the ground state of the system. The condensate shape is determined by the external trap, and it has a cigar-shaped geometry. Fig. 5.3 (a) left row shows the density plot of the cigar-shaped condensate, elongated along the y direction (the weaker confinement axis). This phase is noted as the superfluid phase.

As the rotational frequency is increased, initially the condensate gets expanded along the y axis due to the rotation. The peak density also decreases by a small value. However, for angular frequencies larger than a critical value, a state with a vortex line at the center becomes energetically favorable than a vortex-free state. Fig. 5.3 (b) shows the density plot with the vortex emerging at the center of the condensate. The vortex core is elongated along the dipole polarization axis (z direction in this case). The formation of the vortex is well captured from the phase of the condensate. The phase ($\arg[\psi_{\text{Rot}}(x, y = 0, z)]$) of the wavefunction is displayed in the right column of Fig. 5.3, which shows an increment by 2π by turning around the vortex core once. The emergence of the vortex line unambiguously provides the signature of superfluidity of the condensate.

As the frequency of rotation increases, the ground state transitions to a supersolid state comprised of arrays of density peaks. The density lobes are arranged along the y axis and elongated along the z direction, due to the attractive nature of the dipolar interactions. Left panel of Fig. 5.3 (c) displays the density plot of the supersolid at $\Omega = 2\pi \times 40\text{Hz}$. The periodic density modulation is formed due to the interplay between the trap geometry, the repulsive short-range scattering & repulsive centrifugal interactions due to rotation, and the attractive dipolar interactions. This transition from the BEC to the supersolid state is well captured through the superfluid fraction (f_s) value, calculated through Leggett's upper bound of the superfluid fraction [186]

:

$$f_s = (2L)^2 \left[\int_{-L}^L dq \tilde{n}(q) \int_{-L}^L \frac{dq}{\tilde{n}(q)} \right]^{-1}, \quad (5.7)$$

where q is the axis along which the density modulation is formed (y -axis in this case) and $\tilde{n}(q)$ is the column density integrated over the other two axes. For small rotational frequencies, the Bose gas remains completely superfluid ($f_s = 1$), and with increasing rotation, the superfluid fraction decreases from unity (See Figure 5.5 (b)), indicating the formation of a supersolid state. The rotation-induced transition from a BEC to a supersolid has been predicted in dipolar BECs confined in a toroidal [340] and bubble trap [341], due to their unconventional geometries. These works did not predict the emergence of vortices in the rotation-induced supersolid phase. Here, we also observe the emergence of a pair of vortex lines within the low-density region [244, 247, 249, 251] between two crystal peaks. The presence of these vortices further supports the underlying superfluid nature of the crystal structure. The reduced density at the vortex core corresponds to a displacement of a large number of dipoles, allowing a vortex to be treated as a giant *anti-dipole* [234, 236]. Consequently, vortex-vortex interactions are repulsive along the z direction, positioning them symmetrically on opposite sides of the y axis. As the rotational frequency increases, the number of vortices in the condensate also rises. It becomes energetically favorable to break the condensate into a larger number of density peaks with each adjacent pair separated by a pair of vortices, rather than increasing the number of vortices within the existing two crystalline peaks. With increasing rotation frequency, the repulsion increases along the y axis, and both the number of density lobes and vortices increase. Hence, in this case, we observe the ground state transition between supersolid states comprised of different crystal structures. Fig. 5.4 demonstrates the supersolid-supersolid transition between SSV with 5 density lobes and 9 density lobes, with the vortex number increasing from 8 to 16 in the latter case. If the rotation frequency is higher than the trap frequency along y , i.e., ($\Omega > \omega_y$), the condensate doesn't remain confined within the trap due to high repulsion coming from the rotation. The transition to the supersolid phase shifts to higher Ω values with increasing strength of the short-range interactions. At larger values of the \tilde{g} , we don't observe the formation of the supersolid-vortex state.

The angular momentum across ground-state transition

The operator $\hat{L}_x = (z\hat{p}_y - y\hat{p}_z)$ corresponds to rotation about the x -axis. We investigate the characterization of the angular momentum across the ground-state transition. Fig. 5.5 (a) displays the angular momentum per particle with increasing rotation frequencies for a constant value of \tilde{g} . At low rotation frequencies, $\langle L_x \rangle$ exhibits a slow linear

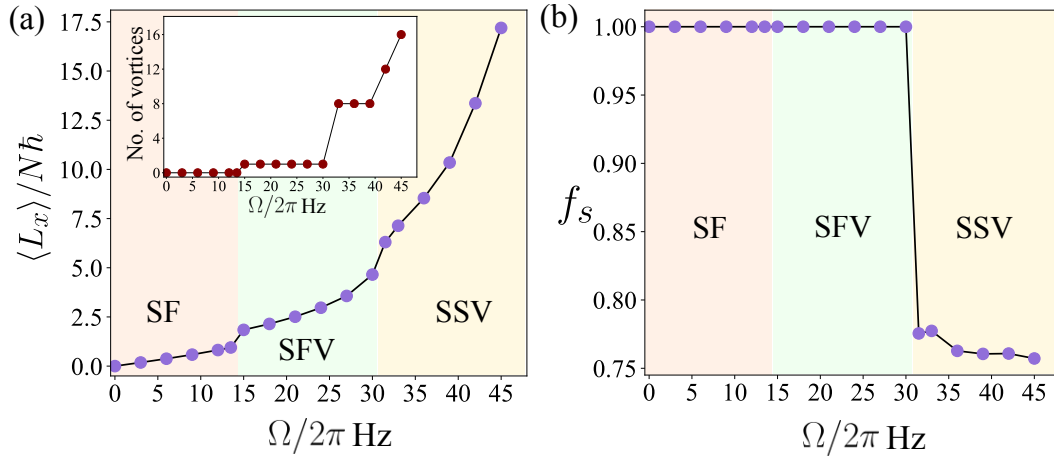


FIGURE 5.5: **Properties across ground-state transition.** (a) The angular momentum ($\langle L_x \rangle / N\hbar$) and (b) Leggett's superfluid fraction f_s with increasing rotation frequency Ω at $a_s = 136a_0$. Inset of (a) shows the number of vortices in the system with varying Ω . All other parameters are the same as Fig. 5.2.

increase. This behavior is attributed to the asymmetric nature of the trap around the axis of rotation, which induces elongation of the condensate along the weaker trap direction as rotation increases. A cylindrically symmetric rotation applies no torque to the condensate, while the asymmetric rotation imparts finite torque in the system. This manifests in a finite value of the angular momentum in the ground-state of the rotating frame, $\langle L_x \rangle = \int \psi^* (yp_z - zp_y) \psi d^3r$, even in the absence of vortices. Although a superfluid is irrotational, this behavior of the angular momentum is attributed to a mechanical drag of the system due to the rotation of the trap and has been predicted in superfluid helium [342] and non-dipolar BECs [332, 343]. In the rotating trap, the atoms at the edges of the condensate move faster than the atoms at the center, creating a spatial variation in the phase $\Phi(r)$ of the macroscopic wave function, $\psi = \sqrt{n(r)} \exp[i\Phi(r)]$. The spatial gradient of the phase profile entirely determines the angular momentum in the vortex-free regime, given by the integral of the velocity field over the condensate, $\langle L_x \rangle = \int (\rho \hbar / m) (\mathbf{r} \times \nabla \Phi)_x d^3r$. As rotation increases, the condensate becomes elongated along the weaker trap direction and extends further from the rotation axis, increasing angular momentum. However, the value of the angular momentum is lower compared to that of a rigid-body rotation, $L_{\text{rigid}} = \Omega \langle y^2 + z^2 \rangle$, which reflects the superfluid nature of the condensate [246, 332].

Once the vortex line emerges in the system, the angular momentum shows a discrete jump, corresponding to the angular momentum carried by the vortex line. Subsequently, within the superfluid-vortex regime, $\langle L_x \rangle$ increases linearly due to the further elongation of the condensate cloud. The transition to the SSV phase is marked by an increase in the number of vortex lines, which is reflected as a jump in the $\langle L_x \rangle$ value. In the SSV phase, the behavior of $\langle L_x \rangle$ is a complex interplay of several

physical contributions. The vortex lines carry a component of the total angular momentum. However, each vortex line contributes an angular momentum less than the quantized value of \hbar due to the reduced superfluid fraction [246], and the overall asymmetry of the condensate [332]. Moreover, the elongation of the cloud increases the moment of inertia, and the presence of the crystalline density peaks provides a solid-like contribution to the angular momentum. This results in a $\langle L_x \rangle$ value closer to the rigid-body rotation, but it doesn't reach L_{rigid} , as each crystal peak retains its individual superfluid character. The number of vortices for $a_s = 136a_0$, with increasing rotation frequency, is shown in the inset of Fig. 5.5 (a). The vortex lines increase from 1 to 8 while transitioning to the SSV phase and gradually increase to 16. Both the increase in vortex numbers and the elongation of the condensate cloud contribute to the increase in angular momentum value.

Signature of crystallization

The static structure factor serves as a novel tool to capture the crystal formation in quantum gases [344, 345]. This quantity has been experimentally measured in a dipolar Bose gas across the superfluid-supersolid transition [146]. In our context, the static structure factor is defined as $\mathcal{S}(k_y) = |n_k|^2$, where $n_k = \int dy n_{1D}(y) e^{-iky}$ is the Fourier transform of the one-dimensional number density. Fig. 5.6 (a) presents the static structure factor for different values of rotation frequency (Ω) for a constant \tilde{g} and displays a key signature of the formation of the periodic density modulation. At smaller Ω , in the superfluid regime, $\mathcal{S}(k_y)$ remains flat at finite momenta values, indicating a lack of spatial ordering. At higher rotation frequencies, $\mathcal{S}(k_y)$ shows a pronounced peak at a finite momentum value, $k_y/2\pi \simeq 0.21$, signifying the formation of a periodic crystal structure. It is an indication of the softening of the roton minimum and the subsequent formation of supersolids. Additionally, a smaller secondary peak is observed at twice the k_y value of the primary peak. This secondary peak might arise due to the linking between the neighboring density peaks.

5.4 Excitation Spectrum of a Q1D Homogeneous DBEC

We investigate the presence of a roton minima of a non-rotating cylindrical dipolar BEC within the laboratory frame.

5.4.1 Bogoliubov-de Gennes excitations

The collective excitations of the system can be expressed in terms of the Bogoliubov quasiparticles, with the excitation spectrum obtained by solving the Bogoliubov-de

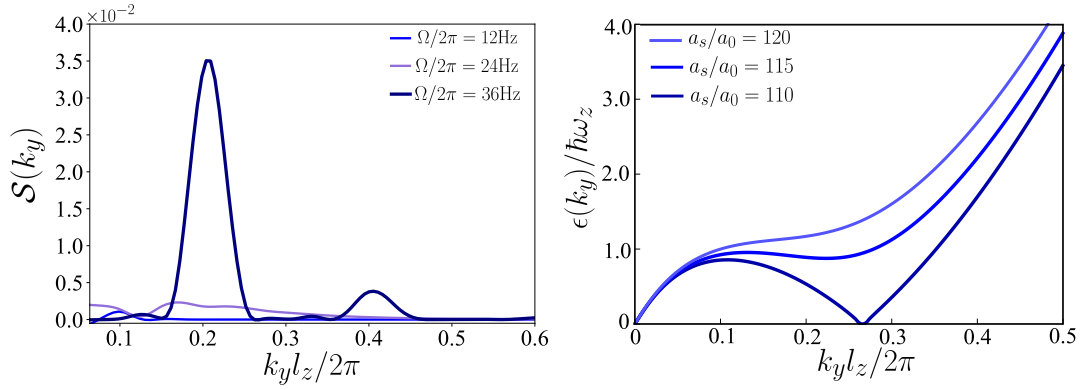


FIGURE 5.6: **Signature of Crystallization.** (a) The static structure factor, $\mathcal{S}(k_y) = |n_k|^2$, $n_k = \int dy n_{1D}(y) e^{-iky}$. The pronounced peak indicates the presence of periodic density modulations in the rotating dipolar BEC. The results are demonstrated for $N = 30000$ Dy atoms with $a_s = 136a_0$, and external trap frequencies, $(\omega_x, \omega_y, \omega_z) = 2\pi \times (150, 50, 150)$ Hz. (b) Excitation spectrum of a Q1D homogeneous dipolar BEC for different scattering lengths (a_s) in the laboratory frame ($\Omega = 0$). The roton mode becomes unstable for $a_s \sim 110a_0$, indicating the emergence of density modulations in the condensate. The results are demonstrated for Dy atoms, and radial trap frequencies, $(\omega_x, \omega_z) = 2\pi \times (150, 150)$ Hz.

Genes (BdG) equations. The BdG equations are derived by linearizing the time-dependent GPE for a small perturbation around the stationary state. The macroscopic wave function is expanded as follows,

$$\psi(\mathbf{r}, t) = e^{-i\mu t/\hbar} \left[\psi_0(\mathbf{r}) + u(\mathbf{r})e^{-i\omega t} + v^*(\mathbf{r})e^{i\omega t} \right], \quad (5.8)$$

where, $\psi_0(\mathbf{r})$ is the stationary state, μ is the chemical potential of the stationary state and $u(\mathbf{r})$, $v(\mathbf{r})$ are the quasiparticle amplitudes. The excitation modes (u, v) and the respective energies ($\hbar\omega$) satisfy the BdG equations,

$$\begin{bmatrix} \mathcal{H} - \mu + X & X \\ -X & -(\mathcal{H} - \mu + X) \end{bmatrix} \begin{bmatrix} u(\mathbf{r}) \\ v(\mathbf{r}) \end{bmatrix} = \hbar\omega \begin{bmatrix} u(\mathbf{r}) \\ v(\mathbf{r}) \end{bmatrix} \quad (5.9)$$

Where X is the exchange operator described as,

$$Xf(\mathbf{r}) = \int d^3r' \psi_0(\mathbf{r}') (g\delta(\mathbf{r} - \mathbf{r}') + V_d(\mathbf{r} - \mathbf{r}')) \psi_0^*(\mathbf{r}') f(\mathbf{r}'). \quad (5.10)$$

5.4.2 Effective Q1D Excitation Spectrum

Since the condensate is cylindrically trapped in our study, we approximate a quasi-one-dimensional (Q1D) condensate along the y axis, where any external trapping potential in the axial (y) direction is neglected and a strong harmonic trapping potential is imposed in the radial (x and z) directions. The dipoles are oriented along the z axis.

We can express the 3D wavefunction in a separable form as $\psi_0(\mathbf{r}) = \phi_\rho(x, z)\psi_y(y)$, where,

$$\phi_\rho(x, z) = \frac{1}{\sqrt{\pi L_x L_z}} \exp\left(-\left(\frac{x^2}{2L_x^2} + \frac{z^2}{2L_z^2}\right)\right),$$

is the ground state of the harmonic oscillator of the radial confinement. Integrating out the radial directions, we obtain the Q1D GPE along the axial direction :

$$i\hbar \frac{\partial \psi_y(y, t)}{\partial t} = \left[-\frac{\hbar^2}{2M} \frac{\partial^2}{\partial y^2} + \frac{g}{2\pi L_x L_z} |\psi_y(y, t)|^2 + \frac{4\pi g_m}{3} \int \frac{dk_y}{2\pi} e^{ik_y y} V_d^{1D}(k_y) n(k_y) \right] \psi_y(y, t), \quad (5.11)$$

where the Q1D dipolar interaction term is expressed as follows:

$$V_d^{1D}(k_y) = \int_{-\infty}^{\infty} dk_x e^{-\frac{1}{2}k_x^2 L_x^2} \left[\frac{2\sqrt{2\pi}}{L_z} - 3e^{-\frac{1}{2}(k_x^2 + k_y^2)L_z^2} \sqrt{k_x^2 + k_y^2} \operatorname{erfc}\left(\frac{\sqrt{(k_x^2 + k_y^2)L_z}}{\sqrt{2}}\right) \right],$$

with $\operatorname{erfc}(q) = 1 - \frac{2}{\sqrt{\pi}} \int_0^q e^{-t^2} dt$.

We employ the same shape approximation [321] for the excitations, $u(\mathbf{r}) = u_y(y)\phi_\rho(x, z)$ and $v(\mathbf{r}) = v_y(y)\phi_\rho(x, z)$ and integrate out $\phi_\rho(x, z)$ from the BdG equations (5.9). For a uniform condensate along the y axis, excitations can be chosen as plane waves. Solving the BdG equations, the dispersion relation along k_y is obtained as follows [274, 318],

$$\epsilon(k_y) = \sqrt{\frac{\hbar^2 k_y^2}{2M} \left[\frac{\hbar^2 k_y^2}{2M} + 2 \left(\frac{gn}{2\pi L_x L_z} + \frac{2g_m n}{3} V_d^{1D}(k_y) \right) \right]}. \quad (5.12)$$

Figure 5.6 (b) presents the excitation spectrum for different values of the scattering interaction strengths. In the high a_s regime, the system maintains a stable condensate state and the spectrum exhibits the presence of roton minima, which eventually soften with the decrease of the scattering length. The softening of the roton mode indicates the roton instability and the formation of the density-modulated state. Here, this phenomenon occurs because a reduction in repulsive scattering interactions enhances the influence of attractive dipolar interactions, thereby leading to the roton softening. Analogously, in the rotating cylindrical dBEC, rotation-induced effects facilitate roton softening even at a constant scattering interaction [74, 346]. In the

rotating system, the quasiparticle spectrum undergoes a Galilean shift, $E \rightarrow E - L_z \Omega$ [234]. This shift causes the roton minima to soften at a critical frequency (Ω_c), which triggers an instability leading to the formation of the density modulation. A similar mechanism of roton softening and subsequent density modulation has been predicted in superfluid ^4He flowing through a pipe with rough walls, where the linear momentum induces a Galilean shift in the energy spectrum.

5.5 Stability of the Rotating Dipolar Bose Gas

This section explores the dynamics and stability of a dipolar BEC in the laboratory frame, subjected to rotation of the external harmonic trap and the magnetic field. We study the dynamics from the real-time evolution of the following time-dependent GPE:

$$i\hbar \frac{\partial}{\partial t} \psi(\mathbf{r}, t) = \left[\frac{-\hbar^2 \nabla^2}{2m} + V^T(\mathbf{r}, t) + g|\psi(\mathbf{r})|^2 + \int d^3 r' V_d(\mathbf{r} - \mathbf{r}', t) |\psi(\mathbf{r}', t)|^2 \right] \psi(\mathbf{r}, t). \quad (5.13)$$

We employ the truncated Wigner formalism to introduce noise into the ground state, thereby simulating quantum fluctuation effects. The initial condensate is taken as the ground state of the static Hamiltonian in Eq. (1.23). We add noise to the ground state, which can seed instabilities in the system dynamics. The initial state used in the simulations is,

$$\psi(\mathbf{r}, 0) = \psi_0(\mathbf{r}) + \sum_j \alpha_j \phi_j(\mathbf{r}), \quad (5.14)$$

where $H_{\text{sp}} \phi_j = \epsilon_j \phi_j$, with ϕ_j being the single-particle harmonic oscillator basis and ϵ_j is the single-particle energy. α_j is a complex Gaussian noise with $\langle \alpha_j \rangle = 0$ and $\langle |\alpha_j|^2 \rangle = 1/2$. We restrict the sum to modes with energies $\epsilon_j \leq \epsilon_{\text{cut}}$. Once the initial state is prepared, it is evolved under the time-dependent Hamiltonian, with the rotation frequency Ω being quenched from zero to a finite value.

We consider a cylindrically trapped dipolar BEC, with the same trap frequencies, $\omega = 2\pi(150, 50, 150)$ Hz, as used in the previous sections. The initial state for these real-time dynamics is generated by adding truncated Wigner noise to the ground state at $\Omega = 0$. The energy cutoff is taken as $\epsilon_{\text{cut}} = \mu$, where μ is the chemical potential of the ground state. We study the dynamics of the condensate in the laboratory frame by instantaneously quenching the rotation frequency from $\Omega = 0$ to $\Omega = \Omega_f$.

Instabilities in the condensate arise from both the rotation of the external trap [347] and the rotating dipole polarization [241–243]. These instabilities can be examined from the behavior of the kinetic energy (E_k) of the condensate. Fig. 5.7 (a) illustrates the evolution of kinetic energy for various rotation frequencies (Ω_f).

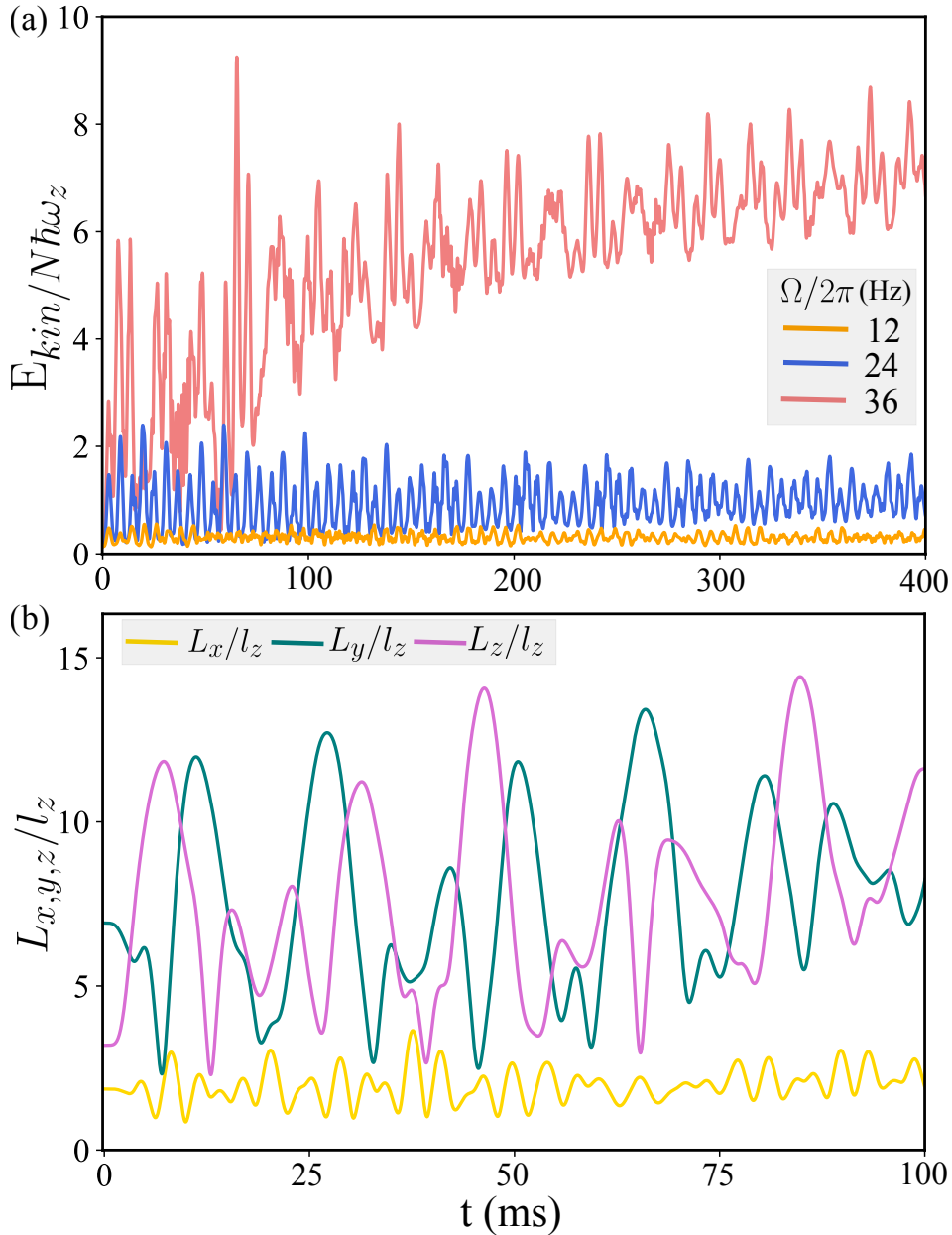


FIGURE 5.7: **Dynamics of the kinetic energy and widths.** (a) Evolution of the condensate's kinetic energy following an instantaneous quench to three different rotation frequencies: $\Omega_f/2\pi = 12$ Hz (orange), 24 Hz (blue), and 36 Hz (red). (b) Dynamics of the widths of the condensate along the x (gold), y (green), and z (magenta) direction for an instantaneous quench to $\Omega_f/2\pi = 36$ Hz. The results are demonstrated for the parameters, $N = 30000$ Dy atoms, $a_s = 160a_0$, and external trap frequencies, $(\omega_x, \omega_y, \omega_z) = 2\pi \times (150, 50, 150)$ Hz.

For smaller Ω_f values, the kinetic energy displays oscillatory behavior, indicating the excitation of collective modes [243]. At higher rotation frequencies, in addition to oscillations, E_k also exhibits a consistent linear increase over time. This growth in kinetic energy at longer times signifies condensate heating, potentially leading to instabilities [42, 335]. As the rotation frequency approaches the trap frequency along

the weakly-trapped direction ($\Omega \rightarrow \omega_y$), the kinetic energy increases more rapidly, and the condensate can become unstable at shorter timescales.

The dynamics of the condensate's widths are presented in Fig. 5.7 (b). The widths in the yz plane exhibit rapid changes with the quenching of the rotation frequency. The out-of-phase oscillation observed in these widths is indicative of the dominant quadrupolar character of the excited mode [243, 335].

Current ongoing investigations involve a more rigorous analysis of the time evolution and dynamical instabilities for linear adiabatic quenches of the rotation frequency. We aim to have a deeper understanding of the instabilities and vortex nucleation processes within this rotating dipolar Bose gas.

5.6 Effect of Trap Geometry

Now, we investigate the effect of the external trap geometry on the formation of the rotation-induced supersolids. The trap aspect ratio is defined as $\lambda = \omega_{x,z}/\omega_y$. While in the previous sections, we investigated a cylindrically trapped dBEC ($\lambda = 3$), here we alter the trap geometry from cylindrical to a spherical shape. The trap frequencies in the x and z directions, ($\omega_x = \omega_z = 2\pi \times 150$ Hz), and the no. of atoms $N = 30000$ are kept constant, consistent with previous sections. We consider a fixed strength of the repulsive scattering interaction ($a_s = 136a_0$) in this section. We study the ground state transitions in the rotating frame by solving Eq. (5.4) in imaginary time evolution.

For a cylindrical trap, the ground state at $\Omega = 0$ manifests as a cigar-shaped BEC elongated along the y (see Fig. 5.3 (a)). As λ decreases, the trap frequencies become stronger in y , which directly influences the shape of the resulting ground state. For instance, at $\lambda = 2$, the elongation along the y axis is reduced, as shown in 5.9 (a). In a completely spherical trap ($\lambda = 1$), the condensate's elongation shifts from the y -direction to the z -direction. This reorientation is a consequence of magnetostriction effects, where the condensate elongates along the polarization direction due to the dominant attractive dipolar interaction along z (see Fig. 5.9 (c)).

The trap geometry significantly alters the transition frequency (Ω) to the supersolid-vortex phase. Fig. 5.8 illustrates the transition between the superfluid-vortex and SSV phase as a function of Ω and λ . The interplay between the trap potential, dipolar interactions, and rotational effects plays a crucial role in this transition. With decreasing λ , the size of the condensate reduces and the gas becomes denser. The stronger attraction between the atoms makes the formation of multiple crystal peaks energetically more challenging. Consequently, the SFV to SSV phase transition shifts to higher rotation frequencies with decreasing λ .

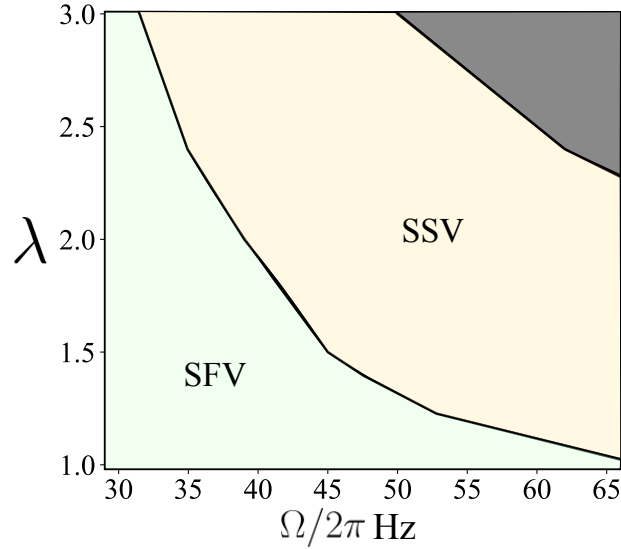


FIGURE 5.8: **Ground state phases with varying trap geometry.** Ground-state transition to supersolid with vortex lines (SSV) phase as a function of the trap aspect ratio (λ) and the rotation frequency (Ω). With decreasing λ , the transition to supersolid requires higher rotation frequencies. The results are shown for $N = 30000$ Dy atoms with $a_s = 136a_0$.

At $\lambda = 3$, the transition to the SSV phase is characterized by the formation of a state with five density peaks and a pair of vortex lines pinned between each pair of density lobes (see Fig. 5.3 (c)). Further increase in Ω leads to an increase in the number of density peaks. Below a critical $\lambda \sim 2$, the transition to the supersolid phase is marked by the appearance of three density peaks. Additionally, the number of vortex lines between each pair of crystal peaks varies with λ . For $\lambda = 2$, at the transition to the supersolid-vortex phase, there is a pair of vortices between the density peaks, and as rotation increases, both the number of crystal peaks and the vortex lines between them increase. Fig. 5.9 (d) depicts a supersolid at $\Omega = 2\pi \times 40$ Hz, exhibiting seven crystal peaks, with four vortices between the central peaks and two vortices emerging between the peaks away from the center. Similarly, at $\lambda = 1$, three density lobes manifest at the ground state for $\Omega = 2\pi \times 100$ Hz, with multiple vortex lines pinned between the crystals (see 5.9 (d)). For smaller λ values, the density lobes are cigar-shaped, resembling the typical cigar droplets observed in experiments with dipolar condensates.

The peak density of the supersolid phase increases with decreasing λ . Notably, the density of these vortex-stabilized supersolids is roughly two orders of magnitude lower compared to the typical density of the droplet supersolids, which are stabilized by the LHY interactions. The density of the supersolids observed here is comparable to the density of the BEC phase, and hence they are termed as *dilute supersolids*. This low-density supersolid regime opens new possibilities for realizing supersolidity in systems with weaker dipolar interactions, such as chromium condensates.

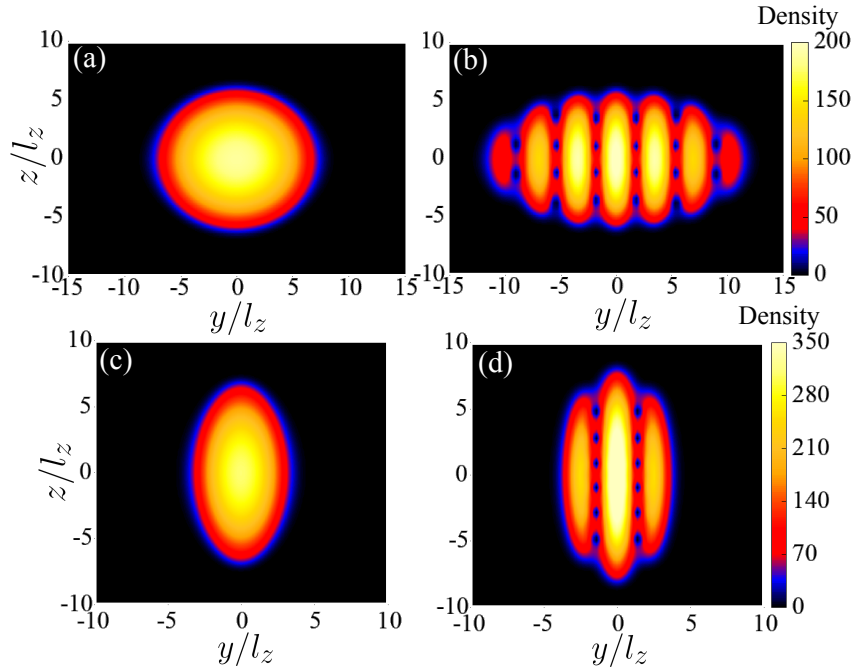


FIGURE 5.9: **Supersolids in different trap geometries.** The upper panel shows the density plots in the yz plane, $|\psi_{Rot}(x=0, y, z)|^2$ at (a) $\Omega = 0$ and (b) $\Omega/2\pi = 40$ Hz for $\lambda = 2$, i.e., external trap frequencies, $(\omega_x, \omega_y, \omega_z) = 2\pi \times (150, 75, 150)$ Hz. The bottom panel shows the density plots at (c) $\Omega = 0$ and (d) $\Omega/2\pi = 100$ Hz for $\lambda = 1$. The other parameters are the same as the Fig. 5.8.

5.7 Conclusion

In this chapter, we investigated the physics of a dipolar Bose gas under the simultaneous rotation of both the external harmonic trap and the dipole polarization direction. We considered a cigar-shaped condensate and explored rotation perpendicular to both the trap's symmetry axis and the dipole polarization direction.

The interplay between the anisotropic trap geometry, the dipolar interaction, and rotation-induced effects drives a ground state transition from a BEC to a supersolid phase as the rotation frequency is varied. Notably, this supersolid is not stabilized by quantum fluctuations, but rather by the emergence of vortex lines. This presents a distinct pathway to create supersolids in dipolar gases, in contrast to those formed by quenching the s-wave scattering length [41, 71] or varying temperature [58, 317]. We also observed the ground-state transition between different supersolid states with varying rotation frequencies. A similar transition was predicted in a doubly dipolar BEC by varying the relative angle between the dipole moments [46]. Additionally, we explored the impact of trap geometry on ground-state transitions by varying the trap's aspect ratio from a cigar to a spherical shape. The dynamical properties of this system under rotation are a subject of ongoing investigation.

Chapter 6

Conclusion

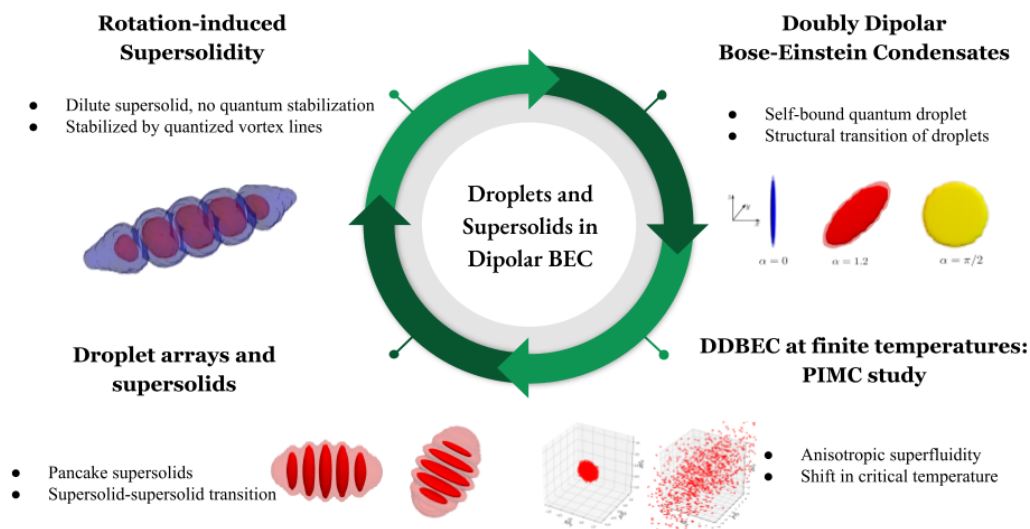


FIGURE 6.1: **Summary of the thesis.** We have primarily investigated droplets and supersolid phases in dipolar BEC. We talk about droplets in doubly dipolar BEC, finite-temperature properties of the doubly dipolar condensate, droplet arrays, and supersolids in DDBEC. Finally, we predict the emergence of a dilute supersolid phase, stabilized by vortex lines in a rotating dipolar Bose gas.

6.1 Summary

In this thesis, we have investigated rich and diverse physics of dipolar quantum gases, with a particular focus on the novel properties emerging from doubly dipolar Bose-Einstein condensates (DDBECs) and the unique formation of rotation-induced supersolids.

The primary research questions I have addressed are the following,

1. What exotic ground state phases can arise in doubly dipolar Bose gases?
2. What are the characteristics of DDBEC with varying temperatures?

3. How does a dipolar Bose gas behave under rotation?

Chapter 2 established the theoretical framework for DDBECs, detailing the Hamiltonian of a Dysprosium atom in the presence of both magnetic and electric fields [44]. The inherent permanent magnetic dipole moment, coupled with an induced electric dipole moment arising from quasi-degenerate opposite-parity states, results in a highly anisotropic doubly dipolar potential. This chapter laid out the generalized Gross-Pitaevskii equation (gGPE), incorporating Lee-Huang-Yang (LHY) corrections for quantum fluctuations, and introduced the methodologies for exploring finite-temperature properties using Path Integral Monte Carlo (PIMC) simulations via Feynman's path integral formulation and the worm algorithm.

Building upon this framework, Chapter 3 investigated the fascinating properties of quantum droplets in DDBECs. We demonstrated the emergence of unique quasi-two-dimensional pancake quantum droplets, a feature not observed in typical dipolar condensates, and illustrated a dimensional crossover from cigar-shaped to pancake droplets through both Gaussian variational methods and numerical gGPE solutions [45, 46]. Furthermore, our PIMC simulations revealed the finite-temperature behavior of these systems [252], showing consistent ground-state transitions with mean-field predictions and highlighting the highly anisotropic superfluid behavior of pancake droplets. We mapped out thermal gas to DDBEC and thermal gas to pancake droplet transitions, noting that the latter transition occurs at higher temperatures. We also demonstrated structural transitions driven by tuning the electric dipole moment strengths. This finite-temperature study paves the way for an experimental realization of a doubly dipolar condensate.

Chapter 4 extended our exploration to the formation of exotic droplet arrays and supersolids within harmonically-trapped DDBECs [46]. The intricate interplay among doubly dipolar interactions, quantum fluctuations, and external confinement was shown to induce novel supersolid-supersolid transitions and distinct pancake supersolids. This chapter also identified the unique appearance of modulated droplets as a hallmark of DDBECs.

In 5, we presented a theoretical prediction for the formation of a dilute supersolid phase in rotating dipolar Bose gases, a mechanism that notably does not rely on stabilization from quantum fluctuations. We employed a simultaneous rotation of the external harmonic trap and the magnetic field to rotate the condensates perpendicular to their dipole polarization axis. The interplay between rotation, trap geometry, and dipolar interactions leads to the spontaneous crystallization of the condensate, accompanied by the emergence of pinned vortex lines.

The summary of the thesis is presented concisely in the Fig. 6.1

6.2 Outlook

Realization of exotic two-dimensional supersolid states

This thesis has investigated the realization of an array of supersolids in Q1D trap geometries. In these trap geometries, we have realized exotic supersolid patterns, but the supersolidity is realized along one dimension. The use of a pancake-like trap geometry, and the broad potential landscape regime of the doubly dipolar interaction can lead to the emergence of exotic other forms of supersolids and density patterns, as explored in the usual dipolar condensates [204–206]. The fascinating physics of two-dimensional quantum-stabilized supersolids in doubly dipolar condensates will be the subject of future studies.

Quantum Monte Carlo study of pancake supersolids

While we have focused on the finite-temperature properties of a single pancake droplet in this thesis, by altering the trap geometry or number of atoms, or even the temperature, multiple pancake droplets can be realized. Through PIMC simulations, future investigation of superfluidity between the droplets will provide insights into novel pancake supersolids predicted in the mean-field work [46]. Exploring the finite temperature properties of pancake supersolids and the transition from a thermal gas to a pancake supersolid may also be the subject of future studies.

Multilayer doubly dipolar BECs

Recent experiments have realized a bilayer system of dipolar dysprosium atoms separated by a mere 50 nanometers [348], which has opened up the possibility to realize novel phenomena in an array of dipolar systems by harnessing the strong inter-layer dipolar interactions. Periodic driving of short-range interactions in an array of homogeneous quasi-one-dimensional (Q1D) dipolar condensates leads to the emergence of transient stripe and checkerboard patterns [349]. The additional control parameters of the relative angle (α) and strength (γ) of the two dipole moments can facilitate the emergence of more exotic pattern formation in an array of doubly dipolar BEC. Moreover, the ability to manipulate the strength of the induced electric dipole moment gives the possibility to periodically drive the long-range interactions, which can lead to novel phenomena in condensate physics. Furthermore, exotic coherent and incoherent density patterns can be engineered using the effect of inter-condensate doubly dipolar interactions, which have been predicted in only magnetic dipolar condensates [350]. The study of scattering between coupled Q1D solitons in a doubly

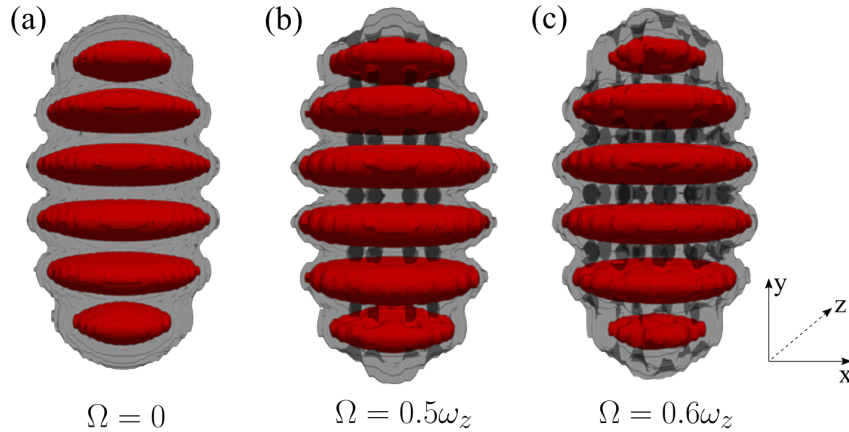


FIGURE 6.2: **Vortex lines through supersolids.** Three-dimensional iso-density plots illustrating the supersolid pancake droplet array (a) ($\Omega = 0$) and (b, c) vortex lines penetrating through the pancake droplets ($\Omega/\omega_z = 0.5, 0.6$). The results are illustrated for the scattering length, $a_s = 295a_0$, $\alpha = \pi/2$, $\gamma = 1$ with $N = 50000$ Dy atoms under an external harmonic trap, $\omega_{x,y,z} = 2\pi(150, 50, 150)$ Hz.

dipolar BEC can also lead to fascinating physics, different from that predicted in dipolar solitons [351].

Dynamics of vortex lines in a pancake supersolid

This thesis has explored the rotation of a dipolar Bose gas under the simultaneous rotation of both the magnetic field and the external harmonic trap. Investigating a doubly dipolar condensate under rotation promises to uncover fascinating new physics. For rotating a doubly dipolar gas, one could also consider implementing a rotating electric field [352], offering an additional degree of experimental control.

A particularly compelling scenario involves the rotation of an array of pancake supersolids. Fig. 6.2 shows the emergence of vortex lines penetrating through the Q2D pancake droplets. The complex dynamics of these vortex lines within a rotating supersolid present a compelling subject for future studies, potentially revealing insights into quantum turbulence in supersolids.

Appendix A

Beyond mean-field LHY corrections

The correction term ΔE to the ground state energy due to the quantum fluctuations is given by [158]:

$$\Delta E = \frac{V}{2} \int \frac{d^3 q}{(2\pi)^3} \left[\epsilon_q - \frac{\hbar^2 \mathbf{q}^2}{2M} - n \tilde{V}_{int}(\mathbf{q}) + \frac{\tilde{V}_{int}(\mathbf{q})^2}{q^2} \frac{Mn^2}{\hbar^2} \right], \quad (\text{A.1})$$

where,

$$\begin{aligned} \tilde{V}_{int}(\mathbf{q}) &= g[1 + \epsilon_{dd}(3 \cos^2 \theta - 1)] = gF_d(\epsilon_{dd}, \theta), \\ \epsilon_q &= \sqrt{\frac{\hbar^2 q^2}{2M} \left(\frac{\hbar^2 q^2}{2M} + 2gnF_d(\epsilon_{dd}, \theta) \right)}. \end{aligned}$$

$$\begin{aligned} \Delta E &= \frac{V}{2} \int \frac{d^3 q}{(2\pi)^3} \left[\sqrt{\frac{\hbar^2 q^2}{2M} \left(\frac{\hbar^2 q^2}{2M} + 2gnF_d(\epsilon_{dd}, \theta) \right)} - \frac{\hbar^2 q^2}{2M} - \right. \\ &\quad \left. ngF_d(\epsilon_{dd}, \theta) + \frac{Mn^2 g^2 F_d(\epsilon_{dd}, \theta)^2}{\hbar^2 q^2} \right]. \end{aligned} \quad (\text{A.2})$$

Carrying out the integration, we get the following:

$$\begin{aligned} \Delta E &= \frac{V}{2} \int_0^\infty \frac{q^2 dq}{(2\pi)^3} \int_0^\pi \sin \theta d\theta \int_0^{2\pi} d\phi \left[\sqrt{\frac{\hbar^2 q^2}{2M} \left(\frac{\hbar^2 q^2}{2M} + 2gnF_d(\epsilon_{dd}, \theta) \right)} \right. \\ &\quad \left. - \frac{\hbar^2 q^2}{2M} - ngF_d(\epsilon_{dd}, \theta) + \frac{Mn^2 g^2 F_d(\epsilon_{dd}, \theta)^2}{\hbar^2 q^2} \right] \\ &= \frac{V}{8\pi^2} \int_0^\pi \sin \theta d\theta \int_0^\infty q^2 dq \left[\sqrt{\frac{\hbar^2 q^2}{2M} \left(\frac{\hbar^2 q^2}{2M} + 2gnF_d(\epsilon_{dd}, \theta) \right)} \right. \\ &\quad \left. - \frac{\hbar^2 q^2}{2M} - ngF_d(\epsilon_{dd}, \theta) + \frac{Mn^2 g^2 F_d(\epsilon_{dd}, \theta)^2}{\hbar^2 q^2} \right]. \end{aligned} \quad (\text{A.3})$$

Now, we do the q integration first by doing a variable change $y = \frac{\hbar q}{\sqrt{2MngF_d(\epsilon_{dd}, \theta)}}$,

$$\begin{aligned}\Delta E &= \frac{V}{8\pi^2} \int_0^\pi \sin \theta d\theta \int_0^\infty y^2 dy \left(\frac{\sqrt{2MngF_d(\epsilon_{dd}, \theta)}}{\hbar} \right)^3 (ngF_d(\epsilon_{dd}, \theta)) (\sqrt{y^2(y^2 + 2)} - 1 - y^2 + \frac{1}{2y^2}) \\ &= \frac{V}{8\pi^2} \int_0^\pi \sin \theta d\theta (ngF_d(\epsilon_{dd}, \theta)) \left(\frac{\sqrt{2MngF_d(\epsilon_{dd}, \theta)}}{\hbar} \right)^3 \int_0^\infty y^2 dy (\sqrt{y^2(y^2 + 2)} - 1 - y^2 + \frac{1}{2y^2}) \\ &= \frac{V}{8\pi^2} \int_0^\pi \sin \theta d\theta (ngF_d(\epsilon_{dd}, \theta)) \left(\frac{\sqrt{2MngF_d(\epsilon_{dd}, \theta)}}{\hbar} \right)^3 \frac{8\sqrt{2}}{15}.\end{aligned}\quad (\text{A.4})$$

(*N.B: The last integrand gives us the value $\frac{8\sqrt{2}}{15}$. If we take the extra two factor proportional to $\frac{v^2}{q^2}$, the only change is, we get the integrand as, $\int_0^\infty y^2 dy (\sqrt{y^2(y^2 + 2)} - 1 - y^2 + \frac{1}{y^2})$, which diverges in the integration limit). Thus

$$\begin{aligned}\Delta E &= \frac{V}{8\pi^2} \int_0^\pi \sin \theta d\theta (ngF_d(\epsilon_{dd}, \theta)) \left(\frac{\sqrt{2MngF_d(\epsilon_{dd}, \theta)}}{\hbar} \right)^3 \frac{8\sqrt{2}}{15} \\ &= \frac{V}{4\pi^2} ng \left(\frac{\sqrt{2Mng}}{\hbar} \right)^3 \frac{8\sqrt{2}}{15} \int_0^\pi \frac{1}{2} \sin \theta d\theta F_d(\epsilon_{dd}, \theta)^{5/2} \\ &= \frac{8V}{15\pi^2} \frac{M^{3/2}}{\hbar^3} n^{5/2} g^{5/2} Q_5(\epsilon_{dd}) \\ &= \frac{8V}{15\pi^2} \frac{M^{3/2}}{\hbar^3} n^{5/2} \left(\frac{4\pi\hbar^2 a_s}{M} \right)^{5/2} Q_5(\epsilon_{dd}) \\ \Delta E &= V \frac{2\pi\hbar^2 a_s n^2}{M} \frac{128}{15} \sqrt{\frac{na_s^3}{\pi}} Q_5(\epsilon_{dd}).\end{aligned}\quad (\text{A.5})$$

where, $Q_5(\epsilon_{dd}) = \int_0^\pi \frac{1}{2} \sin \theta d\theta [1 + \epsilon_{dd}(3 \cos^2 \theta - 1)]^{5/2}$.

The correction in the chemical potential ($\Delta\mu$) is given by:

$$\Delta\mu = \frac{\partial \Delta E}{\partial \Delta N} = \frac{32gn}{3} \sqrt{\frac{na_s^3}{\pi}} Q_5(\epsilon_{dd}).\quad (\text{A.6})$$

Appendix B

Path Integral Monte Carlo Algorithms

B.1 Discrete Path Integrals

For a sufficiently large MT, we can achieve a highly accurate approximation of the density matrix, allowing us to express an explicit form for the low-temperature density matrix. Up to this point, the expansion remains precise, as we express ρ as the convolution of density matrices evaluated at higher temperatures. This approach is analogous to the path integral formulation of quantum mechanics, except that the time variable t is substituted with $i\beta$. Hence, β is referred to as the imaginary time, and τ denotes an imaginary time interval.

Now, consider the Hamiltonian consisting of two parts, kinetic and potential terms, $\mathcal{H} = \mathcal{T} + \mathcal{V}$. Often, the potential energy part of the Hamiltonian is diagonal w.r.t the coordinate basis, hence, it is preferable to decompose the density matrix into a product containing the kinetic \mathcal{T} and potential \mathcal{V} contributions to the Hamiltonian. The difficulty emerges here because these contributions do not commute. This issue can be addressed with the Baker-Campbell-Hausdorff (BCH) formula [353],

$$e^{\mathcal{A}+\mathcal{B}} = e^{\mathcal{A}}e^{\mathcal{B}}e^{\frac{1}{2}[\mathcal{A},\mathcal{B}]} \dots \quad (\text{B.1})$$

In our case, there is a τ coefficient with each operator, and we can write,

$$e^{-\tau(\mathcal{T}+\mathcal{V})} = e^{-\tau\mathcal{T}}e^{-\tau\mathcal{V}}e^{O(\tau^2)} \quad (\text{B.2})$$

As $\tau \rightarrow 0$, the commutator term, which is of the order of τ^2 , becomes very small and thus can be neglected. We can approximate the exact density matrix by the product of the density matrices for \mathcal{T} and \mathcal{V} :

$$e^{-\tau(\mathcal{T}+\mathcal{V})} \simeq e^{-\tau\mathcal{T}}e^{-\tau\mathcal{V}} \quad (\text{B.3})$$

This is known as the "*primitive approximation*".

Concerns may still arise due to the repetition of τ for M times, which, in the limit of $M \rightarrow \infty$, could potentially result in an error. However, the Trotter formula [354] offers a solution, as it applies to self-adjoint linear operators:

$$e^{\mathcal{A}+\mathcal{B}} = \lim_{M \rightarrow \infty} [e^{\mathcal{A}/M} e^{\mathcal{B}/M}]^M \quad (\text{B.4})$$

For our purpose, \mathcal{T} and \mathcal{V} are self-adjoint and we can write,

$$e^{-\beta(\mathcal{T}+\mathcal{V})} = \lim_{M \rightarrow \infty} [e^{-\tau\mathcal{T}} e^{-\tau\mathcal{V}}]^M \quad (\text{B.5})$$

We can write the primitive approximation in the coordinate basis as follows:

$$\rho(\mathbf{R}, \mathbf{R}'; \tau) = \int d\mathbf{R}_1 \langle \mathbf{R} | e^{-\tau\mathcal{T}} | \mathbf{R}_1 \rangle \langle \mathbf{R}_1 | e^{-\tau\mathcal{V}} | \mathbf{R}' \rangle \quad (\text{B.6})$$

and evaluate the kinetic and potential density matrices.

In coordinate representation, the potential operator is diagonal, which makes its matrix elements straightforward. However, the kinetic or free part of the Hamiltonian is not diagonal in the spatial basis. This issue can be resolved by expressing the position eigenstates in terms of free particle plane waves or momentum eigenstates.

$$\psi_{\mathbf{k}}(\mathbf{R}) = \frac{1}{(\sqrt{2\pi})^d} e^{-i\mathbf{k}\cdot\mathbf{R}} \quad (\text{B.7})$$

The free-particle matrix can be calculated explicitly from Eq. (2.24),

$$\langle \mathbf{R} | e^{-\tau\mathcal{T}} | \mathbf{R}_1 \rangle = \int d\mathbf{k} \frac{1}{(2\pi)^d} e^{-i\mathbf{k}\cdot(\mathbf{R}-\mathbf{R}_1) - \tau \frac{\hbar^2}{2m} \mathbf{k}^2} = \frac{1}{(4\pi\lambda\tau)^{d/2}} e^{-\frac{(\mathbf{R}-\mathbf{R}_1)^2}{4\lambda\tau}} \quad (\text{B.8})$$

The expression is the general expression for d spatial dimension, and we have introduced $\lambda = \hbar^2/2m$. We can write the free particle propagator for a single free particle as follows,

$$\rho_{\text{free}}(\mathbf{R}, \mathbf{R}_1; \tau) = \frac{1}{\Lambda_\tau^d} e^{-\frac{\pi(\mathbf{R}-\mathbf{R}_1)^2}{\Lambda_\tau^2}} \quad (\text{B.9})$$

where $\Lambda_\tau = \sqrt{4\pi\lambda\tau}$ is the thermal de Broglie wavelength at the temperature set by the imaginary time step τ .

B.2 Markov Chain and Metropolis Algorithm

The decomposition of the density matrix yields a generic expression for an observable O from its thermodynamic definition:

$$\langle O \rangle = \sum_{\mathcal{P}} \int \int \int d\mathbf{R}_0 d\mathbf{R}_1 \dots d\mathbf{R}_M P(\mathbf{R}_0, \mathbf{R}_1, \dots, \mathbf{R}_M) O(\mathbf{R}_0, \mathbf{R}_M; \mathcal{P}), \quad (\text{B.10})$$

where \mathcal{P} represents a possible permutation of particle indices.

A direct evaluation of such an expectation value involves computing the observable O for each possible configuration, and summing over the entire configuration space weighted by their respective statistical probabilities. A specific configuration, encompassing all bead positions and permutations, is fully described by the extended set of coordinates $C = \{\mathbf{R}_0, \mathbf{R}_1, \dots, \mathbf{R}_M\}$. One can define the normalized probability distribution of a configuration C at equilibrium,

$$\pi(C) = \frac{e^{-S(C)}}{Z}, \quad (\text{B.11})$$

with $S(C)$ being the action.

We use an approach, known as a *sampling method*. Instead of averaging over an exhaustive set of configurations, we can average over a carefully selected subset generated through iterations of this algorithm. If this subset is sufficiently large, it should accurately reproduce the system's thermodynamic properties. This fundamental concept forms the core of the Monte Carlo method.

The exploration of configuration space in stochastic simulations is governed by the formalism of Markov chains. A *Markov chain* is a discrete stochastic sequence of configurations that begins from an initial configuration, and generates subsequent configurations using a defined set of updates, each associated with a specific transition probability, $P(C \rightarrow C')$. Each transition is independent of the history of the chain, i.e., they satisfy *Markov's property*, and the normalization constant $\int dC' P(C \rightarrow C') = 1$. The central objective of constructing such a chain is to ensure convergence to an equilibrium state with the probability distribution $\pi(C)$ that follows the condition:

$$\sum_C \pi(C) P(C \rightarrow C') = \pi(C'). \quad (\text{B.12})$$

To achieve this convergence, the Markov chain performs a random walk within the configuration space. In practical implementations, the transition from one configuration to another is typically decomposed into two stages: i) First, a trial configuration \tilde{C} is constructed, based on a user-defined procedure, with a probability $T(C \rightarrow \tilde{C})$, known as the *sampling rate*. ii) The proposed configuration C' is then either accepted

as the trial configuration, $C' = \tilde{C}$, with an acceptance probability $W(C \rightarrow \tilde{C})$, or it is left unchanged, $C' = C$, with probability $1 - W(C \rightarrow \tilde{C})$. For the walker to produce a stationary distribution, two fundamental principles guide the selection of T and W :

1. **Ergodicity:** For the Markov chain to yield reliable results, it must satisfy the condition of *ergodicity*. This implies that any configuration can be reached from any other configuration within a finite number of steps. The choice of the transition probability $T(C \rightarrow C')$ is determined by the user and depends on the specifics of the model under consideration. It is therefore essential to design T such that no region of configuration space remains inaccessible due to an unsuitable selection. In complex systems, such as those treated with Path Integral Monte Carlo (PIMC), this requirement is addressed by employing a variety of update moves that generate different trial configurations \tilde{C} starting from C . To streamline the evaluation of transition probabilities, it is advisable to ensure that distinct types of moves do not yield identical trial configurations.

2. **Detailed balance:** The detailed balance condition must be fulfilled by the transition probabilities, which states that the probability of being in a configuration C times the transition probability of $C \rightarrow C'$ is equal to the probability of being in a configuration C' times the transition probability of $C' \rightarrow C$. Mathematically, this is expressed as:

$$\pi(C)P(C \rightarrow C') = \pi(C')P(C' \rightarrow C). \quad (\text{B.13})$$

This implies that each transition is reversible. Given two arbitrary configurations C and C' , there always exists a path or sequence of transitions with a combined non-zero transition probability connecting them. It ensures that the entire configuration space can be effectively sampled. Since T is user-defined and π depends on the problem, W is obtained by this condition. The Metropolis technique is a specific approach to guarantee that the transition rules adhere to detailed balance. In the generalized Metropolis procedure [355], which accommodates various sampling distributions, trial moves are accepted with the following probability:

$$W(C \rightarrow C') = \min \left[1, \frac{\pi(C')T(C' \rightarrow C)}{\pi(C)T(C \rightarrow C')} \right]. \quad (\text{B.14})$$

It is important to note that while the satisfaction of both detailed balance and ergodicity is sufficient to guarantee that the Markov chain generates a stationary distribution, it is not strictly necessary. Some walkers do not satisfy detailed balance and produce stationary distributions that correspond with the desired distribution π . A practical example is given in Bernard et al. [356].

At this point, the challenge then lies in judiciously selecting the various moves

and their corresponding $T(C \rightarrow C')$ to ensure comprehensive coverage of the distribution space while simultaneously optimizing the convergence to equilibrium values.

B.3 PIMC Algorithm

In summary, a typical Path Integral Monte Carlo (PIMC) simulation proceeds through the following steps to sample quantum mechanical systems at finite temperatures:

1. **Define update rules:** An ergodic set of updates, each with its associated proposal probability, is derived by ensuring the detailed balance condition (B.13) is satisfied. It's important to note that the ergodicity of these updates is specific to the particular system being simulated.
2. **Approximate density matrix:** An approximate form of the density matrix is computed based on the system Hamiltonian \mathcal{H} . This approximation becomes exact in the limit as the imaginary time step $\tau \rightarrow 0$.
3. **Initialization:** The simulation begins from an arbitrary initial configuration C_k with $k = 0$, which must be consistent with the system parameters defined by the Hamiltonian \mathcal{H} .
4. **Proposal of new configuration:** A new trial configuration C' is generated with a random update from the set constructed in (1). Subsequently, the acceptance probability $W(C \rightarrow C')$ given by (B.14) is evaluated.
5. **Acceptance criteria:** If the acceptance probability $W(C \rightarrow C')$ is larger than a random number $a \in [0, 1)$, the new configuration is added to the chain, i.e., $C_{k+1} = C'$, else the initial configuration is added to the chain, $C_{k+1} = C_k$.
6. **Evaluate observables:** The thermodynamic averages of the desired observables $\{O_i\}$ defined in Eq. (B.10), are evaluated for the newly added member of the Markov chain C_{k+1} .
7. **Iteration:** Set k to $k + 1$.

Steps 3 through 7 are iteratively repeated until a sufficient number of Markov chain entries have been collected to ensure statistical convergence. In the case of a rejection, the old configuration must still be counted as a member of the chain. Failing to include rejected configurations would lead to incorrect simulation results. Furthermore, moves displacing only a single bead are inefficient for exploring the configuration space in PIMC; therefore, multi-slice (or multi-bead) sampling methods are often necessary to achieve adequate convergence.

B.4 Monte Carlo and worm algorithm moves

1. **Rigid translation of world line:** Rigid translation is a crucial update in PIMC simulations, ensuring the system can fully explore its spatial configurations (ergodicity). It works by randomly picking a particle and displacing its entire worldline by a random vector, $\Delta\mathbf{r}$. For free particles, this shift doesn't alter bead-to-bead distances, so relevant density matrix terms cancel out.

The choice of $\Delta\mathbf{r}$'s distribution depends on the context; a uniform distribution within a cube is common. More complex moves, like combining local displacements with lattice jumps for bosons in a square lattice, can also be used.

2. **Displacement of beads in a worldline:** Efficiently sampling Boltzmann worldlines is crucial for accurate simulations. Displacing single beads via a uniform distribution is inefficient due to harmonic bead links.

A more effective approach accounts for these links by drawing new bead positions from a Gaussian distribution. To further boost efficiency by moving multiple beads at once, the Levy bridge procedure is used. This approach replaces a chosen segment of the worldline between two points with newly generated beads, sampled from an appropriate combination of normal distributions. Such an update greatly enhances the convergence of the simulation. For the case of free particles, several equivalent techniques are available and can be implemented with high efficiency. See Ref. [296] for more details.

For any number of beads m , the bridge is constructed with probability

$$p_{\text{bridge}}(\mathbf{r}_1, \dots, \mathbf{r}_{m-1}) = \frac{1}{\rho_{\text{free}}(\mathbf{r}_0, \mathbf{r}_m, m\tau)} \prod_{j=0}^{m-1} \rho_{\text{free}}(\mathbf{r}_j, \mathbf{r}_{j+1}, m\tau). \quad (\text{B.15})$$

3. **Diffusion of an open worldline:** Within the worm algorithm, it is often necessary to extend an open worldline by adding new beads. The most efficient method for this process involves sampling the position of each new bead from a Gaussian distribution centered on the head or tail of the existing worldline. In the case of free particles, subsequent positions can be generated directly from the free-particle density matrix Eq. (B.9). The probability of generating m new bead positions starting from an existing bead is, \mathbf{r}_0 is

$$p_{\text{diffusion}}(\mathbf{r}_1, \dots, \mathbf{r}_m) = \prod_{j=0}^{m-1} \rho_{\text{free}}(\mathbf{r}_j, \mathbf{r}_{j+1}, m\tau). \quad (\text{B.16})$$

Similarly, one can initially advance the particle's position through m slices with a probability $\rho_{\text{free}}(\mathbf{r}_0, \mathbf{r}_m, m\tau)$, and subsequently establish the link between \mathbf{r}_0 and \mathbf{r}_m using (B.15), thus producing an identical probability for a particular bead configuration formation:

$$p_{\text{diffusion}}(\mathbf{r}_1, \dots, \mathbf{r}_m) = \rho_{\text{free}}(\mathbf{r}_0, \mathbf{r}_m, m\tau) p_{\text{bridge}}(\mathbf{r}_1, \dots, \mathbf{r}_{m-1}) = \prod_{j=0}^{m-1} \rho_{\text{free}}(\mathbf{r}_j, \mathbf{r}_{j+1}, \tau). \quad (\text{B.17})$$

- *Rigid Move*: The rigid displacement move in PIMC simulations is vital for achieving ergodicity by translating an entire particle worldline. The rigid move is selected with a predefined probability, p_{rig} . Once chosen, the following steps are executed:

- A particle is randomly selected from the N particles in the system (with a probability of $1/N$). A crucial check is performed to ensure the selected particle constitutes a single, closed worldline; if not, the move is aborted.
- A random displacement vector, $\Delta\mathbf{r}$ is chosen, typically uniformly from a distribution in d dimensions so that $\Delta\mathbf{r}_i \in [-\Delta r_{\text{max}}, \Delta r_{\text{max}}]$. The probability of selecting a specific $\Delta\mathbf{r}$ is $1/(2\Delta r_{\text{max}})^d$.

The sampling rate for this move is $T(C \rightarrow C') = \frac{P_{\text{rig}}}{N(2\Delta r_{\text{max}})^d}$. Since relative bead positions don't change, free-particle density terms cancel. The acceptance probability depends only on the change in potential energy:

$$W(C \rightarrow C') = \frac{\prod_j \rho_{\text{pot}}(\mathbf{r}_j + \Delta\mathbf{r}, \mathbf{r}_{j+1} + \Delta\mathbf{r})}{\prod_j \rho_{\text{pot}}(\mathbf{r}_j, \mathbf{r}_{j+1})}. \quad (\text{B.18})$$

To maximize efficiency, the value of Δr_{max} is dynamically updated based on the acceptance rate; when it is too low, the range of the displacement is decreased, while the range is increased if the acceptance rate becomes close to 1.

- *Wiggle Move*:

This move takes each bead of a chain and displaces it at random. It improves efficiency by drawing bead displacements from a normal distribution based on the free-particle density matrix.

- Select the *wiggle* update with probability p_{wig} .
- Randomly choose a particle with probability $1/N$.
- Randomly select m beads to displace from 1 to \bar{m} (probability $1/\bar{m}$), where \bar{m} is an optimized parameter.

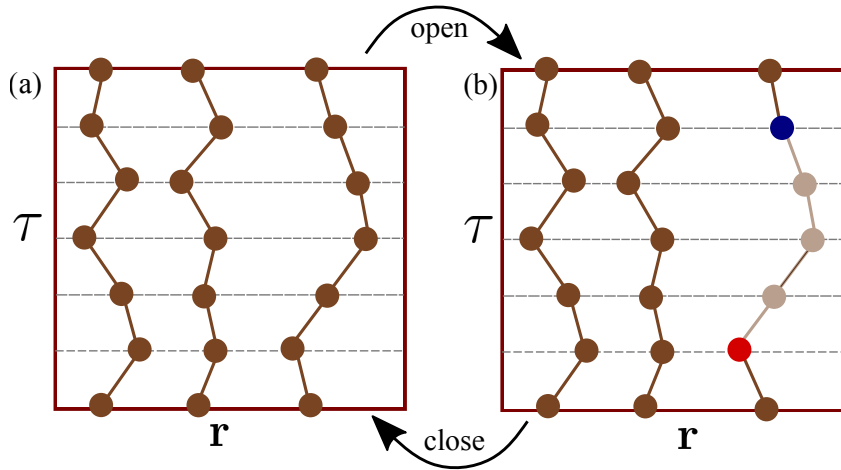


FIGURE B.1: **Open-Close move.** Schematic of the open and close updates. A segment of the path is removed for the *open* move, and an open world line is closed through a *close* move.

- Choose a starting bead i with probability $1/M$, and reject the move if $i + m > M$
- Remove the beads between \mathbf{r}_i and \mathbf{r}_{i+m} and reconstruct the segment using a Levy bridge (B.15).

The sampling rate for proposing a transition is given by

$$T(C \rightarrow C') = \frac{P_{wig}}{\bar{m}NM\rho_{free}(\mathbf{r}_0, \mathbf{r}_m, m\tau)} \prod_{j=0}^{m-1} \rho_{free}(\mathbf{r}'_j, \mathbf{r}'_{j+1}, m\tau), \quad (\text{B.19})$$

where new positions are indicated with \mathbf{r}' . The change in π is due to both the ρ_{free} and ρ_{pot} terms.

The inverse move involves taking the same endpoints $\mathbf{r}_0, \mathbf{r}_m$ and reconstructing the original bridge. The sampling rate for this inverse move is identical to (B.19), simply replacing \mathbf{r}' with \mathbf{r} . This simplification yields the acceptance rate as solely dependent on the ratio of potential energy terms:

$$W(C \rightarrow C') = \frac{\prod_{j=i}^{i+m-1} \rho_{pot}(\mathbf{r}'_j, \mathbf{r}'_{j+1})}{\prod_{j=i}^{i+m-1} \rho_{pot}(\mathbf{r}_j, \mathbf{r}_{j+1})}. \quad (\text{B.20})$$

Now, we focus on the details procedure of the moves arising due to the 'worm' algorithm.

- *Open and Close:*

These pair of moves are complementary, an *open* update moves the ensemble from diagonal to off-diagonal, and can only be attempted when there are no

worms present, and vice versa. Together, the updates respect the detailed-balance condition. An illustration of these moves can be seen in Fig. B.1.

When calculating acceptance rates, both moves must be considered synergistically, as the inverse sampling rate of an *open* move corresponds to the sampling rate of a *close* move, and vice versa. Since these operations alter the number of beads in a worldline, the associated weight term $e^{-\tau\mu}$ must be incorporated into the density matrix.

- The *open* move is chosen with a probability p_{op} .
- A particle is randomly selected from the N particles with a probability of $1/N$. This move can only be attempted when no worms are currently present in the ensemble.
- A segment of m beads is removed from the worldline. The number m is chosen randomly from the interval $[1, \bar{m}]$ with a specific probability of $1/\bar{m}$. Beads between \mathbf{r}_{M-m} and \mathbf{r}_M are removed.
- If the move is accepted, the system configuration changes from N particles to $N - 1$ physical particles plus one worm.

The sampling rate for the open move is given by,

$$T_{op}(C' \rightarrow C) = \frac{p_{op}}{N\bar{m}}. \quad (\text{B.21})$$

The close move, shown in Fig. B.1 (b), provides a detailed balance complement to open and moves the ensemble from off-diagonal back to diagonal.

- The *close* move operates on the sole open worldline, which is missing beads between, for instance, $M - m$ and M .
- A new segment of beads is constructed to form a bridge between \mathbf{r}_{M-m} and \mathbf{r}_m , a probability determined by Eq. (B.15).

The sampling rate for the close move,

$$T_{cl}(C \rightarrow C') = \frac{p_{cl}}{\rho_{free}(\mathbf{r}_{M-m}, \mathbf{r}_m, m\tau)} \prod_{j=M-m}^m \rho_{free}(\mathbf{r}'_j, \mathbf{r}'_{j+1}, \tau). \quad (\text{B.22})$$

The acceptance rate of the open move is

$$W_{op}(C \rightarrow C') = \frac{C p_{cl} N \bar{m} e^{-\tau\mu(m-1)}}{p_{op} \rho_{free}(\mathbf{r}_{M-m}, \mathbf{r}_m, m\tau)} \prod_{j=M-m}^{M-1} \rho_{pot}(\mathbf{r}_j, \mathbf{r}_{j+1}, \tau), \quad (\text{B.23})$$

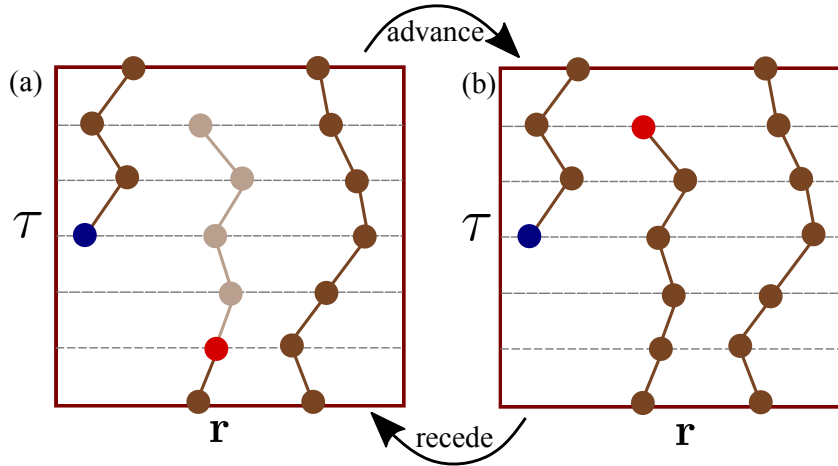


FIGURE B.2: **Advance-recede move.** Schematic of the advance and recede updates. An open world line is extended through an *advance* move by adding a new segment, and a *recede* move is performed by removing the segment.

whereas the acceptance rate of the close move is

$$W_{cl}(C \rightarrow C') = \frac{C p_{op} \rho_{\text{free}}(\mathbf{r}_{M-m}, \mathbf{r}_m, m\tau) e^{\tau\mu(m-1)}}{p_{cl} N \bar{m} \prod_{j=M-m}^{M-1} \rho_{\text{pot}}(\mathbf{r}'_j, \mathbf{r}'_{j+1}, \tau)}. \quad (\text{B.24})$$

The optimization constant C plays a crucial role. Larger values of C increase the probability of *open* moves and decrease that of *close* moves, leading to more simulation time spent sampling off-diagonal (G-sector) configurations. However, care must be taken to ensure C is not excessively small, as this can suppress particle permutations, requiring significantly longer simulation times to achieve proper sampling.

- *Advance and Recede:*

The advance and recede updates do not change the nature of the ensemble and operate only in the off-diagonal case in the presence of a worm. These moves alter the length of the worm by either adding or removing m beads from the *Ira* of the worm. Fig. B.2 illustrates these moves.

- The *advance* move is chosen with probability p_{adv}
- A number of m beads typically chosen in the interval $[1, \bar{m}]$ with probability $1/\bar{m}$ are added. The move is rejected if adding these beads would exceed the total number of time slices, i.e., $m + \mathcal{I} > M$; here \mathcal{I} is the time slice of the worm's head.

- A new segment of beads is constructed starting from the worm's head. The probability of generating this specific sequence of beads is given by the product of free-particle density matrix terms (B.16).

The sampling rate is

$$T_{\text{adv}}(C' \rightarrow C) = \frac{p_{\text{adv}}}{\bar{m}} \prod_{j=\mathcal{I}}^{\mathcal{I}+m-1} \rho_{\text{free}}(\mathbf{r}'_j, \mathbf{r}'_{j+1}, \tau). \quad (\text{B.25})$$

- The *recede* move is chosen with probability p_{rec} .
- m number of beads are selected for removal, chosen from the interval $[1, \bar{m}]$ with probability $1/\bar{m}$.
- Beads are removed from time slice \mathcal{I} to time slice $\mathcal{I} - m$. if $\mathcal{I} - m < 0$, the move is rejected.

The sampling rate for the *recede* move is

$$T_{\text{rec}}(C' \rightarrow C) = \frac{p_{\text{rec}}}{\bar{m}}. \quad (\text{B.26})$$

The acceptance rate of the *recede* move is given by:

$$W_{\text{rec}}(C \rightarrow C') = \frac{p_{\text{adv}} e^{-\tau\mu(m-1)}}{p_{\text{rec}} \prod_{j=\mathcal{I}}^{\mathcal{I}+M-1} \rho_{\text{pot}}(\mathbf{r}_j, \mathbf{r}_{j+1}, \tau)}. \quad (\text{B.27})$$

Conversely, the acceptance rate for the *advance* move reads:

$$W_{\text{adv}}(C \rightarrow C') = \frac{p_{\text{adv}} e^{\tau\mu(m-1)}}{p_{\text{rec}}} \prod_{j=\mathcal{I}}^{\mathcal{I}+M-1} \rho_{\text{pot}}(\mathbf{r}'_j, \mathbf{r}'_{j+1}, \tau). \quad (\text{B.28})$$

- *Swap Move*:

The *swap* update, illustrated in Figure B.3, is a crucial mechanism in the worm algorithm that significantly enhances its sampling efficiency. This move enables two worldlines to connect, thereby forming permutation cycles, which are essential for accurately simulating quantum statistics.

- The *swap* move with probability p_{swap} .
- \bar{m} no. of slices are randomly selected with probability $1/\bar{m}$. If the sum of the head's time slice exceeds the total number of slices, i.e., $\mathcal{I} + m > M$, the move is rejected.

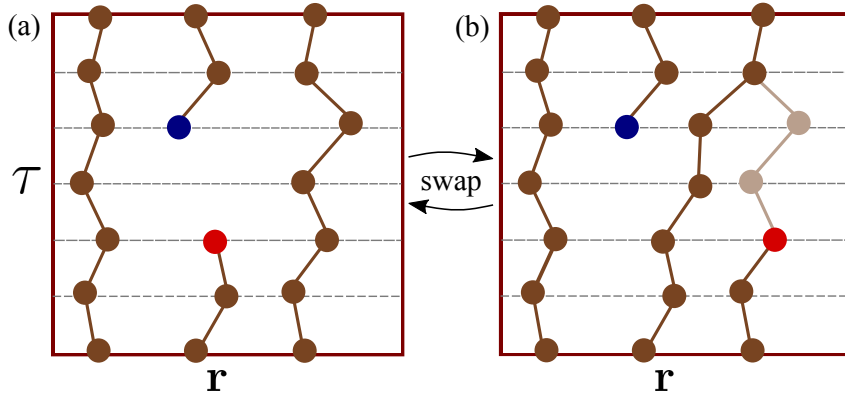


FIGURE B.3: **Swap move.** Schematic for the swap update. A part of a closed world line is taken out and substituted with a new segment joining the two world lines, and the reverse operation is also conducted.

- For all worldlines except the currently open one, w , a probability is assigned to each worldline i :

$$p_i = \rho_{\text{free}}(\mathbf{r}_h^w, \mathbf{r}_{h+m}^i, m\tau) / \sum_i p_i, \quad (\text{B.29})$$

$\sum_i p_i$ serves as a normalization constant. Now, a particle v with probability p_v is selected.

- All beads between \mathbf{r}_I^v and \mathbf{r}_{I+m}^v are removed.
- A new bridge of beads is constructed between \mathbf{r}_I^w and \mathbf{r}_{I+m}^w according to the Levy bridge (B.15).
- A beads on the open worldline \mathbf{r}_j^w , for $j > I + m$ are reassigned to v , and vice-versa. After this operation, now v becomes the new open world line.

The sampling distribution for a *swap* move is given by,

$$T(C \rightarrow C') = \frac{p_{\text{swap}} p_v}{\bar{m} \rho_{\text{free}}(\mathbf{r}_I^w, \mathbf{r}_{I+m}^i, m\tau)} \prod_{j=0}^{m-1} \rho_{\text{free}}(\mathbf{r}'_j, \mathbf{r}'_{j+1}, \tau). \quad (\text{B.30})$$

The inverse move is also a *swap* move. To perform it, a new set of probabilities p'_i must be generated, and the segment between $\mathbf{r}_I^w, \mathbf{r}_{I+m}^v$ is removed.

$$p'_i = \rho_{\text{free}}(\mathbf{r}_I^v, \mathbf{r}_{I+m}^i, m\tau) / \sum_i p'_i. \quad (\text{B.31})$$

where i runs over all particles except v .

The acceptance rate is obtained as follows,

$$W(C \rightarrow C') = \frac{\sum \prod_{j=I}^{I+M-1} \rho_{\text{pot}}(\mathbf{r}'_j, \mathbf{r}'_{j+1}, \tau)}{\sum' \rho_{\text{pot}}(\mathbf{r}^v_j, \mathbf{r}^v_{j+1}, \tau)}. \quad (\text{B.32})$$

Appendix C

Hamiltonian in the rotating frame

C.1 Unitary Operator for Rotation

The unitary operator for rotation about the x axis is defined as:

$$\hat{U}(\Omega t) = \exp\left(-\frac{i\Omega t L_x}{\hbar}\right), \quad (\text{C.1})$$

where L_x is the x -component of the angular momentum operator.

Applying this transformation establishes the following relationship between the laboratory frame and the rotating frame:

$$\psi_{Rot}(\mathbf{r}, t) = \hat{U}^\dagger(\Omega t)\psi(\mathbf{r}, t). \quad (\text{C.2})$$

Therefore,

$$\psi(\mathbf{r}, t) = \hat{U}(\Omega t)\psi_{Rot}(\mathbf{r}, t). \quad (\text{C.3})$$

We replace the $\psi(\mathbf{r}, t)$ in the GPE

$$i\hbar \frac{\partial}{\partial t} \psi(\mathbf{r}, t) = \mathcal{H}(\mathbf{r}, t)\psi(\mathbf{r}, t), \quad (\text{C.4})$$

$$\begin{aligned} i\hbar \frac{\partial}{\partial t} (\hat{U}(\Omega t)\psi_{Rot}(\mathbf{r}, t)) &= \mathcal{H}(\mathbf{r}, t)(\hat{U}(\Omega t)\psi_{Rot}(\mathbf{r}, t)), \\ i\hbar \frac{\partial \hat{U}(\Omega t)}{\partial t} \psi_{Rot} + i\hbar \hat{U}(\Omega t) \frac{\partial \psi_{Rot}(\mathbf{r}, t)}{\partial t} &= \mathcal{H}(\mathbf{r}, t)(\hat{U}(\Omega t)\psi_{Rot}(\mathbf{r}, t)), \\ \Omega L_x \hat{U}(\Omega t)\psi_{Rot}(\mathbf{r}, t) + i\hbar \hat{U}(\Omega t) \frac{\partial \psi_{Rot}(\mathbf{r}, t)}{\partial t} &= \mathcal{H}(\mathbf{r}, t)(\hat{U}(\Omega t)\psi_{Rot}(\mathbf{r}, t)), \\ i\hbar \hat{U}^\dagger(\Omega t) \hat{U}(\Omega t) \frac{\partial \psi_{Rot}(\mathbf{r}, t)}{\partial t} &= [\hat{U}^\dagger(\Omega t)\mathcal{H}(\mathbf{r}, t)\hat{U}(\Omega t) - \Omega L_x] \psi_{Rot}(\mathbf{r}, t), \\ i\hbar \frac{\partial}{\partial t} \psi_{Rot}(\mathbf{r}, t) &= [\hat{U}^\dagger(\Omega t)\mathcal{H}(\mathbf{r}, t)\hat{U}(\Omega t) - \Omega L_x] \psi_{Rot}(\mathbf{r}, t). \end{aligned} \quad (\text{C.5})$$

C.2 Harmonic trap in the rotating frame

First, we compute the term,

$$\hat{U}^\dagger(\Omega t)(y \cos(\Omega t) + z \sin(\Omega t))\hat{U}(\Omega t) = \hat{U}^\dagger(\Omega t)y\hat{U}(\Omega t) \cos(\Omega t) + \hat{U}^\dagger(\Omega t)z\hat{U}(\Omega t) \sin(\Omega t).$$

We use the following Baker-Campbell-Hausdroff (BCH) identity to evaluate the terms,

$$e^A B e^{-A} = B + [A, B] + \frac{1}{2!}[A, [A, B]] + \frac{1}{3!}[[A, [A, [A, B]]] + \dots \quad (\text{C.6})$$

Implementing the BCH identity we evaluate

$$\begin{aligned} \hat{U}^\dagger(\Omega t)y\hat{U}(\Omega t) &= e^{\frac{i\Omega t L_x}{\hbar}} y e^{-\frac{i\Omega t L_x}{\hbar}} \\ &= y + \left[\frac{i\Omega t L_x}{\hbar}, y \right] + \frac{1}{2!} \left[\frac{i\Omega t L_x}{\hbar}, \left[\frac{i\Omega t L_x}{\hbar}, y \right] \right] + \dots \\ &= y + \frac{i\Omega t}{\hbar} [L_x, y] + \frac{(i\Omega t)^2}{2! \hbar^2} [L_x, [L_x, y]] + \dots \\ &= y + \frac{i\Omega t}{\hbar} (i\hbar z) + \frac{(i\Omega t)^2}{2! \hbar^2} [L_x, i\hbar z] + \dots \\ &= y - \Omega t z - \frac{1}{2!} (\Omega t)^2 y + \frac{1}{3!} (\Omega t)^3 z + \dots \\ &= y \left(1 - \frac{1}{2!} (\Omega t)^2 + \dots \right) - z \left(\Omega t - \frac{1}{3!} (\Omega t)^3 + \dots \right). \end{aligned}$$

Collecting the terms of the series, we obtain,

$$\hat{U}^\dagger(\Omega t)y\hat{U}(\Omega t) = y \cos(\Omega t) - z \sin(\Omega t). \quad (\text{C.7})$$

Similarly, we get

$$\hat{U}^\dagger(\Omega t)z\hat{U}(\Omega t) = y \sin(\Omega t) + z \cos(\Omega t). \quad (\text{C.8})$$

Using the above expressions ((C.7), (C.8)) we obtain,

$$\begin{aligned} \hat{U}^\dagger(\Omega t)y(t)\hat{U}(\Omega t) &= \hat{U}^\dagger(\Omega t)(y \cos(\Omega t) + z \sin(\Omega t))\hat{U}(\Omega t) \\ &= \hat{U}^\dagger(\Omega t)y\hat{U}(\Omega t) \cos(\Omega t) + \hat{U}^\dagger(\Omega t)z\hat{U}(\Omega t) \sin(\Omega t) \\ &= (y \cos(\Omega t) - z \sin(\Omega t)) \cos(\Omega t) + (z \cos(\Omega t) + y \sin(\Omega t)) \sin(\Omega t) \\ &= y(\cos^2(\Omega t) + \sin^2(\Omega t)) = y. \end{aligned} \quad (\text{C.9})$$

Following a similar procedure, we get,

$$\hat{U}^\dagger(\Omega t)z(t)\hat{U}(\Omega t) = \hat{U}^\dagger(\Omega t)(z \cos(\Omega t) - y \sin(\Omega t))\hat{U}(\Omega t) = z. \quad (\text{C.10})$$

Thus, we obtain the external harmonic trap potential as,

$$V_{Rot}^T(\mathbf{r}) = \frac{M}{2}(\omega_x^2 x^2 + \omega_y^2 y^2 + \omega_z^2 z^2). \quad (\text{C.11})$$

which is static in the rotating frame.

Similarly, the dipolar interaction term in the rotating frame can be obtained. The dipole polarization direction is given by, $\hat{U}^\dagger(\Omega t)\hat{e}(t)\hat{U}(\Omega t) = z$. The magnetic field is always aligned with the z axis of the rotating frame, $\mathbf{B} = \mathcal{B}\hat{z}$, and dipoles are polarized in the same direction.

Bibliography

- ¹I. Bloch, J. Dalibard, and W. Zwerger, “Many-body physics with ultracold gases”, *Rev. Mod. Phys.* **80**, 885–964 (2008).
- ²R. Blatt and C. F. Roos, “Quantum simulations with trapped ions”, *Nature Physics* **8**, 277–284 (2012).
- ³S. A. Wilkinson and M. J. Hartmann, “Superconducting quantum many-body circuits for quantum simulation and computing”, *Applied Physics Letters* **116**, 230501 (2020).
- ⁴J. S. Douglas, H. Habibian, C.-L. Hung, A. V. Gorshkov, H. J. Kimble, and D. E. Chang, “Quantum many-body models with cold atoms coupled to photonic crystals”, *Nature Photonics* **9**, 326–331 (2015).
- ⁵I. Bloch, J. Dalibard, and S. Nascimbène, “Quantum simulations with ultracold quantum gases”, *Nature Physics* **8**, 267–276 (2012).
- ⁶D. Bluvstein, S. J. Evered, A. A. Geim, S. H. Li, H. Zhou, T. Manovitz, S. Ebadi, M. Cain, M. Kalinowski, D. Hangleiter, J. P. Bonilla Ataides, N. Maskara, I. Cong, X. Gao, P. Sales Rodriguez, T. Karolyshyn, G. Semeghini, M. J. Gullans, M. Greiner, V. Vuletić, and M. D. Lukin, “Logical quantum processor based on reconfigurable atom arrays”, *Nature* **626**, 58–65 (2024).
- ⁷M. H. Anderson, J. R. Ensher, M. R. Matthews, C. E. Wieman, and E. A. Cornell, “Observation of bose-einstein condensation in a dilute atomic vapor”, *science* **269**, 198–201 (1995).
- ⁸K. B. Davis, M. O. Mewes, M. R. Andrews, N. J. van Druten, D. S. Durfee, D. M. Kurn, and W. Ketterle, “Bose-einstein condensation in a gas of sodium atoms”, *Phys. Rev. Lett.* **75**, 3969–3973 (1995).
- ⁹C. C. Bradley, C. A. Sackett, and R. G. Hulet, “Bose-einstein condensation of lithium: observation of limited condensate number”, *Phys. Rev. Lett.* **78**, 985–989 (1997).
- ¹⁰B. DeMarco and D. S. Jin, “Onset of fermi degeneracy in a trapped atomic gas”, *science* **285**, 1703–1706 (1999).

- ¹¹F. Schreck, L. Khaykovich, K. L. Corwin, G. Ferrari, T. Bourdel, J. Cubizolles, and C. Salomon, “Quasipure bose-einstein condensate immersed in a fermi sea”, *Phys. Rev. Lett.* **87**, 080403 (2001).
- ¹²A. G. Truscott, K. E. Strecker, W. I. McAlexander, G. B. Partridge, and R. G. Hulet, “Observation of fermi pressure in a gas of trapped atoms”, *Science* **291**, 2570–2572 (2001).
- ¹³L. Chomaz, I. Ferrier-Barbut, F. Ferlaino, B. Laburthe-Tolra, B. L. Lev, and T. Pfau, “Dipolar physics: a review of experiments with magnetic quantum gases”, *Reports on Progress in Physics* **86**, 026401 (2022).
- ¹⁴D. M. Stamper-Kurn and M. Ueda, “Spinor bose gases: symmetries, magnetism, and quantum dynamics”, *Reviews of Modern Physics* **85**, 1191–1244 (2013).
- ¹⁵A. Browaeys and T. Lahaye, “Many-body physics with individually controlled rydberg atoms”, *Nature Physics* **16**, 132–142 (2020).
- ¹⁶I. Bloch, “Ultracold quantum gases in optical lattices”, *Nature physics* **1**, 23–30 (2005).
- ¹⁷A. Tononi and L. Salasnich, “Low-dimensional quantum gases in curved geometries”, *Nature Reviews Physics* **5**, 398–406 (2023).
- ¹⁸L. Benini, “Cold and ultracold molecules”, *Nature Physics* **20**, 701–701 (2024).
- ¹⁹C. Chin, R. Grimm, P. Julienne, and E. Tiesinga, “Feshbach resonances in ultracold gases”, *Rev. Mod. Phys.* **82**, 1225–1286 (2010).
- ²⁰W. S. Bakr, J. I. Gillen, A. Peng, S. Fölling, and M. Greiner, “A quantum gas microscope for detecting single atoms in a hubbard-regime optical lattice”, *Nature* **462**, 74–77 (2009).
- ²¹C. Gross and W. S. Bakr, “Quantum gas microscopy for single atom and spin detection”, *Nature Physics* **17**, 1316–1323 (2021).
- ²²A. D. Cronin, J. Schmiedmayer, and D. E. Pritchard, “Optics and interferometry with atoms and molecules”, *Rev. Mod. Phys.* **81**, 1051–1129 (2009).
- ²³X. Zhang and J. Ye, “Precision measurement and frequency metrology with ultracold atoms”, *National Science Review* **3**, 189–200 (2016).
- ²⁴G. Barontini, V. Naniyil, J. P. Stinton, D. G. Reid, J. M. F. Gunn, H. M. Price, A. B. Deb, D. Caprioli, and V. Guarrera, “Observation of fermi acceleration with cold atoms”, *Phys. Rev. Lett.* **135**, 025201 (2025).
- ²⁵L. Pitaevskii and S. Stringari, *Bose-einstein condensation and superfluidity*, Vol. 164 (Oxford University Press, 2016).

- ²⁶C. J. Pethick and H. Smith, *Bose–einstein condensation in dilute gases* (Cambridge university press, 2008).
- ²⁷O. Thomas, C. Lippe, T. Eichert, and H. Ott, “Experimental realization of a rydberg optical feshbach resonance in a quantum many-body system”, *Nature communications* **9**, 2238 (2018).
- ²⁸M. Lewenstein, A. Sanpera, and V. Ahufinger, *Ultracold atoms in optical lattices: simulating quantum many-body systems* (OUP Oxford, 2012).
- ²⁹R. Grimm, M. Weidemüller, and Y. B. Ovchinnikov, “Optical dipole traps for neutral atoms”, in , Vol. 42, edited by B. Bederson and H. Walther, *Advances In Atomic, Molecular, and Optical Physics* (Academic Press, 2000), pp. 95–170.
- ³⁰G. Grynberg and C. Robilliard, “Cold atoms in dissipative optical lattices”, *Physics Reports* **355**, 335–451 (2001).
- ³¹J. Dalibard, F. Gerbier, and P. Öhberg, “Colloquium: artificial gauge potentials for neutral atoms”, *Rev. Mod. Phys.* **83**, 1523–1543 (2011).
- ³²M. Aidelsburger, “Artificial gauge fields and topology with ultracold atoms in optical lattices”, *Journal of Physics B: Atomic, Molecular and Optical Physics* **51**, 193001 (2018).
- ³³A. M. Rey, “Synthetic gauge fields for ultracold atoms”, *National Science Review* **3**, 166–167 (2015).
- ³⁴N. Defenu, T. Donner, T. Macrì, G. Pagano, S. Ruffo, and A. Trombettoni, “Long-range interacting quantum systems”, *Rev. Mod. Phys.* **95**, 035002 (2023).
- ³⁵K. Góral, and T. Pfau, “Bose-einstein condensation with magnetic dipole-dipole forces”, *Phys. Rev. A* **61**, 051601 (2000).
- ³⁶T Lahaye, C Menotti, L Santos, M Lewenstein, and T Pfau, “The physics of dipolar bosonic quantum gases”, *Rep. Prog. Phys.* **72**, 126401 (2009).
- ³⁷M. A. Baranov, M. Dalmonte, G. Pupillo, and P. Zoller, “Condensed matter theory of dipolar quantum gases”, *Chemical Reviews* **112**, PMID: 22877362, 5012–5061 (2012).
- ³⁸L. Chomaz, R. M. van Bijnen, D. Petter, G. Faraoni, S. Baier, J. H. Becher, M. J. Mark, F. Waechtler, L. Santos, and F. Ferlaino, “Observation of roton mode population in a dipolar quantum gas”, *Nature physics* **14**, 442–446 (2018).
- ³⁹G. Bismut, B. Laburthe-Tolra, E. Maréchal, P. Pedri, O. Gorceix, and L. Vernac, “Anisotropic excitation spectrum of a dipolar quantum bose gas”, *Phys. Rev. Lett.* **109**, 155302 (2012).

- ⁴⁰M. Schmitt, M. Wenzel, F. Böttcher, I. Ferrier-Barbut, and T. Pfau, “Self-bound droplets of a dilute magnetic quantum liquid”, *Nature* **539**, 259 (2016).
- ⁴¹F. Böttcher, J.-N. Schmidt, M. Wenzel, J. Hertkorn, M. Guo, T. Langen, and T. Pfau, “Transient supersolid properties in an array of dipolar quantum droplets”, *Phys. Rev. X* **9**, 011051 (2019).
- ⁴²Y. Tang, W. Kao, K.-Y. Li, and B. L. Lev, “Tuning the dipole-dipole interaction in a quantum gas with a rotating magnetic field”, *Phys. Rev. Lett.* **120**, 230401 (2018).
- ⁴³S. Moses, J. Covey, M. Miecnikowski, D. Jin, and J. Ye, “New frontiers for quantum gases of polar molecules”, *Nature Physics* **13**, 13–20 (2017).
- ⁴⁴M. Lepers, H. Li, J.-F. m. c. Wyart, G. Quémener, and O. Dulieu, “Ultracold rare-earth magnetic atoms with an electric dipole moment”, *Phys. Rev. Lett.* **121**, 063201 (2018).
- ⁴⁵C. Mishra, L. Santos, and R. Nath, “Self-bound doubly dipolar bose-einstein condensates”, *Phys. Rev. Lett.* **124**, 073402 (2020).
- ⁴⁶R. Ghosh, C. Mishra, L. Santos, and R. Nath, “Droplet arrays in doubly dipolar bose-einstein condensates”, *Phys. Rev. A* **106**, 063318 (2022).
- ⁴⁷G. Anich, N. Höllrigl, M. Kreyer, R. Grimm, and E. Kirilov, “Comprehensive characterization of an apparatus for cold electromagnetic dysprosium dipoles”, *Phys. Rev. A* **110**, 023311 (2024).
- ⁴⁸H. J. Metcalf and P. Van der Straten, *Laser cooling and trapping*, Vol. 61 (Springer Science & Business Media, 1999), p. 051601.
- ⁴⁹F. Gerbier, J. H. Thywissen, S. Richard, M. Hugbart, P. Bouyer, and A. Aspect, “Critical temperature of a trapped, weakly interacting bose gas”, *Phys. Rev. Lett.* **92**, 030405 (2004).
- ⁵⁰L. R. Hofer, G. Lamb, P. Juhász, and R. P. Smith, “Interaction shift of the bose-einstein condensation temperature in a dipolar gas”, *Phys. Rev. A* **111**, L051303 (2025).
- ⁵¹M. A. Kristensen, M. B. Christensen, M. Gajdacz, M. Iglicki, K. Pawłowski, C. Klempt, J. F. Sherson, A. J. Hilliard, and J. J. Arlt, “Observation of atom number fluctuations in a bose-einstein condensate”, *Phys. Rev. Lett.* **122**, 163601 (2019).
- ⁵²M. K. Tey, L. A. Sidorenkov, E. R. S. Guajardo, R. Grimm, M. J. H. Ku, M. W. Zwierlein, Y.-H. Hou, L. Pitaevskii, and S. Stringari, “Collective modes in a unitary fermi gas across the superfluid phase transition”, *Phys. Rev. Lett.* **110**, 055303 (2013).

- ⁵³F. Chevy, V. Bretin, P. Rosenbusch, K. W. Madison, and J. Dalibard, “Transverse breathing mode of an elongated bose-einstein condensate”, *Phys. Rev. Lett.* **88**, 250402 (2002).
- ⁵⁴Z. Hadzibabic, P. Krüger, M. Cheneau, B. Battelier, and J. Dalibard, “Berezinskii–kosterlitz–thouless crossover in a trapped atomic gas”, *Nature* **441**, 1118–1121 (2006).
- ⁵⁵P. Cladé, C. Ryu, A. Ramanathan, K. Helmerson, and W. D. Phillips, “Observation of a 2d bose gas: from thermal to quasicondensate to superfluid”, *Phys. Rev. Lett.* **102**, 170401 (2009).
- ⁵⁶M. J. H. Ku, A. T. Sommer, L. W. Cheuk, and M. W. Zwierlein, “Revealing the superfluid lambda transition in the universal thermodynamics of a unitary fermi gas”, *Science* **335**, 563–567 (2012).
- ⁵⁷M. W. Zwierlein, C. A. Stan, C. H. Schunck, S. M. F. Raupach, A. J. Kerman, and W. Ketterle, “Condensation of pairs of fermionic atoms near a feshbach resonance”, *Phys. Rev. Lett.* **92**, 120403 (2004).
- ⁵⁸J. Sánchez-Baena, C. Politi, F. Maucher, F. Ferlaino, and T. Pohl, “Heating a dipolar quantum fluid into a solid”, *Nature communications* **14**, 1868 (2023).
- ⁵⁹N. Schlosser, G. Reymond, I. Protsenko, and P. Grangier, “Sub-poissonian loading of single atoms in a microscopic dipole trap”, *Nature* **411**, 1024–1027 (2001).
- ⁶⁰M. Greiner, O. Mandel, T. Esslinger, T. W. Hänsch, and I. Bloch, “Quantum phase transition from a superfluid to a mott insulator in a gas of ultracold atoms”, *Nature* **415**, 39–44 (2002).
- ⁶¹R. Jördens, N. Strohmaier, K. Günter, H. Moritz, and T. Esslinger, “A mott insulator of fermionic atoms in an optical lattice”, *Nature* **455**, 204–207 (2008).
- ⁶²Y.-i. Shin, C. H. Schunck, A. Schirotzek, and W. Ketterle, “Phase diagram of a two-component fermi gas with resonant interactions”, *Nature* **451**, 689–693 (2008).
- ⁶³N. Gemelke, X. Zhang, C.-L. Hung, and C. Chin, “In situ observation of incompressible mott-insulating domains in ultracold atomic gases”, *Nature* **460**, 995–998 (2009).
- ⁶⁴U. Schneider, L. Hackermüller, S. Will, T. Best, I. Bloch, T. A. Costi, R. W. Helmes, D. Rasch, and A. Rosch, “Metallic and insulating phases of repulsively interacting fermions in a 3d optical lattice”, *Science* **322**, 1520–1525 (2008).

- ⁶⁵H. Bernien, S. Schwartz, A. Keesling, H. Levine, A. Omran, H. Pichler, S. Choi, A. S. Zibrov, M. Endres, M. Greiner, V. Vuletić, and M. D. Lukin, “Probing many-body dynamics on a 51-atom quantum simulator”, *Nature* **551**, 579–584 (2017).
- ⁶⁶A. Mazurenko, C. S. Chiu, G. Ji, M. F. Parsons, M. Kanász-Nagy, R. Schmidt, F. Grusdt, E. Demler, D. Greif, and M. Greiner, “A cold-atom fermi–hubbard anti-ferromagnet”, *Nature* **545**, 462–466 (2017).
- ⁶⁷G. Semeghini, H. Levine, A. Keesling, S. Ebadi, T. T. Wang, D. Bluvstein, R. Verresen, H. Pichler, M. Kalinowski, R. Samajdar, A. Omran, S. Sachdev, A. Vishwanath, M. Greiner, V. Vuletić, and M. D. Lukin, “Probing topological spin liquids on a programmable quantum simulator”, *Science* **374**, 1242–1247 (2021).
- ⁶⁸Z. Meng, L. Wang, W. Han, F. Liu, K. Wen, C. Gao, P. Wang, C. Chin, and J. Zhang, “Atomic bose–einstein condensate in twisted-bilayer optical lattices”, *Nature* **615**, 231–236 (2023).
- ⁶⁹J. Zhang, Y.-J. Wang, B. Liu, L.-H. Zhang, Z.-Y. Zhang, S.-Y. Shao, Q. Li, H.-C. Chen, Y. Ma, T.-Y. Han, Q.-F. Wang, J.-D. Nan, Y.-M. Yin, D.-Y. Zhu, B.-S. Shi, and D.-S. Ding, *Dynamical topological phase transition in cold rydberg quantum gases*, 2024.
- ⁷⁰H. Kadau, M. Schmitt, M. Wenzel, C. Wink, T. Maier, I. Ferrier-Barbut, and T. Pfau, “Observing the rosenzweig instability of a quantum ferrofluid”, *Nature* **530**, 194–197 (2016).
- ⁷¹L. Chomaz, D. Petter, P. Ilzhöfer, G. Natale, A. Trautmann, C. Politi, G. Durantante, R. M. W. van Bijnen, A. Patscheider, M. Sohmen, M. J. Mark, and F. Ferlaino, “Long-lived and transient supersolid behaviors in dipolar quantum gases”, *Phys. Rev. X* **9**, 021012 (2019).
- ⁷²L. Tanzi, E. Lucioni, F. Famà, J. Catani, A. Fioretti, C. Gabbanini, R. N. Bisset, L. Santos, and G. Modugno, “Observation of a dipolar quantum gas with metastable supersolid properties”, *Phys. Rev. Lett.* **122**, 130405 (2019).
- ⁷³L. Su, A. Douglas, M. Szurek, R. Groth, S. F. Ozturk, A. Krahn, A. H. Hébert, G. A. Phelps, S. Ebadi, S. Dickerson, F. Ferlaino, O. Marković, and M. Greiner, “Dipolar quantum solids emerging in a hubbard quantum simulator”, *Nature* **622**, 724–729 (2023).
- ⁷⁴B. Mukherjee, A. Shaffer, P. B. Patel, Z. Yan, C. C. Wilson, V. Crépel, R. J. Fletcher, and M. Zwierlein, “Crystallization of bosonic quantum hall states in a rotating quantum gas”, *Nature* **601**, 58–62 (2022).
- ⁷⁵A. V. Kravtsov and S. Borgani, “Formation of galaxy clusters”, *Annual Review of Astronomy and Astrophysics* **50**, 353–409 (2012).

- ⁷⁶W. B. Thompson and J. Hubbard, “Long-range forces and the diffusion coefficients of a plasma”, *Rev. Mod. Phys.* **32**, 714–718 (1960).
- ⁷⁷M. M. Gromiha and S. Selvaraj, “Importance of long-range interactions in protein folding”, *Biophysical chemistry* **77**, 49–68 (1999).
- ⁷⁸V. Coropceanu, J. Cornil, D. A. da Silva Filho, Y. Olivier, R. Silbey, and J.-L. Brédas, “Charge transport in organic semiconductors”, *Chemical Reviews* **107**, PMID: 17378615, 926–952 (2007).
- ⁷⁹A. Campa, T. Dauxois, D. Fanelli, and S. Ruffo, *Physics of long-range interacting systems*, Vol. 122 (Oxford University Press, Aug. 2014), p. 163601.
- ⁸⁰L. D. Landau and E. M. Lifshitz, *Quantum mechanics: non-relativistic theory*, Vol. 3 (Elsevier, 2013), p. 163601.
- ⁸¹L. Landau, “On the conservation laws for weak interactions”, *Nuclear Physics* **3**, 127–131 (1957).
- ⁸²W. Bernreuther and M. Suzuki, “The electric dipole moment of the electron”, *Rev. Mod. Phys.* **63**, 313–340 (1991).
- ⁸³D. J. Gross, “The role of symmetry in fundamental physics”, *Proceedings of the National Academy of Sciences* **93**, 14256–14259 (1996).
- ⁸⁴W. Klemperer, K. K. Lehmann, J. K. G. Watson, and S. C. Wofsy, “Can molecules have permanent electric dipole moments?”, *The Journal of Physical Chemistry* **97**, 2413–2416 (1993).
- ⁸⁵T. E. Chupp, P. Fierlinger, M. J. Ramsey-Musolf, and J. T. Singh, “Electric dipole moments of atoms, molecules, nuclei, and particles”, *Rev. Mod. Phys.* **91**, 015001 (2019).
- ⁸⁶M. L. Wall, K. Maeda, and L. D. Carr, “Simulating quantum magnets with symmetric top molecules”, *Annalen der Physik* **525**, 845–865 (2013).
- ⁸⁷W Li, T Pohl, J. Rost, S. T. Rittenhouse, H. R. Sadeghpour, J Nipper, B. Butscher, J. Balewski, V Bendkowsky, R Löw, et al., “A homonuclear molecule with a permanent electric dipole moment”, *Science* **334**, 1110–1114 (2011).
- ⁸⁸A. Griesmaier, J. Werner, S. Hensler, J. Stuhler, and T. Pfau, “Bose-einstein condensation of chromium”, *Phys. Rev. Lett.* **94**, 160401 (2005).
- ⁸⁹K. Aikawa, A. Frisch, M. Mark, S. Baier, A. Rietzler, R. Grimm, and F. Ferlaino, “Bose-einstein condensation of erbium”, *Phys. Rev. Lett.* **108**, 210401 (2012).
- ⁹⁰K. Aikawa, A. Frisch, M. Mark, S. Baier, R. Grimm, and F. Ferlaino, “Reaching fermi degeneracy via universal dipolar scattering”, *Phys. Rev. Lett.* **112**, 010404 (2014).

- ⁹¹M. Lu, N. Q. Burdick, S. H. Youn, and B. L. Lev, “Strongly dipolar bose-einstein condensate of dysprosium”, *Phys. Rev. Lett.* **107**, 190401 (2011).
- ⁹²M. Lu, N. Q. Burdick, and B. L. Lev, “Quantum degenerate dipolar fermi gas”, *Phys. Rev. Lett.* **108**, 215301 (2012).
- ⁹³J. Miao, J. Hostetter, G. Stratis, and M. Saffman, “Magneto-optical trapping of holmium atoms”, *Phys. Rev. A* **89**, 041401 (2014).
- ⁹⁴D. Sukachev, A. Sokolov, K. Chebakov, A. Akimov, S. Kanorsky, N. Kolachevsky, and V. Sorokin, “Magneto-optical trap for thulium atoms”, *Phys. Rev. A* **82**, 011405 (2010).
- ⁹⁵R. Inoue, Y. Miyazawa, and M. Kozuma, “Magneto-optical trapping of optically pumped metastable europium”, *Phys. Rev. A* **97**, 061607 (2018).
- ⁹⁶M. Marinescu and L. You, “Controlling atom-atom interaction at ultralow temperatures by dc electric fields”, *Phys. Rev. Lett.* **81**, 4596–4599 (1998).
- ⁹⁷B. Deb and L. You, “Low-energy atomic collision with dipole interactions”, *Phys. Rev. A* **64**, 022717 (2001).
- ⁹⁸D. C. E. Bortolotti, S. Ronen, J. L. Bohn, and D. Blume, “Scattering length instability in dipolar bose-einstein condensates”, *Phys. Rev. Lett.* **97**, 160402 (2006).
- ⁹⁹K Aikawa, S Baier, A Frisch, M Mark, C Ravensbergen, and F Ferlaino, “Observation of fermi surface deformation in a dipolar quantum gas”, *Science* **345**, 1484–1487 (2014).
- ¹⁰⁰M. A. Baranov, M. S. Mar’enko, V. S. Rychkov, and G. V. Shlyapnikov, “Superfluid pairing in a polarized dipolar fermi gas”, *Phys. Rev. A* **66**, 013606 (2002).
- ¹⁰¹M. A. Baranov, Dobrek, and M Lewenstein, “Bcs pairing in a trapped dipolar fermi gas”, *New Journal of Physics* **6**, 198 (2004).
- ¹⁰²L. M. Sieberer and M. A. Baranov, “Collective modes, stability, and superfluid transition of a quasi-two-dimensional dipolar fermi gas”, *Phys. Rev. A* **84**, 063633 (2011).
- ¹⁰³A. Pikovski, M. Klawunn, G. V. Shlyapnikov, and L. Santos, “Interlayer superfluidity in bilayer systems of fermionic polar molecules”, *Phys. Rev. Lett.* **105**, 215302 (2010).
- ¹⁰⁴A. C. Potter, E. Berg, D.-W. Wang, B. I. Halperin, and E. Demler, “Superfluidity and dimerization in a multilayered system of fermionic polar molecules”, *Phys. Rev. Lett.* **105**, 220406 (2010).
- ¹⁰⁵N. R. Cooper and G. V. Shlyapnikov, “Stable topological superfluid phase of ultracold polar fermionic molecules”, *Phys. Rev. Lett.* **103**, 155302 (2009).

- ¹⁰⁶S. Baier, M. J. Mark, D. Petter, K. Aikawa, L. Chomaz, Z. Cai, M. Baranov, P. Zoller, and F. Ferlaino, “Extended bose-hubbard models with ultracold magnetic atoms”, *Science* **352**, 201–205 (2016).
- ¹⁰⁷A. de Paz, A. Sharma, A. Chotia, E. Maréchal, J. H. Huckans, P. Pedri, L. Santos, O. Gorceix, L. Vernac, and B. Laburthe-Tolra, “Nonequilibrium quantum magnetism in a dipolar lattice gas”, *Phys. Rev. Lett.* **111**, 185305 (2013).
- ¹⁰⁸P. Fersterer, A. Safavi-Naini, B. Zhu, L. Gabardos, S. Lepoutre, L. Vernac, B. Laburthe-Tolra, P. B. Blakie, and A. M. Rey, “Dynamics of an itinerant spin-3 atomic dipolar gas in an optical lattice”, *Phys. Rev. A* **100**, 033609 (2019).
- ¹⁰⁹L. Gabardos, B. Zhu, S. Lepoutre, A. M. Rey, B. Laburthe-Tolra, and L. Vernac, “Relaxation of the collective magnetization of a dense 3d array of interacting dipolar $S = 3$ atoms”, *Phys. Rev. Lett.* **125**, 143401 (2020).
- ¹¹⁰Y. A. Alaoui, B. Zhu, S. R. Muleady, W. Dubosclard, T. Roscilde, A. M. Rey, B. Laburthe-Tolra, and L. Vernac, “Measuring correlations from the collective spin fluctuations of a large ensemble of lattice-trapped dipolar spin-3 atoms”, *Phys. Rev. Lett.* **129**, 023401 (2022).
- ¹¹¹A. de Paz, P. Pedri, A. Sharma, M. Efremov, B. Naylor, O. Gorceix, E. Maréchal, L. Vernac, and B. Laburthe-Tolra, “Probing spin dynamics from the mott insulating to the superfluid regime in a dipolar lattice gas”, *Phys. Rev. A* **93**, 021603 (2016).
- ¹¹²Y. Aziz Alaoui, S. R. Muleady, E. Chaparro, Y. Trifa, A. M. Rey, T. Roscilde, B. Laburthe-Tolra, and L. Vernac, “Measuring bipartite spin correlations of lattice-trapped dipolar atoms”, *Phys. Rev. Lett.* **133**, 203401 (2024).
- ¹¹³S. Lepoutre, L. Gabardos, K. Kechadi, P. Pedri, O. Gorceix, E. Maréchal, L. Vernac, and B. Laburthe-Tolra, “Collective spin modes of a trapped quantum ferrofluid”, *Phys. Rev. Lett.* **121**, 013201 (2018).
- ¹¹⁴H. Matsui, Y. Miyazawa, R. Goto, C. Nakano, Y. Kawaguchi, M. Ueda, and M. Kozuma, *Observation of the einstein-de haas effect in a bose-einstein condensate*, 2025.
- ¹¹⁵E. Haller, M. Gustavsson, M. J. Mark, J. G. Danzl, R. Hart, G. Pupillo, and H.-C. Nägerl, “Realization of an excited, strongly correlated quantum gas phase”, *Science* **325**, 1224–1227 (2009).
- ¹¹⁶Y. Tang, W. Kao, K.-Y. Li, S. Seo, K. Mallayya, M. Rigol, S. Gopalakrishnan, and B. L. Lev, “Thermalization near integrability in a dipolar quantum newton’s cradle”, *Phys. Rev. X* **8**, 021030 (2018).

- ¹¹⁷W. Kao, K.-Y. Li, K.-Y. Lin, S. Gopalakrishnan, and B. L. Lev, “Topological pumping of a 1d dipolar gas into strongly correlated prethermal states”, *Science* **371**, 296–300 (2021).
- ¹¹⁸N. Liebster, M. Sparn, E. Kath, J. Duchene, H. Strobel, and M. K. Oberthaler, “Supersolid-like sound modes in a driven quantum gas”, *Nature Physics* **21**, 1064–1070 (2025).
- ¹¹⁹Bose, “Plancks gesetz und lichtquantenhypothese”, *Zeitschrift für Physik* **26**, 178–181 (1924).
- ¹²⁰A. Einstein, “Quantentheorie des einatomigen idealen gases, zweite abhandlung”, *Berliner Berichte* **122**, 3–14 (1925).
- ¹²¹L. D. Landau and E. M. Lifshitz, *Statistical physics: volume 5*, Vol. 5 (Elsevier, 2013), p. 163601.
- ¹²²W. C. Stwalley, “Stability of spin-aligned hydrogen at low temperatures and high magnetic fields: new field-dependent scattering resonances and predissociations”, *Phys. Rev. Lett.* **37**, 1628–1631 (1976).
- ¹²³J. L. Roberts, N. R. Claussen, J. P. Burke, C. H. Greene, E. A. Cornell, and C. E. Wieman, “Resonant magnetic field control of elastic scattering in cold ^{85}Rb ”, *Phys. Rev. Lett.* **81**, 5109–5112 (1998).
- ¹²⁴S. Inouye, M. R. Andrews, J. Stenger, H.-J. Miesner, D. M. Stamper-Kurn, and W. Ketterle, “Observation of feshbach resonances in a bose–einstein condensate”, *Nature* **392**, 151–154 (1998).
- ¹²⁵N Bogoliubov, “On the theory of superfluidity”, *J. Phys* **11**, 23 (1947).
- ¹²⁶E. P. Gross, “Structure of a quantized vortex in boson systems”, *Il Nuovo Cimento (1955-1965)* **20**, 454–477 (1961).
- ¹²⁷E. P. Gross, “Hydrodynamics of a superfluid condensate”, *Journal of Mathematical Physics* **4**, 195–207 (1963).
- ¹²⁸L. P. Pitaevskii, “Vortex lines in an imperfect bose gas”, *Sov. Phys. JETP* **13**, 451–454 (1961).
- ¹²⁹E. H. Lieb, R. Seiringer, and J. Yngvason, “Bosons in a trap: a rigorous derivation of the gross-pitaevskii energy functional”, *Phys. Rev. A* **61**, 043602 (2000).
- ¹³⁰N. Bigagli, W. Yuan, S. Zhang, B. Bulatovic, T. Karman, I. Stevenson, and S. Will, “Observation of bose–einstein condensation of dipolar molecules”, *Nature* **631**, 289–293 (2024).
- ¹³¹Y. Miyazawa, R. Inoue, H. Matsui, G. Nomura, and M. Kozuma, “Bose-einstein condensation of europium”, *Phys. Rev. Lett.* **129**, 223401 (2022).

- ¹³²S. Yi and L. You, “Trapped atomic condensates with anisotropic interactions”, *Phys. Rev. A* **61**, 041604 (2000).
- ¹³³S. Yi and L. You, “Trapped condensates of atoms with dipole interactions”, *Phys. Rev. A* **63**, 053607 (2001).
- ¹³⁴I. E. Mazets and G. Kurizki, “Modification of scattering lengths via magnetic dipole-dipole interactions”, *Phys. Rev. Lett.* **98**, 140401 (2007).
- ¹³⁵R. Ołdziejewski and K. Jachymski, “Erratum: properties of strongly dipolar bose gases beyond the born approximation [phys. rev. a 94, 063638 (2016)]”, *Phys. Rev. A* **95**, 049901 (2017).
- ¹³⁶A. Litvak, V. Mironov, G. Fraiman, and A. Yunakovskii, “Thermal self-effect of wave beams in a plasma with a nonlocal nonlinearity”, *Sov. J. Plasma Phys.(Engl. Transl.);(United States)* **1**, 163601 (1975).
- ¹³⁷C. Conti, M. Peccianti, and G. Assanto, “Route to nonlocality and observation of accessible solitons”, *Phys. Rev. Lett.* **91**, 073901 (2003).
- ¹³⁸D. H. J. O’Dell, S. Giovanazzi, and C. Eberlein, “Exact hydrodynamics of a trapped dipolar bose-einstein condensate”, *Phys. Rev. Lett.* **92**, 250401 (2004).
- ¹³⁹C. Eberlein, S. Giovanazzi, and D. H. J. O’Dell, “Exact solution of the thomas-fermi equation for a trapped bose-einstein condensate with dipole-dipole interactions”, *Phys. Rev. A* **71**, 033618 (2005).
- ¹⁴⁰J. Stuhler, A. Griesmaier, T. Koch, M. Fattori, T. Pfau, S. Giovanazzi, P. Pedri, and L. Santos, “Observation of dipole-dipole interaction in a degenerate quantum gas”, *Phys. Rev. Lett.* **95**, 150406 (2005).
- ¹⁴¹D. Petter, G. Natale, R. M. W. van Bijnen, A. Patscheider, M. J. Mark, L. Chomaz, and F. Ferlaino, “Probing the roton excitation spectrum of a stable dipolar bose gas”, *Phys. Rev. Lett.* **122**, 183401 (2019).
- ¹⁴²L. Landau, “Theory of the superfluidity of helium ii”, *Phys. Rev.* **60**, 356–358 (1941).
- ¹⁴³L Landau, “On the theory of superfluidity of helium ii”, *J. Phys* **11**, 91–92 (1947).
- ¹⁴⁴L. Santos, G. V. Shlyapnikov, and M. Lewenstein, “Roton-maxon spectrum and stability of trapped dipolar bose-einstein condensates”, *Phys. Rev. Lett.* **90**, 250403 (2003).
- ¹⁴⁵D. H. J. O’Dell, S. Giovanazzi, and G. Kurizki, “Rotons in gaseous bose-einstein condensates irradiated by a laser”, *Phys. Rev. Lett.* **90**, 110402 (2003).

- ¹⁴⁶J. Hertkorn, J.-N. Schmidt, F. Böttcher, M. Guo, M. Schmidt, K. S. H. Ng, S. D. Graham, H. P. Büchler, T. Langen, M. Zwierlein, and T. Pfau, “Density fluctuations across the superfluid-supersolid phase transition in a dipolar quantum gas”, *Phys. Rev. X* **11**, 011037 (2021).
- ¹⁴⁷J.-N. Schmidt, J. Hertkorn, M. Guo, F. Böttcher, M. Schmidt, K. S. H. Ng, S. D. Graham, T. Langen, M. Zwierlein, and T. Pfau, “Roton excitations in an oblate dipolar quantum gas”, *Phys. Rev. Lett.* **126**, 193002 (2021).
- ¹⁴⁸C. Mishra and R. Nath, “Dipolar condensates with tilted dipoles in a pancake-shaped confinement”, *Phys. Rev. A* **94**, 033633 (2016).
- ¹⁴⁹R. Nath and L. Santos, “Faraday patterns in two-dimensional dipolar bose-einstein condensates”, *Phys. Rev. A* **81**, 033626 (2010).
- ¹⁵⁰K. Łakomy, R. Nath, and L. Santos, “Faraday patterns in coupled one-dimensional dipolar condensates”, *Phys. Rev. A* **86**, 023620 (2012).
- ¹⁵¹S. Ronen, D. C. E. Bortolotti, and J. L. Bohn, “Radial and angular rotons in trapped dipolar gases”, *Phys. Rev. Lett.* **98**, 030406 (2007).
- ¹⁵²T. D. Lee, K. Huang, and C. N. Yang, “Eigenvalues and eigenfunctions of a bose system of hard spheres and its low-temperature properties”, *Phys. Rev.* **106**, 1135–1145 (1957).
- ¹⁵³T. D. Lee and C. N. Yang, “Many-body problem in quantum mechanics and quantum statistical mechanics”, *Phys. Rev.* **105**, 1119–1120 (1957).
- ¹⁵⁴L. Pitaevskii and S. Stringari, *Bose-einstein condensation and superfluidity*, Vol. 164 (Oxford University Press, 2016), p. 163601.
- ¹⁵⁵M. Ueda, *Fundamentals and new frontiers of bose-einstein condensation*, Vol. 122 (World Scientific, 2010), p. 163601.
- ¹⁵⁶R. SCHÜTZHOLD, M. UHLMANN, Y. XU, and U. R. FISCHER, “Mean-field expansion in bose–einstein condensates with finite-range interactions”, *International Journal of Modern Physics B* **20**, 3555–3565 (2006).
- ¹⁵⁷A. R. P. Lima and A. Pelster, “Quantum fluctuations in dipolar bose gases”, *Phys. Rev. A* **84**, 041604(R) (2011).
- ¹⁵⁸A. R. P. Lima and A. Pelster, “Beyond mean-field low-lying excitations of dipolar bose gases”, *Phys. Rev. A* **86**, 063609 (2012).
- ¹⁵⁹M. Bender, P.-H. Heenen, and P.-G. Reinhard, “Self-consistent mean-field models for nuclear structure”, *Rev. Mod. Phys.* **75**, 121–180 (2003).

- ¹⁶⁰F. Dalfovo and S. Stringari, “Helium nanodroplets and trapped bose–einstein condensates as prototypes of finite quantum fluids”, *The Journal of Chemical Physics* **115**, 10078–10089 (2001).
- ¹⁶¹D. S. Petrov, “Quantum mechanical stabilization of a collapsing bose-bose mixture”, *Phys. Rev. Lett.* **115**, 155302 (2015).
- ¹⁶²C. R. Cabrera, L. Tanzi, J. Sanz, B. Naylor, P. Thomas, P. Cheiney, and L. Tarruell, “Quantum liquid droplets in a mixture of bose-einstein condensates”, *Science* **359**, 301 (2018).
- ¹⁶³G. Semeghini, G. Ferioli, L. Masi, C. Mazzinghi, L. Wolswijk, F. Minardi, M. Modugno, G. Modugno, M. Inguscio, and M. Fattori, “Self-bound quantum droplets of atomic mixtures in free space”, *Phys. Rev. Lett.* **120**, 235301 (2018).
- ¹⁶⁴I. Ferrier-Barbut, M. Schmitt, M. Wenzel, H. Kadau, and T. Pfau, “Liquid quantum droplets of ultracold magnetic atoms”, *Journal of Physics B: Atomic, Molecular and Optical Physics* **49**, 214004 (2016).
- ¹⁶⁵R. N. Bisset, R. M. Wilson, D. Baillie, and P. B. Blakie, “Ground-state phase diagram of a dipolar condensate with quantum fluctuations”, *Phys. Rev. A* **94**, 033619 (2016).
- ¹⁶⁶D. Baillie and P. B. Blakie, “Droplet crystal ground states of a dipolar bose gas”, *Phys. Rev. Lett.* **121**, 195301 (2018).
- ¹⁶⁷F. Wächtler and L. Santos, “Quantum filaments in dipolar bose-einstein condensates”, *Phys. Rev. A* **93**, 061603(R) (2016).
- ¹⁶⁸L. Chomaz, S. Baier, D. Petter, M. J. Mark, F. Wächtler, L. Santos, and F. Ferlaino, “Quantum-fluctuation-driven crossover from a dilute bose-einstein condensate to a macrodroplet in a dipolar quantum fluid”, *Phys. Rev. X* **6**, 041039 (2016).
- ¹⁶⁹K. E. Strecker, G. B. Partridge, A. G. Truscott, and R. G. Hulet, “Bright matter wave solitons in bose–einstein condensates”, *New Journal of Physics* **5**, 73 (2003).
- ¹⁷⁰K. E. Strecker, G. B. Partridge, A. G. Truscott, and R. G. Hulet, “Formation and propagation of matter-wave soliton trains”, *Nature* **417**, 150–153 (2002).
- ¹⁷¹P. Pedri and L. Santos, “Two-dimensional bright solitons in dipolar bose-einstein condensates”, *Phys. Rev. Lett.* **95**, 200404 (2005).
- ¹⁷²I. Tikhonenkov, B. A. Malomed, and A. Vardi, “Anisotropic solitons in dipolar bose-einstein condensates”, *Phys. Rev. Lett.* **100**, 090406 (2008).
- ¹⁷³M. Raghunandan, C. Mishra, K. Łakomy, P. Pedri, L. Santos, and R. Nath, “Two-dimensional bright solitons in dipolar bose-einstein condensates with tilted dipoles”, *Phys. Rev. A* **92**, 013637 (2015).

- ¹⁷⁴F. Maucher, N. Henkel, M. Saffman, W. Królikowski, S. Skupin, and T. Pohl, “Rydberg-induced solitons: three-dimensional self-trapping of matter waves”, *Phys. Rev. Lett.* **106**, 170401 (2011).
- ¹⁷⁵D. Edler, C. Mishra, F. Wächtler, R. Nath, S. Sinha, and L. Santos, “Quantum fluctuations in quasi-one-dimensional dipolar bose-einstein condensates”, *Phys. Rev. Lett.* **119**, 050403 (2017).
- ¹⁷⁶P. Cheiney, C. R. Cabrera, J. Sanz, B. Naylor, L. Tanzi, and L. Tarruell, “Bright soliton to quantum droplet transition in a mixture of bose-einstein condensates”, *Phys. Rev. Lett.* **120**, 135301 (2018).
- ¹⁷⁷M. Boninsegni and N. V. Prokof'ev, “Colloquium: supersolids: what and where are they?”, *Rev. Mod. Phys.* **84**, 759–776 (2012).
- ¹⁷⁸P. Kapitza, “Viscosity of liquid helium below the λ -point”, *Nature* **141**, 74–74 (1938).
- ¹⁷⁹J. F. Allen and A. Misener, “Flow phenomena in liquid helium ii”, *Nature* **142**, 643–644 (1938).
- ¹⁸⁰L. TISZA, “Transport phenomena in helium ii”, *Nature* **141**, 913–913 (1938).
- ¹⁸¹A. J. Leggett, *Quantum liquids: bose condensation and cooper pairing in condensed-matter systems*, Vol. 122 (Oxford university press, 2006), p. 163601.
- ¹⁸²E. P. Gross, “Unified theory of interacting bosons”, *Phys. Rev.* **106**, 161–162 (1957).
- ¹⁸³O. Penrose and L. Onsager, “Bose-einstein condensation and liquid helium”, *Phys. Rev.* **104**, 576–584 (1956).
- ¹⁸⁴M. A. Kristensen, M. B. Christensen, M. Gajdacz, M. Iglicki, K. Pawłowski, C. Klempt, J. F. Sherson, A. J. Hilliard, and J. J. Arlt, “Observation of atom number fluctuations in a bose-einstein condensate”, *Phys. Rev. Lett.* **122**, 163601 (2019).
- ¹⁸⁵G. V. Chester, “Speculations on bose-einstein condensation and quantum crystals”, *Phys. Rev. A* **2**, 256–258 (1970).
- ¹⁸⁶A. J. Leggett, “Can a solid be "superfluid"?", *Phys. Rev. Lett.* **25**, 1543–1546 (1970).
- ¹⁸⁷E. Kim and M. H. W. Chan, “Probable observation of a supersolid helium phase”, *Nature* **427**, 225–227 (2004).
- ¹⁸⁸D. Y. Kim and M. H. W. Chan, “Absence of supersolidity in solid helium in porous vycor glass”, *Phys. Rev. Lett.* **109**, 155301 (2012).

- ¹⁸⁹J.-R. Li, J. Lee, W. Huang, S. Burchesky, B. Shteynas, F. Ç. Top, A. O. Jamison, and W. Ketterle, “A stripe phase with supersolid properties in spin–orbit-coupled bose–einstein condensates”, *Nature* **543**, 91–94 (2017).
- ¹⁹⁰J. Léonard, A. Morales, P. Zupancic, T. Esslinger, and T. Donner, “Supersolid formation in a quantum gas breaking a continuous translational symmetry”, *Nature* **543**, 87–90 (2017).
- ¹⁹¹G. Biagioni, N. Antolini, A. Alaña, M. Modugno, A. Fioretti, C. Gabbanini, L. Tanzi, and G. Modugno, “Dimensional crossover in the superfluid-supersolid quantum phase transition”, *Phys. Rev. X* **12**, 021019 (2022).
- ¹⁹²A. Alaña, N. Antolini, G. Biagioni, I. n. L. Egusquiza, and M. Modugno, “Crossing the superfluid-supersolid transition of an elongated dipolar condensate”, *Phys. Rev. A* **106**, 043313 (2022).
- ¹⁹³A. Alaña, I. n. L. Egusquiza, and M. Modugno, “Supersolid formation in a dipolar condensate by roton instability”, *Phys. Rev. A* **108**, 033316 (2023).
- ¹⁹⁴G. Natale, R. M. W. van Bijnen, A. Patscheider, D. Petter, M. J. Mark, L. Chomaz, and F. Ferlaino, “Excitation spectrum of a trapped dipolar supersolid and its experimental evidence”, *Phys. Rev. Lett.* **123**, 050402 (2019).
- ¹⁹⁵S. M. Roccuzzo and F. Ancilotto, “Supersolid behavior of a dipolar bose-einstein condensate confined in a tube”, *Phys. Rev. A* **99**, 041601 (2019).
- ¹⁹⁶D. Petter, A. Patscheider, G. Natale, M. J. Mark, M. A. Baranov, R. van Bijnen, S. M. Roccuzzo, A. Recati, B. Blakie, D. Baillie, L. Chomaz, and F. Ferlaino, “Bragg scattering of an ultracold dipolar gas across the phase transition from bose-einstein condensate to supersolid in the free-particle regime”, *Phys. Rev. A* **104**, L011302 (2021).
- ¹⁹⁷J. Hertkorn, F. Böttcher, M. Guo, J. N. Schmidt, T. Langen, H. P. Büchler, and T. Pfau, “Fate of the amplitude mode in a trapped dipolar supersolid”, *Phys. Rev. Lett.* **123**, 193002 (2019).
- ¹⁹⁸L. Tanzi, S. Roccuzzo, E. Lucioni, F. Famà, A. Fioretti, C. Gabbanini, G. Modugno, A. Recati, and S. Stringari, “Supersolid symmetry breaking from compressional oscillations in a dipolar quantum gas”, *Nature* **574**, 382–385 (2019).
- ¹⁹⁹M. Guo, F. Böttcher, J. Hertkorn, J.-N. Schmidt, M. Wenzel, H. P. Büchler, T. Langen, and T. Pfau, “The low-energy goldstone mode in a trapped dipolar supersolid”, *Nature* **574**, 386–389 (2019).
- ²⁰⁰L. Tanzi, J. G. Maloberti, G. Biagioni, A. Fioretti, C. Gabbanini, and G. Modugno, “Evidence of superfluidity in a dipolar supersolid from nonclassical rotational inertia”, *Science* **371**, 1162–1165 (2021).

- ²⁰¹G Biagioni, N Antolini, B Donelli, L Pezzè, A Smerzi, M Fattori, A Fioretti, C Gabbanini, M Inguscio, L Tanzi, et al., “Measurement of the superfluid fraction of a supersolid by josephson effect”, *Nature* **122**, 1–5 (2024).
- ²⁰²Y.-C. Zhang, F. Maucher, and T. Pohl, “Supersolidity around a critical point in dipolar bose-einstein condensates”, *Phys. Rev. Lett.* **123**, 015301 (2019).
- ²⁰³J. Hertkorn, J.-N. Schmidt, M. Guo, F. Böttcher, K. S. H. Ng, S. D. Graham, P. Uerlings, T. Langen, M. Zwierlein, and T. Pfau, “Pattern formation in quantum ferrofluids: from supersolids to superglasses”, *Phys. Rev. Res.* **3**, 033125 (2021).
- ²⁰⁴M. A. Norcia, C. Politi, L. Klaus, E. Poli, M. Sohmen, M. J. Mark, R. N. Bisset, L. Santos, and F. Ferlaino, “Two-dimensional supersolidity in a dipolar quantum gas”, *Nature* **596**, 357–361 (2021).
- ²⁰⁵T. Bland, E. Poli, C. Politi, L. Klaus, M. A. Norcia, F. Ferlaino, L. Santos, and R. N. Bisset, “Two-dimensional supersolid formation in dipolar condensates”, *Phys. Rev. Lett.* **128**, 195302 (2022).
- ²⁰⁶E. Poli, T. Bland, C. Politi, L. Klaus, M. A. Norcia, F. Ferlaino, R. N. Bisset, and L. Santos, “Maintaining supersolidity in one and two dimensions”, *Phys. Rev. A* **104**, 063307 (2021).
- ²⁰⁷L. Onsager, “Statistical hydrodynamics”, *Il Nuovo Cimento (1943-1954)* **6**, 279–287 (1949).
- ²⁰⁸R. P. Feynman, “Chapter ii application of quantum mechanics to liquid helium”, in *Progress in low temperature physics*, Vol. 1 (Elsevier, 1955), pp. 17–53.
- ²⁰⁹W. Fiszdon, “Quantized vortices in helium ii. by r. j. donnelly. cambridge university press, 1991. 346 pp. £95.”, *Journal of Fluid Mechanics* **233**, 691–692 (1991).
- ²¹⁰E. J. Yarmchuk, M. J. V. Gordon, and R. E. Packard, “Observation of stationary vortex arrays in rotating superfluid helium”, *Phys. Rev. Lett.* **43**, 214–217 (1979).
- ²¹¹G. P. Bewley, D. P. Lathrop, and K. R. Sreenivasan, “Visualization of quantized vortices”, *Nature* **441**, 588–588 (2006).
- ²¹²J. R. Abo-Shaer, C. Raman, J. M. Vogels, and W. Ketterle, “Observation of vortex lattices in bose-einstein condensates”, *Science* **292**, 476–479 (2001).
- ²¹³M. W. Zwierlein, J. R. Abo-Shaer, A. Schirotzek, C. H. Schunck, and W. Ketterle, “Vortices and superfluidity in a strongly interacting fermi gas”, *Nature* **435**, 1047–1051 (2005).
- ²¹⁴G. BAYM, C. PETHICK, and D. PINES, “Superfluidity in neutron stars”, *Nature* **224**, 673–674 (1969).

- ²¹⁵D. Pines and M. A. Alpar, “Superfluidity in neutron stars”, *Nature* **316**, 27–32 (1985).
- ²¹⁶M. R. Matthews, B. P. Anderson, P. C. Haljan, D. S. Hall, C. E. Wieman, and E. A. Cornell, “Vortices in a bose-einstein condensate”, *Phys. Rev. Lett.* **83**, 2498–2501 (1999).
- ²¹⁷K. W. Madison, F. Chevy, W. Wohlleben, and J. Dalibard, “Vortex formation in a stirred bose-einstein condensate”, *Phys. Rev. Lett.* **84**, 806–809 (2000).
- ²¹⁸C. Raman, J. R. Abo-Shaeer, J. M. Vogels, K. Xu, and W. Ketterle, “Vortex nucleation in a stirred bose-einstein condensate”, *Phys. Rev. Lett.* **87**, 210402 (2001).
- ²¹⁹J. R. Abo-Shaeer, C. Raman, and W. Ketterle, “Formation and decay of vortex lattices in bose-einstein condensates at finite temperatures”, *Phys. Rev. Lett.* **88**, 070409 (2002).
- ²²⁰B. P. Anderson, P. C. Haljan, C. A. Regal, D. L. Feder, L. A. Collins, C. W. Clark, and E. A. Cornell, “Watching dark solitons decay into vortex rings in a bose-einstein condensate”, *Phys. Rev. Lett.* **86**, 2926–2929 (2001).
- ²²¹T. W. Neely, E. C. Samson, A. S. Bradley, M. J. Davis, and B. P. Anderson, “Observation of vortex dipoles in an oblate bose-einstein condensate”, *Phys. Rev. Lett.* **104**, 160401 (2010).
- ²²²P. C. Haljan, I. Coddington, P. Engels, and E. A. Cornell, “Driving bose-einstein condensate vorticity with a rotating normal cloud”, *Phys. Rev. Lett.* **87**, 210403 (2001).
- ²²³P. Engels, I. Coddington, P. C. Haljan, and E. A. Cornell, “Nonequilibrium effects of anisotropic compression applied to vortex lattices in bose-einstein condensates”, *Phys. Rev. Lett.* **89**, 100403 (2002).
- ²²⁴S. Beattie, S. Moulder, R. J. Fletcher, and Z. Hadzibabic, “Persistent currents in spinor condensates”, *Phys. Rev. Lett.* **110**, 025301 (2013).
- ²²⁵W. J. Kwon, G. Del Pace, K. Xhani, L. Galantucci, A. Muzi Falconi, M. Inguscio, F. Scazza, and G. Roati, “Sound emission and annihilations in a programmable quantum vortex collider”, *Nature* **600**, 64–69 (2021).
- ²²⁶N. Navon, A. L. Gaunt, R. P. Smith, and Z. Hadzibabic, “Emergence of a turbulent cascade in a quantum gas”, *Nature* **539**, 72–75 (2016).
- ²²⁷E. A. L. Henn, J. A. Seman, G. Roati, K. M. F. Magalhães, and V. S. Bagnato, “Emergence of turbulence in an oscillating bose-einstein condensate”, *Phys. Rev. Lett.* **103**, 045301 (2009).

- ²²⁸Y.-J. Lin, R. L. Compton, K. Jiménez-García, J. V. Porto, and I. B. Spielman, “Synthetic magnetic fields for ultracold neutral atoms”, *Nature* **462**, 628–632 (2009).
- ²²⁹D. R. Scherer, C. N. Weiler, T. W. Neely, and B. P. Anderson, “Vortex formation by merging of multiple trapped bose-einstein condensates”, *Phys. Rev. Lett.* **98**, 110402 (2007).
- ²³⁰M. Aidelsburger, J. L. Ville, R. Saint-Jalm, S. Nascimbène, J. Dalibard, and J. Beugnon, “Relaxation dynamics in the merging of N independent condensates”, *Phys. Rev. Lett.* **119**, 190403 (2017).
- ²³¹J.-y. Choi, S. W. Seo, and Y.-i. Shin, “Observation of thermally activated vortex pairs in a quasi-2d bose gas”, *Phys. Rev. Lett.* **110**, 175302 (2013).
- ²³²V. Schweikhard, S. Tung, and E. A. Cornell, “Vortex proliferation in the berezinskii-kosterlitz-thouless regime on a two-dimensional lattice of bose-einstein condensates”, *Phys. Rev. Lett.* **99**, 030401 (2007).
- ²³³L. Klaus, T. Bland, E. Poli, C. Politi, G. Lamporesi, E. Casotti, R. N. Bisset, M. J. Mark, and F. Ferlaino, “Observation of vortices and vortex stripes in a dipolar condensate”, *Nature Physics* **18**, 1453–1458 (2022).
- ²³⁴A. M. Martin, N. G. Marchant, D. H. J. O’Dell, and N. G. Parker, “Vortices and vortex lattices in quantum ferrofluids”, *Journal of Physics: Condensed Matter* **29**, 103004 (2017).
- ²³⁵S. Yi and H. Pu, “Vortex structures in dipolar condensates”, *Phys. Rev. A* **73**, 061602 (2006).
- ²³⁶B. C. Mulkerin, R. M. W. van Bijnen, D. H. J. O’Dell, A. M. Martin, and N. G. Parker, “Anisotropic and long-range vortex interactions in two-dimensional dipolar bose gases”, *Phys. Rev. Lett.* **111**, 170402 (2013).
- ²³⁷Y. Cai, Y. Yuan, M. Rosenkranz, H. Pu, and W. Bao, “Vortex patterns and the critical rotational frequency in rotating dipolar bose-einstein condensates”, *Phys. Rev. A* **98**, 023610 (2018).
- ²³⁸N. R. Cooper, E. H. Rezayi, and S. H. Simon, “Vortex lattices in rotating atomic bose gases with dipolar interactions”, *Phys. Rev. Lett.* **95**, 200402 (2005).
- ²³⁹J. Zhang and H. Zhai, “Vortex lattices in planar bose-einstein condensates with dipolar interactions”, *Phys. Rev. Lett.* **95**, 200403 (2005).
- ²⁴⁰S. Komineas and N. R. Cooper, “Vortex lattices in bose-einstein condensates with dipolar interactions beyond the weak-interaction limit”, *Phys. Rev. A* **75**, 023623 (2007).

- ²⁴¹R. M. W. van Bijnen, D. H. J. O'Dell, N. G. Parker, and A. M. Martin, "Dynamical instability of a rotating dipolar bose-einstein condensate", *Phys. Rev. Lett.* **98**, 150401 (2007).
- ²⁴²S. B. Prasad, T. Bland, B. C. Mulkerin, N. G. Parker, and A. M. Martin, "Instability of rotationally tuned dipolar bose-einstein condensates", *Phys. Rev. Lett.* **122**, 050401 (2019).
- ²⁴³D. Baillie and P. B. Blakie, "Rotational tuning of the dipole-dipole interaction in a bose gas of magnetic atoms", *Phys. Rev. A* **101**, 043606 (2020).
- ²⁴⁴E. Casotti, E. Poli, L. Klaus, A. Litvinov, C. Ulm, C. Politi, M. J. Mark, T. Bland, and F. Ferlaino, "Observation of vortices in a dipolar supersolid", *Nature* **635**, 327–331 (2024).
- ²⁴⁵N. Henkel, F. Cinti, P. Jain, G. Pupillo, and T. Pohl, "Supersolid vortex crystals in rydberg-dressed bose-einstein condensates", *Phys. Rev. Lett.* **108**, 265301 (2012).
- ²⁴⁶S. M. Roccuzzo, A. Gallemí, A. Recati, and S. Stringari, "Rotating a supersolid dipolar gas", *Phys. Rev. Lett.* **124**, 045702 (2020).
- ²⁴⁷A. Gallemí, S. M. Roccuzzo, S. Stringari, and A. Recati, "Quantized vortices in dipolar supersolid bose-einstein-condensed gases", *Phys. Rev. A* **102**, 023322 (2020).
- ²⁴⁸A. Gallemí and L. Santos, "Superfluid properties of a honeycomb dipolar supersolid", *Phys. Rev. A* **106**, 063301 (2022).
- ²⁴⁹F. Ancilotto, M. Barranco, M. Pi, and L. Reatto, "Vortex properties in the extended supersolid phase of dipolar bose-einstein condensates", *Phys. Rev. A* **103**, 033314 (2021).
- ²⁵⁰E. Poli, A. Litvinov, E. Casotti, C. Ulm, L. Klaus, M. J. Mark, G. Lamporesi, T. Bland, and F. Ferlaino, *Synchronization in rotating supersolids*, 2024.
- ²⁵¹E. Poli, T. Bland, S. J. M. White, M. J. Mark, F. Ferlaino, S. Trabucco, and M. Mannarelli, "Glitches in rotating supersolids", *Phys. Rev. Lett.* **131**, 223401 (2023).
- ²⁵²R. Ghosh, M. Ciardi, R. Nath, and F. Cinti, "Path integral monte carlo study of a doubly dipolar bose gas", *Phys. Rev. B* **110**, 014513 (2024).
- ²⁵³J. Aldegunde, and J. M. Hutson, "Ultracold rbsr molecules can be formed by magnetoassociation", *Phys. Rev. Lett.* **105**, 153201 (2010).
- ²⁵⁴M. Tomza, R. González-Férez, C. P. Koch, and R. Moszynski, "Controlling magnetic feshbach resonances in polar open-shell molecules with nonresonant light", *Phys. Rev. Lett.* **112**, 113201 (2014).

- ²⁵⁵B. Pasquiou, A. Bayerle, S. M. Tzanova, S. Stellmer, J. Szczepkowski, M. Parigger, R. Grimm, and F. Schreck, “Quantum degenerate mixtures of strontium and rubidium atoms”, *Phys. Rev. A* **88**, 023601 (2013).
- ²⁵⁶J. F. Barry, D. J. McCarron, E. B. Norrgard, M. H. Steinecker, and D. DeMille, “Magneto-optical trapping of a diatomic molecule”, *Nature* **512**, 286 (2014).
- ²⁵⁷A. Khramov, A. Hansen, W. Dowd, R. J. Roy, C. Makrides, A. Petrov, S. Kotochigova, and S. Gupta, “Ultracold heteronuclear mixture of ground and excited state atoms”, *Phys. Rev. Lett.* **112**, 033201 (2014).
- ²⁵⁸T. M. Rvachov, H. Son, A. T. Sommer, S. Ebadi, J. J. Park, M. W. Zwierlein, W. Ketterle, and A. O. Jamison, “Long-lived ultracold molecules with electric and magnetic dipole moments”, *Phys. Rev. Lett.* **119**, 143001 (2017).
- ²⁵⁹D. Reens, H. Wu, T. Langen, and J. Ye, “Controlling spin flips of molecules in an electromagnetic trap”, *Phys. Rev. A* **96**, 063420 (2017).
- ²⁶⁰A. Guttridge, S. A. Hopkins, M. D. Frye, J. J. McFerran, J. M. Hutson, and S. L. Cornish, “Production of ultracold Cs*Yb molecules by photoassociation”, *Phys. Rev. A* **97**, 063414 (2018).
- ²⁶¹A. Micheli, G. K. Brennen, and P. Zoller, “A toolbox for lattice-spin models with polar molecules”, *Nature Physics* **2**, 341–347 (2006).
- ²⁶²S. L. Cornish, M. R. Tarbutt, and K. R. A. Hazzard, *Quantum computation and quantum simulation with ultracold molecules*, 2024.
- ²⁶³M. Karra, K. Sharma, B. Friedrich, S. Kais, and D. Herschbach, “Prospects for quantum computing with an array of ultracold polar paramagnetic molecules”, *The Journal of Chemical Physics* **144**, 094301 (2016).
- ²⁶⁴M. Hughes, M. D. Frye, R. Sawant, G. Bhole, J. A. Jones, S. L. Cornish, M. R. Tarbutt, J. M. Hutson, D. Jaksch, and J. Mur-Petit, “Robust entangling gate for polar molecules using magnetic and microwave fields”, *Phys. Rev. A* **101**, 062308 (2020).
- ²⁶⁵J. J. Hudson, D. M. Kara, I. J. Smallman, B. E. Sauer, M. R. Tarbutt, and E. A. Hinds, “Improved measurement of the shape of the electron”, *Nature* **473**, 493–496 (2011).
- ²⁶⁶E. Abrahamsson, T. V. Tscherbul, and R. V. Krems, “Inelastic collisions of cold polar molecules in nonparallel electric and magnetic fields”, *The Journal of Chemical Physics* **127**, 044302 (2007).

- ²⁶⁷J. J. Park, Y.-K. Lu, A. O. Jamison, T. V. Tscherbul, and W. Ketterle, “A feshbach resonance in collisions between triplet ground-state molecules”, *Nature* **614**, 54–58 (2023).
- ²⁶⁸S. Finelli, A. Ciamei, B. Restivo, M. Schemmer, A. Cosco, M. Inguscio, A. Trenkwalder, K. Zaremba-Kopczyk, M. Gronowski, M. Tomza, and M. Zaccanti, “Ultracold LiCr: a new pathway to quantum gases of paramagnetic polar molecules”, *PRX Quantum* **5**, 020358 (2024).
- ²⁶⁹T. Maier, I. Ferrier-Barbut, H. Kadau, M. Schmitt, M. Wenzel, C. Wink, T. Pfau, K. Jachymski, and P. S. Julienne, “Broad universal feshbach resonances in the chaotic spectrum of dysprosium atoms”, *Phys. Rev. A* **92**, 060702 (2015).
- ²⁷⁰N. Leefer, A. Cingöz, and D. Budker, “Measurement of hyperfine structure and isotope shifts in the dy 421 nm transition”, *Opt. Lett.* **34**, 2548–2550 (2009).
- ²⁷¹F. Wächtler and L. Santos, “Ground-state properties and elementary excitations of quantum droplets in dipolar bose-einstein condensates”, *Phys. Rev. A* **94**, 043618 (2016).
- ²⁷²H. Saito, “Path-integral monte carlo study on a droplet of a dipolar bose–einstein condensate stabilized by quantum fluctuation”, *J. Phys. Soc. Jap.* **85**, 053001 (2016).
- ²⁷³L.-J. He, F. Maucher, and Y.-C. Zhang, “Infrared cutoff for dipolar droplets”, *Phys. Rev. A* **110**, 053316 (2024).
- ²⁷⁴D. Baillie, R. M. Wilson, and P. B. Blakie, “Collective excitations of self-bound droplets of a dipolar quantum fluid”, *Phys. Rev. Lett.* **119**, 255302 (2017).
- ²⁷⁵A. Macia, J. Sánchez-Baena, J. Boronat, and F. Mazzanti, “Droplets of trapped quantum dipolar bosons”, *Phys. Rev. Lett.* **117**, 205301 (2016).
- ²⁷⁶F. Cinti, A. Cappellaro, L. Salasnich, and T. Macrì, “Superfluid filaments of dipolar bosons in free space”, *Phys. Rev. Lett.* **119**, 215302 (2017).
- ²⁷⁷F. Cinti and M. Boninsegni, “Classical and quantum filaments in the ground state of trapped dipolar bose gases”, *Phys. Rev. A* **96**, 013627 (2017).
- ²⁷⁸C. Staudinger, F. Mazzanti, and R. E. Zillich, “Self-bound bose mixtures”, *Phys. Rev. A* **98**, 023633 (2018).
- ²⁷⁹G. E. Astrakharchik, and J. Boronat, “Universality in ultradilute liquid bose-bose mixtures”, *Phys. Rev. A* **99**, 023618 (2019).
- ²⁸⁰F. Böttcher, M. Wenzel, J.-N. Schmidt, M. Guo, T. Langen, I. Ferrier-Barbut, T. Pfau, R. Bombín, J. Sánchez-Baena, J. Boronat, and F. Mazzanti, “Dilute dipolar quantum droplets beyond the extended gross-pitaevskii equation”, *Phys. Rev. Research* **1**, 033088 (2019).

- ²⁸¹R. K. Kumar, L. E. Young-S., D. Vudragović, A. Balaž, P. Muruganandam, and S. Adhikari, “Fortran and c programs for the time-dependent dipolar gross–pitaevskii equation in an anisotropic trap”, *Computer Physics Communications* **195**, 117–128 (2015).
- ²⁸²D. M. Ceperley, “Path integrals in the theory of condensed helium”, *Rev. Mod. Phys.* **67**, 279–355 (1995).
- ²⁸³P. Jain, F. Cinti, and M. Boninsegni, “Structure, bose-einstein condensation, and superfluidity of two-dimensional confined dipolar assemblies”, *Phys. Rev. B* **84**, 014534 (2011).
- ²⁸⁴K. Nho and D. P. Landau, “Bose-einstein condensation of trapped atoms with dipole interactions”, *Phys. Rev. A* **72**, 023615 (2005).
- ²⁸⁵M. Boninsegni, “Morphology of dipolar bose droplets”, *Results in Physics* **31**, 104935 (2021).
- ²⁸⁶R. P. Feynman, *Statistical mechanics: a set of lectures*, Vol. 99 (Westview Press, 1998), p. 023618.
- ²⁸⁷L. Schulman, *Techniques and applications of path integration*, Vol. 99, Dover Books on Physics (Dover Publications, 2012), p. 023618.
- ²⁸⁸N. V. Prokof’ev, B. V. Svistunov, and I. S. Tupitsyn, “Exact, complete, and universal continuous-time worldline monte carlo approach to the statistics of discrete quantum systems”, *Journal of Experimental and Theoretical Physics* **87**, 310–321 (1998).
- ²⁸⁹M. Boninsegni, N. Prokof’ev, and B. Svistunov, “Worm algorithm for continuous-space path integral monte carlo simulations”, *Phys. Rev. Lett.* **96**, 070601 (2006).
- ²⁹⁰M. Boninsegni, N. V. Prokof’ev, and B. V. Svistunov, “Worm algorithm and diagrammatic monte carlo: a new approach to continuous-space path integral monte carlo simulations”, *Phys. Rev. E* **74**, 036701 (2006).
- ²⁹¹J. Cao and B. J. Berne, “A new quantum propagator for hard sphere and cavity systems”, *The Journal of Chemical Physics* **97**, 2382–2385 (1992).
- ²⁹²H. P. Büchler, E. Demler, M. Lukin, A. Micheli, N. Prokof’ev, G. Pupillo, and P. Zoller, “Strongly correlated 2d quantum phases with cold polar molecules: controlling the shape of the interaction potential”, *Phys. Rev. Lett.* **98**, 060404 (2007).
- ²⁹³A. Filinov, N. V. Prokof’ev, and M. Bonitz, “Berezinskii-kosterlitz-thouless transition in two-dimensional dipole systems”, *Phys. Rev. Lett.* **105**, 070401 (2010).

- ²⁹⁴T. Dornheim, “Path-integral monte carlo simulations of quantum dipole systems in traps: superfluidity, quantum statistics, and structural properties”, *Phys. Rev. A* **102**, 023307 (2020).
- ²⁹⁵F. Cinti and M. Boninsegni, “Absence of superfluidity in 2d dipolar bose striped crystals”, *Journal of Low Temperature Physics* **196**, 413–422 (2019).
- ²⁹⁶M. Ciardi, “Correlated phases of bosons in novel geometries”, PhD thesis (U. Florence (main), 2024), p. 023618.
- ²⁹⁷P. Sindzingre, M. L. Klein, and D. M. Ceperley, “Path-integral monte carlo study of low-temperature ^4He clusters”, *Phys. Rev. Lett.* **63**, 1601–1604 (1989).
- ²⁹⁸T. Zeng and P.-N. Roy, “Microscopic molecular superfluid response: theory and simulations”, *Reports on Progress in Physics* **77**, 046601 (2014).
- ²⁹⁹I. Ferrier-Barbut, H. Kadau, M. Schmitt, M. Wenzel, and T. Pfau, “Observation of quantum droplets in a strongly dipolar bose gas”, *Phys. Rev. Lett.* **116**, 215301 (2016).
- ³⁰⁰W. Krauth, “Quantum monte carlo calculations for a large number of bosons in a harmonic trap”, *Phys. Rev. Lett.* **77**, 3695–3699 (1996).
- ³⁰¹S. Pilati, K. Sakkos, J. Boronat, J. Casulleras, and S. Giorgini, “Equation of state of an interacting bose gas at finite temperature: a path-integral monte carlo study”, *Phys. Rev. A* **74**, 043621 (2006).
- ³⁰²M. Holzmann, W. Krauth, and M. Naraschewski, “Precision monte carlo test of the hartree-fock approximation for a trapped bose gas”, *Phys. Rev. A* **59**, 2956–2961 (1999).
- ³⁰³Y. Kora and M. Boninsegni, “Patterned supersolids in dipolar bose systems”, *Journal of Low Temperature Physics* **197**, 337–347 (2019).
- ³⁰⁴K. Nho and D. P. Landau, “Finite-temperature properties of quasi-two-dimensional bose-einstein condensates”, *Phys. Rev. A* **73**, 033606 (2006).
- ³⁰⁵P. Grüter, D. Ceperley, and F. Laloë, “Critical temperature of bose-einstein condensation of hard-sphere gases”, *Phys. Rev. Lett.* **79**, 3549–3552 (1997).
- ³⁰⁶K. Nho and D. P. Landau, “Bose-einstein condensation temperature of a homogeneous weakly interacting bose gas: path integral monte carlo study”, *Phys. Rev. A* **70**, 053614 (2004).
- ³⁰⁷T. T. Nguyen, A. J. Herrmann, M. Troyer, and S. Pilati, “Critical temperature of interacting bose gases in periodic potentials”, *Phys. Rev. Lett.* **112**, 170402 (2014).

- ³⁰⁸M. Holzmann and Y. Castin, “Pair correlation function of an inhomogeneous interacting bose-einstein condensate”, *The European Physical Journal D-Atomic, Molecular, Optical and Plasma Physics* **7**, 425–432 (1999).
- ³⁰⁹F. Cinti, P. Jain, M. Boninsegni, A. Micheli, P. Zoller, and G. Pupillo, “Supersolid droplet crystal in a dipole-blockaded gas”, *Phys. Rev. Lett.* **105**, 135301 (2010).
- ³¹⁰F. Cinti, T. Macrì, W. Lechner, G. Pupillo, and T. Pohl, “Defect-induced supersolidity with soft-core bosons”, *Nat. Commun.* **5**, 3235 (2014).
- ³¹¹G. Spada, S. Pilati, and S. Giorgini, “Attractive solution of binary bose mixtures: liquid-vapor coexistence and critical point”, *Phys. Rev. Lett.* **131**, 173404 (2023).
- ³¹²R. Gautier, H. Yao, and L. Sanchez-Palencia, “Strongly interacting bosons in a two-dimensional quasicrystal lattice”, *Phys. Rev. Lett.* **126**, 110401 (2021).
- ³¹³M. Ciardi, T. Macrì, and F. Cinti, “Finite-temperature phases of trapped bosons in a two-dimensional quasiperiodic potential”, *Phys. Rev. A* **105**, L011301 (2022).
- ³¹⁴M. Ciardi, A. Angelone, F. Mezzacapo, and F. Cinti, “Quasicrystalline bose glass in the absence of disorder and quasidisorder”, *Phys. Rev. Lett.* **131**, 173402 (2023).
- ³¹⁵V. M. Pérez-García, H. Michinel, J. I. Cirac, M. Lewenstein, and P. Zoller, “Dynamics of bose-einstein condensates: variational solutions of the gross-pitaevskii equations”, *Phys. Rev. A* **56**, 1424–1432 (1997).
- ³¹⁶P. Ilzhöfer, M. Sohmen, G. Durastante, C. Politi, A. Trautmann, G. Natale, G. Morpurgo, T. Giamarchi, L. Chomaz, M. Mark, et al., “Phase coherence in out-of-equilibrium supersolid states of ultracold dipolar atoms”, *Nature Physics* **17**, 356–361 (2021).
- ³¹⁷L.-J. He, J. Sánchez-Baena, F. Maucher, and Y.-C. Zhang, “Accessing elusive two-dimensional phases of dipolar bose-einstein condensates by finite temperature”, *Phys. Rev. Res.* **7**, 023019 (2025).
- ³¹⁸P. B. Blakie, D. Baillie, and S. Pal, “Variational theory for the ground state and collective excitations of an elongated dipolar condensate”, *Communications in Theoretical Physics* **72**, 085501 (2020).
- ³¹⁹T. Bland, E. Poli, L. A. P. n. Ardila, L. Santos, F. Ferlaino, and R. N. Bisset, “Alternating-domain supersolids in binary dipolar condensates”, *Phys. Rev. A* **106**, 053322 (2022).
- ³²⁰S. Pal, D. Baillie, and P. B. Blakie, “Excitations and number fluctuations in an elongated dipolar bose-einstein condensate”, *Phys. Rev. A* **102**, 043306 (2020).
- ³²¹D. Baillie and P. B. Blakie, “A general theory of flattened dipolar condensates”, *New Journal of Physics* **17**, 033028 (2015).

- ³²²D. Trypogeorgos, A. Gianfrate, M. Landini, D. Nigro, D. Gerace, I. Carusotto, F. Riminucci, K. W. Baldwin, L. N. Pfeiffer, G. I. Martone, M. De Giorgi, D. Ballarini, and D. Sanvitto, “Emerging supersolidity in photonic-crystal polariton condensates”, *Nature* **639**, 337–341 (2025).
- ³²³Y.-C. Zhang, T. Pohl, and F. Maucher, “Phases of supersolids in confined dipolar bose-einstein condensates”, *Phys. Rev. A* **104**, 013310 (2021).
- ³²⁴B. T. E. Ripley, D. Baillie, and P. B. Blakie, “Two-dimensional supersolidity in a planar dipolar bose gas”, *Phys. Rev. A* **108**, 053321 (2023).
- ³²⁵Y. Pomeau and S. Rica, “Dynamics of a model of supersolid”, *Phys. Rev. Lett.* **72**, 2426–2429 (1994).
- ³²⁶F. Böttcher, J.-N. Schmidt, J. Hertkorn, K. S. H. Ng, S. D. Graham, M. Guo, T. Langen, and T. Pfau, “New states of matter with fine-tuned interactions: quantum droplets and dipolar supersolids”, *Reports on Progress in Physics* **84**, 012403 (2020).
- ³²⁷A. Recati and S. Stringari, “Supersolidity in ultracold dipolar gases”, *Nature Reviews Physics* **5**, 735–743 (2023).
- ³²⁸D. H. J. O’Dell and C. Eberlein, “Vortex in a trapped bose-einstein condensate with dipole-dipole interactions”, *Phys. Rev. A* **75**, 013604 (2007).
- ³²⁹R. K. Kumar, T. Sriraman, H. Fabrelli, P. Muruganandam, and A. Gammal, “Three-dimensional vortex structures in a rotating dipolar bose–einstein condensate”, *Journal of Physics B: Atomic, Molecular and Optical Physics* **49**, 155301 (2016).
- ³³⁰M. N. Tengstrand, D. Boholm, R. Sachdeva, J. Bengtsson, and S. M. Reimann, “Persistent currents in toroidal dipolar supersolids”, *Phys. Rev. A* **103**, 013313 (2021).
- ³³¹S. B. Prasad, B. C. Mulkerin, and A. M. Martin, “Arbitrary-angle rotation of the polarization of a dipolar bose-einstein condensate”, *Phys. Rev. A* **103**, 033322 (2021).
- ³³²J. J. García-Ripoll and V. M. Pérez-García, “Anomalous rotational properties of bose-einstein condensates in asymmetric traps”, *Phys. Rev. A* **64**, 013602 (2001).
- ³³³E. Lundh, J.-P. Martikainen, and K.-A. Suominen, “Vortex nucleation in bose-einstein condensates in time-dependent traps”, *Phys. Rev. A* **67**, 063604 (2003).
- ³³⁴S. Ghosh and R. Sachdeva, *Synthetic gauge fields for ultra cold atoms: a primer*, 2014.
- ³³⁵S. Giovanazzi, A. Görlitz, and T. Pfau, “Tuning the dipolar interaction in quantum gases”, *Phys. Rev. Lett.* **89**, 130401 (2002).

- ³³⁶T. Bland, G. Lamporesi, M. J. Mark, and F. Ferlaino, “Vortices in dipolar Bose–Einstein condensates”, en, *Comptes Rendus. Physique* **24**, 133–152 (2023).
- ³³⁷A. L. Fetter, “Rotating trapped bose-einstein condensates”, *Rev. Mod. Phys.* **81**, 647–691 (2009).
- ³³⁸H. T. Stoof, K. B. Gubbels, and D. Dickerscheid, *Ultracold quantum fields*, Vol. 99 (Springer, 2009), p. 023618.
- ³³⁹M. Abad, M. Guilleumas, R. Mayol, M. Pi, and D. M. Jezek, “Vortices in bose-einstein condensates with dominant dipolar interactions”, *Phys. Rev. A* **79**, 063622 (2009).
- ³⁴⁰M. N. Tengstrand, D. Bohlm, R. Sachdeva, J. Bengtsson, and S. M. Reimann, “Persistent currents in toroidal dipolar supersolids”, *Phys. Rev. A* **103**, 013313 (2021).
- ³⁴¹H. S. Ghosh, S. Halder, S. Das, and S. Majumder, “Induced supersolidity and hypersonic flow of a dipolar bose-einstein condensate in a rotating bubble trap”, *Phys. Rev. A* **110**, 033322 (2024).
- ³⁴²A. L. Fetter, “Vortex nucleation in deformed rotating cylinders”, *Journal of Low Temperature Physics* **16**, 533–555 (1974).
- ³⁴³M. Linn, M. Niemeyer, and A. L. Fetter, “Vortex stabilization in a small rotating asymmetric bose-einstein condensate”, *Phys. Rev. A* **64**, 023602 (2001).
- ³⁴⁴R. Landig, F. Brennecke, R. Mottl, T. Donner, and T. Esslinger, “Measuring the dynamic structure factor of a quantum gas undergoing a structural phase transition”, *Nature Communications* **6**, 7046 (2015).
- ³⁴⁵J. Hofmann and W. Zwerger, “Universal relations for dipolar quantum gases”, *Phys. Rev. Res.* **3**, 013088 (2021).
- ³⁴⁶S. Sinha and G. V. Shlyapnikov, “Two-dimensional bose-einstein condensate under extreme rotation”, *Phys. Rev. Lett.* **94**, 150401 (2005).
- ³⁴⁷S. Sinha and Y. Castin, “Dynamic instability of a rotating bose-einstein condensate”, *Phys. Rev. Lett.* **87**, 190402 (2001).
- ³⁴⁸L. Du, P. Barral, M. Cantara, J. de Hond, Y.-K. Lu, and W. Ketterle, “Atomic physics on a 50-nm scale: realization of a bilayer system of dipolar atoms”, *Science* **384**, 546–551 (2024).
- ³⁴⁹S. Nadiger, S. M. Jose, R. Ghosh, I. Kaur, and R. Nath, “Stripe and checkerboard patterns in a stack of driven quasi-one-dimensional dipolar condensates”, *Phys. Rev. A* **109**, 033309 (2024).

- ³⁵⁰P. Nayak, R. Ghosh, and R. Nath, “Density engineering via intercondensate dipole-dipole interactions”, *Phys. Rev. A* **110**, 053319 (2024).
- ³⁵¹G. Hegde, P. Nayak, R. Ghosh, and R. Nath, “Soliton dimer–soliton scattering in coupled quasi-one-dimensional dipolar bose–einstein condensates”, *Journal of Physics B: Atomic, Molecular and Optical Physics* **54**, 205301 (2021).
- ³⁵²Y. Jin, K. Shen, P. Ju, X. Gao, C. Zu, A. J. Grine, and T. Li, “Quantum control and berry phase of electron spins in rotating levitated diamonds in high vacuum”, *Nature Communications* **15**, 5063 (2024).
- ³⁵³J. E. Campbell, “On a law of combination of operators (second paper)”, *Proceedings of the London Mathematical Society* **s1-29**, 14–32 (1897).
- ³⁵⁴H. F. Trotter, “On the product of semi-groups of operators”, *Proceedings of the American Mathematical Society* **10**, 545–551 (1959).
- ³⁵⁵H.-J. Bär and P. Bopp, “M. h. kalos and p. a. whitlock: monte carlo methods, volume i: basics, john wiley and sons, new york, chichester, brisbane, toronto and singapore 1986, library of congress qa298.k35 1986. 186 seiten mit einem index, preis: £ 29.00”, *Berichte der Bunsengesellschaft für physikalische Chemie* **92**, 560–560 (1988).
- ³⁵⁶E. P. Bernard, W. Krauth, and D. B. Wilson, “Event-chain monte carlo algorithms for hard-sphere systems”, *Phys. Rev. E* **80**, 056704 (2009).



American Physical Society Reuse and Permissions License

25-Jul-2025

This license agreement between the American Physical Society ("APS") and Ratheejit Ghosh ("You") consists of your license details and the terms and conditions provided by the American Physical Society and SciPris.

Licensed Content Information

License Number: RNP/25/JUL/093834
License date: 25-Jul-2025
DOI: 10.1103/PhysRevA.106.063318
Title: Droplet arrays in doubly dipolar Bose-Einstein condensates
Author: Ratheejit Ghosh et al.
Publication: Physical Review A
Publisher: American Physical Society
Cost: USD \$ 0.00

Request Details

Does your reuse require significant modifications: No
Specify intended distribution locations: Worldwide
Reuse Category: Reuse in a thesis/dissertation
Requestor Type: Author of requested content
Items for Reuse: Whole Article
Format for Reuse: Print and Electronic
Total number of print copies: Up to 1000

Information about New Publication:

University/Publisher: Indian Institute of Science Education and Research, Pune
Title of dissertation/thesis: Droplets and Supersolids in Dipolar Bose-Einstein Condensates
Author(s): Ratheejit Ghosh
Expected completion date: Jul. 2025

License Requestor Information

Name: Ratheejit Ghosh
Affiliation: Individual
Email Id: ratheejit.ghosh@students.iiserpune.ac.in
Country: India



American Physical Society Reuse and Permissions License

25-Jul-2025

This license agreement between the American Physical Society ("APS") and Ratheejit Ghosh ("You") consists of your license details and the terms and conditions provided by the American Physical Society and SciPris.

Licensed Content Information

License Number: RNP/25/JUL/093835
License date: 25-Jul-2025
DOI: 10.1103/PhysRevB.110.014513
Title: Path integral Monte Carlo study of a doubly dipolar Bose gas
Author: Ratheejit Ghosh et al.
Publication: Physical Review B
Publisher: American Physical Society
Cost: USD \$ 0.00

Request Details

Does your reuse require significant modifications: No
Specify intended distribution locations: Worldwide
Reuse Category: Reuse in a thesis/dissertation
Requestor Type: Author of requested content
Items for Reuse: Whole Article
Format for Reuse: Print and Electronic
Total number of print copies: Up to 1000

Information about New Publication:

University/Publisher: Indian Institute of Science Education and Research, Pune
Title of dissertation/thesis: Droplets and Supersolids in Dipolar Bose-Einstein Condensates
Author(s): Ratheejit Ghosh
Expected completion date: Jul. 2025

License Requestor Information

Name: Ratheejit Ghosh
Affiliation: Individual
Email Id: ratheejit.ghosh@students.iiserpune.ac.in
Country: India



American Physical Society Reuse and Permissions License

16-Jul-2025

This license agreement between the American Physical Society ("APS") and Ratheejit Ghosh ("You") consists of your license details and the terms and conditions provided by the American Physical Society and SciPris.

Licensed Content Information

License Number: RNP/25/JUL/093556
License date: 16-Jul-2025
DOI: 10.1103/PhysRevLett.107.190401
Title: Strongly Dipolar Bose-Einstein Condensate of Dysprosium
Author: Mingwu Lu et al.
Publication: Physical Review Letters
Publisher: American Physical Society
Cost: USD \$ 0.00

Request Details

Does your reuse require significant modifications: No
Specify intended distribution locations: Worldwide
Reuse Category: Reuse in a thesis/dissertation
Requestor Type: Student
Items for Reuse: Figures/Tables
Number of Figure/Tables: 1
Figure/Tables Details: Fig.2: TOF profiles of the spin-purified Dy gas for three evaporation time constants
Format for Reuse: Electronic and Print
Total number of print copies: Up to 1000

Information about New Publication:

University/Publisher: Indian Institute of Science Education and Research, Pune
Title of dissertation/thesis: Droplets and Supersolids in Dipolar Bose-Einstein Condensates
Author(s): Ratheejit Ghosh
Expected completion date: Jul. 2025

License Requestor Information

Name: Ratheejit Ghosh
Affiliation: Individual
Email Id: ratheejit.ghosh@students.iiserpune.ac.in
Country: India



American Physical Society Reuse and Permissions License

16-Jul-2025

This license agreement between the American Physical Society ("APS") and Ratheejit Ghosh ("You") consists of your license details and the terms and conditions provided by the American Physical Society and SciPris.

Licensed Content Information

License Number: RNP/25/JUL/093557
License date: 16-Jul-2025
DOI: 10.1103/PhysRevLett.108.215301
Title: Quantum Degenerate Dipolar Fermi Gas
Author: Mingwu Lu, Nathaniel Q. Burdick, and Benjamin L. Lev
Publication: Physical Review Letters
Publisher: American Physical Society
Cost: USD \$ 0.00

Request Details

Does your reuse require significant modifications: No
Specify intended distribution locations: Worldwide
Reuse Category: Reuse in a thesis/dissertation
Requestor Type: Student
Items for Reuse: Figures/Tables
Number of Figure/Tables: 1
Figure/Tables Details: Fig.2: Single shot time-of-flight absorption image
Format for Reuse: Print and Electronic
Total number of print copies: Up to 1000

Information about New Publication:

University/Publisher: Indian Institute of Science Education and Reserach, Pune
Title of dissertation/thesis: Droplets and Supersolids in Dipolar Bose-Einstein Condensates
Author(s): Ratheejit Ghosh
Expected completion date: Jul. 2025

License Requestor Information

Name: Ratheejit Ghosh
Affiliation: Individual
Email Id: ratheejit.ghosh@students.iiserpune.ac.in
Country: India

SPRINGER NATURE LICENSE
TERMS AND CONDITIONS

Jul 16, 2025

This Agreement between Ratheejit Ghosh ("You") and Springer Nature ("Springer Nature") consists of your license details and the terms and conditions provided by Springer Nature and Copyright Clearance Center.

License Number	6070881037761
License date	Jul 16, 2025
Licensed Content Publisher	Springer Nature
Licensed Content Publication	Nature
Licensed Content Title	Observation of Bose–Einstein condensation of dipolar molecules
Licensed Content Author	Niccolò Bigagli et al
Licensed Content Date	Jun 3, 2024
Type of Use	Thesis/Dissertation
Requestor type	academic/university or research institute
Format	print and electronic
Portion	figures/tables/illustrations
Number of figures/tables/illustrations	1
Would you like a high resolution image with your order?	no

Will you be translating?	no
Circulation/distribution	1 - 29
Author of this Springer Nature content	no
Title of new work	Droplets and Supersolids in Dipolar Bose-Einstein Condensates
Institution name	Indian Institute of Science Education and Research, Pune
Expected presentation date	Jul 2025
Portions	Figure 1
The Requesting Person / Organization to Appear on the License	Ratheejit Ghosh
Requestor Location	Mr. Ratheejit Ghosh IISER Pune hostel 2 IISER Internal road IISER Internal road Pune, IISER PUNE 411008 India
Billing Type	Invoice
Billing Address	Mr. Ratheejit Ghosh IISER Pune hostel 2 IISER Internal road IISER Internal road Pune, India 411008
Total	0.00 USD
Terms and Conditions	

Springer Nature Customer Service Centre GmbH Terms and Conditions

The following terms and conditions ("Terms and Conditions") together with the terms specified in your [RightsLink] constitute the License ("License") between you as Licensee and Springer Nature Customer Service Centre GmbH as Licensor. By clicking 'accept' and completing the transaction for your use of the material ("Licensed

**SPRINGER NATURE LICENSE
TERMS AND CONDITIONS**

Jul 16, 2025

This Agreement between Ratheejit Ghosh ("You") and Springer Nature ("Springer Nature") consists of your license details and the terms and conditions provided by Springer Nature and Copyright Clearance Center.

License Number	6070810330222
License date	Jul 16, 2025
Licensed Content Publisher	Springer Nature
Licensed Content Publication	Nature
Licensed Content Title	Observing the Rosensweig instability of a quantum ferrofluid
Licensed Content Author	Holger Kadau et al
Licensed Content Date	Feb 1, 2016
Type of Use	Thesis/Dissertation
Requestor type	academic/university or research institute
Format	print and electronic
Portion	figures/tables/illustrations
Number of figures/tables/illustrations	1
Would you like a high resolution image with your order?	no

Will you be translating?	no
Circulation/distribution	1 - 29
Author of this Springer Nature content	no
Title of new work	Droplets and Supersolids in Dipolar Bose-Einstein Condensates
Institution name	Indian Institute of Science Education and Research, Pune
Expected presentation date	Jul 2025
Portions	Figure 1.
The Requesting Person / Organization to Appear on the License	Ratheejit Ghosh
Requestor Location	IISER Pune hostel 2 IISER Internal road IISER Internal road PUNE, IISER PUNE 411008 India
Billing Type	Invoice
Billing Address	Mr. Ratheejit Ghosh IISER Pune hostel 2 IISER Internal road Pashan PUNE, India 411008
Total	0.00 USD
Terms and Conditions	

Springer Nature Customer Service Centre GmbH Terms and Conditions

The following terms and conditions ("Terms and Conditions") together with the terms specified in your [RightsLink] constitute the License ("License") between you as Licensee and Springer Nature Customer Service Centre GmbH as Licensor. By clicking 'accept' and completing the transaction for your use of the material ("Licensed

**SPRINGER NATURE LICENSE
TERMS AND CONDITIONS**

Jul 23, 2025

This Agreement between Ratheejit Ghosh ("You") and Springer Nature ("Springer Nature") consists of your license details and the terms and conditions provided by Springer Nature and Copyright Clearance Center.

License Number	6074801485556
License date	Jul 23, 2025
Licensed Content Publisher	Springer Nature
Licensed Content Publication	Nature
Licensed Content Title	Observation of vortices in a dipolar supersolid
Licensed Content Author	Eva Casotti et al
Licensed Content Date	Nov 6, 2024
Type of Use	Thesis/Dissertation
Requestor type	academic/university or research institute
Format	print and electronic
Portion	figures/tables/illustrations
Number of figures/tables/illustrations	1
Would you like a high resolution image with your order?	no

Will you be translating?	no
Circulation/distribution	1 - 29
Author of this Springer Nature content	no
Title of new work	Droplets and Supersolids in Dipolar Bose-Einstein Condensates
Institution name	Indian Institute of Science Education and Research, Pune
Expected presentation date	Jul 2025
Portions	Figure 3\2. Magnetostirring.
The Requesting Person / Organization to Appear on the License	Ratheejit Ghosh
Requestor Location	Mr. Ratheejit Ghosh IISER Pune hostel 2 IISER Internal road IISER Internal road Pune, IISER PUNE 411008 India
Billing Type	Invoice
Billing Address	Mr. Ratheejit Ghosh IISER Pune hostel 2 IISER Internal road IISER Internal road Pune, India 411008
Total	0.00 USD
Terms and Conditions	

Springer Nature Customer Service Centre GmbH Terms and Conditions

The following terms and conditions ("Terms and Conditions") together with the terms specified in your [RightsLink] constitute the License ("License") between you as Licensee and Springer Nature Customer Service Centre GmbH as Licensor. By clicking 'accept' and completing the transaction for your use of the material ("Licensed



American Physical Society Reuse and Permissions License

23-Jul-2025

This license agreement between the American Physical Society ("APS") and Ratheejit Ghosh ("You") consists of your license details and the terms and conditions provided by the American Physical Society and SciPris.

Licensed Content Information

License Number: RNP/25/JUL/093728
License date: 23-Jul-2025
DOI: 10.1103/PhysRevLett.122.183401
Title: Probing the Roton Excitation Spectrum of a Stable Dipolar Bose Gas
Author: D. Petter et al.
Publication: Physical Review Letters
Publisher: American Physical Society
Cost: USD \$ 0.00

Request Details

Does your reuse require significant modifications: No
Specify intended distribution locations: Worldwide
Reuse Category: Reuse in a thesis/dissertation
Requestor Type: Student
Items for Reuse: Figures/Tables
Number of Figure/Tables: 1
Figure/Tables Details: Fig. 2. Excitation spectra
Format for Reuse: Print and Electronic
Total number of print copies: Up to 1000

Information about New Publication:

University/Publisher: Indian Institute of Science Education and Research, Pune
Title of dissertation/thesis: Droplets and Supersolids in Dipolar Bose-Einstein Condensates
Author(s): Ratheejit Ghosh
Expected completion date: Jul. 2025

License Requestor Information

Name: Ratheejit Ghosh
Affiliation: Individual
Email Id: ratheejit.ghosh@students.iiserpune.ac.in
Country: India



American Physical Society Reuse and Permissions License

17-Jul-2025

This license agreement between the American Physical Society ("APS") and Ratheejit Ghosh ("You") consists of your license details and the terms and conditions provided by the American Physical Society and SciPris.

Licensed Content Information

License Number: RNP/25/JUL/093585
License date: 17-Jul-2025
DOI: 10.1103/PhysRevA.110.023311
Title: Comprehensive characterization of an apparatus for cold electromagnetic dysprosium dipoles
Author: Gregor Anich et al.
Publication: Physical Review A
Publisher: American Physical Society
Cost: USD \$ 0.00

Request Details

Does your reuse require significant modifications: No
Specify intended distribution locations: Worldwide
Reuse Category: Reuse in a thesis/dissertation
Requestor Type: Student
Items for Reuse: Figures/Tables
Number of Figure/Tables: 1
Figure/Tables Details: Figure 1. Relevant atomic states and optical transitions used in the experiment.
Format for Reuse: Print and Electronic
Total number of print copies: Up to 1000

Information about New Publication:

University/Publisher: Indian Institute of Science Education and Research, Pune
Title of dissertation/thesis: Droplets and Supersolids in Dipolar Bose-Einstein Condensates
Author(s): Ratheejit Ghosh
Expected completion date: Jul. 2025

License Requestor Information

Name: Ratheejit Ghosh
Affiliation: Individual
Email Id: ratheejit.ghosh@students.iiserpune.ac.in
Country: India